



HAL
open science

Controlling earthQuakes (CoQuake) in the laboratory using pertinent fault stimulating techniques

Georgios Tzortzopoulos

► **To cite this version:**

Georgios Tzortzopoulos. Controlling earthQuakes (CoQuake) in the laboratory using pertinent fault stimulating techniques. Civil Engineering. École centrale de Nantes, 2021. English. NNT : 2021ECDN0060 . tel-03670423

HAL Id: tel-03670423

<https://theses.hal.science/tel-03670423>

Submitted on 17 May 2022

HAL is a multi-disciplinary open access archive for the deposit and dissemination of scientific research documents, whether they are published or not. The documents may come from teaching and research institutions in France or abroad, or from public or private research centers.

L'archive ouverte pluridisciplinaire **HAL**, est destinée au dépôt et à la diffusion de documents scientifiques de niveau recherche, publiés ou non, émanant des établissements d'enseignement et de recherche français ou étrangers, des laboratoires publics ou privés.

THÈSE DE DOCTORAT DE

L'ÉCOLE CENTRALE DE NANTES

ÉCOLE DOCTORALE N° 602
Sciences pour l'Ingénieur
Spécialité : *Génie Civil*

Par

Georgios TZORTZOPOULOS

**Controlling earthQuakes (CoQuake) in the laboratory
using pertinent fault stimulating techniques**

Thèse présentée et soutenue à l'École Centrale de Nantes, le 17 Décembre 2021
Unité de recherche : UMR 6183, Institut de recherche en Génie Civil et Mécanique (GeM)

Rapporteurs avant soutenance :

André NIEMEIJER Professeur associé, Utrecht University, Pays-Bas
Gioacchino VIGGIANI Professeur des universités, Université Grenoble Alpes, France

Composition du Jury :

Président :	Franck PLESTAN	Professeur des universités, École Centrale de Nantes, France
Examineurs :	Jean-Philippe AVOUAC	Professeur, California Institute of Technology, États-Unis
	Rachel GELET	Maître de conférences, Université de Nantes, France
	Ares ROSAKIS	Professeur, California Institute of Technology, États-Unis
	Jean-François SEMBLAT	Professeur, ENSTA Paris, France
Dir. de thèse :	Ioannis STEFANOOU	Professeur des universités, École Centrale de Nantes, France

Acknowledgment: This work was supported by the European Research Council (ERC) under the European Union Horizon 2020 research and innovation program (Grant agreement no. 757848 CoQuake), <http://coquake.com>.



CoQuake.com



European Research Council
Established by the European Commission



*Some people want it to happen,
some wish it would happen,
others **make it happen.***

Michael Jordan



Acknowledgements

This manuscript encapsulates 3 years of intense work in the CoQuake (ERC) project. This journey was started in the Navier laboratory of ENPC (Paris, France) and it was finished in the GeM laboratory of ECN (Nantes, France). During this period, I had the pleasure to interact with many people who supported and advised me. Therefore, this part of my thesis is devoted to them.

First and foremost, I would like to thank my thesis director and supervisor Prof. Ioannis Stefanou for our long discussions as well as for his support and guidance whenever I needed help. The example he sets as a mentor is one I will try to aspire to in my future career.

Next, I would like to acknowledge the members of my PhD committee for their acceptance to evaluate my work and for their active participation during my defense. More specifically, I would like to thank the two reviewers, Prof. André Niemeijer and Prof. Gioacchino Viggiani, for the time they devoted to read and comment my thesis. Moreover, I want to thank the remaining members of my committee, the president of the jury Prof. Franck Plestan and the examiners Prof. Jean-Philippe Avouac, Dr. Rachel Gelet, Prof. Ares Rosakis and Prof. Jean-François Semblat, for the stimulating questions and remarks they raised during my defense.

Now it's time to thank my colleagues in the CoQuake group with whom I was spending most of my time in the lab and with some of them I was closely collaborating: Philipp, Timos, Alex, Filippo, Pravin, Diego, Abdallah, and Ahmad.

Furthermore, I would like to acknowledge all the people I interacted with in both Navier and GeM laboratories, as well as all those I met in Paris and in Nantes.

Finally, I want to thank my mother Georgia, my father Panagiotis and my brother Haris for their continuous support and care they provided me during my PhD studies. Last but not least, I would like to show my appreciation and gratitude to Athina for her nonstop support during these 3 years. Especially, during the last months of my thesis, where I was extremely stressed, she was always there to calm me down, to encourage me to move forward and to help me overcome every difficulty.

Abstract

Anthropogenic seismicity has been increased since the last decades due to the intense human activity for energy production. However, despite the fact that merely injection of fluids can induce/trigger earthquakes, in this thesis, we show that the strategic interplay between fluid extractions and injections can control such seismic events and eventually prevent them. More specifically, a novel mathematical framework of robust earthquake control is built which in turn is exploited in numerical simulations of strike-slip faults and gas reservoirs, as well as in new laboratory experiments of decimetric scale.

First, the key parameters which constitute a conventional earthquake mitigation strategy are identified. Surrogate experiments on absorbent porous paper show that without the precise knowledge of the fault properties, fluid injections risk to nucleate faster a large seismic event.

In order to tackle such uncertainties, rigorous mathematical tools are developed using modern control theory. These tools require minimal information of fault's properties and frictional characteristics to assure robustness. Numerical simulations on strike-slip faults verify that earthquake prevention is possible, even in the presence of diffusion processes and the absence of sufficient measurements both in time and space. Going a step further, the developed control techniques can also be applied in large gas reservoirs, where the desired gas production can be achieved assuring acceptable seismicity levels.

Finally, during this thesis, a novel triplet apparatus of decimetric scale has been designed, constructed and calibrated accordingly. Pressure control can be achieved, in this machine, in real-time, through a fast response electro-pneumatic pressure regulator. As a proof of concept, the developed controller is plugged in this apparatus and by using sand-based 3D-printed specimens (to promote experimental repeatability), we manage, for the first time, to prevent laboratory earthquakes and drive the system aseismically to an equilibrium point of lower energy.

Keywords: Controlling earthQuakes (CoQuake); Fault Mechanics; Robust Control; Surrogate Experiments; Double-Direct Shear Apparatus; Induced Seismicity.

Résumé

La sismicité anthropique a augmenté depuis les dernières décennies en raison de l'intense activité humaine pour la production d'énergie. Cependant, malgré le fait que la simple injection de fluides peut induire/déclencher des tremblements de terre, dans cette thèse, nous montrons que l'interaction stratégique entre les extractions et les injections de fluides peut contrôler de tels événements sismiques et éventuellement les prévenir. Plus précisément, nous construisons un nouveau cadre mathématique de contrôle robuste des tremblements de terre, qui est ensuite exploité dans des simulations numériques de failles de glissement et de réservoirs de gaz, ainsi que dans de nouvelles expériences de laboratoire à l'échelle décimétrique.

Tout d'abord, les paramètres clés qui constituent une stratégie conventionnelle d'atténuation des séismes sont identifiés. Des expériences de substitution sur du papier poreux absorbant montrent que sans la connaissance précise des propriétés de la faille, les injections de fluide risquent de déclencher plus rapidement un grand événement sismique.

Afin de faire face à de telles incertitudes, des outils mathématiques rigoureux sont développés en utilisant la théorie moderne du contrôle. Ces outils nécessitent un minimum d'informations sur les propriétés de la faille et les caractéristiques de frottement pour assurer la robustesse. Des simulations numériques sur des failles à glissement latéral vérifient que la prévention des séismes est possible, même en présence de processus de diffusion et en l'absence de mesures suffisantes dans le temps et l'espace. En allant plus loin, les techniques de contrôle développées peuvent également être appliquées dans les grands réservoirs de gaz, où la production de gaz souhaitée peut être atteinte en garantissant des niveaux de sismicité acceptables.

Enfin, au cours de cette thèse, un nouvel appareil à triplets d'échelle décimétrique a été conçu, construit et calibré en conséquence. Le contrôle de la pression peut être réalisé, dans cet appareil, en temps réel, grâce à un régulateur de pression électro-pneumatique à réponse rapide. Comme preuve de concept, le régulateur développé est branché dans cet appareil et en utilisant des spécimens imprimés en 3D à base de sable (pour promouvoir la répétabilité expérimentale), nous parvenons, pour la première fois, à prévenir les tremblements de terre en laboratoire et à conduire le système de manière asismique vers un point d'équilibre de plus faible énergie.

Mots clés : Controlling earthQuakes (CoQuake) ; Mécanique des Failles ; Contrôle Robuste ; Expériences de Substitution ; Appareil de Cisaillement Double-Direct ; Sismicité Induite.

Contents

Acknowledgements	vii
Abstract	ix
Résumé	xi
Contents	xvi
Introduction	1
1 Qualitative behavior of earthquakes	5
1.1 Friction laws	5
1.1.1 Slip-weakening friction	6
1.1.2 Slip-rate weakening friction	6
1.1.3 Rate-and-state friction	7
1.1.4 Multiphysics couplings and friction	9
1.2 Spring-slider reduced order model	9
1.2.1 LSA with slip-weakening friction	13
1.2.2 LSA with rate-and-state friction	14
1.2.3 Qualitative behavior of isolated earthquake events	18
2 Paper-Quakes: A paradigm of earthquake mitigation and anthropogenic seismicity	23
2.1 Introduction	23
2.2 Paper-Quakes vs. Earth-Quakes	24
2.3 From seismic to aseismic rupture	27
2.4 Earthquake mitigation by fault segmentation and fluid injections	28
2.5 Insights on the governing parameters of the proposed earthquake mitigation strategy	33

3	Robust control theory for earthquake prevention	37
3.1	Introduction	37
3.2	Robust controller for a class of nonlinear systems with matched uncertainties	39
3.2.1	Robust stabilization	41
3.2.2	Robust tracking	43
3.3	Robust controller for a class of nonlinear systems with unmatched uncertainties	46
3.4	Full-order observer for a class of nonlinear systems	51
4	Robust control of seismic faults	57
4.1	Strike-slip fault dynamics	57
4.1.1	Rate-and-state friction	61
4.1.2	Slip-weakening friction	63
4.2	Robust control of seismic faults adjusting directly the fluid pressure on the fault by monitoring the whole state-space	66
4.2.1	Rate-and-state friction law	72
4.2.2	Slip-weakening friction law	77
4.3	Robust control of seismic faults coupled with diffusion processes using distant fluid injections by monitoring only surface deformation	79
4.3.1	Application with a single source	85
4.3.2	Application with multiple sources	88
4.4	Non-local robust control of seismicity rate	93
5	Design of a novel double-direct shear apparatus for controlling earthquakes in the laboratory	99
5.1	Review on pre-existing triplet machines for reproducing earthquake-like instabilities	99
5.2	Description of the experimental apparatus	101
5.3	Sensors, data acquisition and real-time data processing	103
5.4	Specimen properties	105
5.5	Frictional properties and nominal friction	106
5.6	Reproducing earthquake-like instabilities	109
5.7	Design of a digital controller	112
5.7.1	Digitization of the cost function of continuous-time linear systems .	113
5.7.2	Integral control for tracking a reference input	116

5.7.3	Nominal system and uncertainties	117
6	Controlling earthquake-like instabilities in the laboratory	123
6.1	Stabilization	123
6.2	Inducing controlled, slow slip - Tracking	127
6.3	Upscaling to a real fault scenario	129
6.3.1	Earthquake prevention by stabilization	131
6.3.2	Earthquake prevention by energy relaxation	132
6.4	Limitations and perspectives	134
	Conclusions and future work	137
	References	149
	List of publications	171
A	Paper Towel: experimental characterization, modeling and scaling laws	173
A.1	Experimental configuration	173
A.2	Mechanical properties of absorbent porous paper	175
A.3	Spring-paper model	176
A.4	Induced stress drop upon wetting	179
A.5	Real scale fault characteristics	180
A.6	Scaling laws	180
A.7	Model assumptions and limitations	183
B	Sand-Based 3D-Printed (S3DP) material: experimental characteriza- tion	185
B.1	Sand-based 3D-printed material composition	185
B.2	Unconfined compression tests	185
B.3	Direct shear experiments on flat interfaces	190
C	Design of analogue fault gouges with custom frictional properties using the S3DP material	195
C.1	Design of interfaces with custom frictional properties	195
C.2	Wear and gouge formation	197
C.3	Direct shear experiments with designed roughness	199
C.3.1	Effect of material composition	202

C.3.2	Effect of normal stress	205
C.4	Validation of the designed model for the design of frictional interfaces . . .	205
D	Design of the triplet experiment using FEM	211
D.1	Experimental setup	211
D.1.1	Optimization of specimen's geometry	213
D.1.2	Coulomb friction laws for the contact interface	214
D.2	Dynamic instability and earthquake nucleation	215
E	Scaling laws for the double-direct shear configuration	221
F	Controlling earthquakes in the laboratory using robust continuous-time controllers	227
F.1	Control objective	227
F.2	Control design	229
F.2.1	Sliding-Mode based control	229
F.2.2	LQR based Control	233
F.2.3	Control strategies comparison	236
F.3	Experimental comparison of the performance of three continuous-time robust controllers	238

Introduction

Earthquakes are one of the most destructive phenomena of the whole spectrum of natural disasters. The consequences of an earthquake are often irreversible and financially devastating. Apart from tectonic earthquakes, there are also earthquakes which are triggered unintentionally by injecting fluids in the earth's crust (see oil recovery, wastewater disposal, deep geothermal energy, etc.) (Elsworth et al., 2016; Foulger et al., 2018; McGarr et al., 2002; Rubinstein & Mahani, 2015; Schultz et al., 2020, among others). Independently of the origin, an earthquake is a dynamic instability that occurs when the elastic unloading of the rocks surrounding the fault zone cannot be counterbalanced by fault friction. The released elastic energy travels up to the surface in form of seismic waves (Semblat & Pecker, 2009) destroying world's infrastructure and most importantly causing several human losses (Jones, 2018). Nevertheless, most of the energy is dissipated due to friction. Friction determines the nucleation of an earthquake, the evolution of seismic slip and the magnitude of seismic events (Scholz, 2002). Friction is therefore of paramount importance for studying earthquake nucleation, its dynamic characteristics and potential mitigation strategies.

Experimental research aims to capture frictional behavior qualitatively and quantitatively on (relatively) small-scale specimens made of either rock or surrogate materials with or without gouge, in order to give implications on the large fault-scale characteristics and the dynamics of earthquake ruptures (Anthony & Marone, 2005; Brune & Anooshehpour, 1998; Burridge & Knopoff, 1967; Caniven et al., 2015; Corbi et al., 2013; Daniels & Hayman, 2008; J. H. Dieterich, 1979, 1981a; J. H. Dieterich & Kilgore, 1994; Heslot et al., 1994; Hulbert et al., 2019; Kammer & McLaskey, 2019; Ke et al., 2018; King, 1994; Knuth & Marone, 2007a; Latour et al., 2013; Lockner et al., 1982; Mclasley & Yamashita, 2017; Nasuno et al., 1998; Niemeijer & Spiers, 2007; Popov et al., 2012; Reber et al., 2014; Ritter et al., 2016; Rosakis et al., 1999; Rosenau et al., 2009; Rosenau et al., 2010; Roshankhah et al., 2018; Rubino et al., 2017; Rubinstein et al., 2012; Scholz, 2002; Schulze, 2003; M. M. Scuderi et al., 2015; Svetlizky, 2019; Varamashvili et al., 2008; Xia & Rosakis, 2021; Yamashita et al., 2018, among others). In addition, experiments at the fault-scale have been carried out (see Cappa et al., 2019; Guglielmi et al., 2015; Raleigh

et al., 1976), however due to the involved risks and costs, they are scarce.

Among these experimental campaigns, there is a plethora of laboratory and field experiments studying the transition from seismic to aseismic slip during fluid injections (Cappa et al., 2019; Guglielmi et al., 2015; Lockner et al., 1991; Tinti et al., 2016; Tzortzopoulos, Braun, et al., 2021; Zang et al., 2019, among others). These works stress the immediate need for fault stabilization and reduction of induced seismicity due to the intense human activity for energy production in the last decades (McGarr et al., 2002). Traffic-light systems (Bommer et al., 2015; Hofmann et al., 2019; Kwiatek et al., 2019) and fracture caging (Frash et al., 2021; Z. Li et al., 2021) are some representative techniques proposed in the literature for minimizing seismicity.

A great variety of numerical and theoretical works is also targeted to improving our current understanding on friction, earthquake nucleation and arrest due to fluid injections (see S. Barbot et al., 2012; Bhattacharya & Viesca, 2019; Larochelle et al., 2021; Mollon et al., 2020; Semblat et al., 2021; Tal et al., 2020, and references therein). Another class of methods is based on the prediction of the evolution of the system and the adjustment of the fluid pressure to avoid probable future seismic events (Gualandi et al., 2020).

However, the main arising question is that as long as unconstrained fluid injections increase the tremors in a seismogenic region, what happens when the fluid flux is regulated in such a way to decline seismicity? The seminal field tests in Rangely, Colorado (Raleigh et al., 1976), demonstrated exactly this scenario. While underground pore pressure was increasing due to intense fluid injections, the seismicity was growing as well. On the contrary, when backflowing was set in the installed wells, the seismicity in the region was arrested. This study can be considered as the first earthquake control attempt taking place in a fully monitored region under almost ideal conditions. Unfortunately, though, real fault systems are sparsely monitored and the exact knowledge of the reservoir and frictional characteristics is rare.

In this Thesis, we propose a robust earthquake mitigation strategy using fluid injections allowing the knowledge of only minimal and not even precise information about the frictional and mechanical characteristics of the fault system. This approach is based on the mathematical theory of control and it is experimentally validated in the laboratory using a novel double-direct shear apparatus of decimetric scale.

Control theory is a discipline of applied mathematics which deals with the control of dynamical systems (Ackermann, 1985; Franklin et al., 2018; Franklin et al., 1998; Khalil,

2013, 2015; Lewis et al., 2012; Ogata, 2010; A. I. Vardoulakis, 2012). Given a set of tuning variables (inputs), an algorithm is designed (controller) in such a way that the system is driven to a desired state assuring, all the time, stability of the closed-loop system (dynamical system + controller). However, all the systems cannot be controlled. Here, we show that control theory can be applied to regulate the salient unstable dynamics of a fault system. We exploit the dependence of friction on pressure (Terzaghi’s principle of effective stress) and use it as a backdoor (input) for altering the dynamics of the underlying dynamical system.

The present manuscript is organized as follows. Chapter 1 provides the conditions under which a seismic slip occurs adopting either slip-weakening (Andrews, 1976; Kanamori & Brodsky, 2004; Scholz, 2002; Stefanou, 2019; Tzortzopoulos, Braun, et al., 2021, among others) or rate-and-state friction law (Rice & Ruina, 1983; Ruina, 1983; Scholz, 2002, among others). Next, the dynamic response of the spring-slider (reduced order) model is qualitatively presented for building understanding. In Chapter 2, analogue experiments on absorbent porous paper highlight the key parameters and limitations of earthquake mitigation strategies inspired by industrial practices using consecutive fluid injections. Identifying the need for a more robust approach tackling parameter uncertainties and unmodeled dynamics, such as friction and elasticity (among others), we develop, in Chapter 3, a robust mathematical framework using *Control Theory*. The proposed control approach needs minimal and not even precise information about the characteristics of the fault system. Next, this theory is tested numerically in Chapter 4 considering real isolated fault configurations including diffusion phenomena and sparse spatial measurements. In case of imprecise knowledge of the geometry and location of the fault network, a non-local approach can be combined as well. Finally, in Chapters 5 and 6, we validate that our control strategy also works in laboratory models of earthquake system using a novel double-direct shear apparatus. Obtaining adequate scaling laws (Appendix E), we scale these results to a real strike-slip fault.

Notice that the Appendices of this Thesis should not be considered merely as a supplementary material of the aforementioned Chapters. Instead, completed side tasks, which couldn’t be integrated in the main body of this work, are present there. Particularly, in Appendices A and B, we characterize two new surrogate rock-like materials made of kitchen roll paper and 3D-printing with sand particles, respectively. By adequately crafting the interface of the latter, we can customize the frictional properties of the sheared interfaces in the laboratory (Appendix C). Finally, in Appendix F, more advanced continuous-time

controllers are designed, implemented and compared on the basis of our experimental setup.

To sum up, the main objectives of this Thesis, that go a step further than the existing state-of-the-art, are to:

1. Design and perform experiments in the laboratory, capturing the main dynamics of the earthquake instability and the effect of fluid injections using analogue materials such as Paper Towel and Sand-based 3D-Printed (S3DP) materials;
2. Design, assemble and calibrate a novel double-direct shear apparatus of decimetric scale;
3. Develop a mathematical framework based on *Control Theory* for earthquake prevention using fluid injections and/or extractions incorporating diffusion phenomena and sparse measurements in space;
4. Perform laboratory experiments to explore the possibility of earthquake control.

Qualitative behavior of earthquakes

Central in the earthquake phenomenon is friction. In this chapter, we present an overview of the most widely used frictional models in fault mechanics. It turns out that all of them share the same property of Lipschitz continuity, which is a key element for applying the nonlinear control theory presented later in this thesis.

The simplest earthquake model, in the literature, is the single-degree-of-freedom, spring-slider model. By using this reduced-order model coupled with an adequate constitutive friction law, we are able to study the response of earthquakes in an average sense and draw qualitative conclusions. Adopting the slip-weakening and the rate-and-state friction laws, we (re-)derive the conditions under which frictional instabilities (earthquakes) can take place. Finally, using the same laws, numerical simulations have also been conducted highlighting the characteristic dynamic response of the spring-slider system.

1.1 Friction laws

In the frame of fault mechanics, the most common frictional models that can lead to earthquake-like instabilities are the Slip-Weakening (SW), Slip-Rate Weakening (SRW) and Rate-and-State Friction (RSF) laws (see Byerlee, 1978; J. H. Dieterich, 1981a; Kanamori & Brodsky, 2004; Scholz, 2002, among others). More advanced constitutive models have also been proposed in the literature. These physics-based models can take into account in an indirect manner various Thermo-Hydro-Chemo-Mechanical phenomena that arise during frictional sliding (see S. D. Barbot, 2019a; Barras et al., 2019; Bhattacharya & Viesca, 2019; Chester, 1994; Collins-Craft et al., 2020; Gelet et al., 2012; Kenigsberg et al., 2020; Lachenbruch, 1980; Rattetz et al., 2018a; Rattetz et al., 2018a; Rattetz & Veveakis, 2020; Rudnicki & Chen, 1988; Stathas, 2021; Vardoulakis, 2000, and references therein, among others). Nevertheless, despite the rich literature on that topic, the quantification of the frictional properties of a fault is not a trivial task and it would always lead to estimations characterized by large uncertainties (cf. Rice, 2006).

However, this does not mean that these uncertainties are unbounded. In the following paragraphs we present the abovementioned popular frictional models and we show that they are Lipschitz continuous functions. This property is useful for our developments in Chapters 3-5 and Appendix F, assuring that our control approach is applicable even without precise knowledge of the exact frictional parameters and their spatial distribution.

1.1.1 Slip-weakening friction

In the slip-weakening friction law, the coefficient of friction, μ , evolves from an initial value μ_{\max} (static friction coefficient), to a residual one μ_{res} (kinetic friction coefficient) (see Scholz, 2002, and references therein). This transition is made in a characteristic slip distance d_c^{sw} (Kanamori & Brodsky, 2004). The slip-weakening law is often expressed through the following exponential decay function, whose parameters can be calibrated based on experimental data:

$$\mu = \mu(\delta) = \mu_{\text{res}} + \Delta\mu e^{-\frac{\delta}{d_c^{\text{sw}}}}, \quad (1.1)$$

where $\delta > 0$ is the slip and $\Delta\mu = \mu_{\max} - \mu_{\text{res}} > 0$. Exploiting the properties of the exponential function it is easy to show that there exists $\beta \geq \frac{\Delta\mu}{d_c^{\text{sw}}} > 0$ such that:

$$|\mu(\delta) - \mu(0)| \leq \beta|\delta|. \quad (1.2)$$

1.1.2 Slip-rate weakening friction

Another law that is frequently met in the literature, is the slip-rate weakening friction law, in which the friction coefficient is expressed in terms of the slip-rate, $v > 0$, i.e. $\mu = \mu(v)$. An example of such a law is given in Huang and Turcotte (1992) and takes the form:

$$\mu = \mu(v) = \frac{\mu_{\max}}{1 + \frac{v}{v_c}}, \quad (1.3)$$

where v_c is a characteristic velocity describing the friction coefficient drop due to slip-rate weakening. Again, it is straightforward to show that there exists $\beta \geq \frac{\mu_{\max}}{v_c} > 0$ such that:

$$|\mu(v) - \mu(0)| \leq \beta|v|. \quad (1.4)$$

1.1.3 Rate-and-state friction

The most popular friction law that is used for applications in fault mechanics is the rate-and-state friction law (J. H. Dieterich, 1979; Ruina, 1983). According to this model, friction depends logarithmically on the slip-rate and on a state variable, θ , that reflects microscopic processes related to contact asperities, healing and creep. The internal state variable, θ , can be expressed mainly either by the aging law (J. H. Dieterich, 1979) or the slip law (Ruina, 1983). The former is adopted in this thesis:

$$\mu(v, \theta) = \mu_0 + a \ln \frac{v}{v_0} + b \ln \frac{\theta}{\theta_0}, \quad (1.5a)$$

$$\dot{\theta} = 1 - \frac{v\theta}{d_c^{\text{rsf}}}, \quad (1.5b)$$

where μ_0 is a reference value of the coefficient of friction when an element slides with the steady-state velocity v_0 and the state variable is equal to $\theta_0 = \frac{d_c^{\text{rsf}}}{v_0}$. The parameters a , b and d_c^{rsf} are material properties which can be estimated performing velocity stepping experiments (see Appendix B for more details). Assuming Coulomb's friction law, the resulting shear stress is:

$$\tau(v, \theta) = \tau_0 + A \ln \frac{v}{v_0} + B \ln \frac{\theta}{\theta_0}, \quad (1.6a)$$

$$\dot{\theta} = 1 - \frac{v\theta}{d_c^{\text{rsf}}}, \quad (1.6b)$$

where $\tau_0 = \mu_0 \sigma'_n$, $A = a \sigma'_n$, $B = b \sigma'_n$, and σ'_n is the effective normal stress acting on the sheared interface. Let $\psi = B \ln \frac{\theta}{\theta_0}$, then Eq. (1.6) becomes:

$$\tau(v, \psi) = \tau_0 + A \ln \frac{v}{v_0} + \psi, \quad (1.7a)$$

$$\dot{\psi} = \frac{B}{d_c^{\text{rsf}}} \left(v_0 e^{-\frac{\psi}{B}} - v \right), \quad (1.7b)$$

Despite the success of this empirical constitutive law to represent experimental data, it does not have a sound thermodynamical basis allowing for a proper balance of energies through external powers and dissipation (Pipping, 2019). This mathematical drawback can be alleviated by proper regularization. Pipping (2019) adopted two possible regularizations that, in the frame of the aging law for the state evolution, can lead to a well defined boundary value problem with unique solution in space and time. According to this author,

the friction coefficient can be given using any of the two following expressions:

$$\tau = \tau_r(v, \psi) = A \sinh \frac{v}{2v_\psi} \quad (1.8)$$

or

$$\tau = \tau_t(v, \psi) = A \ln^+ \frac{v}{v_\psi}, \quad (1.9)$$

where $\ln^+ x = \ln(\max(1, x))$ and:

$$v_\psi = v_0 e^{-\frac{\tau_0 + \psi}{A}}. \quad (1.10)$$

It can be shown that (Pipping, 2019):

$$|\tau_r(v, \psi_2) - \tau_r(v, \psi_1)| \leq |\tau_t(v, \psi_2) - \tau_t(v, \psi_1)| \leq A \left| \ln \frac{v_{\psi_2}}{v_{\psi_1}} \right| = |\psi_2 - \psi_1|, \quad (1.11)$$

where we set $\psi_1 = \psi(t_1)$, $\psi_2 = \psi(t_2)$, with $t_2 > t_1$. The state variable, ψ , satisfies the general evolution law:

$$\dot{\psi} + \lambda(\psi) = f(v), \quad (1.12)$$

where $\lambda(\psi)$ is a non-decreasing function and $f(v)$ is Lipschitz. In the special case of the aging law, $\lambda(\psi) = -\frac{B}{d_{\text{rsf}}} v_0 e^{-\psi}$ and $f(v) = -\frac{B}{d_{\text{cst}}} v$. By integrating Eq. (1.12) with respect to time and using the non-decreasing property of $\lambda(\psi)$ we obtain $\psi_2 - \psi_1 \leq \int_{t_1}^{t_2} f(v) dt$.

In the case of the aging law it holds:

$$|\psi_2 - \psi_1| \leq \frac{B}{d_{\text{cst}}} |\delta(t_2) - \delta(t_1)|. \quad (1.13)$$

Using Eqs. (1.11) and (1.13), we can finally show that there exist $\bar{\beta}_1 \geq \frac{B}{d_{\text{cst}}} > 0$ and $\bar{\beta}_2 \geq A > 0$, such that:

$$|\tau(v, \psi) - \tau(0, 0)| \leq \bar{\beta}_1 |\delta| + \bar{\beta}_2 |v|. \quad (1.14)$$

By dividing Eq. (1.14) with the effective normal stress σ_n' , we get:

$$|\mu(v, \psi) - \mu(0, 0)| \leq \beta_1 |\delta| + \beta_2 |v|, \quad (1.15)$$

where $\beta_1 \geq \frac{b}{d_{\text{cst}}} > 0$ and $\beta_2 \geq a > 0$. It is worth noticing, that this bound is a combination of the bounds for slip and slip-rate weakening friction found in Sections 1.1.1 and 1.1.2, respectively.

1.1.4 Multiphysics couplings and friction

Due to the various complex phenomena that take place in nature, frictional weakening may depend also on temperature, T , fluid pressure, P , chemical reactions, χ , and other multiphysics phenomena. The evolution of these phenomena may depend directly or indirectly on the slip, δ , the slip-rate, v , and on time. We consider these phenomena as unmodeled and uncertain dynamics and we assume them to satisfy the following bound:

$$|\mu(\delta, v, T, P, \chi, \dots, t) - \mu_0| \leq \beta_1 |\delta| + \beta_2 |v| \quad (1.16)$$

with $\beta_1 > 0$, $\beta_2 > 0$ and μ_0 being a reference friction coefficient. The explicit dependence of the friction coefficient on time, t , represents unmodeled and uncertain physical processes that can influence friction.

The above inequality signifies that the friction coefficient is a Lipschitz continuous function in terms of slip and slip-rate. Lipschitz continuity is a reasonable assumption given the finiteness in energy of any physical process that can influence the evolution of the friction coefficient. Therefore, the evolution of several multiphysics phenomena could be roughly estimated in specific situations and conservative bounds for the coefficients β_1 and β_2 could be, in principle, estimated.

1.2 Spring-slider reduced order model

The dynamics of earthquakes can be represented, in average/energetical terms, through the spring-slider analogue system (Kanamori & Brodsky, 2004; Scholz, 2002; Stefanou & Tzortzopoulos, 2021; Stefanou, 2019; Tzortzopoulos, Braun, et al., 2021; Tzortzopoulos et al., 2019, among others). As shown in Figure 1.1, this reduced order model can be described by a mass-spring-damper system. This system consists of a mobilized mass, m , which slides on top of a frictional surface (equivalent to a fault) by applying a constant velocity, v_∞ (equivalent to the far-field movement of the tectonic plates), at the extremity of a Kelvin-Voigt configuration comprising of a spring with stiffness k (equivalent to the apparent elasticity of the host rock) and a dashpot with damping coefficient η (equivalent to the apparent viscosity of the surrounding rocks). On the frictional interface, the effective “overburden” normal stress, σ'_n is applied. The shear stress, τ , which is developed during shearing is governed by Coulomb’s constitutive friction law.

According to Kanamori and Brodsky (2004) and Scholz (2002), during the earthquake

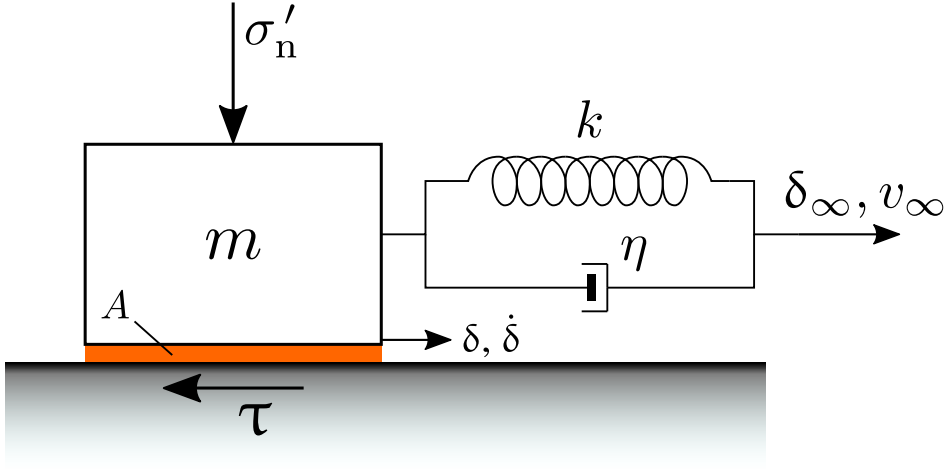


Figure 1.1 – Sketch of the spring-slider analogue system.

event, approximately a cuboid of size L_{ac} (practically the fault length) is mobilized. Therefore, the mass of an isolated fault can be expressed as (Stefanou, 2019; Tzortzopoulos, Braun, et al., 2021):

$$m = \alpha_1 \rho L_{ac}^3, \quad (1.17)$$

where ρ is the density of the surrounding rocks and α_1 is a constant of the order of unity. In addition, the apparent elasticity per unit area of the fault can be calculated as (J. H. Dieterich, 1979, among others):

$$\bar{k} = \alpha_2 \frac{G}{L_{ac}}, \quad (1.18)$$

where G is the shear-modulus of the host rock, α_2 is of the order of unity and $\bar{k} = k/L_{ac}^2$. The shear wave velocity of the material can be obtained from the following relation:

$$v_s = \sqrt{\frac{G}{\rho}}. \quad (1.19)$$

The damping coefficient η , is given by:

$$\eta = 2\zeta m \omega_n, \quad (1.20)$$

where ζ is the damping ratio and:

$$\omega_n = \sqrt{\frac{\bar{k}}{m}} = \sqrt{\frac{\alpha_2}{\alpha_1}} \frac{v_s}{L_{ac}} \quad (1.21)$$

is the natural frequency of the system. Equivalently, its normalized viscosity is given by:

$$C_v = \frac{\eta}{L_{ac}} = 2\sqrt{\alpha_1\alpha_2}\zeta\rho L_{ac}v_s. \quad (1.22)$$

Applying the force balance equation, the spring-slider system (see Figure 1.1) can be represented by the following mathematical model:

$$m\ddot{\delta} = -\mu(t, \delta, \dot{\delta})\sigma'_n A + k(\delta_\infty(t) - \delta) + \eta(v_\infty - \dot{\delta}), \quad (1.23)$$

where $A = L_{ac}^2$ is the effective contact area, $\delta_\infty = v_\infty t$ the displacement of the extremity of the Kelvin-Voigt configuration, $\mu(t, \delta, \dot{\delta})$ the coefficient of friction (see Section 1.1), δ , $\dot{\delta}$, and $\ddot{\delta}$ the slip, slip-rate and acceleration of the mobilized block, respectively.

In the following subsections, we will perform Linear Stability Analysis (LSA) in order to study the stability of the spring-slider analogue model under the presence of either slip-weakening (see Section 1.2.1) or rate-and-state friction laws (see Section 1.2.2). LSA is carried out on the dimensionless form of Eq. (1.23), namely:

$$d'' = -\mu(\hat{t}, d, d')\hat{\sigma}'_n \hat{N} + \hat{k}(d_\infty(\hat{t}) - d) + \hat{\eta}(q_\infty - d'), \quad (1.24)$$

by introducing a characteristic time T , a characteristic length D and a characteristic pressure P as follows:

$$t = \hat{t}T, \quad (1.25)$$

$$\delta = dD, \quad (1.26)$$

$$\sigma'_n = \hat{\sigma}'_n P, \quad (1.27)$$

$$\delta_\infty = d_\infty D, \quad (1.28)$$

$$v_\infty = q_\infty \frac{D}{T}, \quad (1.29)$$

where \hat{t} , d , $\hat{\sigma}'_n$, d_∞ , and q_∞ are the dimensionless time, slip, effective normal stress, far-field displacement and velocity, respectively. The dimensionless coefficients \hat{N} , \hat{k} and $\hat{\eta}$ in Eq.

(1.24) are given from the expressions below:

$$\hat{N} = \frac{APT^2}{mD} = \frac{PT^2}{\alpha_1 \rho L_{ac} D}, \quad (1.30)$$

$$\hat{k} = \frac{kT^2}{m} = \frac{\alpha_2}{\alpha_1} \left(\frac{v_s T}{L_{ac}} \right)^2, \quad (1.31)$$

$$\hat{\eta} = \frac{\eta T}{m} = 2\sqrt{\alpha_2} \zeta \frac{v_s}{L_{ac}} T. \quad (1.32)$$

When an earthquake occurs, the stored elastic energy in the equivalent spring (see Eq. (1.18)) is released abruptly resulting in a reduction of the apparent shear stress by $\Delta\tau$. The motion of the block stops when a new equilibrium point (of lower energy) is reached. The observed maximum slip obeys the following linear relation (Kanamori & Brodsky, 2004):

$$\delta_{\max} = \alpha_3 \frac{\Delta\tau}{\bar{k}} = \frac{\alpha_3}{\alpha_2} \frac{\Delta\tau}{G} L_{ac}, \quad (1.33)$$

where \bar{k} is given from Eq. (1.18) and α_3 is of the order of unity. The duration of the instability is:

$$t_{\text{inst}} = \frac{\alpha_4 \pi}{\omega_n} = \frac{\alpha_4 \pi}{\sqrt{\alpha_2}} \frac{L_{ac}}{v_s}, \quad (1.34)$$

where ω_n is obtained from Eq. (1.21) and α_4 depends mainly on the damping ratio, ζ . In the case, for instance, critical damping is adopted, $\alpha_4 = 2$. Notice that both δ_{\max} and t_{inst} scale linearly with the fault length, L_{ac} . Combining Eqs. (1.33) and (1.34), we can estimate the maximum slip-rate of the dynamic event as follows (Kanamori & Brodsky, 2004):

$$v_{\max} = \alpha_5 \frac{\delta_{\max}}{t_{\text{inst}}} = \frac{\alpha_3 \alpha_5}{\pi \sqrt{\alpha_2} \alpha_4} \frac{\Delta\tau}{G} v_s, \quad (1.35)$$

where α_5 is a constant which approximately spans from 1 to 2. In this study, we consider $\alpha_5 = 2$. In real in-situ cases, the average maximum developed slip-rate, v_{\max} , is of the order of 0.1 m/s ($\alpha_2 = \alpha_3 = 1$, $\alpha_4 = \alpha_5 = 2$, $\Delta\tau = 3$ MPa, $G = 30$ GPa, and $\rho = 2500$ kg/m³), independently of the fault length. The resulting magnitude of the nucleated earthquake can be estimated using the expression below (Kanamori & Brodsky, 2004; Scholz, 2002; Tzortzopoulos, Braun, et al., 2021, among others):

$$M_w = \frac{2}{3} \log M_0 - 6.07, \quad (1.36)$$

where:

$$M_0 = \alpha_6 \Delta \tau L_{ac}^3 \quad (1.37)$$

should be used in [N.m] and $\alpha_6 \approx 1$.

1.2.1 LSA with slip-weakening friction

In this paragraph, we adopt the slip-weakening friction law as introduced in Eq. (1.1). Notice that the displacement at the tip of the spring, d_∞ , is a function of time. Therefore, Eq. (1.24) is a non-autonomous nonlinear differential equation. To overpass this problem and study the stability of the system using the 1st Lyapunov method for stability (Brauer & Nohel, 2012), a double-scale asymptotic approach is employed (Stefanou, 2019). This method can be applied due to the fact that the time-scale of the far-field movement (q_∞) is many orders of magnitude larger than the characteristic time-scale of the instability event (\hat{t}). Consequently, by applying the procedure described in Stefanou (2019), the system that we will study in this Section corresponds to the fast time-scale (zero-order) and can be expanded in first-order differential equations ($q = d'$) as follows:

$$\begin{cases} q' = -\hat{N}\mu(d)\hat{\sigma}'_n + \hat{k}(d_\infty - d) - \hat{\eta}q, \\ d' = q, \end{cases} \quad (1.38a)$$

$$(1.38b)$$

where here d_∞ is a constant. Consequently, the set of equilibrium points ($q'^* = d'^* = 0$) at time $\hat{t} = \hat{t}^*$ of Eqs. (1.38) indicated by the superscript $*$ is described by:

$$\begin{cases} q^* = 0, \\ d^* = d_\infty - \mu(d^*)\hat{\sigma}'_n \frac{\hat{N}}{\hat{k}}. \end{cases} \quad (1.39a)$$

$$(1.39b)$$

In order to find under which conditions the above system is Lyapunov stable, we perform a Linear Stability Analysis (LSA or 1st Lyapunov method for stability) (Brauer & Nohel, 2012). The resulting *Jacobian* matrix calculated at the equilibrium point (q^*, d^*) is:

$$J = \begin{bmatrix} -\hat{\eta} & -\hat{k} - \frac{\partial \mu(d)}{\partial d} \Big|_{d=d^*} \hat{\sigma}'_n \hat{N} \\ 1 & 0 \end{bmatrix}. \quad (1.40)$$

Let $\mu_d^* = \frac{\partial \mu(d)}{\partial d} \Big|_{d=d^*} \stackrel{\text{(Eq. (1.1))}}{=} -\frac{\Delta \mu}{\hat{d}_c^{\text{sw}}} e^{-d^*/\hat{d}_c^{\text{sw}}}$, where $d_c^{\text{sw}} = \hat{d}_c^{\text{sw}} D$, the corresponding charac-

teristic equation is:

$$s^2 + \hat{\eta}s + \left(\hat{k} + \mu_d^* \hat{\sigma}'_n \hat{N}\right) = 0, \quad (1.41)$$

where s is the set of *eigenvalues* of the *Jacobian* matrix J . According to *Descartes' rule of signs*, if the nonzero terms of a single-variable polynomial with real coefficients are ordered by descending variable exponent, then the number of positive roots of the polynomial is either equal to the number of sign changes between consecutive (nonzero) coefficients, or is less than it by an even number. In particular, if the number of sign changes is zero or one, the number of positive roots equals the number of sign changes.

Therefore, as always $\hat{\eta} > 0$ (see Eq. (1.32)), if the coefficient of the last term in Eq. (1.41) is positive, we conclude that the J matrix has either two negative or two complex conjugate eigenvalues with negative real part ($-\hat{\eta}/2 < 0$). Consequently, the equilibrium point (q^*, d^*) is Lyapunov stable (Brauer & Nohel, 2012).

On the other hand, if the coefficient of the last term in Eq. (1.41) is negative, Eq. (1.41) has one positive and one negative real roots. In this case, the equilibrium point (q^*, d^*) is Lyapunov unstable (Brauer & Nohel, 2012). Eventually, the instability condition of this equilibrium point, given slip-weakening friction law is given by the following inequality:

$$\hat{k} < \hat{k}_c^{\text{sw}} = -\mu_d^* \hat{\sigma}'_n \hat{N} = \frac{\Delta\mu}{\hat{d}_c^{\text{sw}}} e^{-d^*/\hat{d}_c^{\text{sw}}} \hat{\sigma}'_n \hat{N}. \quad (1.42)$$

and in dimensional form:

$$k < k_c^{\text{sw}} = \frac{\Delta\mu}{d_c^{\text{sw}}} e^{-\delta^*/d_c^{\text{sw}}} \sigma'_n A, \quad (1.43)$$

or equivalently:

$$\bar{k} < \bar{k}_c^{\text{sw}} = \frac{\sigma'_n \Delta\mu}{d_c^{\text{sw}}} e^{-\delta^*/d_c^{\text{sw}}}, \quad (1.44)$$

where $\delta^* = d^*D$. We can observe that the above inequality is in accordance with the nominal studies of J. H. Dieterich (1979), Scholz (2002), and Stefanou (2019).

1.2.2 LSA with rate-and-state friction

In this paragraph, we adopt the rate-and-state friction law as introduced in Eq. (1.7). The internal state variable obeys the aging law derived by J. H. Dieterich (1979). Considering the system of Eqs. (1.24), we expect the equilibrium point in terms of the slip-rate to be at zero ($q^* = 0$), as exactly in the case of the slip-weakening friction in Eq. (1.39). However, due to the logarithmic nature of the rate-and-state friction law, zero velocity

would correspond to singular values in friction. Therefore, in order to study stability of the spring-slider reduced order system coupled with rate-and-state friction, we have to assure nonzero velocities and shift the system accordingly. Let the differential equations of interest be:

$$\begin{cases} d'' = -\tau(d', \hat{\psi})\hat{N} + \hat{k}(d_\infty - d) + \hat{\eta}(q_\infty - d'), & (1.45a) \\ \hat{\psi}' = \frac{\hat{B}}{\hat{d}_c^{\text{rsf}}} \left(\hat{v}_0 e^{-\frac{\hat{\psi}}{\hat{B}}} - d' \right), & (1.45b) \end{cases}$$

where:

$$\psi = \hat{\psi}P, \quad (1.46a)$$

$$B = \hat{B}P, \quad (1.46b)$$

$$d_c^{\text{rsf}} = \hat{d}_c^{\text{rsf}}D, \quad (1.46c)$$

$$v_0 = \hat{v}_0 \frac{D}{T}. \quad (1.46d)$$

Let $u_s = d_\infty - d$ and $q = d'$, then Eq. (1.45) becomes:

$$\begin{cases} q' = -\tau(q, \hat{\psi})\hat{N} + \hat{k}u_s + \hat{\eta}(q_\infty - q), & (1.47a) \\ u_s' = q_\infty - q, & (1.47b) \\ \hat{\psi}' = \frac{\hat{B}}{\hat{d}_c^{\text{rsf}}} \left(\hat{v}_0 e^{-\frac{\hat{\psi}}{\hat{B}}} - q \right). & (1.47c) \end{cases}$$

Consequently, the set of equilibrium points ($q^* = u_s^* = \hat{\psi}^* = 0$) at time $\hat{t} = \hat{t}^*$ of Eqs. (1.47) indicated by the superscript $*$ is described by:

$$\begin{cases} q^* = q_\infty, & (1.48a) \\ u_s^* = \tau(q^*, \hat{\psi}^*) \frac{\hat{N}}{\hat{k}}, & (1.48b) \\ \hat{\psi}^* = -\hat{B} \ln \frac{q^*}{\hat{v}_0}. & (1.48c) \end{cases}$$

In order to find under which conditions the above system is Lyapunov stable, we perform a Linear Stability Analysis (LSA or 1st Lyapunov method for stability) (Brauer & Nohel, 2012). The resulting *Jacobian* matrix calculated at the equilibrium point ($q^*, u_s^*, \hat{\psi}^*$)

is:

$$J = \begin{bmatrix} -\hat{\eta} - \frac{\hat{A}\hat{N}}{q_\infty} & \hat{k} & -\hat{N} \\ -1 & 0 & 0 \\ -\frac{\hat{B}}{\hat{d}_c^{\text{rsf}}} & 0 & -\frac{q_\infty}{\hat{d}_c^{\text{rsf}}} \end{bmatrix}. \quad (1.49)$$

The corresponding characteristic equation is:

$$P(s) = s^3 + s^2 \left[\hat{\eta} + \frac{q_\infty}{\hat{d}_c^{\text{rsf}}} + \frac{\hat{A}\hat{N}}{q_\infty} \right] + s \left[\hat{k} + \hat{\eta} \frac{q_\infty}{\hat{d}_c^{\text{rsf}}} + (\hat{A} - \hat{B}) \frac{\hat{N}}{\hat{d}_c^{\text{rsf}}} \right] + \hat{k} \frac{q_\infty}{\hat{d}_c^{\text{rsf}}} = 0, \quad (1.50)$$

where s is the set of *eigenvalues* of the *Jacobian* matrix J . In general, it's not trivial to find the roots of a cubic polynomial symbolically, as the one in Eq. (1.50) (even if a closed-form solution is available). For finding the instability condition, therefore, we will follow the procedure described in Rice and Ruina (1983). The difference here, however, is the fact that not only inertial but also viscous forces are incorporated for the stability analysis.

To begin with, let $\hat{k} = 0$, then Eq. (1.50) becomes:

$$s \left(\underbrace{s^2 + s \left[\hat{\eta} + \frac{q_\infty}{\hat{d}_c^{\text{rsf}}} + \frac{\hat{A}\hat{N}}{q_\infty} \right] + \left[\hat{\eta} \frac{q_\infty}{\hat{d}_c^{\text{rsf}}} + (\hat{A} - \hat{B}) \frac{\hat{N}}{\hat{d}_c^{\text{rsf}}} \right]}_{Q(s)} \right) = 0, \quad (1.51)$$

One trivial root is $s = 0$. The remaining two solutions are the roots of the quadratic polynomial $Q(s)$. $Q(s)$ has the same form as the one handled in Eq. (1.41). The second coefficient is always positive and, therefore, $Q(s)$ has one negative and one positive real roots if:

$$\hat{\eta} < (\hat{B} - \hat{A}) \frac{\hat{N}}{q_\infty}, \quad (1.52)$$

Eventually, if $\hat{k} = 0$, the polynomial $P(s)$ has three distinct real roots (one positive, one negative and one zero) if the condition of Eq. (1.52) is satisfied. In this case, according to the 1st Lyapunov stability method (Brauer & Nohel, 2012), the equilibrium point $(q^*, u_s^*, \hat{\psi}^*)$ is unstable.

Now, we will explore the nature of the roots of $P(s)$, while $\hat{k} \rightarrow \infty$. To do that, we calculate the discriminant of $P(s)$, $\Delta(P(s))$, and we collect the powers of \hat{k} . The coefficient of the leading term is -4 and therefore $\lim_{\hat{k} \rightarrow \infty} \Delta(P(s)) = -\infty < 0$. In that case, $P(s)$ has

one real (s_1) and two complex conjugate roots ($s_{2,3}$), with:

$$\lim_{\hat{k} \rightarrow \infty} s_1 = -\frac{q_\infty}{\hat{d}_c^{\text{rsf}}} < 0, \quad (1.53)$$

$$\lim_{\hat{k} \rightarrow \infty} \text{Re}(s_{2,3}) = -\frac{\hat{A}\hat{N} + \hat{\eta}q_\infty}{2q_\infty} < 0. \quad (1.54)$$

Therefore, we can conclude that the equilibrium point (q^*, u_s^*, ψ^*) is stable when $\hat{k} \rightarrow \infty$.

Assuming continuity, a real root or a complex conjugate pair must pass into the domain $\text{Re}(s) > 0$ as \hat{k} reduces from ∞ to 0 (Rice & Ruina, 1983). The crossing point cannot be neither the origin nor infinity as none of them satisfy Eq. (1.50). Consequently, a pair of conjugate imaginary roots crosses the imaginary axis when the normalized stiffness takes its critical value \hat{k}_c^{rsf} . At the crossing point, $P(\pm i\hat{\beta}) = 0$. After some rearrangements, we get:

$$P(\pm i\hat{\beta}) = \hat{k}_c^{\text{rsf}} \frac{q_\infty}{\hat{d}_c^{\text{rsf}}} - \hat{\beta}^2 \left(\frac{q_\infty}{\hat{d}_c^{\text{rsf}}} + \frac{\hat{A}\hat{N}}{q_\infty} + \hat{\eta} \right) \pm i\hat{\beta} \left(\hat{\eta} \frac{q_\infty}{\hat{d}_c^{\text{rsf}}} + \hat{k}_c^{\text{rsf}} + (\hat{A} - \hat{B}) \frac{\hat{N}}{\hat{d}_c^{\text{rsf}}} - \hat{\beta}^2 \right) = 0. \quad (1.55)$$

This is a system of two equations (real and imaginary part) and two unknowns (\hat{k}_c^{rsf} and $\hat{\beta}$). The imaginary part should be equal to zero:

$$\text{Im}(P(\pm i\hat{\beta})) = 0 \Rightarrow \underbrace{\hat{\beta} = 0}_{\text{Impossible: } P(0) = \hat{k}_c^{\text{rsf}} \frac{q_\infty}{\hat{d}_c^{\text{rsf}}} \neq 0} \quad \text{or} \quad \hat{\beta}^2 = \hat{\eta} \frac{q_\infty}{\hat{d}_c^{\text{rsf}}} + \hat{k}_c^{\text{rsf}} + (\hat{A} - \hat{B}) \frac{\hat{N}}{\hat{d}_c^{\text{rsf}}}. \quad (1.56)$$

Considering now the real part of Eq. (1.55) to be zero and substituting Eq. (1.56) yields:

$$\text{Re}(P(\pm i\hat{\beta})) = 0 \Rightarrow \hat{k}_c^{\text{rsf}} = \underbrace{\frac{(\hat{B} - \hat{A})\hat{N} - \hat{\eta}q_\infty}{\hat{d}_c^{\text{rsf}}}}_{>0 \text{ (Eq. (1.52))}} \left(1 + \frac{q_\infty^2}{(\hat{A}\hat{N} + \hat{\eta}q_\infty)\hat{d}_c^{\text{rsf}}} \right). \quad (1.57)$$

Substituting Eq. (1.57) into Eq. (1.56), the frequency of oscillations (Hopf bifurcation) at the critical point, $\hat{\beta}$, can be obtained:

$$\hat{\beta} = \frac{q_\infty}{\hat{d}_c^{\text{rsf}}} \sqrt{\frac{(\hat{B} - \hat{A})\hat{N} - \hat{\eta}q_\infty}{\hat{A}\hat{N} + \hat{\eta}q_\infty}} > 0. \quad (1.58)$$

From the previous derivations, the equilibrium point $(q^*, u_s^*, \hat{\psi}^*)$ is Lyapunov unstable when the following instability condition is satisfied:

$$\hat{k} < \hat{k}_c^{\text{rsf}} = \frac{(\hat{B} - \hat{A}) \hat{N} - \hat{\eta} q_\infty}{\hat{d}_c^{\text{rsf}}} \left(1 + \frac{q_\infty^2}{(\hat{A} \hat{N} + \hat{\eta} q_\infty) \hat{d}_c^{\text{rsf}}} \right). \quad (1.59)$$

This limit is an extension of the ones derived in Rice and Ruina (1983) and Ruina (1983) as, here, elastic, inertial, and viscous forces are included. For clarity, below, we present the dimensional form of Eq. (1.59):

$$k < k_c^{\text{rsf}} = \frac{(b-a) \sigma'_n A - \eta v_\infty}{d_c^{\text{rsf}}} \left(1 + \frac{m v_\infty^2}{(a \sigma'_n A + \eta v_\infty) d_c^{\text{rsf}}} \right), \quad (1.60)$$

or equivalently:

$$\bar{k} < \bar{k}_c^{\text{rsf}} = \frac{(b-a) \sigma'_n - 2\sqrt{\alpha_1 \alpha_2} \zeta \rho v_s v_\infty}{d_c^{\text{rsf}}} \left(1 + \frac{\alpha_1 \rho v_\infty^2}{a \sigma'_n + 2\sqrt{\alpha_1 \alpha_2} \zeta \rho v_s v_\infty} \cdot \frac{L_{\text{ac}}}{d_c^{\text{rsf}}} \right). \quad (1.61)$$

We can observe that the presence of viscosity, η , in Eq. (1.60), relaxes the instability criterion favoring stability. In addition, if $\eta = 0$, we retrieve the instability condition found in Rice and Ruina (1983). Furthermore, if we neglect also inertial forces ($m = \eta = 0$), we can find the condition derived in the seminal paper of Ruina (1983) considering only elastic forces.

1.2.3 Qualitative behavior of isolated earthquake events

Consider an isolated idealized fault with average mechanical and frictional properties (both for SW and RSF friction) as summarized in Table 1.1. We can quantify the average response of this fault by employing the spring-slider reduced-order model as introduced in this Section. The apparent stiffness per unit area of the analogue fault is given by Eq. (1.18) and it is equal to $\bar{k} = 6$ MPa/m. First, let us assume that the frictional behavior of the fault obeys the slip-weakening friction law (see Sections 1.1.1 and 1.2.1). The characteristic stiffness per unit area of the frictional interface is equal to $\bar{k}_c^{\text{sw}} = 37.5$ MPa/m (considering $\delta^* = 0$). Therefore, the instability condition in Eq. (1.44) is satisfied and a seismic event will occur.

In Figure 1.2, we present the response of the spring-slider system during an earthquake. On the left (Figure 1.2a), we observe that due to the frictional instability, the fault slipped

Table 1.1 – (a) In-situ properties of the isolated fault. (b) Slip-weakening frictional characteristics (see also Section 1.1.1). (c) Rate-and-state frictional characteristics (see also Section 1.1.3). The variables with superscript “est” correspond to the estimated earthquake response considering Eqs. (1.33)-(1.37). $\Delta\tau^{\text{est}}$ in Table 1.1c is given by Eq. (1.63).

(a)					
L_{ac}	G	σ'_n	ρ	ζ	v_∞
[km]	[GPa]	[MPa]	[kg/m ³]	[-]	[cm/year]
5	30	37.5	2500	1	1

(b)						
$\Delta\mu$	μ_{res}	d_c^{sw}	$\delta_{\text{max}}^{\text{est}}$	$t_{\text{inst}}^{\text{est}}$	$v_{\text{max}}^{\text{est}}$	M_w^{est}
[-]	[-]	[mm]	[m]	[s]	[m/s]	[-]
0.1	0.5	100	0.63	9.1	0.18	5.7

(c)									
μ_0	v_0	a	b	d_c^{rsf}	$\Delta\tau^{\text{est}}$	$\delta_{\text{max}}^{\text{est}}$	$t_{\text{inst}}^{\text{est}}$	$v_{\text{max}}^{\text{est}}$	M_w^{est}
[-]	[m/s]	[-]	[-]	[mm]	[MPa]	[m]	[s]	[m/s]	[-]
0.55	$4 \cdot 10^{-6}$	0.01	0.015	10	3.73	0.63	9.1	0.13	5.7

0.63 m in ~ 10 s developing a maximum velocity of 0.11 m/s. Notice that these values are close to the ones estimated (see Table 1.1b) by using the scaled Eqs. (1.33)-(1.37) (Kanamori & Brodsky, 2004). On the right (Figure 1.2b), the frictional response in terms of the accumulated slip is plotted. At point *A*, the fault is reactivated and the instability is nucleated. The system follows the black curve until it reaches a new equilibrium point (point *B*) of lower energy. During the earthquake event, the spring is unloaded with a rate $-\bar{k}$ with respect to slip as indicated with the red dashed line. The shaded area between the two curves corresponds to the released elastic energy per unit area, \bar{E}_R . Finally, the resulting earthquake magnitude can be computed using Eq. (1.36) and is equal to $M_w = 5.7$.

Apart from the radiated energy, \bar{E}_R , there are also another two major energy forms which complete the energy budget during an earthquake event (Kanamori & Brodsky,

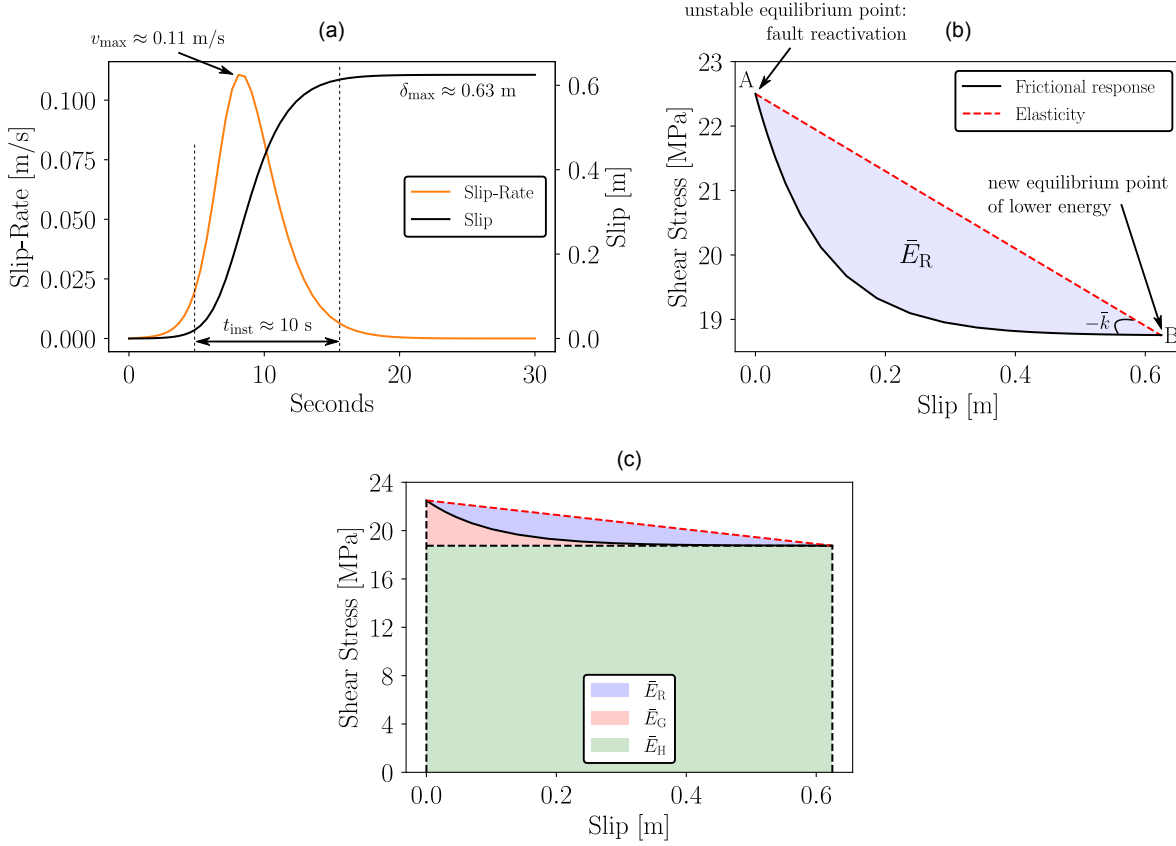


Figure 1.2 – Response of the fault described in Table 1.1a-b during an earthquake event (SW friction law). (a) Slip-rate (orange curve) and slip (black curve) in terms of time. (b) Frictional (black curve) and spring (red dashed line) in terms of slip. The shaded area corresponds to the released elastic energy per unit area, \bar{E}_R . (c) The energy budget (Kanamori & Brodsky, 2004). The blue filled area indicates the radiated energy per unit area, \bar{E}_R as in subfigure (b). The red filled area corresponds to the fracture energy per unit area, \bar{E}_G , while the green shaded area corresponds to the frictional dissipation per unit area, \bar{E}_H .

2004; Kanamori & Rivera, 2006). These are illustrated in Figure 1.2c. The red shaded area corresponds to the fracture energy per unit area, \bar{E}_G , while the green filled area corresponds to the frictional energy per unit area, \bar{E}_H . We can observe that most of the stored energy is dissipated due to friction. Only a small portion is radiated to the environment (blue shaded area) and travels through waves to the surface. Yet, it is enough to destroy world's infrastructure and cause loss of human lives.

Let us now assume that the frictional behavior of the fault is governed by the rate-and-state friction law (see Subsections 1.1.3 and 1.2.2). The characteristic stiffness per unit area of the sheared interfaces is equal to $\bar{k}_c^{\text{rsf}} = 18.75$ MPa/m (see Eq. (1.61)). Therefore,

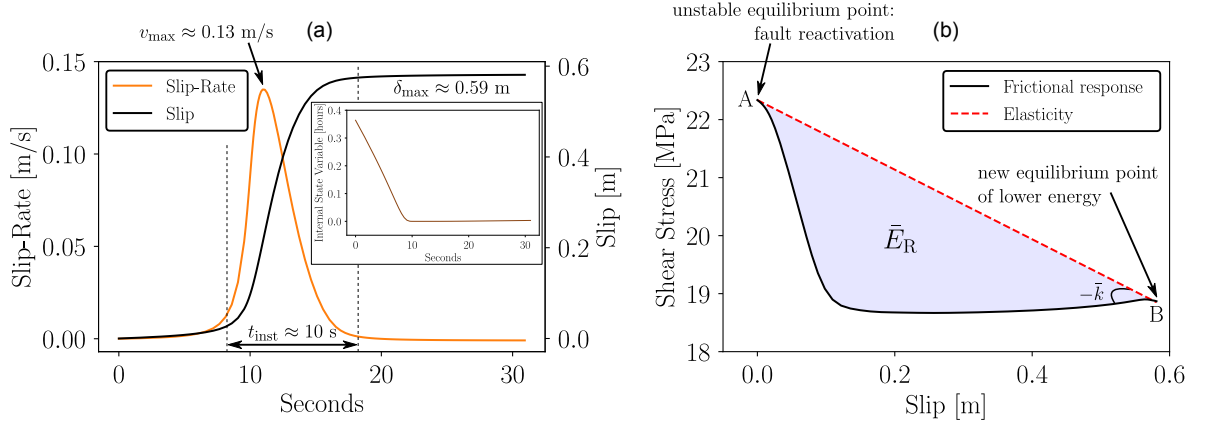


Figure 1.3 – Response of the fault described in Table 1.1a and c during an earthquake event (RSF friction law). (a) Slip-rate (orange curve) and slip (black curve) in terms of time. Inset: Evolution of internal state variable, θ , in terms of time. (b) Frictional (black curve) and spring (red dashed line) in terms of slip. The shaded area corresponds to the released elastic energy per unit area, \bar{E}_R .

the instability condition in Eq. (1.61) is satisfied assuring unstable behavior.

In Figure 1.3, the response of the reduced-order model is illustrated during an isolated seismic event. We can observe that the system behaves almost identically with the previous case during the dynamic instability where slip-weakening friction was adopted. Even the estimated values in Table 1.1c corroborate that. The inset of Figure 1.3a shows the evolution of the internal state variable, θ (see Eq. (1.5)), in terms of time.

However, the calculation of the estimated values in Table 1.1c is not as straightforward as in the slip-weakening scenario (see Table 1.1b). There is no direct way of calculating $\Delta\tau^{\text{est}}$. According to Cao and Aki (1987), the stress drop of a uniform fault is estimated by the following equation:

$$\Delta\tau^{\text{est}} = (A - B) \ln \frac{v_{\min}}{v_{\max}}. \quad (1.62)$$

Considering that the minimum velocity of the fault is approximately equal to the far-field movement of the tectonic plates ($v_{\min} = v_{\infty}$) and substituting Eqs. (1.19) and (1.33)-(1.35) into Eq. (1.62), we get:

$$\Delta\tau^{\text{est}} = (A - B) \ln \left(\frac{\pi\sqrt{\alpha_2}\alpha_4}{\alpha_3\alpha_5} \frac{v_{\infty}G}{v_s\Delta\tau^{\text{est}}} \right). \quad (1.63)$$

The above nonlinear algebraic equation can be solved numerically for $\Delta\tau^{\text{est}}$. Therefore, the response of the dynamic event can be further estimated using Eqs. (1.33)-(1.37) as in

the slip-weakening case resulting to a maximum slip of $\delta_{\max} = 0.59$ m and a maximum slip-rate of $v_{\max} = 0.13$ m/s (see Table 1.1).

It is worth emphasizing that several other methods can be used apart from the spring-slider representation in order to simulate the dynamics of a fault. The underlying continuum elastodynamic problem of seismic slip can be discretized with any of the following procedures: Finite Element Method, Finite Differences, Boundary Element Method, spectral methods, model reduction methods, among others (see S. D. Barbot, 2019b; Boyd, 2000; Erickson et al., 2020; Laroche et al., 2021). Such a discretization is attempted in Chapters 3 and 4.

Paper-Quakes: A paradigm of earthquake mitigation and anthropogenic seismicity

Earthquakes nucleate when large amounts of elastic energy, stored in the earth's crust, are suddenly released due to abrupt sliding over a fault. Fluid injections can reactivate existing seismogenic faults and induce/trigger earthquakes by increasing fluid pressure. In this chapter, we develop an analogous experimental system of simultaneously loaded and wetted absorbent porous paper to quantify theoretically the process of wetting-induced earthquakes. This strategy allows us to gradually release the stored energy by provoking low intensity tremors. We identify the key parameters that control the outcome of the applied injection strategy, which include the initial stress state, fault segmentation, and segment-activation rate. Subsequent injections, initiated at high stress levels, can drive the system faster towards its instability point, nucleating a large earthquake. Starting at low stress levels, however, they can reduce the magnitude of the natural event by at least one unit.

2.1 Introduction

It is well recognized today that humans can cause earthquakes (Foulger et al., 2018; Guglielmi et al., 2015; McGarr et al., 2002; Raleigh et al., 1976). Examples of anthropogenic seismicity involve earthquakes provoked by large artificial water reservoirs such as dams (Gupta, 2002), mining (T. Li et al., 2007), underground nuclear explosions (Hamilton et al., 1972) or by fluid injections in the earth's crust (Ellsworth, 2013; Garagash & Germanovich, 2012; Rubinstein & Mahani, 2015; Schultz et al., 2020). The latter type of anthropogenic seismicity is of particular interest, due to the numerous ongoing industrial applications (Hosseini et al., 2018; Rubinstein & Mahani, 2015). These anthropogenic seismic events could shift the Gutenberg and Richter (1954) power law, which describes the relationship between the total number of earthquakes and their magnitudes, towards

smaller events.

This idea is similar to the one traditionally used for reducing the risk of large snow avalanches. Snow avalanches follow the same frequency-magnitude distributions as natural earthquakes do (Birkeland & Landry, 2002). Nowadays, it is common practice to avoid large avalanches by provoking smaller ones. Similarly, large earthquakes could be probably mitigated by inducing low intensity tremors. This is what is called in this Chapter earthquake mitigation. This notion was first mentioned by Raleigh et al. (1976), but has not been explored further since.

Surrogate materials can effectively substitute in-situ rock and gouge materials (Rose-nau et al., 2017). Some examples of such materials are sandpaper (King, 1975), cardboard (Heslot et al., 1994), pasta (Knuth & Marone, 2007b), steel (Popov et al., 2012), hydrogel (Latour et al., 2013) and puffed rice (Einav & Guillard, 2018), among others. Here we use absorbent porous paper as an analogue fault material to explore earthquake mitigation. We show that it can be an ideal low-cost surrogate material for reproducing earthquake-like instabilities in the laboratory. Wetting the absorbent paper allows us not only to weaken the material but also to induce small instabilities. By deriving adequate scaling laws (see Appendix A.6), we can simulate fluid injections and study the transition from seismic (unstable, sudden) to aseismic (stable, creep-like) slip of an ideal fault (Cappa et al., 2019; Stefanou, 2019).

2.2 Paper-Quakes vs. Earth-Quakes

Consider an isolated planar dip-slip fault, as depicted in Figure 2.1a, with a length of $L_{ac}^{real} = 6.5$ km dipped at an angle of 60° (see also Appendix A.5). Based on its properties and assuming a square rupture area ($A^{real} \approx (L_{ac}^{real})^2$), this fault leads to an earthquake of $M_w \approx 6$ (see Appendix A.6). The energy budget is contained in a single sheet of absorbent paper which, consequently, can represent this fault (see also Appendices A.1-A.2) if strained as shown in Figure 2.1b. Long range interactions with other faults are not considered in this Chapter.

The energetic equivalence of the paper analogue with a real fault can be observed in Figures 2.2a-c. The progressive accumulation of elastic energy in the rocks surrounding the fault zone is taken into account by a spring attached at the one end of the sheet (Figures 2.2b-c). The apparent stiffness of the spring is chosen to represent the real system. A constant slow velocity is applied at the extremity of this spring, simulating the slow far-

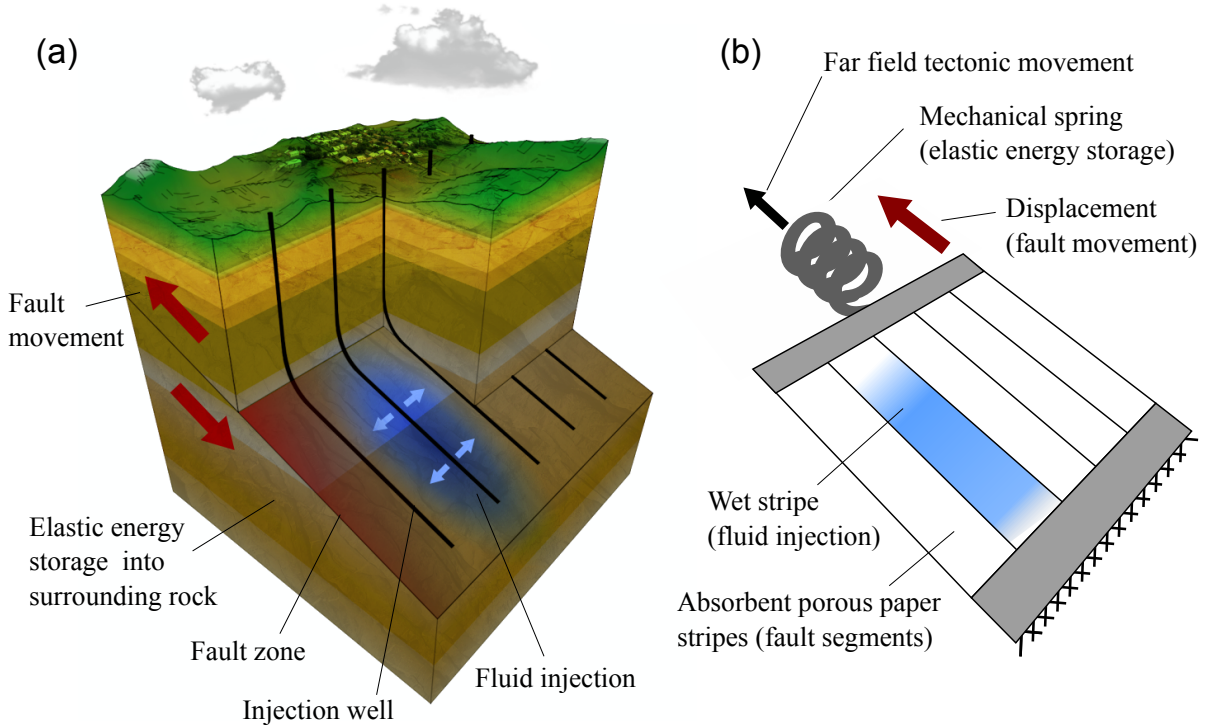


Figure 2.1 – (a) Simplified dip-slip fault where the fault zone area is divided in five segments parallel to the slip direction. Five wells allow to inject fluid into each segment independently. (b) Surrogate laboratory experiment consisting of five parallel stripes of absorbent paper, held together at their ends by clamps. Far-field movement is applied through a mechanical spring. The paper stripes can be wetted individually.

field tectonic loading. Finally, paper has a non-negligible softening branch that simulates the critical slip-weakening distance d_c^{sw} of faults (see Section 1.1.1 and also Scholz, 2002) (Figure 2.2d).

We can also simulate fluid injections by simply wetting the paper sheet. In a fault system, the apparent friction drops when fluids under pressure are injected into the fault zone due to the decrease of the effective normal stress. Similarly, porous paper shows a noticeable stress drop when it is wetted due to the reduction of its strength (Figures 2.2d and 2.5a). The ratio of the shear stress drop of real faults to the strength weakening of porous paper is defined here by the scaling factor a , which is a free parameter in our model (see also Appendix A.6). Finally, opposite to wetting, healing could be considered by drying the paper stripes, which could potentially lead to repeatedly growing slip events. However, this is out of the scope of the present example, which focuses on earthquake mitigation by fault reactivation.

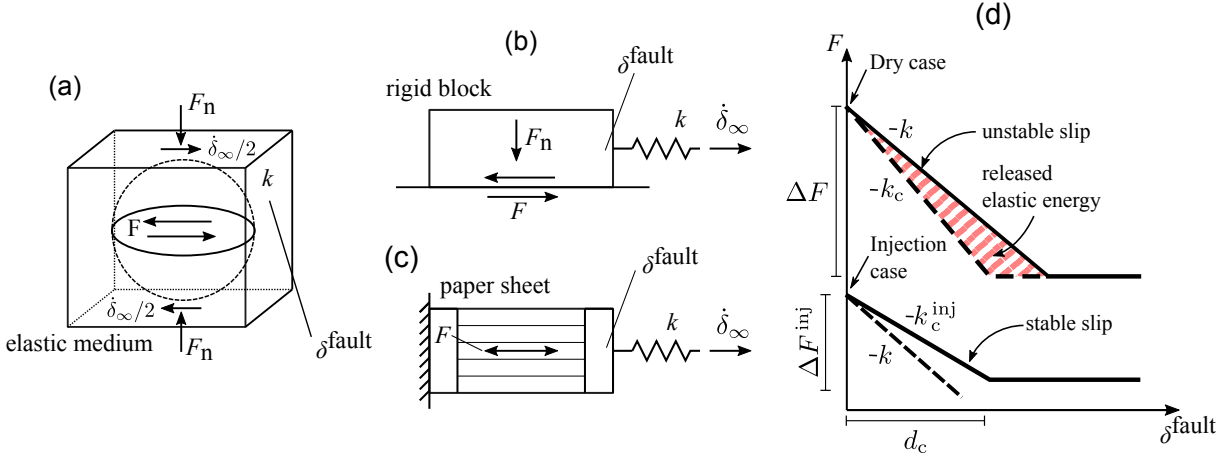


Figure 2.2 – (a) Pre-existing fault within an elastic medium of stiffness k , loaded by a very low velocity, $\dot{\delta}_{\infty}$. Normal forces F_n act on the fault, while frictional forces F are generated along the interface (Reid, 1910). (b) Spring-slider model (Scholz, 2002), composed of a rigid block, which is pulled through a spring over a rough surface. (c) Paper-spring model, where a stripe of paper is pulled through an elastic spring. (d) Schematic force-displacement diagram in which the post-peak properties are modified due to fluid injection on the fault (wetting in the porous paper case), allowing transition from unstable to stable slip.

Notice that the fluid diffusion process which takes place during injections in wellbores can be considered in our analogue model in two ways, by water absorption of porous paper and by progressive wetting of many isolated stripes (see Figures 2.1b, 2.2c and Section 2.4). Assuring that tectonic loading is much slower (see Section 2.5 for more details) than diffusion, only the latter way is examined in this Chapter.

The configuration shown in Figures 2.1b and 2.2c leads to a sudden release of the elastic energy upon rupture, in the same way as the energy stored in the rocks surrounding the fault zone is released during an earthquake. Note that typical failure modes II and/or III that take place during seismic slip in faults are represented here by a mode I failure of the porous paper. These systems are equivalent in terms of energy budget (Nussbaum & Ruina, 1987), provided that appropriate scaling laws are applied. By using these scaling laws (see Appendix A.6) and measuring the elastic energy E_R^{paper} that accompanies paper failure in the surrogate system, one can estimate the earthquake magnitude M_w of the real system as follows:

$$M_w = \frac{2}{3} \log_{10} (E_R^{\text{paper}}) + 6.36 \quad (E_R^{\text{paper}} \text{ in Nm}) \quad (2.1)$$

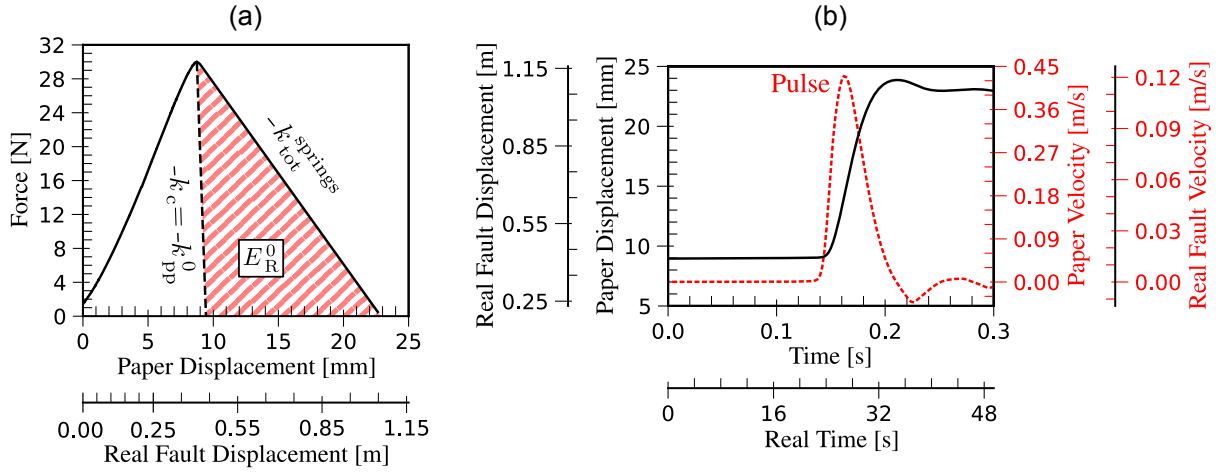


Figure 2.3 – (a) Force-paper displacement diagram of a paper sheet experiment, showing paper behavior without a spring (black dashed line) and with a spring attached to one end (black solid line). The red hatched area, E_R^0 , corresponds to the elastic energy released during the unloading. (b) Pulse-like velocity (red dotted line) of the dynamic paper sheet experiment, with corresponding slip (black solid line). The additional axes scale the respective quantities to the real fault case (cf. Appendix A.6).

In Figure 2.3a, we present the force-displacement evolution of a paper sheet that is put under tension as described above. In the beginning, the porous paper shows a linear behavior up to its peak strength. Then, a fracture appears in the paper sheet and the spring is unloaded abruptly. The energy that is released during the unloading is equal to $E_R^{\text{paper}} = E_R^0 = 0.201 \text{ Nm}$ (red hatched area), corresponding to an equivalent earthquake of $M_w = 5.9$ according to Eq. (2.1). This dynamic instability can also be observed by the velocity pulse shown in Figure 2.3b, illustrating the analogy between paper-quakes and earth-quakes (Kanamori & Brodsky, 2004) (see also Movie S1 in Tzortzopoulos, Braun, et al., 2021).

2.3 From seismic to aseismic rupture

A seismic rupture, i.e. an earthquake, is a dynamic instability that happens when the (elastic) unloading of the rocks surrounding the fault zone cannot be counterbalanced by fault friction. A necessary but not sufficient condition for the occurrence of this instability is the reactivation of the fault. We say that a fault is reactivated when the shear stress on the fault area is high enough for frictional slip to take place. However, this slip can be slow (aseismic) or sudden and abrupt (seismic), depending on the amount of slip weakening

(Figure 2.2d). In Section 1.2.1, the condition for sudden, unstable slip is re-derived (J. H. Dieterich, 1979; Kanamori & Brodsky, 2004; Scholz, 2002; Stefanou, 2019):

$$k < k_c^{\text{sw}} = \frac{\Delta F}{d_c^{\text{sw}}}, \quad (2.2)$$

where k is the apparent stiffness of the rocks surrounding the fault zone for the real system, and k_c^{sw} is the critical stiffness. In a real scenario, the drop of shear force is $\Delta F = A^{\text{real}} \Delta \tau^{\text{real}}$, where $\Delta \tau^{\text{real}}$ is the apparent shear stress drop of the fault zone. The stiffness k is proportional to the effective elastic shear modulus of the surrounding rocks G^{real} , and inversely proportional to the fault length $L_{\text{ac}}^{\text{real}}$, i.e. $k \propto G^{\text{real}}/L_{\text{ac}}^{\text{real}}$ (see also Eq. (1.18)). Moreover, according to Coulomb friction $\tau = \mu \sigma'_n$, where $\sigma'_n = \sigma_n - p_w$ is the effective normal stress, σ_n is the total normal stress, which is a fraction of the overburden load, depending on the tectonic setting, and p_w is the fluid pressure.

Therefore, fluid injections have a double effect. On the one hand, they can reactivate a fault by increasing p_w , reduce its strength and promote frictional slip (Cappa et al., 2019). On the other hand, they can reduce k_c^{sw} as they make the post-peak slope less steep (Lockner et al., 1991; M. Scuderi, Collettini, Viti, et al., 2017) (Figure 2.2d). Consequently, in an earthquake mitigation attempt, one could adjust fluid pressure in such a way to avoid sudden, seismic slip and promote stable, creep-like rupture (Stefanou, 2019).

2.4 Earthquake mitigation by fault segmentation and fluid injections

Controlling the fluid pressure simultaneously, across an entire fault of several kilometers, seems impossible with current technologies. Yet, we could imagine to divide the potential rupture area into several zones and inject fluids through a network of well-bores (Figure 2.1a). In this way, the energy stored in the system could be in theory released gradually, mitigating the maximum earthquake magnitude.

The rupture area of our fault scenario is divided into five segments and so is the paper sheet, as shown in Figures 2.1a-b. In order to have a better understanding of the behavior of the segmented paper sheet (Figure 2.1b) under wetting, we tested first a single segment (Figure 2.4a). In Figure 2.5a, we show the transition from seismic rupture to an aseismic one by wetting. While the dry sample fails suddenly, liberating energy $E_{\text{R}}^{\text{dry}} = 9.2 \text{ Nmm}$ (red hatched area), the wet sample fails progressively with $E_{\text{R}}^{\text{wet}} \approx 0$, i.e. aseismically (see

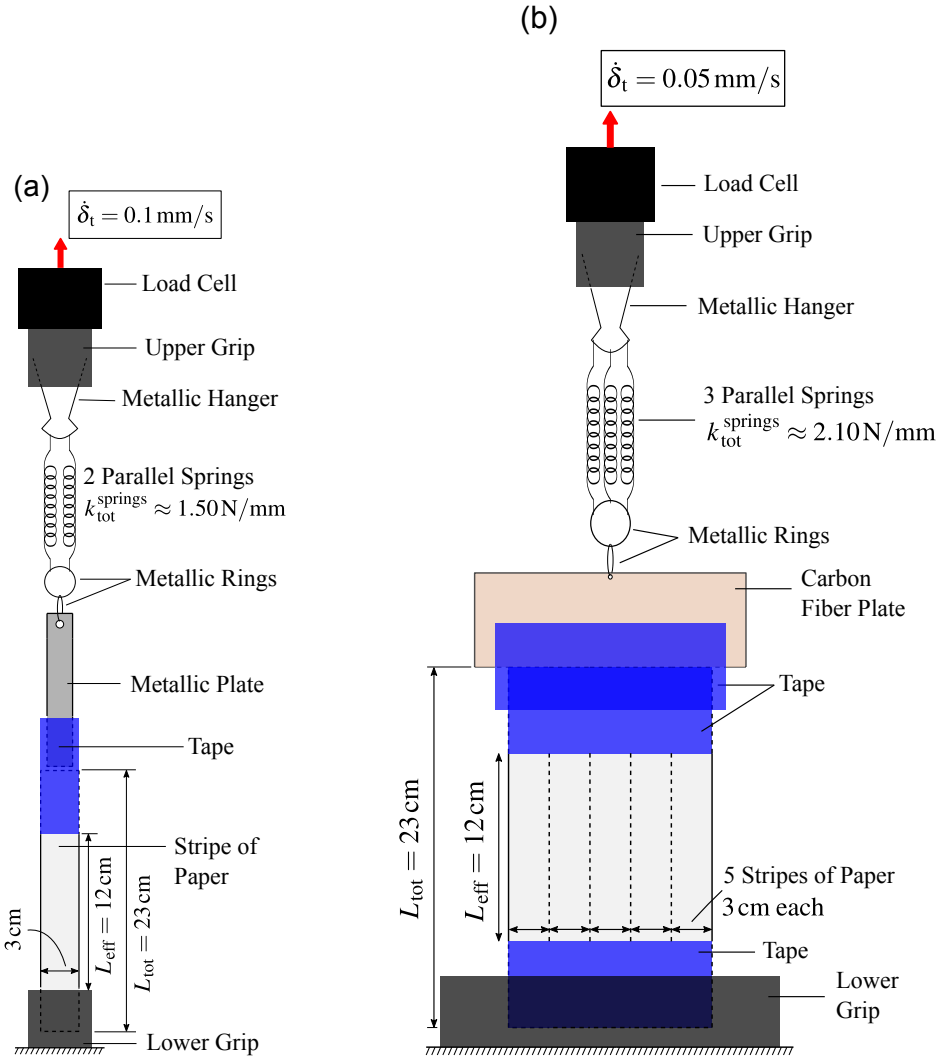


Figure 2.4 – (a) Experimental assembly of a single paper stripe. Two parallel springs ($k_{\text{tot}}^{\text{springs}} = 1.50 \text{ N/mm}$) are connected on top of the specimen to store the elastic energy during the experiment. (b) Assembly of five paper stripes. Here, three parallel springs are added with $k_{\text{tot}}^{\text{springs}} = 2.10 \text{ N/mm}$.

also Movie S2 in Tzortzopoulos, Braun, et al., 2021).

Figure 2.5b corroborates the aseismic failure of the single stripe when wet. In particular, the time-profiles of displacement and velocity are presented and compared for both dry and wet samples. While the dry sample slips abruptly, the wet sample reaches the same displacement in an almost constant, slow velocity, which is two orders of magnitude smaller than the peak velocity of the dry case (see also Movie S2 in Tzortzopoulos, Braun, et al., 2021). If we apply our scaling laws on the experimental data (see Appendix A.6),

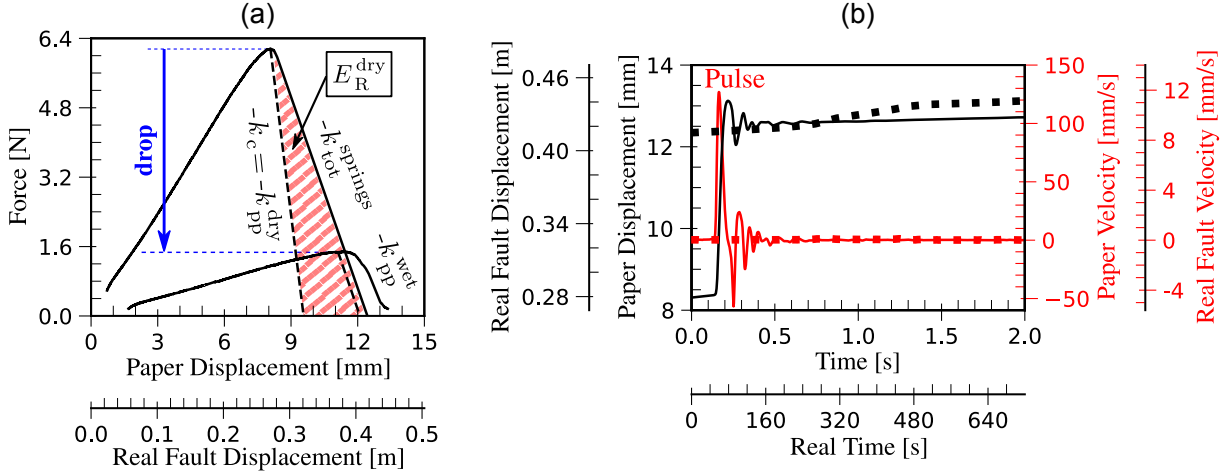


Figure 2.5 – (a) Force-paper displacement diagram of representative dry and wet experiments, for a single paper stripe. Post-peak slope reduction ($k_{pp}^{dry} > k_{pp}^{wet}$) and force drop are observed. In this example, a dynamic instability happens in the dry case ($k_{tot}^{springs} < k_{pp}^{dry}$) releasing energy E_R^{dry} (red hatched area). In the wet case no instability occurs ($k_{tot}^{springs} > k_{pp}^{wet}$). (b) Paper displacement (black) and velocity (red) evolution with time for dry (solid lines) and wet (dotted lines). The stabilizing effect of wetting is apparent. The additional axes scale the respective quantities to the real fault case (cf. Appendix A.6).

the dry single-stripe test gives an earthquake of magnitude $M_w = 4.5$, which is nucleated in a normal fault with a length of $L_{ac}^{real} = 1.3$ km.

Focusing on our surrogate experiment, five stripes (see Figure 2.4b) are put in tension and are wetted subsequently to simulate multiple discrete fluid injections. A certain amount of fluid is injected each time assuring fast saturation all over the respective fault segment. Until the completion of the injection strategy, no more fluid is injected on an already saturated segment. The injection program starts before reaching instability, at a stress level $R = 20\%$ (Figure 2.6a), where R is the ratio of the tensile force at the first injection over the maximum tensile resistance (leading to the large event). Wetting one stripe is performed approximately every 1 mm of total displacement (segment-activation rate = 3 stripes/min). This displacement corresponds to ~ 5 cm of average slip over the real fault zone (see also Appendix A.4 and Movies S1 and S3 in Tzortzopoulos, Braun, et al., 2021).

Each fluid injection is accompanied by an instantaneous stress drop and stress redistribution over the intact, dry porous paper stripes (Cappa et al., 2019; Harris, 1998) (Figure 2.6a). Due to these stress drops, energy is released abruptly, corresponding to the

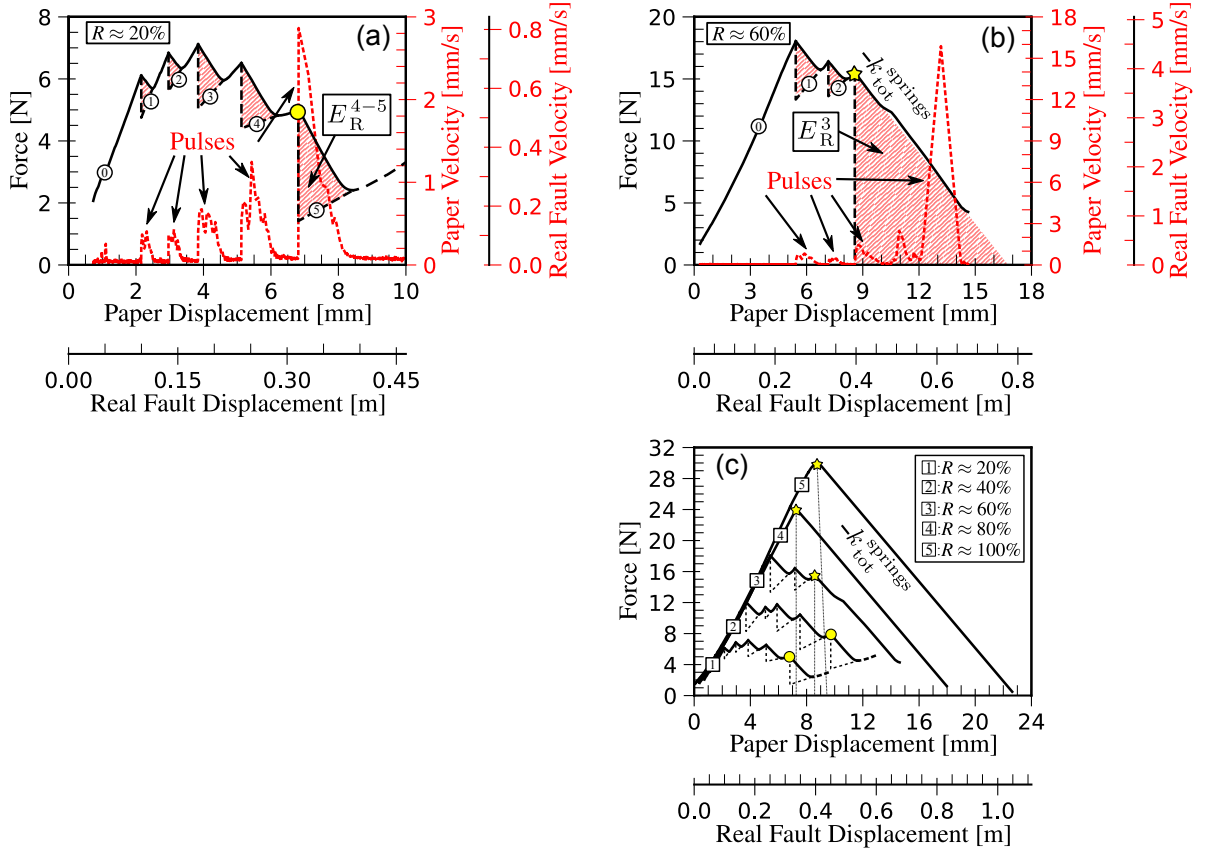


Figure 2.6 – Wetting scenarios starting at (a) $R = 20\%$ and (b) $R = 60\%$. Force (equivalent friction, black solid lines) and velocity (equivalent slip-rate, red dotted lines) evolve with displacement (equivalent slip). Circled numbers depict the number of wetted paper stripes (reactivated fault segments). In (a), the maximum earthquake event takes place at the fifth injection (yellow filled circle) and releases E_R^{4-5} . In (b), the sample fails dynamically at the third injection (yellow filled star) and all remaining elastic energy is released abruptly (rupture of the entire fault area outside the injection area). (c) Force-paper displacement for scenarios started at different stress levels R . The yellow filled star indicates that global failure occurs before wetting all the stripes (i.e. rupture outside the injection region).

triggering of small dynamic events (red hatched areas). Ideally, we would like to minimize their magnitudes or assure aseismic slip after each injection. The maximum magnitude among these smaller events characterizes the effectiveness of the earthquake mitigation strategy.

Figure 2.6a shows the energy release and the developed velocities during this injection program in our experiment. In the same plot we present also the corresponding magnitudes

of displacement and velocity that would develop in the real fault system. A sequence of dynamic events are triggered with magnitudes: $M_w^{0-1} = 3.9$, $M_w^{1-2} = 3.9$, $M_w^{2-3} = 4.3$, $M_w^{3-4} = 4.4$ and $M_w^{4-5} = 4.7$. It is worth emphasizing that the released energy increases with subsequent slip and it is maximum after the last injection ($E_R^{4-5} = 2.94 \text{ Nmm}$), which is 68 times smaller than the energy of the large natural event. Therefore, we were able to mitigate the initial natural earthquake event of magnitude $M_w = 5.9$ to five smaller earthquake events, whose maximum magnitude (yellow filled circle in Figure 2.6a) is $M_w = 4.7$. In terms of velocities (red dotted line in Figure 2.6a), after each injection, we observe a distinct pulse corresponding to the released dynamic energy.

The system behaved differently when the injections started at a stress level ratio $R = 60\%$ (Figure 2.6b, see also Movie S4 in Tzortzopoulos, Braun, et al., 2021). In this case, three dynamic events are triggered with magnitudes: $M_w^{0-1} = 4.7$, $M_w^{1-2} = 4.5$ and $M_w^3 = 5.5$. A large event followed the third injection (yellow filled star in Figure 2.6b), leading to seismic rupture. Energetically speaking, this event ($M_w^3 = 5.5$) is equivalent to the natural earthquake event ($M_w = 5.9$, see also Figures 2.3a-b).

In Figure 2.6c, we show the energy release for injections started at different stress level ratios with the same segment-activation rate as before. In the case of $R \approx 100\%$, no injection can be carried out, as any tiny perturbation leads directly to an earthquake nucleation (yellow filled star) of magnitude $M_w^0 = 5.9$ (Figures 2.3a-b). At $R = 40\%$, all five injections are accomplished as in $R = 20\%$. These injections result in a series of five induced earthquakes where their maximum magnitude (yellow filled circle) is $M_w^{4-5} = 4.8$. When $R = 80\%$, though, a dynamic rupture occurs (yellow filled star) after the first injection leading to an earthquake event of $M_w^1 = 5.8$, similar to the case of $R = 60\%$ (Figure 2.6b).

The experimental observations show clearly that as the stress level at the initiation of the injection process becomes smaller, so does the magnitude of the subsequent events. In other words, a sequence of earthquakes could be triggered, showing a maximum magnitude which is at least one order of magnitude smaller than the natural earthquake.

Notice that our study is in agreement with the findings of the modeling work of van der Elst et al. (2016). As we can observe in Figure 2.6c, the natural earthquake event (curve 5) is the maximum event that can be nucleated in a fault in terms of energy, no matter how much fluid volume has been injected into the fault and no matter when the injection commences. Notice that in this setup, the redistribution is quasi-uniform and may not capture phenomena related to real fault geometries.

2.5 Insights on the governing parameters of the proposed earthquake mitigation strategy

The proposed analogy between uniaxial tension experiments of absorbent porous paper and a real fault system is based on energy considerations. Our model is a pertinent example for building understanding regarding possible mitigation of the earthquake phenomenon (for a synthesis of the main assumptions and limitations we refer to Appendix A.7). Intuitively, our approach could help to limit anthropogenic seismicity (Shapiro et al., 2013) during fluid injections in the earth’s crust, in parallel with the Traffic Light System (TLS) (Bommer et al., 2006; Edwards et al., 2015) and fracture caging methods (Z. Li et al., 2021) used in deep geothermal projects.

It is worth emphasizing that, according to our experiments, preceding small seismic events do not guarantee the avoidance of large ones. Even though the released energy in induced events is always smaller than the natural event, subsequent injections can drive the system faster towards its instability point, provoking a large event (Figures 2.6b-c). These events ($R = 60\%$ and 80% in our experiments) would correspond to anthropogenic seismicity when significant amounts of fluid are injected in the earth’s crust, close to critically stressed tectonic faults. On the other hand, we showed scenarios of progressive wetting, where the maximum seismic moment could be reduced by one order of magnitude (Figures 2.6a and c). Therefore, an important aspect, necessary for the possible mitigation in this scenario, is the relatively low initial stress level ($R = 20\%$ and 40% in our experiments). Therefore, the earthquake mitigation strategy can succeed only if the injection process starts at relatively low stress levels.

Besides the in-situ stress level, the paper experiments uncovered two additional factors which govern the magnitude of induced events. These factors are the segment-activation rate, which expresses the number of segments that are wetted per unit of time, and the number of segments that our samples are divided into. In order to explore the response of the fault system under the variation of these two additional factors, we use a multi spring-slider model (see Appendices A.3-A.4).

The segment-activation rate can be seen as the rate under which we force the system to release its internal (potential/elastic) energy. According to our experiments and this model, this rate has to be fast enough to outpace the progressive energy build-up due to the far-field tectonic displacements. When our segment-activation rate is fast enough, the system releases its internal energy and the large event is avoided. It seems that this is the

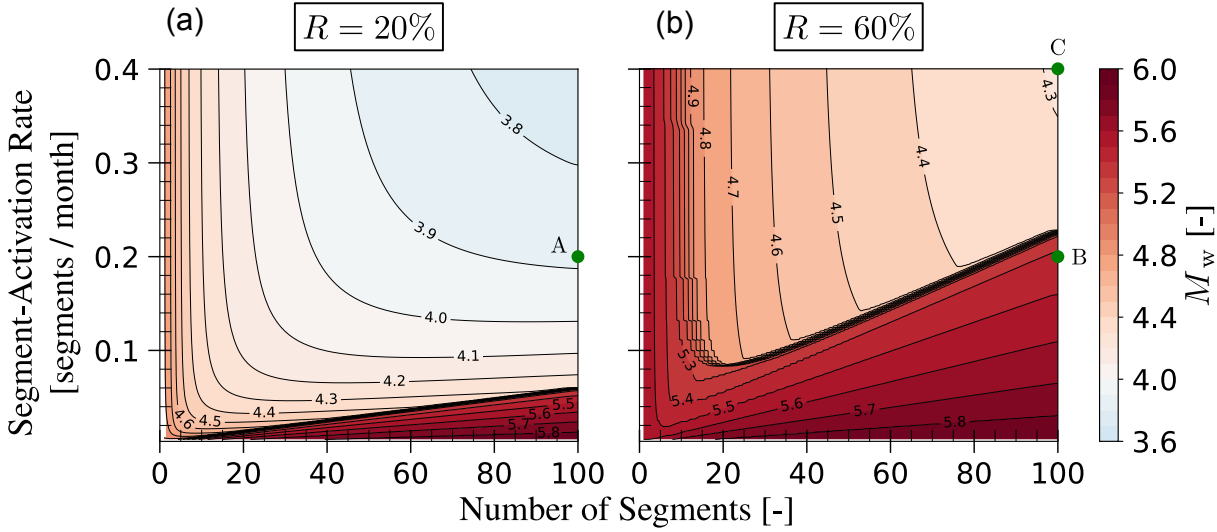


Figure 2.7 – The maximum magnitude is plotted as a function of the segment-activation rate, number of fault segments and two different stress levels, based on our fault scenario: (a) $R = 20\%$ and (b) $R = 60\%$.

case in many industrial projects that involve injections of large amounts of fluids in the earth’s crust (Grigoli et al., 2018; Guglielmi et al., 2015; McGarr, 2014).

According to Hosseini et al. (2018), fluid boundary conditions play an important role in induced seismicity. In our experimental work, fluid boundary conditions are expressed through segmentation by adjusting plastic (impermeable) barriers between the stripes (see also Appendix A.4). Each injection leads to only one seismic event resulting in a linear relation between the number of cumulative events in the fault and the time, presuming constant segment-activation rate. Eventually, the number of segments, that a fault has been divided into, depicts the maximum number of stimulated events.

In the absence of impermeable barriers, high number of segments would represent better the physical reality, where the distribution of injection pressure does not occur instantly over a region (paper segment), but follows a diffusion process (Bhattacharya & Viesca, 2019). The diffusion process due to fluid injection in faults is equivalent to the progressive wetting of paper stripes. If we assume, for instance, a high-permeable damage fault zone with hydraulic diffusivity of the surrounding rocks of the order of 10^{-1} to 10^1 m^2/s (values taken from Lim et al., 2020), the time it takes for each segment ($1.3 \times 6.5 \text{ km}^2$) to be saturated after fluid injection ranges between 10 to 980 days, respectively. In Figure 2.6a, where the experimental results of the proposed injection strategy are presented, the segment-activation rate is 3 stripes/min, which corresponds to 0.01 segments/month in

a real case scenario. Therefore, the above evaluated diffusion time is sufficient enough in order to assure fast saturation of each segment.

Figure 2.7 presents the computed magnitude of the maximum earthquake event that would occur, as a function of segment-activation rate and number of segments. For instance, under a given rate of one injection per five months and for $R = 20\%$, one obtains a maximum $M_w \approx 3.9$, when segmenting the fault into 100 parts (point A, Figure 2.7a). For $R = 60\%$, though, the injection program leads to a large event of $M_w \approx 5.4$, close to the natural one of $M_w \approx 5.9$ (point B, Figure 2.7b). Doubling the rate from one to two injections per five months reduces the maximum event to $M_w \approx 4.3$ (point C, Figure 2.7b).

Despite the numerous uncertainties in the properties of the earth's crust (Cornet, 2019), our experiments (Figure 2.6c) and model (Figure 2.7) reveal the strong dependency between the outcome of the injection strategy and the three aforementioned key parameters (initial stress level, segment-activation rate and segmentation). By adequately controlling these parameters, we managed to artificially reduce the stored elastic energy in an analogue tectonic fault. However, in practice these parameters are hard to control and other strategies based on the mathematical theory of control could provide rigorous alternatives (Stefanou & Tzortzopoulos, 2021; Stefanou, 2019). Such a strategy is developed in the following Chapter 3.

Robust control theory for earthquake prevention

In the previous Chapter, we highlighted some key parameters which could eventually lead to a successful earthquake mitigation strategy. However, in reality, it's difficult to estimate these parameters in-situ. Therefore, fluid injections could risk to nucleate faster the fault system resulting in a large earthquake event. Here, we present a rigorous mathematical framework which can handle such matched and unmatched uncertainties as well as unmodeled dynamics by just solving numerically two decoupled algebraic riccati equations. This framework is based on modern robust control theory. Finally, in case where insufficient measurements are provided, an observer design approach is developed.

3.1 Introduction

Control theory deals with the control of dynamical systems. Given a set of tuning parameters (so-called *input* to the system), an algorithm is designed in such a way that the system is driven to a desired state assuring, all the time, stability of the closed-loop system (dynamical system + controller). A general map of the extent of control theory and its capabilities is illustrated in Figure 3.1 made by Douglas (2020). The most commonly used control theories are: *classical control theory, modern control theory, and robust control theory.*

Classical control theory focuses mainly on linear (or linearized) systems where a transfer function representation is possible (Ogata, 2010; A. I. Vardoulakis, 2012, among others). The frequency response of such plants can be studied and adequate controllers can be designed. However, this theory is handy only for Single-Input-Single-Output (SISO) linear systems. When the number of inputs and outputs increases (Multiple-Inputs-Multiple-Outputs (MIMO) systems) the extension of the theory exists for linear time-invariant systems (A. Vardoulakis et al., 2021). However, when nonlinearities become dominant the

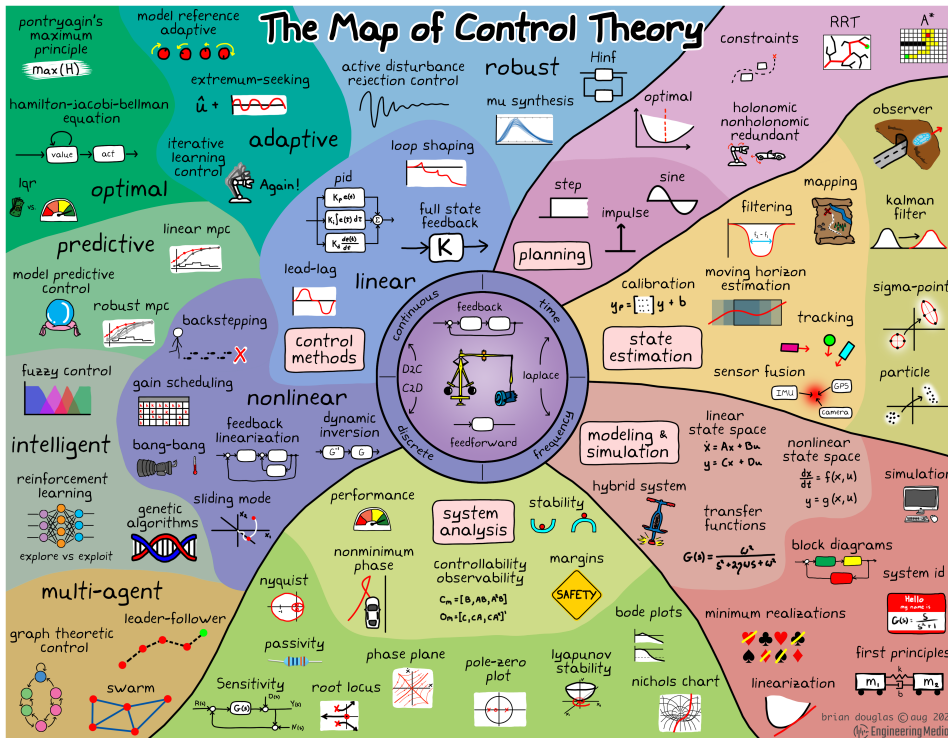


Figure 3.1 – The map of control theory made by Douglas (2020).

control design may be easier using *modern control theory* (Franklin et al., 2018; Lewis et al., 2012; Ogata, 2010). Modern control theory is based on time-domain analyses. Given a model of the plant in state-space representation, a controller can be designed in order to stabilize the system in its equilibrium point or drive it steadily in a new equilibrium point of lower energy.

The drawback of this theory is that it doesn't account for errors or uncertainties between the model and the real plant. In other words, when such a controller is connected with the actual system, the stability of the closed-loop system is not guaranteed (Ogata, 2010). To avoid this, we have to set up the range of the uncertainties and design the control system in such a way that the closed-loop system remains stable within this range. This design is based on the *robust control theory* (Khalil, 2013, 2015; Ogata, 2010).

In this Chapter, we develop robust full-state negative feedback controllers for a class of nonlinear systems accounting for both matched and unmatched uncertainties (see Sections 3.2 and 3.3 and also Khalil, 2013). These controllers can be applied not only in stabilization problems but also in tracking ones (Khalil, 2015). Our design approach is based on the *backstepping* technique (Khalil, 2013) and its novelty relies on the fact that

it accounts for uncertainties also in the input matrix. The controllers can be derived by solving numerically two decoupled Continuous-time Algebraic Riccati Equations (CAREs) resulting in control matrices of constant gains which are easy to implement numerically. Last but not least, it assures robustness and exponential stability without constraints on the state trajectories (Mattei, 2015). More advanced control designs coupling the backstepping technique with sliding modes are proposed in Guenoune et al. (2015), Guenoune et al. (2017, among others).

The aforementioned control design demands to measure in real-time all the degrees-of-freedom (dofs) of the plant. However, in reality, the amount and quality of measurements are not always sufficient. Therefore, there is a need for estimating the dofs of the plant by designing an observer. Here, a full-order Luenberger-like observer is employed (Phanomchoeng & Rajamani, 2010; Raghavan & Hedrick, 1994; Rajamani, 1998; Zhu & Han, 2002). Notice that the presence of this observer doesn't influence the robustness and stability of the already designed controller following the Theorem presented in Khalil (2015).

3.2 Robust controller for a class of nonlinear systems with matched uncertainties

The class of nonlinear systems, that is studied herein, is represented by the following non-linear system of ordinary differential equations:

$$x' = A(t, x)x + B(t, x)u + g(t, x), \quad (3.1a)$$

$$y = C_o x, \quad (3.1b)$$

where $x \in \mathbb{R}^n$ is the state vector, $u \in \mathbb{R}^p$ the input vector, and $y \in \mathbb{R}^m$ the output vector. $g \in \mathbb{R}^n$, $A \in \mathbb{R}^{n \times n}$, and $B \in \mathbb{R}^{n \times p}$ are vector and matrices, respectively, with potential nonlinear elements. $C_o \in \mathbb{R}^{m \times n}$ is the output matrix and $t \geq 0$ the (normalized) time. Note that $(.)' = \frac{d(.)}{dt}$. We assume that the above system is shifted in such a way that the origin ($x = 0$) is an equilibrium, i.e. $x' = 0$.

In the context of this thesis, the vector $g(x, t)$ contains the frictional terms of the system. The matrix $A(t, x)$ represents elastic, viscoelastic or inelastic phenomena of the rock surrounding the fault zone. Its exact components are determined by spatially discretizing the differential operators that correspond to (visco-)elastic and inertia effects on the basis of appropriate discretization methods. The matrix $B(t, x)$ contains the influence of

injected fluid pressure changes (input u) to the dynamics of the system through friction or through the diffusivity of the surrounding rocks. Both matrices $A(t, x)$ and $B(t, x)$ can contain uncertainties and unmodelled dynamics (see for instance Schneider-Muntau et al., 2021). Therefore, we decompose them into a nominal (known) and perturbed/deviated (unknown/uncertain) part:

$$A(t, x) = A_0 + \Delta A(t, x), \quad (3.2a)$$

$$B(t, x) = B_0 + \Delta B(t, x), \quad (3.2b)$$

where A_0 and B_0 are chosen to be constant matrices, such that the pair (A_0, B_0) to be stabilizable (for the definition of stabilizability see Ogata, 2010). ΔA and ΔB are perturbations from the nominal system. This additive decomposition is always possible for the applications presented in this work.

Inserting Eqs. (3.2) into Eq. (3.1a), we obtain:

$$x' = A_0 x + B_0 u + \Delta B(t, x)u + f(t, x), \quad (3.3)$$

where $f(t, x) = \Delta A(t, x)x + g(t, x)$. Assuming *matched uncertainties* (Khalil, 2015), the vector f can be rewritten as $f(t, x) = B_0 B_0^+ f(t, x)$, where $B_0^+ \in \mathbb{R}^{p \times n}$ is the *Moore-Penrose inverse matrix* of B_0 . *Matched uncertainties* correspond to the uncertainties which enter the system through the same channel as the control input u . After rearrangement of some terms, Eq. (3.3) yields:

$$x' = A_0 x + \Delta B(t, x)u + B_0 (u + h(t, x)), \quad (3.4)$$

where $h(t, x) = B_0^+ f(t, x)$ is assumed to be bounded as follows:

$$\|h(t, x)\| \leq \|Gx\|, \quad (3.5)$$

with $G \in \mathbb{R}^{p \times n}$, and $\|\cdot\|$ being the 2-norm. Lipschitz continuity with respect to the states is a special case of Eq. (3.5). In particular, if we assume that $G^T G = \beta^2 I_n$, where I_n is the identity matrix of size n , Eq. (3.5) becomes:

$$\|h(t, x)\|^2 \leq x^T G^T G x \Leftrightarrow \|h(t, x)\|^2 \leq \beta^2 \|x\|^2 \Leftrightarrow \|h(t, x)\| \leq \beta \|x\|, \quad (3.6)$$

where $\beta > 0$. Therefore, if friction is Lipschitz (see Chapter 1) and ΔA bounded, then

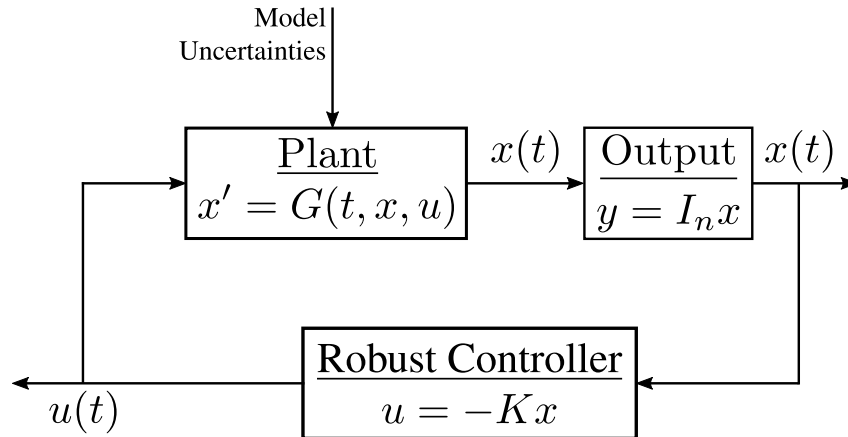


Figure 3.2 – Block diagram of the closed-loop system for stabilization problems. A robust full-state negative feedback controller is designed to stabilize the plant, given by Eq. (3.1), to the origin.

$h(t, x)$ is also Lipschitz.

The dynamics of the above system will be controlled using the mathematical theory of control and more specifically the *Lyapunov Redesign* method (Khalil, 2013, 2015). The target is to update the input, u , which in the applications presented in this thesis corresponds to the pressure of fluids injected (added) and/or extracted (removed) at the frictional interface level in order to stabilize it, i.e. to avoid abrupt, seismic slip and sudden energy release. The term stability is used here in the Lyapunov sense (i.e., the system remains close to its equilibrium state under small perturbations from it; for a rigorous mathematical definition of Lyapunov stability we refer to Lyapunov (1966) and Brauer and Nohel (2012)).

3.2.1 Robust stabilization

We consider a *robust full-state negative feedback* control system as depicted in Figure 3.2. The *Plant* block contains the multivariable system to be controlled, described by Eq. (3.1), and the *Robust Controller* block is the linear robust negative feedback controller we need to design. $y(t)$ is the output of the closed-loop (controlled) system (here all the states of the system can be measured: $y = x$) and $u(t)$ the input of the plant. We seek the controller that can immobilize the system, i.e. $\lim_{t \rightarrow \infty} x = 0$. In the frame of the mathematical theory of control, this process is called *asymptotic stabilization*.

Let the scalar function $V(x) = x^T \Theta x > 0$ for all non-zero $x \in \mathbb{X} \subset \mathbb{R}^n$ and $V(0) = 0$.

Under these conditions, $\Theta \in \mathbb{R}^{n \times n}$ is called *positive definite*, i.e. $\Theta \succ 0$, (or *negative definite* if $x^T \Theta x < 0 \forall x \in \mathbb{X} \subset \mathbb{R}^n \setminus \{0\}$, i.e. $\Theta \prec 0$). The following inequalities are true for the Lyapunov candidate:

$$\lambda_{\min}(\Theta) \|x\|^2 \leq V(x) \leq \lambda_{\max}(\Theta) \|x\|^2, \quad (3.7)$$

$$\left\| \frac{\partial V(x)}{\partial x} \right\| \leq 2\lambda_{\max}(\Theta) \|x\|, \quad (3.8)$$

where $\lambda_{\min}(\Theta) > 0$ and $\lambda_{\max}(\Theta) > 0$ are the minimum and maximum eigenvalues of the positive definite matrix Θ , respectively. We will design a negative full-state feedback ($C_o = I_n$) robust controller of the form $u = -Kx = -R^{-1}B_0^T \Theta x$, where $K \in \mathbb{R}^{p \times n}$ is the constant gain matrix and $R \in \mathbb{R}^{p \times p}$ a positive-definite matrix to be defined.

According to Lyapunov's stability theorem (see *Lyapunov's Second Method*, Brauer & Nohel, 2012), if there exists $V(x) > 0$ for which $\frac{dV(x)}{dt} = V'(x)$ is strictly negative $\forall x \in \mathbb{X} \subset \mathbb{R}^n \setminus \{0\}$, then the origin of the system, $x = 0$, is asymptotically stable. In addition, if $V'(x) < -\alpha_7 \|x\|^2$, with $\alpha_7 > 0$, then the origin of the system, $x = 0$, is exponentially stable. If \mathbb{X} extends over the whole real n -dimensional Euclidean space, then the origin is *globally* asymptotically/exponentially stable, respectively. Differentiating $V(x)$ with respect to time we obtain:

$$V' = x'^T \Theta x + x^T \Theta x' \quad (3.9a)$$

$$\stackrel{\text{Eq.(3.4)}}{=} x^T \left(A_0^T \Theta + \Theta A_0 - \Theta B_0 R^{-1} B_0^T \Theta \right) x - x^T \Theta B_0 R^{-1} B_0^T \Theta x - 2x^T \Theta \frac{B_0 R^{-1} \Delta B^T + \left(B_0 R^{-1} \Delta B^T \right)^T}{2} \Theta x + 2x^T \Theta B_0 h. \quad (3.9b)$$

The first term of Eq. (3.9b) is part of a Continuous Algebraic Riccati Equation (CARE, see also Zhou et al., 1996) of the form:

$$A_0^T \Theta + \Theta A_0 - \Theta B_0 R^{-1} B_0^T \Theta = -Q \quad (3.10)$$

that can be solved numerically. $Q \in \mathbb{R}^{n \times n}$ is chosen to be *positive definite*. Equation (3.10) has a unique positive definite solution $\Theta \succ 0$ if the pair (A_0, B_0) is stabilizable, Q is (at least) *positive semi-definite* (i.e. $Q \succeq 0$ if $x^T Q x \geq 0 \forall x \in \mathbb{X} \subset \mathbb{R}^n \setminus \{0\}$) and $R \succ 0$ (Lewis et al., 2012). Moreover, should we design the nominal matrix B_0 such that the non-Hermitian matrix $B_0 R^{-1} \Delta B^T$ to be always positive semi-definite, the third term of

Eq. (3.9b) is a non-positive number. Setting $z = R^{-1/2}B_0^T\Theta x$, Eq. (3.9) becomes:

$$V' \leq -x^T Q x - z^T z + 2z^T R^{1/2} h, \quad (3.11)$$

where $R^{-1} = R^{-1/2}R^{-1/2}$. We choose the matrix Q to be positive definite and we build it in such a way that Eq. (3.11) to be strictly negative for any given pair of (t, x) . Such a design should contain the uncertainties and non-linearities embedded in vector h (see Eq. (3.5)). Let:

$$Q = Q_0 + \left\| R^{1/2} \right\|^2 G^T G, \quad (3.12)$$

where $Q_0 \succ 0$ is to be specified depending on the application. Substituting Eq. (3.12) to Eq. (3.11) yields:

$$V' \leq -x^T Q_0 x - \left\| R^{1/2} \right\|^2 x^T G^T G x - z^T z + 2z^T R^{1/2} h \quad (3.13a)$$

$$\stackrel{\text{Eq. (3.5)}}{\leq} -x^T Q_0 x - \left\| R^{1/2} \right\|^2 \|Gx\|^2 - \|z\|^2 + 2 \left\| R^{1/2} \right\| \|z\| \|Gx\| \quad (3.13b)$$

$$\leq -x^T Q_0 x - \underbrace{\left(\left\| R^{1/2} \right\| \|Gx\| - \|z\| \right)^2}_{\geq 0} \quad (3.13c)$$

$$\leq -\underbrace{x^T Q_0 x}_{> 0} \leq -\lambda_{\min}(Q_0) \|x\|^2 < 0, \quad (3.13d)$$

where $\lambda_{\min}(Q_0) > 0$ is the minimum eigenvalue of the positive definite matrix Q_0 . The above inequality is valid for any $x \in \mathbb{R}^n$. Therefore, the closed-loop system of Figure 3.2 is globally exponentially stable. Consequently, independently of the initial conditions, $\lim_{t \rightarrow \infty} x(t) = 0$, with $\frac{\lambda_{\min}(Q_0)}{\lambda_{\max}(\Theta)}$ rate of convergence or higher (Khalil, 2015).

3.2.2 Robust tracking

We consider a *robust full-state negative feedback* control system as depicted in Figure 3.3. The *Plant* block and the *Robust Controller* are defined exactly as in Section 3.2.1. $r(t)$ is a desired state of the system, such that $\lim_{t \rightarrow \infty} x_t = r$ or, equivalently, $\lim_{t \rightarrow \infty} e = 0$. To accomplish that, we augment the plant with a number of single integrators. Here, we adopt specific forms for r (e.g. constant, non null velocity, polynomial) in order to drive the system smoothly to a desired stable equilibrium point and dissipate the energy in a controlled manner. In the frame of the mathematical theory of control, this process is called *tracking*. A special case of tracking is the stabilization problem presented in Section

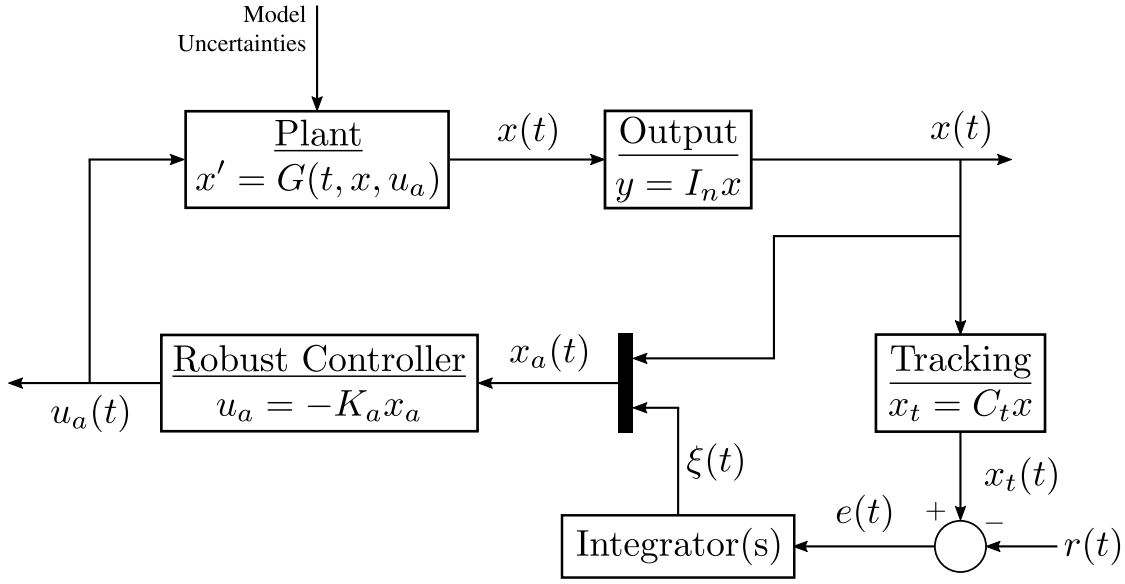


Figure 3.3 – Block diagram of the closed-loop system for tracking problems. A robust full-state negative feedback controller is designed in such a way that the plant given by Eq. (3.1) tracks a reference trajectory $r(t)$.

3.2.1, if we set $r(t) = 0$.

Let $r(t) \in \mathbb{R}^q$ denote the reference input signals that we want to track, with $q \leq p$ (see Lewis et al., 2012). For this purpose we apply the method of *integral action* (Khalil, 2015). Assuming that the dynamics of the designed controller are well represented by q single integrators, and that the reference input vector $r(t)$ is a step command with magnitude r_0 , the compensator dynamics can be expressed by the following set of equations:

$$\xi' = e = C_t x - r_0, \quad (3.14a)$$

$$w = \xi, \quad (3.14b)$$

where $\xi \in \mathbb{R}^q$ expresses the integral of the error between the actual and the desired state r_0 . The multiplication with the matrix $C_t \in \mathbb{R}^{q \times n}$ expresses a linear combination of the outputs of the system in which we want to apply tracking (Eq. (3.1)) and $w \in \mathbb{R}^q$ is the controller's output vector for tracking (see also Figure 3.3).

By augmenting the system of Eqs. (3.1) with Eqs. (3.14), we get:

$$\underbrace{\begin{bmatrix} x' \\ \xi' \end{bmatrix}}_{x'_a} = \underbrace{\begin{bmatrix} A & O_{n \times q} \\ C_t & O_{q \times q} \end{bmatrix}}_{A_a} \underbrace{\begin{bmatrix} x \\ \xi \end{bmatrix}}_{x_a} + \underbrace{\begin{bmatrix} B \\ O_{q \times p} \end{bmatrix}}_{B_a} \underbrace{[u]}_{u_a} + \underbrace{\begin{bmatrix} O_{n \times q} \\ -I_q \end{bmatrix}}_{R_a} [r_0] + \underbrace{\begin{bmatrix} g \\ O_{q \times 1} \end{bmatrix}}_{g_a}, \quad (3.15a)$$

$$\underbrace{\begin{bmatrix} y \\ w \end{bmatrix}}_{y_a} = \underbrace{\begin{bmatrix} C_o & O_{m \times q} \\ O_{q \times n} & I_q \end{bmatrix}}_{C_a} \underbrace{\begin{bmatrix} x \\ \xi \end{bmatrix}}_{x_a}, \quad (3.15b)$$

where $O_{i \times j}$ denote the zero matrix with i rows and j columns. In compact form the above equations are written as follows:

$$x'_a = A_a x_a + B_a u_a + R_a r_0 + g_a, \quad (3.16a)$$

$$y_a = C_a x_a. \quad (3.16b)$$

Considering again full-state feedback ($C_a = I_{n+q}$), the input vector u_a is of the form:

$$u_a = -K_a x_a. \quad (3.17)$$

At steady-state Eqs. (3.16) yield:

$$0 = A_a x_a^* + B_a u_a^* + R_a r_0 + g_a^*, \quad (3.18a)$$

$$y_a^* = C_a x_a^*. \quad (3.18b)$$

By applying the transformation $\tilde{x}_a(t) = x_a(t) - x_a^*$, $\tilde{y}_a(t) = y_a(t) - y_a^*$, $\tilde{u}_a(t) = u_a(t) - u_a^*$, $\tilde{g}_a(t) = g_a(t) - g_a^*$, Eqs. (3.16) become:

$$\tilde{x}'_a = A_a \tilde{x}_a + B_a \tilde{u}_a + \tilde{g}_a, \quad (3.19a)$$

$$\tilde{y}_a = C_a \tilde{x}_a. \quad (3.19b)$$

Using the same transformation, Eq. (3.17) becomes:

$$\tilde{u}_a = -K_a \tilde{x}_a. \quad (3.20)$$

The above system of equations is of the form of Eqs. (3.1) for which a robust stabilizing controller was derived in Section 3.2.1. Consequently, if the input respects Eq. (3.20) or,

equivalently, Eq. (3.17), then $\lim_{t \rightarrow \infty} e(t) = 0$ or $\lim_{t \rightarrow \infty} x_t = r_0$ and so the constant reference input signal r_0 is tracked robustly. For time varying reference trajectories, $r(t)$, we expect a steady state error, which can be attenuated either by adding more integrators (i.e. q double integrators, see also Appendix F) or by increasing the relevant integral action gains.

3.3 Robust controller for a class of nonlinear systems with unmatched uncertainties

When the uncertainties of the nominal state-space model are not in the range of the nominal input matrix as in Section 3.2, then the control design has to tackle the so-called *unmatched uncertainties*. The method we will apply here is inspired by *Lyapunov Redesign*, *Backstepping*, and *Recursive Lyapunov Redesign* techniques (Khalil, 2013, 2015; Krokavec & Filasová, 2000; Lin, 2000; Lin et al., 1990; Lin & Olbrot, 1996; Lin & Zhang, 1993; Mattei, 2015; Petersen, 1987; Qu, 1992; Qu, 1995; Qu & Dorsey, 1991; Qu, 1993, among others).

Consider the following two nonlinear subsystems:

$$x' = A(t, x)x + B(t, x)v + g(t, x), \quad (3.21a)$$

$$v' = A_v(t, v)v + B_z(t, v)u + g_z(t, x, v), \quad (3.21b)$$

where $x \in \mathbb{R}^n$, $v \in \mathbb{R}^p$ are the states of the system, $g \in \mathbb{R}^n$, $u \in \mathbb{R}^r$ is the input vector, $g_z \in \mathbb{R}^p$, $A \in \mathbb{R}^{n \times n}$, $B \in \mathbb{R}^{n \times p}$, $A_v \in \mathbb{R}^{p \times p}$, and $B_z \in \mathbb{R}^{p \times r}$. Let $x_u^T = \{x \ v\}^T$. We assume that the above system is shifted in such a way that the origin ($x_u = 0$) is an equilibrium, i.e. $x'_u = 0$.

Notice that the system of Eqs. (3.21a) should contain matched parameter uncertainties aligned with v . Again, the $A(t, x)$ and $B(t, x)$ matrices represent elastic and viscoelastic phenomena, the geometry of the fault, its exact position and the tectonic setting, while the nonlinear function $g(t, x)$ contains the frictional terms of the system as in Section 3.2.

In the context of this thesis, Eq. (3.21b) corresponds to the diffusion equation with r sources. Consequently, $A_v(t, x, z)$ and $B_z(t, x, z)$ matrices contain the diffusivity of the surrounding rocks which could vary in space and its estimation is difficult (Segall & Rice, 1995). Moreover, they include other uncertain variables such as the distance of the fault from the sources.

Unlike the works presented in Khalil (2013) and Mattei (2015) (among others), the control design we present in this Section accounts also for uncertainties in the input matrix B_z . In addition, even if Eq. (3.21b) is not a scalar ordinary differential equation ($p > 1$) whose uncertainties are in the range of u (matched uncertainties), our approach could provide a robust controller. Finally, robustness is guaranteed without applying any constraints in the evolution of the states or the inputs (Mattei, 2015).

Following the backstepping technique (Khalil, 2013), first, we design a controller for Eq. (3.21a) considering as *virtual* input vector, the state $v \rightarrow v^* = \psi(x)$ using $V(x) = x^T \Theta x$ as Lyapunov function (see Section 3.2). Performing the change of variables $z = v - v^* = v - \psi(x)$ and employing a Lyapunov function $V_b(x)$, we will show that a robust full-state negative feedback controller, $u(z)$, can be designed. In the frame of this thesis, the input vector, $u(z)$, represents the pressure (or the flux) of fluids injected (added) and/or extracted (removed) at the level of the wells which are installed in a distance from an isolated fault.

To begin with, a robust virtual (stabilizing or tracking) full-state feedback controller can be designed using the procedure described in Section 3.2 for Eq. (3.21a), namely:

$$v^* = \psi(x) = -Kx = -R^{-1}B_0^T \Theta x, \quad (3.22)$$

where matrix K is the constant control gains matrix, B_0 the nominal matrix of $B(t, x)$, R a design positive definite matrix and Θ the unique positive definite solution of the CARE defined in Eq. (3.33). Adopting the following change of variables:

$$z = v - v^* = v - \psi(x) = v + Kx, \quad (3.23a)$$

$$v = z - Kx \quad (3.23b)$$

and substituting Eq. (3.23b) into Eqs. (3.21) yields:

$$x' = [A(t, x) - B(t, x)K]x + B(t, x)z + g(t, x), \quad (3.24a)$$

$$z' = \underbrace{[A_v(t, x, z)z + KB(t, x)]}_{A_z(t, x, z)}z + B_z(t, x, z)u + g_z(t, x, z) + [KA(t, x) - \underbrace{(A_v(t, x, z) + KB(t, x))}_{A_z(t, x, z)}K]x + Kg(t, x). \quad (3.24b)$$

By rearranging some terms, we get:

$$x' = [A(t, x) - B(t, x)K]x + g(t, x) + B(t, x)z, \quad (3.25a)$$

$$z' = A_{z0}z + \Delta B_z(t, x, z)u + B_{z0}[u + \underbrace{B_{z0}^+ (\Delta A_z(t, x, z)z + g_z(t, x, z))}_{h_z(t, x, z)}] + \quad (3.25b)$$

$$+ KB_0 \underbrace{B_0^+ (\Delta A(t, x)x + g(t, x))}_{h(t, x)} + KA_0x - A_z(t, x, z)Kx, \quad (3.25c)$$

where we assume that the *pseudoinverse* matrices B_0^+ and B_{z0}^+ of B_0 and B_{z0} , respectively, exist. Moreover, it is assumed that the uncertain matrices $A_z(t, x, z)$ and $B_z(t, x, z)$ are able to be decomposed to a nominal and a perturbed/deviated part as follows:

$$A_z(t, x, z) = A_{z0} + \Delta A_z(t, x, z), \quad (3.26)$$

$$B_z(t, x, z) = B_{z0} + \Delta B_z(t, x, z), \quad (3.27)$$

where B_{z0} is chosen such that the non-Hermitian matrix $B_{z0}R_z^{-1}\Delta B_z^T$ to be always positive semi-definite. Note that R_z is designed to be a positive-definite matrix. The uncertain/nonlinear functions is assumed to be bounded as indicated below:

$$\|h(t, x)\| = \|B_0^+ (\Delta A(t, x)x + g(t, x))\| \leq \|Gx\|, \quad (3.28)$$

$$\|h_z(t, x, z)\| = \|B_{z0}^+ (\Delta A_z(t, x, z)z + g_z(t, x, z))\| \leq \|G_x x\| + \|G_z z\|, \quad (3.29)$$

$$\|B(t, x)z\| \leq \beta_B \|B_0\| \|z\|, \quad (3.30)$$

$$\|A_z(t, x, z)Kx\| \leq \beta_{A_z} \|A_{z0}\| \|Kx\|, \quad (3.31)$$

where β_B and β_{A_z} are positive coefficients and $G \in \mathbb{R}^{p \times n}$, $G_x \in \mathbb{R}^{r \times n}$, and $G_z \in \mathbb{R}^{r \times p}$.

Let's now focus on the structure of the second subsystem in Eq. (3.25). We can observe that the terms that exist in Eq. (3.25b) resemble the ones of Eq. (3.4). Therefore, if we virtually isolate Eq. (3.25b), a robust full-state negative feedback controller can be designed following the procedure described in Section 3.2. Eventually, by employing $V_z(z) = z^T \Theta_z z$ as a Lyapunov candidate, the control input u is given by:

$$u = u(z) = -K_z z = -R_z^{-1} B_{z0}^T \Theta_z z, \quad (3.32)$$

where K_z is the constant control gains matrix and Θ_z is the unique positive-definite solution of Eq. (3.34).

Consequently, in order to stabilize the system of Eqs. (3.25), we have to obtain the unique positive definite solution of the following two uncoupled CAREs:

CARE #1:

$$\begin{aligned} & (\alpha_8 A_0^T) \Theta + \Theta (\alpha_8 A_0) - \Theta B_0 (\alpha_8 R^{-1} - \alpha_9^2 R^{-1} R^{-1}) B_0^T \Theta = \\ & = -\alpha_8 Q_0 - \alpha_8 \|R^{1/2}\|^2 G^T G - \beta_B^2 \|B_0\|^2 I_n - \alpha_9^2 G_x^T G_x - \alpha_9^2 A_0^T A_0 - \alpha_9^2 G^T G, \end{aligned} \quad (3.33)$$

CARE #2:

$$\begin{aligned} & (\alpha_9 A_{z0}^T) \Theta_z + \Theta_z (\alpha_9 A_{z0}) - \Theta_z (\alpha_9 B_{z0} R_z^{-1} B_{z0}^T - B_{z0} B_{z0}^T - K B_0 B_0^T K^T - K K^T - \\ & - \beta_{A_z}^2 \|A_{z0}\|^2 I_p) \Theta_z = -\alpha_9 Q_{z0} - \alpha_9 \|R_z^{1/2}\|^2 G_z^T G_z - \alpha_8^2 \|\Theta\|^2 I_p, \end{aligned} \quad (3.34)$$

where α_8 and α_9 are positive constants, Q_0 and Q_{z0} are chosen to be positive definite. By properly tuning the coefficients α_8 and α_9 and the square matrices Q_0 , R , Q_{z0} , and R_z , the two CAREs above can have unique positive-definite solutions (see also Section 3.2): Θ for CARE #1 and Θ_z for CARE #2.

More specifically, CARE #1 has a unique positive definite solution if the pair $(\alpha_8 A_0, B_0)$ is stabilizable, the matrix $\alpha_8 R^{-1} - \alpha_9^2 R^{-1} R^{-1}$ is strictly positive-definite, and the right-hand-side (rhs) of Eq. (3.33) is a negative semi-definite matrix.

On the other hand, CARE #2 has a unique positive definite solution if the pair $(\alpha_9 A_{z0}, I_p)$ is stabilizable, the matrix inside the parenthesis of the third term of Eq. (3.34) is strictly positive-definite, and the rhs of Eq. (3.34) is a negative semi-definite matrix.

Therefore, we can design a robust full-state negative feedback controller for the system in Eqs. (3.25). As a Lyapunov candidate, following the backstepping method (Khalil, 2013, 2015), we obtain:

$$V_b(x, z) = \alpha_8 V(x) + \alpha_9 V_z(z) = \alpha_8 x^T \Theta x + \alpha_9 z^T \Theta_z z > 0 \quad (3.35)$$

for all non-zero $(x, z) \in \mathbb{X} \subset \mathbb{R}^{n+p}$ and $V_b(0) = 0$. Let $x_b^T = \{x \ z\}^T$, the following inequalities are true for the Lyapunov candidate:

$$\lambda_{\min}(\alpha_8 \Theta, \alpha_9 \Theta_z) \|x_b\|^2 \leq V_b(x, z) \leq \lambda_{\max}(\alpha_8 \Theta, \alpha_9 \Theta_z) \|x_b\|^2, \quad (3.36)$$

$$\left\| \frac{\partial V_b(x, z)}{\partial x_b} \right\| \leq 2\lambda_{\max}(\alpha_8 \Theta, \alpha_9 \Theta_z) \|x_b\|, \quad (3.37)$$

where $\lambda_{\min}(\alpha_8\Theta, \alpha_9\Theta_z) > 0$ and $\lambda_{\max}(\alpha_8\Theta, \alpha_9\Theta_z) > 0$ are the minimum and maximum eigenvalues of the positive definite matrix $\begin{bmatrix} \alpha_8\Theta & O_{n \times p} \\ O_{p \times n} & \alpha_9\Theta_z \end{bmatrix}$, respectively. Calculating the time derivative of the Lyapunov candidate in Eq. (3.35) and using Eqs. (3.22), (3.28)-(3.31), (3.32), and (3.33)-(3.34), we get:

$$V'_b = 2\alpha_8 x^T \Theta x' + 2\alpha_9 z^T \Theta_z z' \quad (3.38a)$$

$$= 2\alpha_8 x^T \Theta [(A - BK) + g] + 2\alpha_8 x^T \Theta Bz + 2\alpha_9 z^T \Theta_z [(A_z - B_z K_z) + g_z] + 2\alpha_9 z^T \Theta_z (KB_0 h + KA_0 x - A_z Kx) \quad (3.38b)$$

$$\begin{aligned} &\leq -\alpha_8 \lambda_{\min}(Q_0) \|x\|^2 - \alpha_9 \lambda_{\min}(Q_{z0}) \|z\|^2 - \\ &\underbrace{\left(\beta_B^2 \|B_0\|^2 x^T x + \alpha_8^2 \|\Theta\|^2 z^T z - 2\alpha_8 x^T \Theta Bz \right)}_{\geq 0} - \\ &\underbrace{\left(\alpha_9^2 x^T G_x^T G_x x + z^T \Theta_z B_{z0} B_{z0}^T \Theta_z z - 2\alpha_9 \|B_{z0}^T \Theta_z z\| \|G_x x\| \right)}_{\geq 0} - \\ &\underbrace{\left(\alpha_9^2 x^T G^T G x + z^T \Theta_z K B_0 B_0^T K^T \Theta_z z - 2\alpha_9 z^T \Theta_z K B_0 h \right)}_{\geq 0} - \\ &\underbrace{\left(\alpha_9^2 x^T A_0^T A_0 x + z^T \Theta_z K K^T \Theta_z z - 2\alpha_9 z^T \Theta_z K A_0 x \right)}_{\geq 0} - \\ &\underbrace{\left(\alpha_9^2 x^T K^T K x + \beta_{A_z}^2 \|A_{z0}\|^2 z^T \Theta_z \Theta_z z + 2\alpha_9 z^T \Theta_z A_z Kx \right)}_{\geq 0} \end{aligned} \quad (3.38c)$$

$$< -\lambda_{\min}(\alpha_8 Q_0, \alpha_9 Q_{z0}) \|x_b\|^2 < 0, \quad (3.38d)$$

where $\lambda_{\min}(\alpha_8 Q_0, \alpha_9 Q_{z0}) > 0$ is the minimum eigenvalue of the positive-definite matrix $\begin{bmatrix} \alpha_8 \lambda_{\min}(Q_0) I_n & O_{n \times p} \\ O_{p \times n} & \alpha_9 \lambda_{\min}(Q_{z0}) I_p \end{bmatrix}$. Note that $\lambda_{\min}(Q_0) > 0$ and $\lambda_{\min}(Q_{z0}) > 0$ are the minimum eigenvalues of the positive-definite matrices Q_0 and Q_{z0} , respectively. In addition, the under-braced terms in Eq. (3.38c) can be proven to be positive scalars using the identity rule:

$$\pm X^T Y \pm Y^T X \leq X^T X + Y^T Y \Leftrightarrow (X^T \pm Y^T)(X \pm Y) \geq 0, \quad (3.39)$$

which is true for any arbitrary matrices X and Y of appropriate dimensions.

Therefore, the system of Eqs. (3.21) is globally exponentially stable (Khalil, 2015).

The expression of the input u can be obtained from Eq. (3.32), namely:

$$u(x, v) = -K_z z \stackrel{\text{Eq.(3.23a)}}{=} -K_z (v + Kx), \quad (3.40)$$

where K and K_z are taken from Eqs. (3.22) and (3.32), respectively. The procedure presented in this Section can be applied either to stabilization or tracking problems as introduced in Section 3.2. In case of stabilization, independently of the initial conditions, $\lim_{t \rightarrow \infty} x_u(t) = 0$. In case of tracking, q single integrators can be embedded in either of the subsystems in Eq. (3.21). In this work, we integrate them along with Eq. (3.21a) and therefore, $\lim_{t \rightarrow \infty} x_t(t) = r_0$, for constant references. For time varying reference trajectories, $r(t)$, though, we expect a steady state error, which can be attenuated either by adding more integrators (i.e. q double integrators, see also Appendix F) or by increasing the relevant integral action gains. Finally, the rate of convergence in both stabilization and tracking problems is $\frac{\lambda_{\min}(\alpha_8 Q_0, \alpha_9 Q_z)}{\lambda_{\max}(\alpha_8 \Theta, \alpha_9 \Theta_z)}$ or higher (Khalil, 2015).

3.4 Full-order observer for a class of nonlinear systems

The control design presented in Sections 3.2 and 3.3 requires complete knowledge of the states x and x_u , in real-time. In the context of Chapter 4, this would correspond to know the slip, slip-rate, and effective normal stress for every single element in the strike-slip fault. However, in reality, this is not feasible because the measurements that we can obtain are spatially sparse (e.g. GPS measurements regarding the movement of the surface of the surrounding fault area, INSAR, sensors installed in the earth's crust and other indirect measurements based on inversion techniques). Therefore, the challenge here is to recreate/estimate the states by just acquiring sparse measurements in space. These estimations can be used as a feedback to the controller designed in Sections 3.2 and 3.3. The block diagram of the resulting closed-loop system is depicted in Figure 3.4.

For this purpose, we adopt a full-order observer, which is able to estimate the states of the system taking into account parameter uncertainties. Consider the nonlinear differential equations presented below:

$$x' = A(t, x)x + B(t, x)u + g(t, x), \quad (3.41a)$$

$$y = C_o x, \quad (3.41b)$$

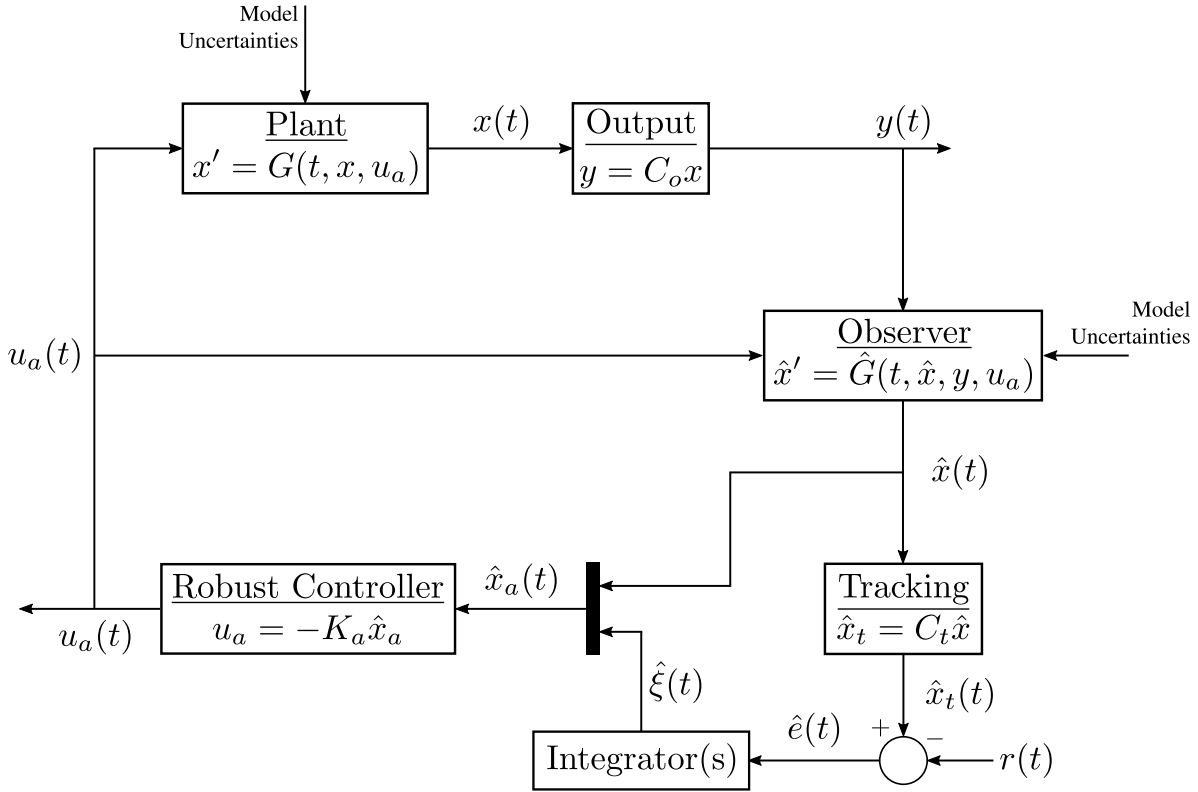


Figure 3.4 – Block diagram of the closed-loop system augmented by the observer. The estimated states, \hat{x} , are used as feedback to the robust controller designed in Sections 3.2 and 3.3.

where $x \in \mathbb{R}^n$ is the state vector, $u \in \mathbb{R}^p$ the input vector, and $y \in \mathbb{R}^m$ the output vector. $g \in \mathbb{R}^n$, $A \in \mathbb{R}^{n \times n}$, and $B \in \mathbb{R}^{n \times p}$ are vector and matrices, respectively, with potential nonlinear elements. $C_o \in \mathbb{R}^{m \times n}$ is the output matrix and $t \geq 0$ the (normalized) time. Note that $(\cdot)' = \frac{d(\cdot)}{dt}$. We assume again that the above system is shifted in such a way that the origin ($x = 0$) is an equilibrium, i.e. $x' = 0$.

As we mentioned in the beginning of this Section, we account for parameter uncertainties and, therefore, the matrices $A(t, x)$ and $B(t, x)$ can be decomposed as follows:

$$A(t, x) = A_0 + \Delta A(t, x), \quad (3.42a)$$

$$B(t, x) = B_0 + \Delta B(t, x), \quad (3.42b)$$

where A_0 and B_0 are chosen to be constant matrices defining the nominal system. ΔA and ΔB are perturbations from the nominal system. This additive decomposition is always

possible for the applications presented in this work. Notice that we assume that the pair (A_0, C_o) is observable (for the definition of observability see Ogata, 2010). By substituting Eqs. (3.42) into Eq. (3.41a) yields:

$$x' = A_0x + B_0u + \Delta A(t, x)x + \Delta B(t, x)u + g(t, x). \quad (3.43)$$

The observer dynamics are comprised of a copy of the nominal plant (Eq. (3.43)) plus a correction term concerning the measurements:

$$\hat{x}' = A_0\hat{x} + B_0u + \hat{g}(t, \hat{x}) + L(y - \hat{y}), \quad (3.44a)$$

$$\hat{y} = C_o\hat{x}, \quad (3.44b)$$

where \hat{g} is an estimate of the nonlinear function g . This design is based on *Luenberger-like* observers (Khalil, 2015; Phanomchoeng & Rajamani, 2010; Raghavan & Hedrick, 1994; Rajamani, 1998; Zhu & Han, 2002). By replacing the outputs y and \hat{y} with their respective expressions results:

$$\hat{x}' = A_0\hat{x} + B_0u + \hat{g}(t, \hat{x}) + LC_o \underbrace{(x - \hat{x})}_{\tilde{e}}. \quad (3.45)$$

Let $\tilde{e} = x - \hat{x}$. By substituting Eq. (3.43) from Eq. (3.45), we get:

$$\tilde{e}' = (A_0 - LC_o)\tilde{e} + \underbrace{g(t, x) - \hat{g}(t, \hat{x})}_{\tilde{g}(t, x, \hat{x})} + (\Delta A - \Delta BK)\hat{x}, \quad (3.46)$$

where we replaced $u = -K\hat{x}$. The control gain matrix K can be calculated using the techniques proposed in Sections 3.2 and 3.3. Furthermore, we assume that the function $\tilde{g}(t, x, \hat{x})$ is Lipschitz:

$$\|\tilde{g}(t, x, \hat{x})\| \leq \beta_o \|\tilde{e}\|, \quad (3.47)$$

with $\beta_o > 0$. The matrix L has to be designed in such a way that the matrix $A_0 - LC_o$ is *Hurwitz* (Ogata, 2010). As far as the pair (A_0, C_o) is observable, even “brute force”, *pole-placement* techniques can be used to calculate the observer matrix L (Franklin et al., 2018; Ogata, 2010). Here, for the design of the L matrix, we use the fact that the controller and the observer are dual systems (Lewis et al., 2012). Therefore, L is given by the following relation:

$$L^T = R_L^{-1}C_o^T P_L, \quad (3.48)$$

where R_L is a positive-definite matrix to be defined and P_L is the unique positive-definite solution of the following CARE:

$$A_0 P_L + P_L A_0^T - P_L C_o^T R_L^{-1} C_o^T P_L = -Q_L, \quad (3.49)$$

where Q_L is again a positive-definite matrix to be defined. Consequently, the square matrix $A_0 - LC_o$ is stable as all its eigenvalues are placed in the left half-plane of the imaginary axis.

The design of the observer in Eq. (3.44) is successful if the error, \tilde{e} , between the actual states (x) and the estimated ones (\hat{x}), converges to zero asymptotically or, even better, exponentially, i.e. $\lim_{t \rightarrow \infty} \tilde{e} = 0$. Therefore, in order to study the stability of the error dynamics presented in Eq. (3.46), we employ the following Lyapunov candidate:

$$V_o(\tilde{e}) = \tilde{e}^T \Theta_o \tilde{e}, \quad (3.50)$$

where Θ_o is the positive definite solution of the *Lyapunov Equation* (LE) defined below:

$$(A_0 - LC_o)^T \Theta_o + \Theta_o (A_0 - LC_o) = -Q_o, \quad (3.51)$$

where Q_o is designed to be a positive-definite matrix. The following inequalities are true for the Lyapunov candidate:

$$\lambda_{\min}(\Theta_o) \|\tilde{e}\|^2 \leq V(\tilde{e}) \leq \lambda_{\max}(\Theta_o) \|\tilde{e}\|^2, \quad (3.52)$$

$$\left\| \frac{\partial V(\tilde{e})}{\partial \tilde{e}} \right\| \leq 2\lambda_{\max}(\Theta_o) \|\tilde{e}\|, \quad (3.53)$$

where $\lambda_{\min}(\Theta_o) > 0$ and $\lambda_{\max}(\Theta_o) > 0$ are the minimum and maximum eigenvalues of the positive definite matrix Θ_o , respectively. Calculating the time derivative of Eq. (3.50), we get:

$$\begin{aligned} V_o' &= \tilde{e}^T \left[(A_0 - LC_o)^T \Theta_o + \Theta_o (A_0 - LC_o) \right] \tilde{e} + 2\tilde{e}^T \Theta_o \tilde{g} + 2\tilde{e}^T \Theta_o (\Delta A - \Delta BK) \hat{x} \\ &\stackrel{\text{Eq. (3.51)}}{=} -\lambda_{\min}(Q_o) \|\tilde{e}\|^2 + 2\beta_o \|\Theta_o\| \|\tilde{e}\|^2 + 2\tilde{e}^T \Theta_o (\Delta A - \Delta BK) \hat{x}, \end{aligned} \quad (3.54)$$

where $\lambda_{\min}(Q_o) > 0$ is the minimum eigenvalue of the positive-definite matrix Q_o . If:

$$\beta_o < \frac{\lambda_{\min}(Q_o)}{2 \|\Theta_o\|}, \quad (3.55)$$

then Eq. (3.54) becomes:

$$V'_o \leq -\alpha_{10} \|\tilde{e}\|^2 + 2 \|\tilde{e}\| \|\Theta_o (\Delta A - \Delta BK)\| \|\hat{x}\|, \quad (3.56)$$

where α_{10} is a positive constant. We want the above inequality to be negative in order to assure that the error dynamics are at least asymptotically stable. However, at this stage, we cannot guarantee this. For that, we introduce the notion of *Input to State Stability* (ISS) (for more information see Khalil, 2015). We can infer that the above inequality is negative outside a ball with radius:

$$\|\tilde{e}\| \geq \underbrace{\frac{2 \|\Theta_o (\Delta A - \Delta BK)\|}{\theta_1 \alpha_{10}}}_{\text{radius of attraction}} \|\hat{x}\|, \quad (3.57)$$

where θ_1 is a positive constant between 0 and 1. Outside this region, the system is stable, however, inside this region, we can conclude nothing about the behavior of the system (stable or unstable). In the case where the condition of Eq. (3.55) is not satisfied the respective region of attraction is given by the following relation:

$$\|\tilde{e}\| \geq \underbrace{\frac{2 \|\Theta_o\|}{\theta_2 \lambda_{\min}(Q_o)} (\|\hat{x}\| \|\Delta A - \Delta BK\| + \|\tilde{g}\|)}_{\text{radius of attraction}}, \quad (3.58)$$

where θ_2 is a positive constant between 0 and 1. The regions of attraction defined above could be extremely large allowing significant instabilities in the *black box* which is encapsulated inside the aforementioned radius. Certainly, there would be better approaches for observer design, in the literature, which could minimize the region of attraction or even eliminate it. However, such an observer design is out of the scope of this Thesis. Here, we want to highlight the capabilities of control theory in the earthquake control problem. Of course, more advanced tools can be used in order to increase the performance and account for uncertainties also in the observer design. Therefore, in this Thesis, and specifically in the following Chapter, the observer will be designed without accounting for any uncertainty allowing the nominal system and the parameters of the specific applications

to coincide. In this case, we expect an exponential convergence of the estimation error to the origin.

The question which arises now is if we can use the control design developed in Sections 3.2 and 3.3 using as feedback the estimations of the states, \hat{x} , and not the actual states, x (see also Figure 3.4). In other words, is the closed-loop, plant-observer-controller, system still exponentially stable? The answer to this crucial question is provided in a *Theorem* presented in Khalil (2015). This theorem states that if the origin of the plant with the full-state negative feedback controller (without observer) is exponentially stable and the error dynamics of the Luenberger-like observer are also exponentially stable, then the origin of the plant-observer-controller system is exponentially stable (Khalil, 2015).

Robust control of seismic faults

In the previous Chapter, we developed the mathematical framework for the design of robust controllers in order to drive a class of nonlinear systems to a desired state assuring, all the time, stability of the closed-loop system. Here, we apply this approach to a strike-slip fault configuration. First, the example of measuring all the states and actuating the pressure at every single point is presented. In this example, a rate-and-state and slip-weakening frictional behavior are examined and compared. Going a step further, we present a more realistic scenario. In this, diffusion processes are included allowing to model the influence of distant fluid injections to the fault region. For this scenario, we measure only the average deformation of the fault at the surface. Despite the presence of uncertainties in the model parameters as well as of insufficient measurements, we show that using the control strategy developed in the previous Chapter, earthquake control is possible. Finally, we proceed with a non-local scenario, where we control the seismicity in the region of a reservoir by adjusting the fluxes in the surrounding wells maintaining the desired fluid production levels.

4.1 Strike-slip fault dynamics

In this Section, we present the dynamics of the isolated strike-slip fault configuration illustrated in Figure 4.1a. The fault is just beneath the surface and it covers a rectangular area of $L_x \times L_z$ in the x- and z-directions, respectively. We assume also that the fault is adequately oriented in the tectonic stress regime for slip to occur. For the discretization of the fault area, we use a regular mesh with N_x elements along x-axis and N_z elements along z-axis. Therefore, the total number of elements covering the fault area is $n_f = N_x \times N_z$. The size of each element is equal to $D_x \times D_z$, where $D_x = \frac{L_x}{N_x}$ and $D_z = \frac{L_z}{N_z}$. The dynamics of the strike-slip fault can be represented, at first approximation, by the following ordinary

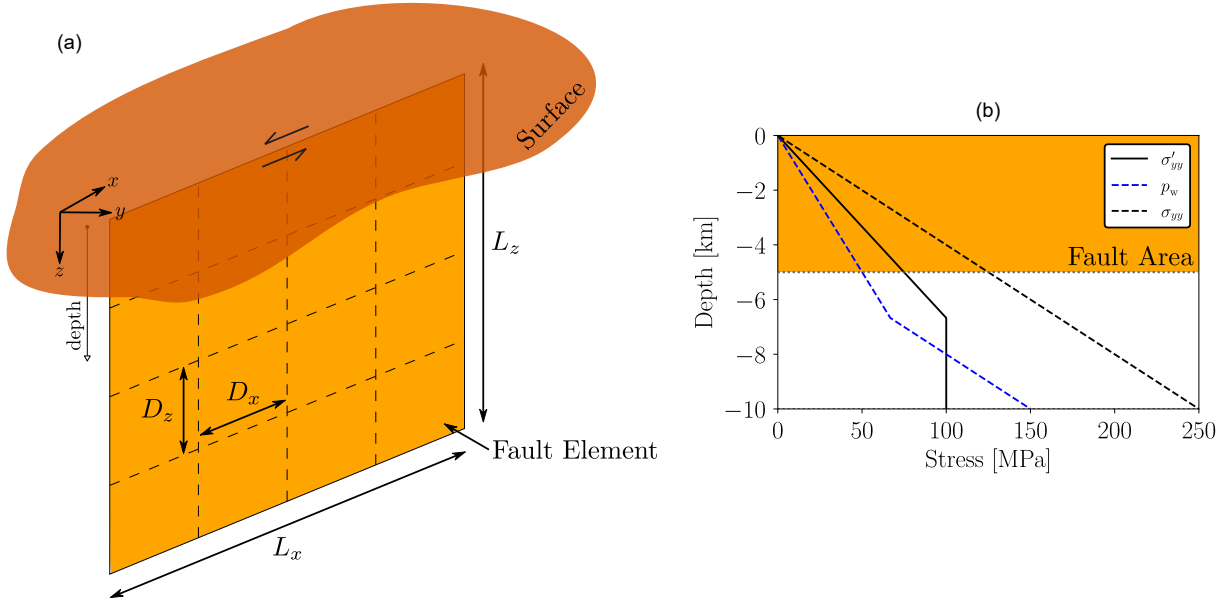


Figure 4.1 – (a) Sketch of a strike-slip fault configuration discretized in $N_x \times N_z$ elements. (b) In-situ pore fluid pressure p_w , in-situ normal stress σ_{yy} and effective normal stress σ'_{yy} as a function of depth.

differential equation in matrix form:

$$M\ddot{\delta} = -F_r + K(\delta_\infty(t) - \delta) + H(v_\infty - \dot{\delta}), \quad (4.1)$$

where $\delta, \dot{\delta}, \ddot{\delta} \in \mathbb{R}^{n_f}$ are the vectors that contain respectively the slip, slip-rate, and acceleration of each individual element, $F_r \in \mathbb{R}^{n_f}$ is the frictional response, $\delta_\infty \in \mathbb{R}^{n_f}$ and $v_\infty \in \mathbb{R}^{n_f}$ are the far-field slip and slip-rate of the tectonic plates, respectively. Moreover, $M \in \mathbb{R}^{n_f \times n_f}$ is the mass matrix, $K \in \mathbb{R}^{n_f \times n_f}$ the elasticity matrix, and $H \in \mathbb{R}^{n_f \times n_f}$ the viscosity matrix.

For the simulations presented in this Chapter, a dynamic approach has been employed, adopting a lumped mass matrix in order to represent the mobilized mass during a seismic event:

$$M = \frac{m}{N_x N_z} I_{n_f} = \rho L_y D_x D_z I_{n_f}, \quad (4.2)$$

where I_{n_f} is the identity matrix of size n_f . As mentioned in Section 1.2 and more specifically in Eq. (1.17), during an earthquake, we assume that a cuboid of rock mass $m = \rho L_x L_y L_z$ is mobilized. ρ is the density of the surrounding rocks and $L_y = \min(L_x, L_z)$. Other, more accurate, formulations are of course possible (see Erickson et al., 2020, among

others). Following Eq. (1.20), the viscosity matrix is given by:

$$H = 2\zeta M\Omega_n, \quad (4.3)$$

where ζ is the damping ratio and Ω_n the natural frequency of the system:

$$\Omega_n = \sqrt{M^{-1}K}. \quad (4.4)$$

The square root above is defined for matrices. Finally, the frictional response is obtained by the following expression:

$$F_r = \mu(t, \delta, \dot{\delta}) (\sigma'_n - p) D_x D_z, \quad (4.5)$$

where $\mu(t, \delta, \dot{\delta})$ is the coefficient of friction, σ'_n the effective normal stress, and p any fluid pressure variations in the fault interface when the controller is activated (see Chapter 3). The effective normal stress $\sigma'_n = \sigma'_{yy}$ varies with depth as shown in Figure 4.1b. Dividing Eq. (4.1) by the scalar product $D_x D_z$ and substituting Eqs. (4.2)-(4.5), we get:

$$\rho L_y \ddot{\delta} = -\mu(t, \delta, \dot{\delta}) (\sigma'_n - p) + \bar{K}(\delta_\infty(t) - \delta) + \bar{H}(\nu_\infty - \dot{\delta}), \quad (4.6)$$

where:

$$\bar{K} = \frac{1}{D_x D_z} K = G K_{\text{con}}, \quad (4.7)$$

$$\Omega_n \stackrel{\text{Eq. (4.4)}}{=} \sqrt{\frac{G}{\rho L_y} K_{\text{con}}} = \underbrace{\frac{v_s}{L_y}}_{\omega_n} \sqrt{L_y K_{\text{con}}}, \quad (4.8)$$

$$\bar{H} = 2\zeta \rho L_y \Omega_n = 2\zeta \rho L_y \omega_n \sqrt{L_y K_{\text{con}}}, \quad (4.9)$$

where K_{con} is the connectivity matrix obtained using the theory presented in Chinnery (1963) and Rice (1993). It is worth emphasizing that several methods can be used in order to discretize the differential operator representing the underlying continuum elastodynamic problem of seismic slip (e.g. Finite Element Method, Finite Differences, Boundary Element Method, spectral methods, model reduction methods, among others (see S. D. Barbot, 2019b; Boyd, 2000; Erickson et al., 2020; Larochelle et al., 2021)). In most cases, the resulting discretized equations will finally take the form of Eq. 3.1 and, consequently, the control theory presented in Chapter 3 can be applied.

Introducing a characteristic time T , a characteristic length D and a characteristic pressure P , and dividing by the scalar product ρL_y , the system of Eqs. (4.6) becomes:

$$d'' = - \underbrace{\frac{PT^2}{\rho L_y D}}_{\hat{N} \in \mathbb{R}} \mu(\hat{t}, d, d') (\hat{\sigma}'_n - \hat{p}) + \underbrace{\frac{GT^2}{\rho L_y^2}}_{\hat{k} \in \mathbb{R}^{n_f \times n_f}} L_y K_{\text{con}} (d_\infty(\hat{t}) - d) + \underbrace{2\zeta \omega_n T \sqrt{L_y K_{\text{con}}}}_{\hat{\eta} \in \mathbb{R}^{n_f \times n_f}} (q_\infty - d'), \quad (4.10)$$

with (see also Section 1.2):

$$t = \hat{t}T, \quad (4.11)$$

$$\delta = dD, \quad (4.12)$$

$$\sigma'_n = \hat{\sigma}'_n P, \quad (4.13)$$

$$p = \hat{p}P, \quad (4.14)$$

$$\delta_\infty = d_\infty D, \quad (4.15)$$

$$v_\infty = q_\infty \frac{D}{T}, \quad (4.16)$$

where \hat{t} , d , $\hat{\sigma}'_n$, \hat{p} , d_∞ , and q_∞ are the dimensionless time, slip, effective normal stress, injected fluid pressure change, far-field displacement and velocity, respectively. Hence, Eq. (4.10) can be rewritten as:

$$d'' = -\mu(\hat{t}, d, d') (\hat{\sigma}'_n - \hat{p}) \hat{N} + \hat{k}(d_\infty(\hat{t}) - d) + \hat{\eta}(q_\infty - d'), \quad (4.17)$$

which resembles in structure with Eq. (1.24) of the spring-slider model presented in Section 1.2. In this Chapter, we are focusing on isolated dynamic events. Performing a double-scale asymptotic analysis (see Stefanou, 2019), we can shift the above system in such a way that the origin coincides with an (unstable) equilibrium point (see Chapter 1 and particularly Section 1.2) and study the dynamic response of the fast-time scale:

$$\begin{cases} \tilde{q}' = -\hat{\eta}\tilde{q} - \hat{k}\tilde{d} + \hat{N}\mu\hat{p} - \hat{N}(\mu - \mu^*)\hat{\sigma}'_n, \\ \tilde{d}' = \tilde{q}, \end{cases} \quad (4.18a)$$

$$(4.18b)$$

where the superscript $\tilde{}$ corresponds to the perturbed from the equilibrium point variables. In addition, $\mu = \mu(\hat{t} + \hat{t}^*, \tilde{d} + d^*, \tilde{q} + q^*)$ and $\mu^* = \mu(\hat{t}^*, d^*, q^*)$. The superscript $*$ denotes the equilibrium point ($\tilde{q}' = \tilde{d}' = 0$). We can observe that the origin ($\tilde{q} = \tilde{d} = \tilde{p} = 0$) is

an (potentially unstable) equilibrium point. In this formulation, zero slip-rate ($\tilde{d}' = 0$) corresponds to zero relative slip-rate with respect to the far-field movement of the tectonic plates (q_∞). The matrix form of Eq. (4.18) is:

$$\begin{Bmatrix} \tilde{q}' \\ \tilde{d}' \end{Bmatrix} = \begin{bmatrix} -\hat{\eta} & -\hat{k} \\ I_{n_f} & O_{n_f \times n_f} \end{bmatrix} \begin{Bmatrix} \tilde{q} \\ \tilde{d} \end{Bmatrix} + \begin{bmatrix} \hat{N}\mu \\ O_{n_f \times p_f} \end{bmatrix} \{\hat{p}\} + \begin{Bmatrix} -\hat{N}(\mu - \mu^*)\hat{\sigma}'_n \\ O_{n_f \times 1} \end{Bmatrix}, \quad (4.19)$$

where p_f corresponds to the number of actuators, we employ.

In the following two subsections, we present the dynamic response ($\hat{p}(t) = 0$) of a strike-slip fault (see Figure 4.1a) governed by Eq. (4.19) and adopting either rate-and-state (see Section 1.1.3) or slip-weakening (see Section 1.1.1) friction law. For these academic examples, the frictional and mechanical properties of the isolated fault are summarized in Table 4.1.

4.1.1 Rate-and-state friction

The truncated version of the rate-and-state friction law is considered using the aging law for the evolution of the state (see Section 1.1.3 and particularly Eq. 1.9). The parameters a , b and d_c^{rsf} are spatially distributed using a log-normal distribution with average $a^{\text{avg}} = 0.010$, $b^{\text{avg}} = 0.015$ and $(d_c^{\text{rsf}})^{\text{avg}} = 10$ mm and standard deviation corresponding to 5% of these average values (see Table 4.1c). These frictional parameters are kept constant over each element of the discretization during the simulations. This stochastic distribution of the frictional parameters over the fault area represents heterogeneities that exist in real faults and show that the proposed control approach is insensitive to this kind of uncertainties.

The fault area is discretized into $N_x \times N_z = 20 \times 20$ elements. This discretization is fine enough as the elements have a characteristic size of 0.25 km, which is sufficiently lower than the minimum nucleation size, $h_{\min}^* = 0.60$ km ($\frac{h}{h^*} \approx 0.4$) in order to assure that each element cannot act independently of one another (Rice, 1993). The nucleation size over the fault area is illustrated in Figure 4.2a. It is calculated (element-wise) as (see Rice, 1993):

$$h^* = \frac{2}{\pi} \frac{Gd_c}{(b-a)\sigma'_n} \frac{1 + r_d^2/(1-\nu)}{(1 + r_d^2)^{1/2}}, \quad (4.20)$$

where $r_d = \frac{D_z}{D_x}$ and ν is Poisson's ratio. If one considers the average RSF parameters, then the average nucleation size over the fault surface is equal to $h_{\text{avg}}^* = 1.68$ km, which

Table 4.1 – (a) In-situ properties of the simulated isolated fault. (b) Slip-weakening frictional characteristics (see also Section 1.1.1). (c) Rate-and-state frictional characteristics (see also Section 1.1.3). The variables with superscript “avg” correspond to spatially distributed quantities whose average values over the fault area are provided. The variables with superscript “est” correspond to the estimated earthquake response considering Eqs. (1.33)-(1.37). $\Delta\tau^{\text{est}}$ in Table 1.1c is calculated by Eq. (1.63).

(a)						
$L_x = L_y = L_z$	G	$(\sigma'_n)_{\text{avg}}$	ρ	ν	ζ	v_∞
[km]	[GPa]	[MPa]	[kg/m ³]	[-]	[-]	[cm/year]
5	30	37.5	2500	0.25	0.8	1

(b)						
$\Delta\mu^{\text{avg}}$	$\mu_{\text{res}}^{\text{avg}}$	$(d_c^{\text{sw}})_{\text{avg}}$	$\delta_{\text{max}}^{\text{est}}$	$t_{\text{inst}}^{\text{est}}$	$v_{\text{max}}^{\text{est}}$	M_w^{est}
[-]	[-]	[mm]	[m]	[s]	[m/s]	[-]
0.1	0.5	100	0.63	9.1	0.13	5.7

(c)									
μ_0	v_0	a^{avg}	b^{avg}	$(d_c^{\text{rsf}})_{\text{avg}}$	$\Delta\tau^{\text{est}}$	$\delta_{\text{max}}^{\text{est}}$	$t_{\text{inst}}^{\text{est}}$	$v_{\text{max}}^{\text{est}}$	M_w^{est}
[-]	[m/s]	[-]	[-]	[mm]	[MPa]	[m]	[s]	[m/s]	[-]
0.55	$4 \cdot 10^{-6}$	0.01	0.015	10	3.73	0.63	9.1	0.13	5.7

is smaller than the equivalent length of the fault ($L_x = L_y = L_z = 5$ km). As a result the system is unstable and a dynamic event is expected. Remark that when $h < h^*$, the system/element is stable, while when $h > h^*$, it is unstable (see Rice, 1993, and also Section 1.2).

In Figure 4.3a, we present the average response of the strike-slip fault for a single (isolated) typical dynamic event. The maximum reported velocity (averaged over the fault surface) is 0.10 m/s corresponding to a maximum slip of 0.6 m. This dynamic event is associated with a stress drop of approximately 3.6 MPa (Figure 4.3b) resulting in an earthquake of magnitude $M_w \approx 5.7$. The slip-rate distribution in the fault region when the maximum average slip-rate occurs (point A in Figure 4.3a) is illustrated in Figure 4.3c. The distribution is not symmetric due to the presence of frictional heterogeneities (see Figure 4.2a). In addition, the average evolution of the RSF state variable is plotted

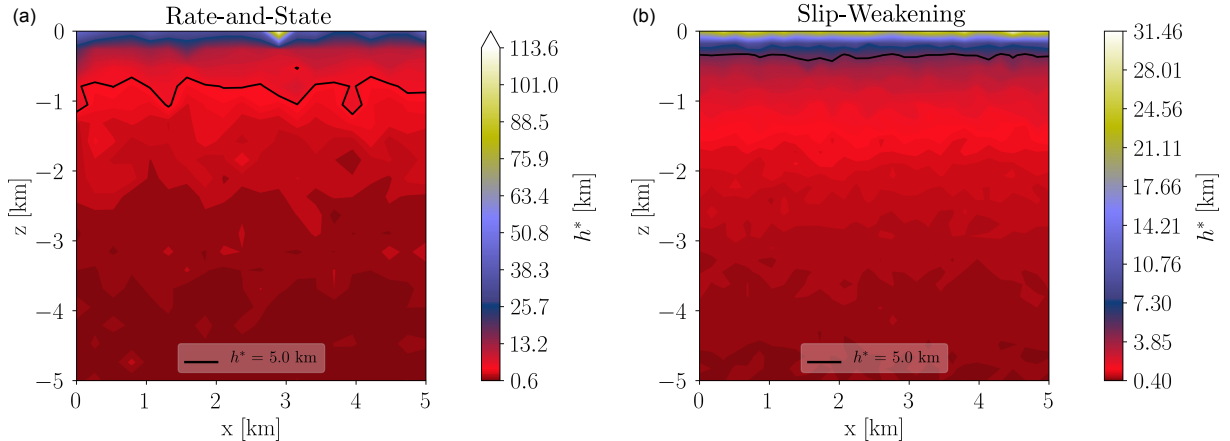


Figure 4.2 – Contour plots illustrating the distribution of nucleation size (activation length) over the fault area due to statistical heterogeneities for the (a) rate-and-state ($n_f = 400$ elements), and (b) slip-weakening ($n_f = 900$ elements) friction law. The black contour line depicts the region in the fault where the nucleation size is equal to $h^* = 5$ km.

in Figure 4.3d. We can observe that the average dynamic response of the strike-slip fault configuration is close to the one estimated in Table 4.1c.

4.1.2 Slip-weakening friction

The exponential slip-weakening friction law is considered as introduced in Sections 1.1.1 and 1.2.1. The parameters $\Delta\mu$, μ_{res} and d_c^{sw} are spatially distributed using a log-normal distribution with average $\Delta\mu^{\text{avg}} = 0.10$, $\mu_{\text{res}}^{\text{avg}} = 0.50$ and $(d_c^{\text{sw}})^{\text{avg}} = 100$ mm and standard deviation corresponding to 5% of these average values (see Table 4.1b). These frictional parameters are kept constant over each element of the discretization during the simulations. This stochastic distribution of the frictional parameters over the fault area represents heterogeneities that exist in real faults and show that the proposed control approach is insensitive to this kind of uncertainties.

The fault area is discretized into $N_x \times N_z = 30 \times 30$ elements. This discretization is fine enough as the elements have a characteristic size of 0.16 km, which is sufficiently lower than the minimum nucleation size, $h_{\text{min}}^* = 0.40$ km ($\frac{h}{h^*} \approx 0.4$) in order to assure that each element cannot act independently of one another. In this example, we use more elements than the one in Section 4.1.1 to maintain the ratio $\frac{h}{h^*}$ constant at 0.4 for the two simulations. The nucleation size over the fault area is illustrated in Figure 4.2b. It is

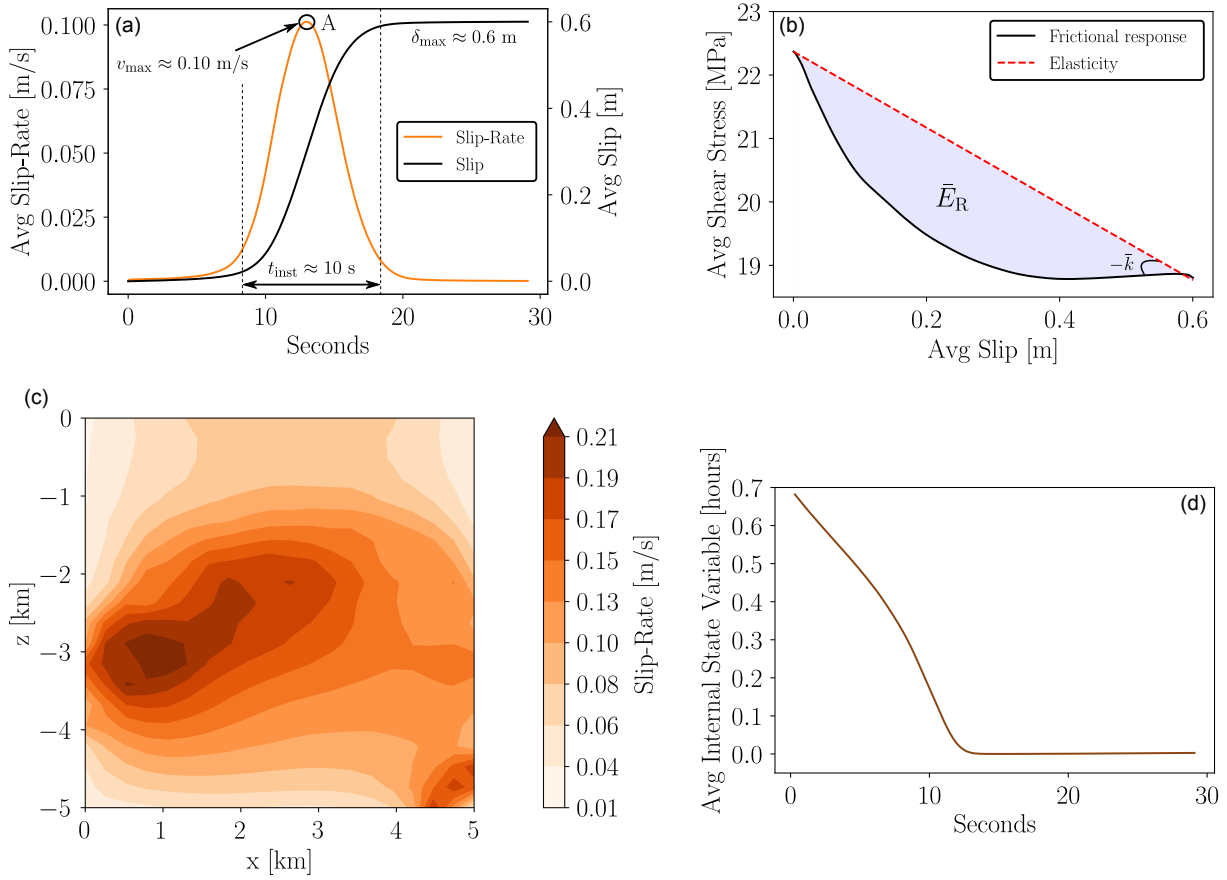


Figure 4.3 – Open-loop response of the strike-slip fault for a single dynamic event with rate-and-state friction ($n_f = 400$ elements). (a) Average slip (black) and slip-rate (orange) in terms of time. (b) Corresponding average shear stress evolution in terms of slip. (c) Slip-rate distribution along the strike-slip fault. The snapshot is taken at the maximum developed average velocity during the earthquake event (point A in subfigure (a)). (d) Average RSF state variable in function of time.

calculated (element-wise) as (based on Rice, 1993):

$$h^* = \frac{2 Gd_c}{\pi \Delta\mu\sigma'_n} \frac{1 + r_d^2/(1 - \nu)}{(1 + r_d^2)^{1/2}}. \quad (4.21)$$

If one considers the average SW parameters, then the average nucleation size over the fault surface is equal to $h_{\text{avg}}^* = 0.84$ km, which is smaller than the equivalent length of the fault ($L_x = L_y = L_z = 5$ km). As a result the system is unstable and a dynamic event is expected.

In Figure 4.4a, we present the average response of the strike-slip fault for a single

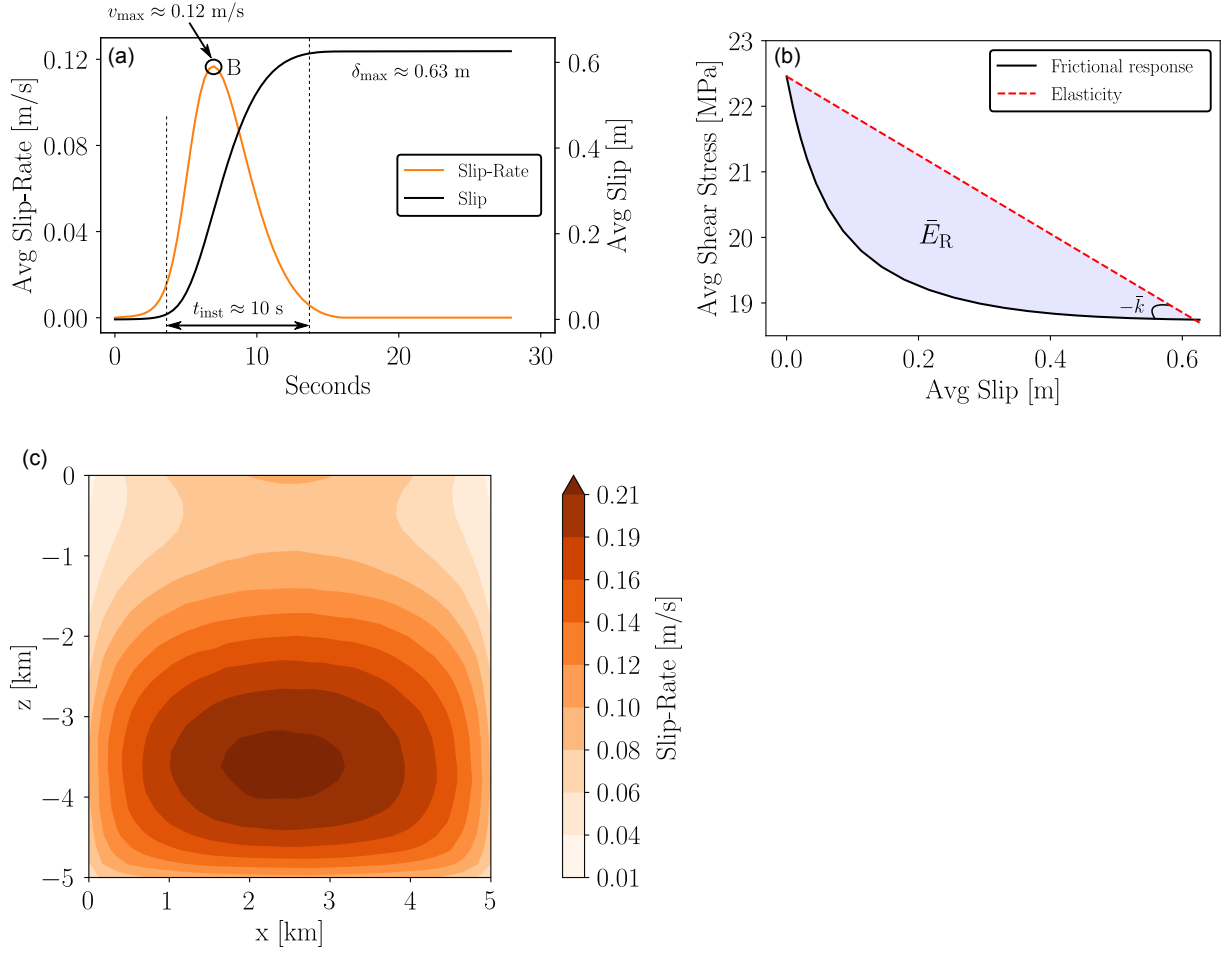


Figure 4.4 – Open-loop response of the strike-slip fault for a single dynamic event with slip-weakening friction ($n_f = 900$ elements). (a) Average slip (black) and slip-rate (orange) in terms of time. (b) Corresponding average shear stress evolution in terms of slip. (c) Slip-rate distribution along the strike-slip fault. The snapshot is taken at the maximum developed average velocity during the earthquake event (point B in subfigure (a)).

(isolated) typical dynamic event. The maximum reported velocity (averaged over the fault surface) is 0.12 m/s corresponding to a maximum slip of 0.63 m. This dynamic event is associated with a stress drop of approximately 3.7 MPa (Figure 4.4b) resulting in an earthquake of magnitude $M_w \approx 5.7$. The slip-rate distribution in the fault region when the maximum average slip-rate occurs (point B in Figure 4.4a) is illustrated in Figure 4.4c. We can observe that the average dynamic response of the strike-slip fault configuration is close to the one estimated in Table 4.1b as well as with the one presented in Section 4.1.1.

4.2 Robust control of seismic faults adjusting directly the fluid pressure on the fault by monitoring the whole state-space

Consider the isolated fault studied in the previous Section (see also Table 4.1). Independently of the choice of the friction law (rate-and-state or slip-weakening), when the fault is sufficiently loaded, an earthquake of magnitude $M_w = 5.7$ is provoked. In order to prevent this dynamic instability and alter the dynamics of the open-loop system (fault), we design a robust full-state feedback controller as presented in Chapter 3. As input variables, we consider the variation of the pore pressure in the fault interface. As seen in Eq. (4.19) and using *Terzaghi's principle of effective stress*, we can use pore-pressure adjustments as a backdoor to influence the dynamics of the fault and convert its behavior from seismic to aseismic.

For this academic example, we assume that we can adjust the pressure of each individual element directly on the fault level by monitoring the whole state-space, a.k.a slip and slip-rate of each distinct fault element (see Figure 4.5a). This trivial example helps us build understanding on how effective this control strategy could be. In addition, we can compare more efficiently the control strategies applied under rate-and-state and slip-weakening friction law. However, in reality, it is impossible to separately control each element on the fault surface and monitor all the degrees of freedom of a fault. For these reasons, a more elaborate example which considers distant injection wells and sparse measurements is presented in Section 4.3.

In this Chapter, we apply only *tracking* control strategies using n_f single integrators to track the slip trajectory of each element (see black curve in Figure 4.5b). In other words, we build the controller in such a way that the fault system is driven aseismically from its unstable equilibrium point to a stable one of lower energy (see Section 3.2.2) following the black curve in Figure 4.5b. For that, we use as a reference slip trajectory for each fault element the following piece-wise function:

$$\begin{cases} r(t) = d_{\max} s^3 (10 - 15s + 6s^2), & s \leq 0.5, & (4.22a) \\ r(t) = \frac{15}{8} d_{\max} s - \frac{7}{16} d_{\max}, & s > 0.5, & (4.22b) \end{cases}$$

where $s = \frac{t}{t_{\text{op}}}$, t_{op} is the operation time of the controller, and d_{\max} is the desired maximum

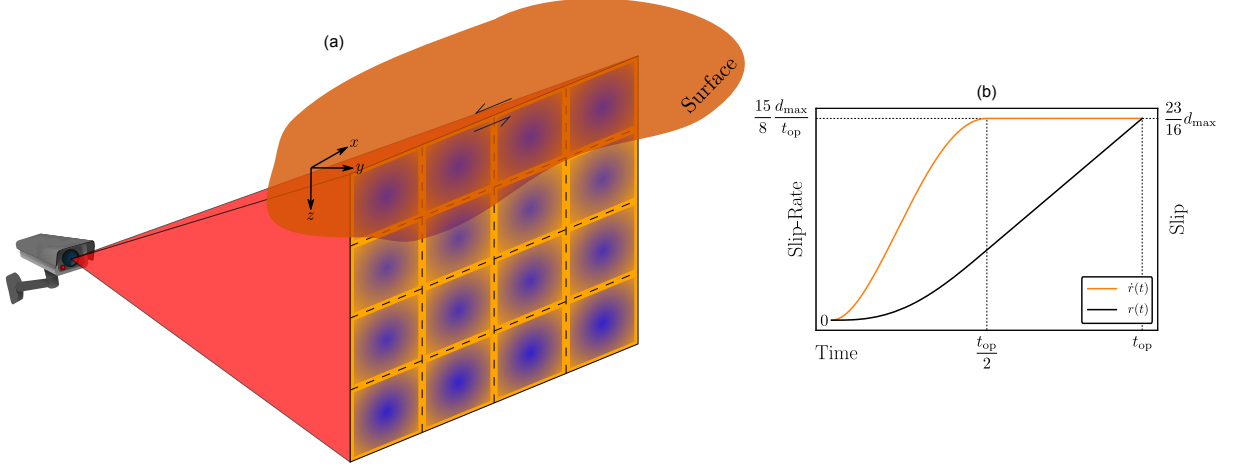


Figure 4.5 – (a) Sketch of a strike-slip fault configuration discretized in $N_x \times N_z$ elements. When the control strategy starts, the pore-pressure can be adjusted at each individual fault element (blue shaded patches) by monitoring the whole fault region (camera + red shaded projection). (b) Reference slip (black curve) and slip-rate (orange curve) trajectories for the tracking control strategy (see Section 3.2.2).

slip of each fault element. According to this reference slip trajectory, the expected maximum imposed slip rate of each element is $\frac{15}{8} \frac{d_{\max}}{t_{\text{op}}}$ obtained half-way through the controller operation. This slip-rate is designed to be maintained constant afterwards until the end of the operation (see orange curve in Figure 4.5b).

The exact values of the mechanical and frictional properties of a fault region are rarely known. Therefore, the control design has to account for parameter uncertainties and unexpected frictional variations. Knowing the range of each parameter, we can design a robust controller using the procedure described in Section 3.2. Table 4.2 contains the ranges of all parameters of interest for the example presented in this Section. Note that the range of uncertainty connected with each parameter could be as large as required. In Section 3.2, we mathematically proved that there would always exist a robust controller if the uncertainties and the nonlinearities are a Lipschitz function (see Eq. (3.6) and Eq. (4.32)). However, there is an important trade-off to consider here. Large deviations from the actual values could lead to fast response of the actuator(s). This fast response, though, might not be technologically feasible. Therefore, constraints on the input signal should be considered (Lewis et al., 2012) and/or the operation time of the control strategy should be elongated. However, this investigation is out of the scope of the current Thesis and further research is needed to assure applicability of the current approach to a real in-situ case.

Table 4.2 – Nominal, minimum and maximum values considered for the mechanical and frictional properties of the fault during the design of the robust continuous-time controller.

Variable	Symbol	Unit	Min. Value	Max. Value	Nominal Value
fault activation length	L_y	km	2	10	6
shear modulus	G	GPa	28	40	34
density of rocks	ρ	kg/m ³	2400	3000	2700
damping ratio	ζ	-	0	1.2	0.6
initial effective normal stress	σ'_n	MPa	-	≤ 150	-
minimum friction coefficient	μ_{\min}	-	≥ 0.04	-	-
RSF parameters	a	-	-	≤ 0.120	-
	b	-	-	≤ 0.175	-
	d_c^{rsf}	mm	≥ 0.84	-	-
SW parameters	$ \Delta\mu $	-	-	≤ 0.4	-
	d_c^{sw}	mm	≥ 5	-	-

For the design of the robust controller introduced in the previous paragraphs, let's start from the dimensionless form of motion equation given by Eq. (4.19):

$$\underbrace{\begin{Bmatrix} \tilde{q}' \\ \tilde{d}' \end{Bmatrix}}_{x'} = \underbrace{\begin{bmatrix} -\hat{\eta} & -\hat{k} \\ I_{n_f} & O_{n_f \times n_f} \end{bmatrix}}_{A(t,x)} \underbrace{\begin{Bmatrix} \tilde{q} \\ \tilde{d} \end{Bmatrix}}_x + \underbrace{\begin{bmatrix} \hat{N}\mu \\ O_{n_f \times p_f} \end{bmatrix}}_{B(t,x)} \underbrace{\{\hat{p}\}}_u + \underbrace{\begin{Bmatrix} -\hat{N}(\mu - \mu^*)\hat{\sigma}'_n \\ O_{n_f \times 1} \end{Bmatrix}}_{g(t,x)}. \quad (4.23)$$

The states of the system (x) are the slip (\tilde{d}) and slip-rate (\tilde{q}) of each distinct element ($n = 2n_f$), while as input vector (u), we consider at first the pore-pressure changes (\hat{p}) at each element ($p_f = n_f$). Moreover, the system parameters in A , B and g can show spatio-temporal variations. In addition, \hat{k} , $\hat{\eta}$ and \hat{N} are given from Eq. (4.10). For the frictional behavior (μ) of the fault, both rate-and-state and slip-weakening friction laws are adopted.

We can observe that the form of Eq. (4.23) resembles Eq. (3.1) where the control theory presented in Chapter 3 is based on. Furthermore, the linearized to the origin version of Eq. (4.23) results in a controllable system (Franklin et al., 2018; Ogata, 2010). Therefore, a robust controller can be designed for stabilizing the fault system (see Section 3.2.1).

The difference of this example with the Burridge-Knopoff model, presented in Stefanou and Tzortzopoulos (2021), is the long-range interactions along the points of the fault area. The elastodynamic equations of motion (see Eq. (4.1)) are discretized using the approach described in Chinnery (1963) and Rice (1993) (quasi-static limit). This leads to a full matrix K_{con} . Notice that one could also design the controller using a simplified band

matrix emerging from the 1D or the 2D Generalized Burridge-Knopoff approximations (see Stefanou & Tzortzopoulos, 2021). In this case, the non-zero, off-diagonal terms would have to be considered as uncertainties, according to the theoretical developments presented in Chapter 3. However, in these applications, we consider the full matrix K_{con} corresponding to the exact strike-slip configuration for the design of the controller.

To derive the tracking robust controller, we augment Eq. (4.23) with n_f single integrators (see also Section 3.2.2):

$$\underbrace{\begin{Bmatrix} x' \\ \xi' \end{Bmatrix}}_{x'_a} = \underbrace{\begin{bmatrix} A & O_{2n_f \times n_f} \\ C_t & O_{n_f \times n_f} \end{bmatrix}}_{A_a(t, x_a)} \underbrace{\begin{Bmatrix} x \\ \xi \end{Bmatrix}}_{x_a} + \underbrace{\begin{bmatrix} B \\ O_{n_f \times p_f} \end{bmatrix}}_{B_a(t, x_a)} \underbrace{\{\hat{p}\}}_{u_a} + \underbrace{\begin{bmatrix} O_{2n_f \times n_f} \\ -I_{n_f} \end{bmatrix}}_{R_a} \underbrace{\{r(t)\}}_r + \underbrace{\begin{Bmatrix} g \\ O_{n_f \times 1} \end{Bmatrix}}_{g_a(t, x_a)}, \quad (4.24)$$

where $C_t = \begin{bmatrix} O_{n_f \times n_f} & I_{n_f} \end{bmatrix}$ contains the degrees of freedom for tracking the reference slip trajectory provided in Figure 4.5b, namely the slip of each fault element. If instead of tracking the trajectory given in Eq. (4.22), we set a constant reference target, for instance $r_0 = \frac{23}{16}d_{\text{max}}$, then Eq. (4.24) takes the form of Eq. (3.16). Following the procedure described in Sections 3.2.1 and 3.2.2, we can design a robust full state negative feedback controller where the constant reference input signal r_0 is tracked robustly. For time varying reference trajectories, we expect a steady state error, which we practically eliminate here by increasing the relevant integral action gains by tuning appropriately the elements of the design positive-definite matrices Q_0 and R (see Section 3.2).

For the control design (Section 3.2), the uncertainties of the $A_a(t, x_a)$ and $B_a(t, x_a)$ matrices should be taken into consideration. According to Eq. (3.2):

$$A_a(t, x_a) = \underbrace{\begin{bmatrix} -\hat{\eta}_0 & -\hat{k}_0 & O_{n_f \times n_f} \\ I_{n_f} & O_{n_f \times n_f} & O_{n_f \times n_f} \\ O_{n_f \times n_f} & I_{n_f} & O_{n_f \times n_f} \end{bmatrix}}_{A_0} + \underbrace{\begin{bmatrix} -\Delta\hat{\eta} & -\Delta\hat{k} & O_{n_f \times n_f} \\ O_{n_f \times n_f} & O_{n_f \times n_f} & O_{n_f \times n_f} \\ O_{n_f \times n_f} & O_{n_f \times n_f} & O_{n_f \times n_f} \end{bmatrix}}_{\Delta A(t, x_a)}, \quad (4.25)$$

$$B_a(t, x_a) = \underbrace{\begin{bmatrix} (\hat{N}\mu)_{\min} I_{n_f \times p_f} \\ O_{n_f \times p_f} \\ O_{n_f \times p_f} \end{bmatrix}}_{B_0} + \underbrace{\begin{bmatrix} \hat{N}\Delta\mu \\ O_{n_f \times p_f} \\ O_{n_f \times p_f} \end{bmatrix}}_{\Delta B(t, x_a)}, \quad (4.26)$$

where $\hat{\eta}_0, \hat{k}_0 \in \mathbb{R}^{n_f \times n_f}$ are the nominal matrices of system's viscosity and elasticity, respectively (see column ‘‘Nominal Value’’ in Table 4.2). The nominal matrix $B_0 \in \mathbb{R}^{3n_f \times p_f}$

should be designed with the scalar product of the minimum expected coefficient of friction times the minimum \hat{N} parameter (including a safety factor if necessary). $I_{n_f \times p_f}$ is a matrix of size $n_f \times p_f$ with unity elements. The quantities with the prefix 'Δ' correspond to the uncertainties of the respective variables. Note that $\Delta\hat{\eta}, \Delta\hat{k} \in \mathbb{R}^{n_f \times n_f}$ and $\Delta\mu \in \mathbb{R}^{n_f}$. The pseudoinverse matrix of B_0 is:

$$B_0^+ = \begin{bmatrix} \frac{1}{(\hat{N}\mu)_{\min}} I_{p_f \times n_f} & O_{p_f \times n_f} & O_{p_f \times n_f} \end{bmatrix}. \quad (4.27)$$

Notice that, by definition, $B_0^+ B_0 = I_{p_f}$. The nonlinear vector $h_a(t, x_a) \in \mathbb{R}^{p_f}$, defined in Eq. (3.4), becomes:

$$h_a(t, x_a) = B_0^+ (\Delta A(t, x_a)x_a + g_a(t, x_a)). \quad (4.28)$$

We want $h_a(t, x_a)$ to be a Lipschitz continuous function. Indeed:

$$\begin{aligned} \|h_a(t, x_a)\| &= \left\| B_0^+ (\Delta A(t, x_a)x_a + g_a(t, x_a)) \right\| \\ &\leq \left\| B_0^+ \right\| (\|\Delta A(t, x_a)\| \|x_a\| + \|g_a(t, x_a)\|) \\ &\leq \left\| B_0^+ \right\| \left(\|\Delta A\|_{\max} \|x_a\| + \|\hat{N}\hat{\sigma}'_n\| \|\mu - \mu^*\| \right), \end{aligned} \quad (4.29)$$

where $\|\Delta A\|_{\max}$ corresponds to the maximum allowed deviation from the selected nominal values (see columns “Min Value” and “Max Value” in Table 4.2) concerning the elasticity and viscosity (see Eq. (4.10)). Notice that a safety factor can be added in all the bounds related to uncertainties in order to increase the robustness of the system with the trade-off of reducing its performance. The Lipschitz bound, β_f , of $\|\mu - \mu^*\|$ with respect to the states exists as shown in Section 1.1 for the most widely used friction laws in fault mechanics. Specifically, for the rate-and-state friction law, $\beta_f = \beta_{\text{rsf}}$ is given by:

$$\|\mu - \mu^*\| \leq \underbrace{\sqrt{a_{\max}^2 + \left(\frac{Db}{d_c^{\text{rsf}}}\right)_{\max}^2}}_{\beta_{\text{rsf}}} \|x_a\|, \quad (4.30)$$

where a_{\max} and $\left(\frac{Db}{d_c^{\text{rsf}}}\right)_{\max}$ are the maximum values of the respective RSF parameters and D is the length scaling factor (see Section 4.1). For the slip-weakening friction law, $\beta_f = \beta_{\text{sw}}$

is given by:

$$\|\mu - \mu^*\| \leq \underbrace{\left| \frac{\Delta\mu}{d_c^{sw}} \right|_{\max}}_{\beta_{sw}} \|x_a\|, \quad (4.31)$$

where $\left| \frac{\Delta\mu}{d_c^{sw}} \right|_{\max}$ is the maximum expected slip-weakening rate. These bounds of friction (either RSF or SW) are presented in Table 4.2 for the example studied in this Section.

Therefore, Eq. (4.29), becomes:

$$\|h_a(t, x_a)\| \leq \underbrace{\left\| B_0^+ \right\| \left(\|\Delta A\|_{\max} + \beta_f \|\hat{N}\hat{\sigma}'_n\|_{\max} \right)}_{\beta_{c1}} \|x_a\| = \beta_{c1} \|x_a\|, \quad (4.32)$$

where $\beta_{c1} = \left\| B_0^+ \right\| \left(\|\Delta A\|_{\max} + \beta_f \|\hat{N}\hat{\sigma}'_n\|_{\max} \right)$ is the Lipschitz bound of $h_a(t, x_a)$. $\|\hat{N}\hat{\sigma}'_n\|_{\max}$ can be calculated using again the values provided in Table 4.2 (see also Eq. (4.10)). Consequently, the robust controller can be calculated by solving numerically the Continuous-time Algebraic Riccati Equation (CARE) given by Eq. (3.10). There exists always a positive-definite solution Θ for this CARE as discussed in Section 3.2. Therefore, the input signal takes the following form:

$$u_a = -K_a x_a = -R^{-1} B_0^T \Theta x_a, \quad (4.33)$$

where $R \in \mathbb{R}^{p_f \times p_f}$ is chosen to be a positive-definite matrix.

The controller given by Eq. (4.33) can be used for the whole range of parameters summarized in Table 4.2. To sum up, only the following ranges of the mechanical and frictional properties of the fault region (including a safety factor) have to be known for the robust control design presented in this Section:

1. **minimum and maximum** estimation of the **density** of the surrounding rocks,
2. **minimum and maximum** estimation of the **length** of the fault,
3. **minimum and maximum** estimation of the **shear modulus** of the rock,
4. **minimum and maximum** estimation of the **damping ratio**,
5. **maximum** estimation of the **effective normal stress** on the fault interface (before the activation of the controller),
6. **minimum** estimation of the **friction coefficient** and the **characteristic frictional distance** (regardless of the adopted friction law),

7. **maximum** estimation of the **a and b RSF parameters**, and
8. **maximum** estimation of the **SW stress drop**.

Notice that all the above-mentioned bounds must be strictly positive. As we have already discussed, these minimum and maximum estimations can be arbitrarily stretched to either end in order to increase the region of robustness of the designed controller. However, if we are reckless, we risk to demand fast response from the actuators. Fast pressure rates might be technologically inapplicable with the current knowledge. The activation of the controller, in such a situation, might have unexpected consequences or even provoke an earthquake comparable to the natural one (see Section 4.1 and Chapter 2). Therefore, further study has to be done for extending the control design presented in Chapter 3 accounting also for input and performance constraints as well as measurement noise.

In the following two subsections, we apply the controller designed here to the fault configuration described in Section 4.1 adopting either rate-and-state or slip-weakening friction law, respectively.

4.2.1 Rate-and-state friction law

In order to release the stored elastic energy and drive the fault to a new equilibrium point of lower energy, we apply the controller designed above (see also Figure 4.5). As shown in Section 1.1.3, rate-and-state friction is a Lipschitz function and, therefore, it can be bounded by the states of the system (see Eq. (1.15) and Eq. (4.30)).

For the simulations, we use the characteristics of the fault presented in Section 4.1.1 (see also Table 4.1 and Figure 4.3). The discretization and the spatial distribution of the frictional properties (see Figure 4.2a) of the fault region remain unchanged. For the design of the controller, we follow the procedure described above using the minimum, maximum, and nominal values of the mechanical and RSF properties of the system summarized in Table 4.2.

For tracking, we set as reference/target trajectory, a low velocity, which, on average over the fault area, evolves smoothly (see Figure 4.5b) from the far-field tectonic velocity (cm/yr) to approximately 1.9 mm/s (see Figure 4.6a). In this way, a new equilibrium point of lower energy is given as a target. Alternatively, the strategy presented in Stefanou and Tzortzopoulos (2021) could be used for setting the average target slip velocity. The duration of the control operation is set equal to $t_{op} = 10$ min.

In Figure 4.6a-b, we show the average response of the fault after the application of

4.2. Robust control of seismic faults adjusting directly the fluid pressure on the fault by monitoring the whole state-space

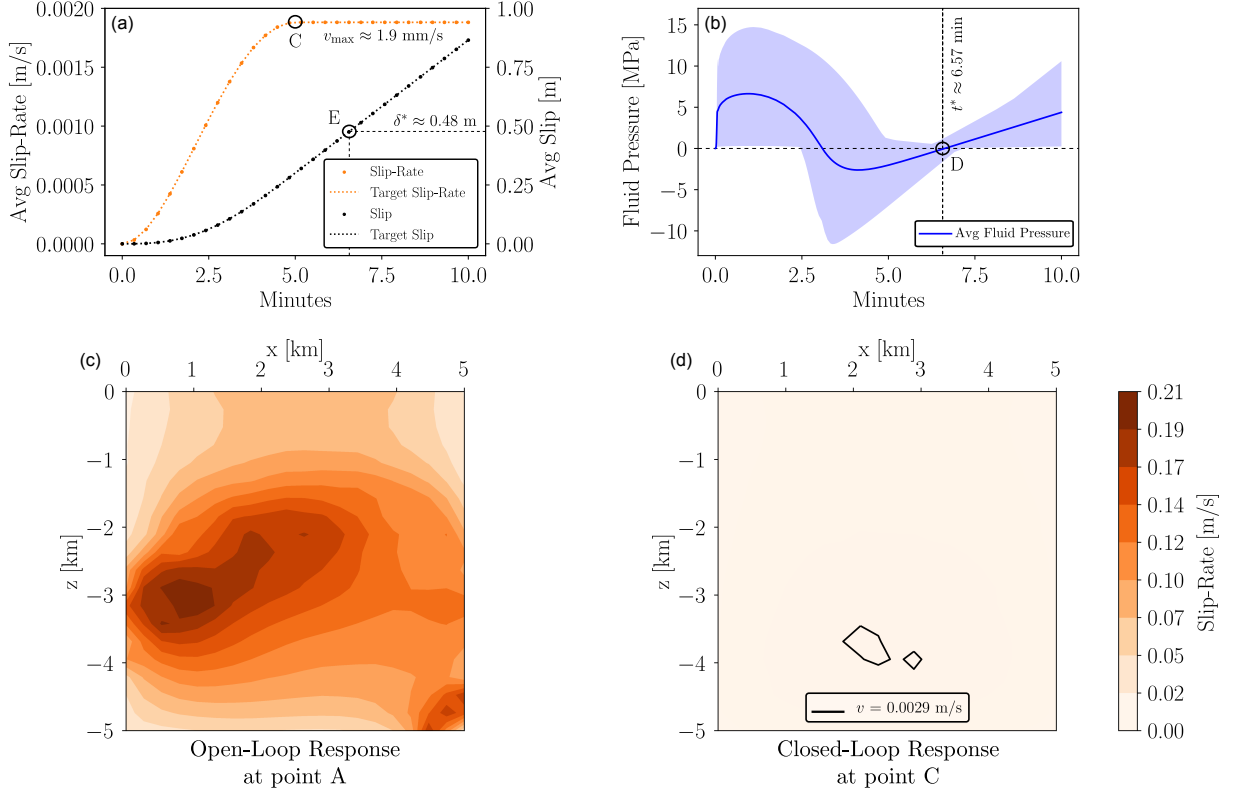


Figure 4.6 – Closed-loop response of the strike-slip fault after the application of the controller adopting rate-and-state friction law ($n_f = 400$ elements). (a) Average slip (black dotted curve) and slip-rate (orange dotted curve) in terms of time. The controller successfully achieves the target/reference slip (black dashed line) and slip-rate (orange dashed line). (b) Evolution of the average applied fluid pressure change (output of the controller). The blue shaded area corresponds to the envelope of pressures developed over the surface of the fault.

Comparison of slip-rate distribution along the strike-slip fault between the open-loop, uncontrolled (c) and the closed-loop, controlled (d) system. The open-loop snapshot (c) is taken at the maximum developed average velocity during the earthquake event (point A in Figure 4.3a), while the closed-loop one (d) at the maximum developed average velocity during the applied control strategy (point C in subfigure (a)).

our controller. The evolution of slip and slip-rate, in Figure 4.6a, follows, as expected, the design/target slip-rate. From this plot, we can conclude that the fault can be driven into its designed new equilibrium point aseismically. In the example presented here, the maximum average slip velocity developed was approximately 2 orders of magnitude smaller than the earthquake event presented in Figure 4.3a.

In Figure 4.6b, we present the evolution of the average over the fault area fluid pressure

change in function of the operational time (output of the controller vs time). The controller regulates automatically the fluid pressure in order to achieve the reference/target slow slip. We chose to activate the controller on the verge of the unstable seismic event, in order to model the worst case scenario. If the controller was activated before, then the regulated fluid pressure change would follow a smoother evolution.

We observe that at the beginning of the operation, i.e. from $t = 0$ to $t \approx 1.5$ min, the controller increases the fluid pressure (positive fluid pressure change) in order to accelerate sliding from the far-field velocity to the target slip-rate. Then, from $t \approx 1.5 - 4$ min, the regulator automatically decreases the pressure (negative fluid pressure change), in order to stabilize the system and avoid run-off. Next, from $t \approx 4 - 6.5$ min, the controller gradually restores the pressure. At $t^* \approx 6.5$ min, the new equilibrium point of lower energy is reached (point D in Figure 4.6b) because the fluid pressure is fully restored to zero. Finally, positive fluid pressure changes are observed from $t \approx 6.5$ to $t = 10$ min for guaranteeing the continuation of creep-like, aseismic slip with the target slip-rate. In this last part of the operation all the elements of the fault have entered in a (dynamically) stable state of lower energy and the controller could be deactivated. This behavior is qualitatively similar with the one obtained in Stefanou and Tzortzopoulos (2021) for the Generalized Burridge-Knopoff model.

In this example, the fluid pressure changes vary between -10 (fluid withdrawal) and $+15$ MPa (fluid injection), approximately. Notice that if one thought to stabilize the system by simply satisfying the stability condition (see Eq. (4.20)) emerging from the expression of the nucleation length (assuming that the frictional parameters are somehow known), this would be impossible because any stress drop due to fluid pressure increase, would cause an earthquake event of higher magnitude due to the decrease of the residual shear stress.

A comparison between the open-loop, uncontrolled system and the closed-loop, controlled one is given in Figure 4.6c-d, in terms of slip-rates. Both figures display the spatial distribution of the slip-rates at times corresponding to the maximum average slip-rate of each simulation (i.e. at points A and C, see Figure 4.3a and 4.6a, respectively). The maximum developed slip-rate of the controlled system is ~ 0.0029 m/s (see black contour line, Figure 4.6d), which is negligible compared to the maximum slip-rate developed during the simulated earthquake instability (~ 0.2 m/s, see Figure 4.6c).

It should be mentioned here, that the rate-dependent nature of the friction law influences the outcome of the controller (fluid pressure) as well as deviates the position of

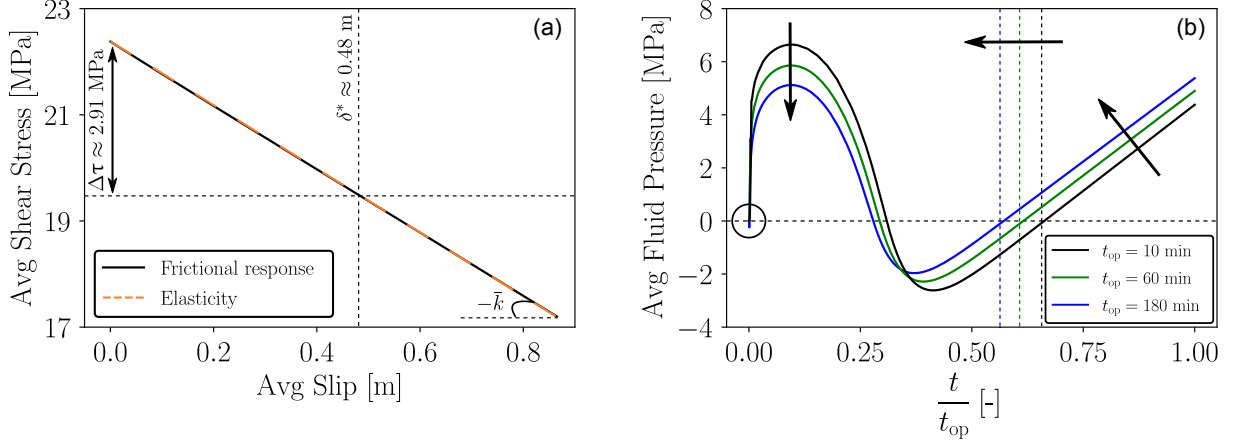


Figure 4.7 – (a) Frictional (black curve) and elastic (orange curve) response in terms of the average slip of the fault. (b) Comparison of the average fluid pressure in terms of normalized time for three different operation times ($t_{op} = 10, 60, 180$ min).

the new equilibrium point. We can observe this by focusing on points D and E in Figures 4.6b and a, respectively. We expect the average slip of the fault at these points to be equal to the resulted average slip of the earthquake event presented in Figure 4.3a, i.e. $\delta(t^*) = \delta^* = 0.6$ m. However, at point E, the average slip is below 0.5 m. Setting the maximum average slip-rate equal to $v_{\max} = 1.9$ mm/s (see Figure 4.6a), the expected shear stress drop reduces from 3.73 MPa (see Table 4.1c) to 2.91 MPa (see Eq. (1.62)). Consequently, this reduced shear stress drop leads to a reduced maximum average slip, i.e. $\delta^* = 0.48$ m (point E in Figure 4.6a). The exact time at which the fault has slipped that much is at $t^* = \left(\frac{2.91}{3.73} + \frac{7}{16}\right) \frac{8}{15} t_{op} = 6.57$ min (see Eq. (4.22)).

During the control strategy, the average shear stress drops linearly along with the elastic stiffness of the fault region ($\bar{k} = \frac{G}{L_y}$, on average, see orange dashed line in Figure 4.7a) with respect to the average slip of the fault as it is illustrated in Figure 4.7a.

Notice that the system was controlled in a relatively fast operation time ($t_{op} = 10$ min). In case an even slower transition is needed, the reference trajectory and/or the operation time can be adjusted as desired. However, as the friction law is rate dependent, the response of the closed-loop system varies as described in the previous paragraphs (see also Figure 4.6a-b). This behavior is depicted in Figure 4.7b, where three different operation times ($t_{op} = 10, 60, 180$ min) are compared. We can observe that as the operation time of the control strategy increases, less fluid extraction is needed (negative fluid pressure change) in order to stabilize the fault (see circle). In addition, the initial peak of the fluid pressure change (see vertical arrow) decreases. Furthermore, the new equilibrium point is

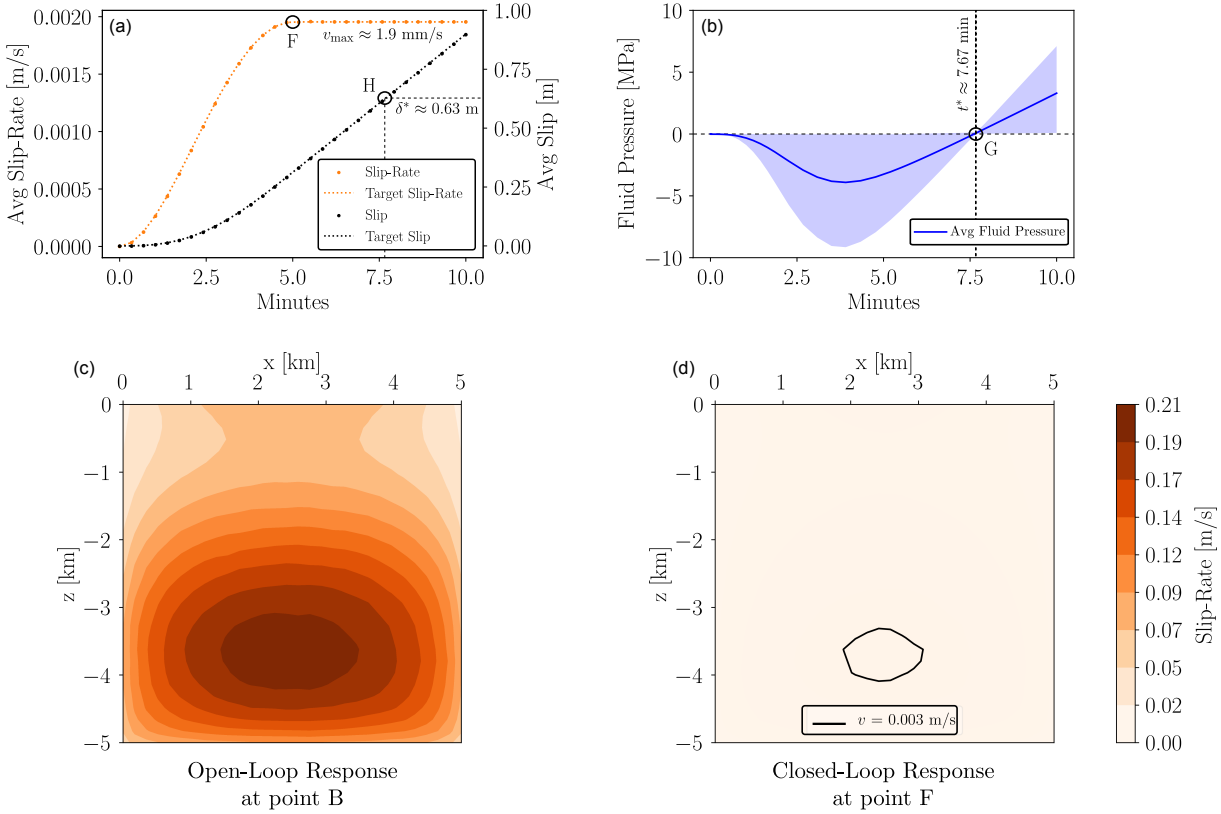


Figure 4.8 – Closed-loop response of the strike-slip fault after the application of the controller adopting slip-weakening friction law ($n_f = 900$ elements). (a) Average slip (black dotted curve) and slip-rate (orange dotted curve) in terms of time. The controller successfully achieves the target/reference slip (black dashed line) and slip-rate (orange dashed line). (b) Evolution of the average applied fluid pressure change (output of the controller). The blue shaded area corresponds to the envelope of pressures developed over the surface of the fault.

Comparison of slip-rate distribution along the strike-slip fault between the open-loop, uncontrolled (c) and the closed-loop, controlled (d) system. The open-loop snapshot (c) is taken at the maximum developed average velocity during the earthquake event (point B in Figure 4.4a), while the closed-loop one (d) at the maximum developed average velocity during the applied control strategy (point F in subfigure (a)).

reached in less slip (see horizontal arrow). Finally, when the constant target slip-rate is reached ($t/t_{\text{op}} = 0.5$), the fluid pressure change increases with approximately the same rate (with respect to the normalized time).

4.2.2 Slip-weakening friction law

For the simulations with the slip-weakening friction law, we use the characteristics of the fault presented in Section 4.1.2 (see also Table 4.1 and Figure 4.4). The discretization and the spatial distribution of the frictional properties (see Figure 4.2b) of the fault region remain unchanged. For the design of the controller, we follow the procedure described above using the minimum, maximum, and nominal values of the mechanical and SW properties of the system summarized in Table 4.2. For tracking, we set the same reference/target trajectory as described in Section 4.2.1. The duration of the control operation is set equal to $t_{\text{op}} = 10$ min.

In Figure 4.8a-b, we show the average response of the fault after the application of our controller. The evolution of slip and slip-rate, in Figure 4.8a, follows, as expected, the design/target slip-rate. From this plot, we can conclude that the fault can be driven into its designed new equilibrium point aseismically. In the example presented here, the maximum average slip velocity developed was approximately 2 orders of magnitude smaller than the earthquake event presented in Figure 4.4a. Notice that the system was controlled in a relatively fast operation time (10 min). In case an even slower transition is needed, the reference trajectory and/or the operation time can be adjusted as desired. Contrary to what we observed in Section 4.2.1, varying the operational time doesn't influence the pore pressure evolution depicted in Figure 4.8b. This is not unexpected as friction is rate independent, in this case.

In Figure 4.8b, we present the evolution of the average over the fault area fluid pressure change in function of the operational time (output of the controller vs time). The controller automatically regulates the fluid pressure in order to achieve the reference/target slow slip/slip-rate. We chose to activate the controller on the verge of the unstable seismic event, in order to model the worst case scenario. If the controller was activated before, then the regulated fluid pressure change would follow a smoother evolution.

We observe that at the beginning of the operation, i.e. from $t = 0$ to $t \approx 4$ min, the regulator automatically decreases the pressure (negative fluid pressure change), in order to stabilize the system and avoid run-off. Next, from $t \approx 4 - 7.5$ min, the controller gradually restores the pressure. At $t^* \approx 7.5$ min, the new equilibrium point of lower energy is reached (point G in Figure 4.8b) because the fluid pressure is fully restored to zero. Finally, positive fluid pressure changes are observed from $t \approx 7.5$ to $t = 10$ min for guaranteeing the continuation of creep-like, aseismic slip with the target slip-rate. In this last part of the operation all the elements of the fault have entered in a (dynamically)

stable state of lower energy and the controller could be deactivated.

It should be mentioned here that the average slip of the fault is approximately equal to the resulted average slip of the earthquake event presented in Figure 4.4a, namely $\delta(t^*) = \delta^* = 0.63$ m (see point H in Figure 4.8a). The fault reaches its new equilibrium at $t^* = \frac{23}{30}t_{\text{op}} = 7.67$ min (see Eq. (4.22) and point G in Figure 4.8b).

A comparison between the open-loop, uncontrolled system and the closed-loop, controlled one is given in Figure 4.8c-d, in terms of slip-rates. Both figures display the spatial distribution of the slip-rates at times corresponding to the maximum average slip-rate of each simulation (i.e. at points B and F, see Figure 4.4a and 4.8a, respectively). The maximum developed slip-rate of the controlled system is ~ 0.003 m/s (see black contour line, Figure 4.8d), which is negligible compared to the maximum slip-rate developed during the simulated earthquake instability (~ 0.2 m/s, see Figure 4.8c).

Comparing the closed-loop response between the rate-and-state and slip-weakening cases (Figures 4.6 and 4.8), we observe a smoother pore pressure evolution in the slip-weakening case. In addition, due to the absence of rate-dependencies, with slip-weakening, the system reaches the predefined equilibrium point calculated based on the rupture event (see Table 4.1). On the other hand, with rate-and-state friction, we showed that as the operation time increases, the system is able to reach a stable regime earlier than expected (see Figure 4.7b). This leads to a more time/money-friendly approach as the target of reaching a new stable equilibrium point is achieved faster even if the relaxation of the stored-elastic energy in the fault system is less in this case. Therefore, the slip-weakening friction law seems to represent the worst case scenario as far as it concerns the unstable dynamics of the system and, therefore, it is adopted in the next Section 4.3 for the physical system. Nevertheless, it should be pointed out that a single controller could be designed covering SW or RSF or any other bounded friction evolution by appropriately choosing the frictional bounds for the design.

These academic examples show how seismic instabilities can be prevented and how controlled, slow-slip can be induced by fluid pressure adjustment, using the theory developed in this work. However, in this example the fluid pressure has to be adjusted independently over the elements of the fault area and diffusion phenomena are not considered. On the one hand, these phenomena can introduce a delay to the closed-loop system, but, on the other hand, can allow to cover large fault areas with a limited number of wells for optimal control. In addition, in this Section, we assumed that we could monitor all the degrees of freedom of the strike-slip fault. The influence of the diffusion phenomena and sparse

measurements in space is studied in the following Section.

4.3 Robust control of seismic faults coupled with diffusion processes using distant fluid injections by monitoring only surface deformation

The example presented in the previous Section revealed that there exists indeed the possibility of earthquake control using the theory developed in Chapter 3. However, in contrast to the previous applications, in practice, we cannot adjust the pressure at each fault element separately. In addition, in reality, we are not able to inspect the whole fault region in order to acquire sufficient measurements for tracking control. These two issues are being tackled in this Section. We also account for the delay which might be introduced in the closed-loop system due to the presence of diffusion phenomena while fluid injections take over. Moreover, we assume a more realistic scenario where the only available measurement is the average deformation of the fault at the surface, for instance through GPS measurements. Note that poroelasticity (Rousseau et al., 2020; Segall & Lu, 2015), or other complex phenomena and unmodeled dynamics, are not considered in this work, and future investigation is needed in order to check the robustness of the control strategies proposed in Chapter 3.

Diffusion phenomena are considered by augmenting our system of study with the 1D diffusion equation with N sources (Segall & Rice, 1995). Each source influences a specific segment of the area of the fault interface of characteristic size equal to the distance of the source from the fault (see Figure 4.9). The 1D diffusion equation for this case has the following form:

$$\dot{p} = c_d(p_\infty - p), \quad (4.34)$$

where $p \in \mathbb{R}^N$ is the pore pressure at the fault level, $p_\infty \in \mathbb{R}^N$ the pore pressure at the injection point, $c_d = \frac{c_{hy}}{L_d^2}$ is the diffusivity, and c_{hy} the hydraulic diffusivity. Following the procedure described in Chapter 1 and Section 4.1, we obtain the scaled and shifted to the origin form of Eq. (4.34):

$$\hat{\dot{p}}' = -\hat{c}_d \hat{p} + \hat{c}_d \hat{p}_\infty, \quad (4.35)$$

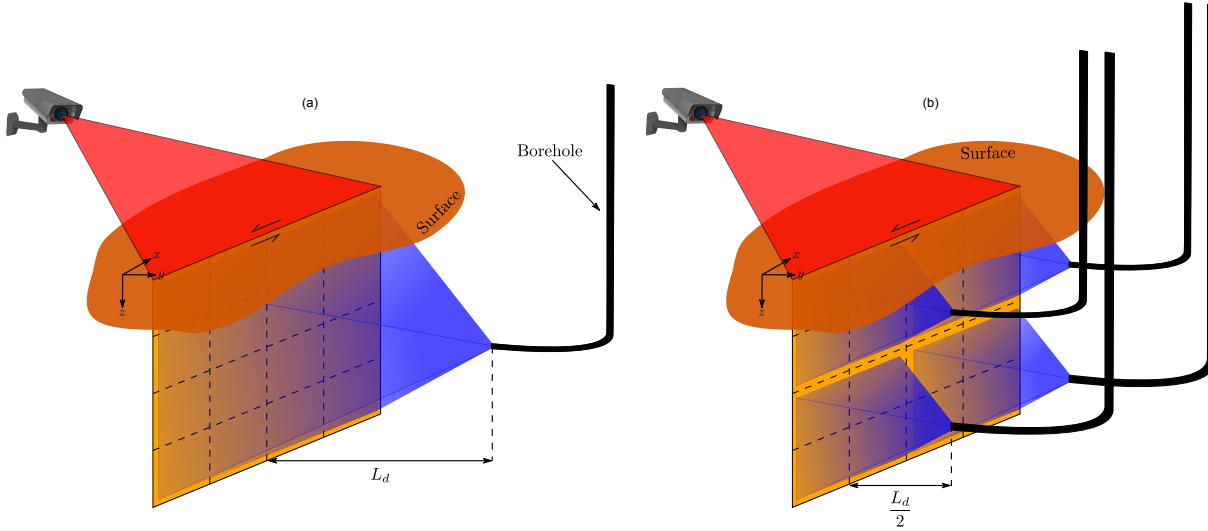


Figure 4.9 – Sketch of a strike-slip fault configuration discretized in $N_x \times N_z$ elements. When the control strategy starts, the pore-pressure at each borehole can be adjusted adequately. Each borehole influences a segment of the fault region which doesn't intersect with any neighbor borehole (blue shaded diffusion scheme). Two scenarios are illustrated: (a) single borehole and (b) four boreholes. The monitoring takes place only on the surface of the fault (camera + red shaded projection).

where:

$$p_\infty = \hat{p}_\infty P, \quad (4.36)$$

$$c_d = \frac{\hat{c}_d}{T}, \quad (4.37)$$

with P and T being the stress and time scaling factors, respectively. If we couple Eq. (4.35) with Eq. (4.24), we get the full system of interest:

$$x'_a = A_a(t, x_a)x_a + B_a(t, x_a)\hat{p} + R_a r + g_a(t, x_a), \quad (4.38a)$$

$$\hat{p}' = -\hat{c}_d \hat{p} + \hat{c}_d \hat{p}_\infty, \quad (4.38b)$$

where $[x_a \ \hat{p}]^T$ forms the state-space of the system and \hat{p}_∞ is considered as the (new) control input of the above system.

As in Sections 4.1 and 4.2, the A_a matrix represents elastic and viscoelastic phenomena, B_a the influence of pressure changes to the dynamics of the system through friction and g_a contains the frictional terms of the system. The term $R_a r$ stands for the tracking procedure. However, the control design is based on a constant reference input $r(t) = r_0$

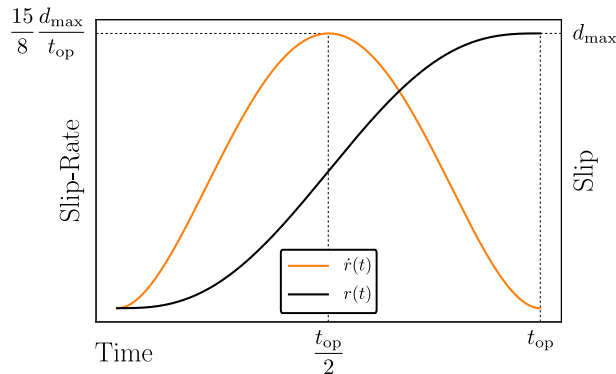


Figure 4.10 – Reference slip (black curve) and slip-rate (orange curve) trajectories for the tracking control strategy (see Section 3.2.2).

and when we shift again the system to its new equilibrium point, this term disappears (see Sections 4.2 and 3.2.2).

Here, the integral action, which is embedded in Eq. (4.38a), doesn't contain (necessarily) n_f single integrators as in Section 4.2. In Lewis et al. (2012), it is mentioned that it's not possible to have more integrators than actuators. Therefore, the number of single integrators in this Section is equal to N , i.e. the number of boreholes available to control the dynamic nature of the fault region.

In this Section, the tracking policy is based on driving each sub-region to a desired state (in average sense) following a smooth sigmoid function. The reference slip and slip-rate signals are illustrated in Figure 4.10 and given respectively by:

$$r(t) = d_{\max} s^3 (10 - 15s + 6s^2), \quad (4.39a)$$

$$\dot{r}(t) = 30 \frac{d_{\max}}{t_{\text{op}}} s^2 (s - 1)^2, \quad (4.39b)$$

where $s = \frac{t}{t_{\text{op}}}$, t_{op} is the operation time of the controller, and d_{\max} is the desired maximum slip of each segment (see Figure 4.9). The expected maximum slip rate of each sub-region is $\frac{15}{8} \frac{d_{\max}}{t_{\text{op}}}$ obtained half-way through the controller operation (see Figure 4.10).

The system in Eq. (4.38) has the same form as the one in Eq. (3.21) for designing a controller which tackles unmatched uncertainties. Furthermore, the linearized to the origin version of Eq. (4.38) results in a controllable system. Therefore, the control design procedure described in Section 3.3 can be applied.

The controller design presented in Section 3.3 assumes that the mechanics (see Eq. (4.38a)) contain only structured (matched) uncertainties. Only in this case, the controller

is robust to compensate parameter uncertainties in elasticity, viscosity (matrix $A_a(t, x_a)$ in Eq. (4.38a)) and frictional weakening (vector $g_a(t, x_a)$ in Eq. (4.38a)). In other words, we don't explore here the effect of unmodeled dynamics of finer scales emerging from the mechanical system. Consequently, we subdivide the fault area to as many segments as the available “control” wells.

For the design, the two Continuous-time Algebraic Riccati Equations (CAREs) given by Eqs. (3.33) and (3.34) have to be solved numerically. Notice that the two CAREs are uncoupled and each one can be solved separately from one another. In parallel, the four inequalities given by Eqs. (3.28)-(3.31) have to be satisfied.

Inequality Eq. (3.28) corresponds to the parameter uncertainties and nonlinearities which are present in Eq. (4.38a) (fault dynamics). The bound of this inequality has already been provided in Section 4.2 and particularly in Eq. (4.32). Next, Eq. (3.30) asks for an upper bound of the friction coefficient. Finally, inequalities Eq. (3.29) and Eq. (3.31) demand the minimum and maximum bounds of diffusivity and friction. The latter two bounds depend also on the solution of the CARE #1 (see Eq. (3.33)).

Consequently, the resulted control input \hat{p}_∞ is given by the following expression (see Eq. (3.40)):

$$\hat{p}_\infty = -K_z (\hat{p} + K_a x_a), \quad (4.40)$$

where K_a is the gain matrix obtained from the solution of the CARE #1 (Eq. (3.33)) and K_z the gain matrix obtained from the solution of the CARE #2 (Eq. (3.34)).

The above robust controller needs to measure the whole state-space in order to provide the pore pressure increments to the respective boreholes. However, in reality, the acquired measurements are sparse in space. Therefore, an observer has to be built (see Section 3.4). If the system of study is observable, given the set of available measurements, the observer can recreate the states of this system allowing the usage of the already designed controller.

The observer design presented in Section 3.4 and in Khalil (2015) takes into consideration parameter uncertainties in both the state and the input matrices. However, as we can observe in Eqs. (3.57) and (3.58), these uncertainties could dramatically increase the region of attraction of the estimation error. Therefore, despite the large range of uncertainties considered for the control design (see Section 4.2 and Table 4.2), the observer, finally, is designed by assuming that we know *a priori* the mechanical and frictional properties of the fault area (no uncertainties considered here).

In the literature, there exist numerous methods, where a robust observer is designed

for nonlinear systems accounting for parameter uncertainties. Such methods could be the Linear Matrix Inequality (Rajamani et al., 2020), Sliding Modes Observer (Shtessel et al., 2015), High Gain Observer (Khalil, 2015, 2017), to mention a few. Another alternative would be to calculate a Reduced Order Model (ROM) of the plant (e.g. Brunton & Kutz, 2019). This would sufficiently reduce the state-space of the model and adequate observer design could be performed using the above techniques. However, this is out of the scope of this work. What is addressed in this Thesis, is an example where the simulation and observer parameters are the same, helping us to illustrate the fact that the proposed control strategy can be applied, even in the absence of sufficient measurements.

The plant of Eq. (4.38) (without the integrators) can be represented as follows in matrix form:

$$\underbrace{\begin{Bmatrix} x'_a \\ \hat{p}' \end{Bmatrix}}_{x'_e} = \underbrace{\begin{bmatrix} A_a(t, x_a) & B_a(t, x_a) \\ O_{N \times 2nf} & -\hat{c}_d \end{bmatrix}}_{A_e} \underbrace{\begin{Bmatrix} x_a \\ \hat{p} \end{Bmatrix}}_{x_e} + \underbrace{\begin{bmatrix} O_{2nf \times N} \\ \hat{c}_d \end{bmatrix}}_{B_e} \underbrace{\{\hat{p}_\infty\}}_{u_e} + \underbrace{\begin{Bmatrix} g_a(t, x_a) \\ O_{N \times 1} \end{Bmatrix}}_{g_e(t, x_e)}, \quad (4.41)$$

where in short:

$$\begin{cases} x'_e = A_e x_e + B_e u_e + g_e(t, x_e), & (4.42a) \\ y = C_o x_e, & (4.42b) \end{cases}$$

where y is the measured average surface deformation and C_o the output matrix.

The adopted estimator is a Luenberger observer (Franklin et al., 2018; Khalil, 2015). Practically, it's a copy of the plant of the system plus a correction term. Therefore, the observer equation yields to be:

$$\begin{cases} \hat{x}'_e = A_e \hat{x}_e + B_e u_e + g_e(t, \hat{x}_e) + L(y - \hat{y}), & (4.43a) \\ \hat{y} = C_o \hat{x}_e, & (4.43b) \end{cases}$$

where \hat{x}_e is the estimated vector of the actual states, x_e , \hat{y} is the estimated surface deformation and L is the observer matrix to be chosen properly. Notice that the plant Eq. (4.42) and the observer Eq. (4.43) have the same form with Eq. (3.41) and Eq. (3.44), respectively. In addition, the linearized to the origin version of Eq. (4.42) results in an observable system (Franklin et al., 2018; Ogata, 2010) due to the presence of the fully-populated elasticity matrix. Therefore, a robust observer can be designed using the methodology described in Section 3.4. For that, the Lipschitz bound of the nonlinear function $g_e(t, x_e) - g_e(t, \hat{x}_e)$ has to be determined. This can be retrieved using the boundness

of friction derived in Chapter 1 and applied in Section 4.2. Consequently (see also Section 4.2):

$$\|g_e(t, x_e) - g_e(t, \hat{x}_e)\| \leq \beta_f \left\| \hat{N} \hat{\sigma}'_n \right\|_{\max} \|e\|, \quad (4.44)$$

where $e = x_e - \hat{x}_e$ is the estimation error.

It should be mentioned here that the robust controller obtained from Eq. (4.40) considering full-state feedback remains robust, even if we replace the actual states with the estimated ones derived from the observer of Eq. (4.43) (see Section 3.4 and also Khalil, 2015). Therefore, the input pressure at the injection point is given by the relation below:

$$\hat{p}_\infty = \begin{bmatrix} -K_z K_a & -K_z \end{bmatrix} \hat{x}_e. \quad (4.45)$$

For the illustrative examples, presented in the next subsection, we consider as many boreholes as the elements that the fault area has been divided into. This allows us to design a robust controller (see Eq. (4.45)) for the same parameter uncertainties with the ones given in Table 4.2 using the theory introduced in Section 3.3. In Table 4.3, we present the updated version of the Table by adding the bounds of the nominal and maximum friction as well as the nominal, minimum and maximum values of the diffusivity, c_d . Uncertainties in diffusivity can be addressed to hydraulic diffusivity, c_{hy} , and permeability, k_{per} , or even the effective distance of influence of the wells, L_d . For example, considering the limits of diffusivity provided in Table 4.3, for constant $L_d = 5$ km, the permeability in the surrounding of the fault area could vary from $k_{per}^{\min} = 10^{-18}$ m² to $k_{per}^{\max} = 10^{-8}$ m², assuming CO₂ as fluid (*fluid dynamic viscosity* = $6.3 \cdot 10^{-11}$ MPa.s and *mixture compressibility* = $2.3 \cdot 10^{-3}$ MPa⁻¹).

Furthermore, the friction law employed for the following simulations is the slip-weakening friction law chosen as the worst case scenario (see Section 4.2.2). Finally, the observer design considers the same parameters between the simulation and the observer as it is already discussed in the previous paragraphs.

The controller given by Eq. (4.45) can be used for the whole range of parameters summarized in Table 4.3. To sum up, only the following ranges of the mechanical and frictional properties of the fault region (including a safety factor) have to be known for the robust control design presented in this Section:

1. **minimum and maximum** estimation of the **density** of the surrounding rocks,
2. **minimum and maximum** estimation of the **length** of the fault,
3. **minimum and maximum** estimation of the **shear modulus** of the rock,

Table 4.3 – Nominal, minimum and maximum values considered for the mechanical and frictional properties of the fault during the design of the robust continuous-time controller.

Variable	Symbol	Unit	Min. Value	Max. Value	Nominal Value
fault activation length	L_y	km	2	10	6
shear modulus	G	GPa	28	40	34
density of rocks	ρ	kg/m ³	2400	3000	2700
damping ratio	ζ	-	0	1.2	0.6
initial effective normal stress	σ'_n	MPa	-	≤ 150	-
friction coefficient	μ	-	0.04	100	0.6
diffusivity	c_d	yr ⁻¹	10^{-5}	10^5	1
SW parameters	$ \Delta\mu $	-	-	≤ 0.4	-
	d_c^{sw}	mm	≥ 5	-	-

4. **minimum and maximum** estimation of the **damping ratio**,
5. **maximum** estimation of the **effective normal stress** on the fault interface (before the activation of the controller),
6. **minimum and maximum** estimation of the **diffusivity**,
7. **minimum and maximum** estimation of the **friction coefficient**,
8. **minimum** estimation of the **SW characteristic frictional distance**,
9. **maximum** estimation of the **SW stress drop**.

Notice that all the above limits are strictly positive numbers.

4.3.1 Application with a single source

Consider an idealized and isolated strike-slip fault as the one studied in Sections 4.1 and 4.2 (see Table 4.1). We place the single well at a distance $L_d = 5$ km from the fault's center (see Figure 4.9a). This distance is sufficiently large to consider that when the fluid reaches the fault level, the pressure front is quasi-uniform and it covers all the fault area (see Figure 4.9a). As we mentioned above, the controller developed in Section 3.3 is robust when the number of elements of the fault area is equal to the number of available wells. Therefore, in this specific example, our configuration reduces to the spring-slider reduced order model (single element). This configuration will help us build understanding regarding the influence of the hydraulic diffusivity/permeability of the rocks surrounding the fault region to the developed pressures in the borehole level.

The dynamics of this system can be simulated by Eq. (4.38). The frictional interface obeys the slip-weakening friction law. Moreover, the frictional properties of the fault are

identical to the one employed in Sections 4.1.2 and 1.2.3. As shown there, when the fault is critically stressed, we expect a dynamic instability to occur. The injected fluid is a high-pressurized CO₂ resulting in a hydraulic diffusivity of $c_{\text{hy}} = 0.7 \text{ m}^2/\text{s}$ (*permeability*, $k_{\text{par}} = 10^{-13} \text{ m}^2$). Consequently, the diffusivity is equal to $c_d = \frac{c_{\text{hy}}}{L_d^2} \approx 0.9 \text{ year}^{-1}$.

In Figure 4.11a, we present again the (average) response of the strike-slip fault for a single (isolated) typical dynamic event. The maximum reported velocity (averaged over the fault surface) is 0.11 m/s corresponding to a maximum slip of 0.63 m. This dynamic event is associated with a stress drop of approximately 3.8 MPa (Figure 4.11b) resulting in an earthquake of magnitude $M_w \approx 5.7$.

In order to prevent such an earthquake, we employ the control strategy developed earlier in this Section and in Chapter 3. The control objective is to release the stored elastic energy in a slow-aseismic way, assuring stability throughout the whole process.

In this example, we have a Single Input and Single Output (SISO) system. The input is the pressure adjustment in the well level and the output is the unique measurement we obtain, i.e. the average deformation of the fault at the surface (see Figure 4.9a). As we have discussed in this Section, given Eq. (4.38), we can design a robust controller with the form of Eq. (4.45) which takes into consideration the range of parameter uncertainties summarized in Table 4.3. In addition, an observer is constructed of the form Eq. (4.43).

As mentioned above, as far as there exists only one actuator (a single borehole), we can track only one reference signal. This signal is chosen to be the average slip over the fault region. The slip reference trajectory has the sigmoid shape depicted in Figure 4.10. The displacement target is set to be equal to the maximum slip of the open-loop system, i.e. $d_{\text{max}} \approx 0.63 \text{ m}$. The borehole is scheduled to operate for about $t_{\text{op}} = 3 \text{ years}$. Therefore, we expect a maximum controlled slip-rate of the order of 10^{-8} m/s ($\sim 30 \text{ cm/year}$) during this period. Notice that due to the far-field movement of the tectonic plates ($v_\infty = 1 \text{ cm/year}$), during the control strategy, we expect the fault to slip an extra 3 cm, namely we expect the maximum slip of the fault to be $d_{\text{max}} \approx 0.66 \text{ m}$ (see Figure 4.11c).

In Figure 4.11c, we show the (average) response of the system after applying our control strategy. We can infer that the tracking is almost identical to the reference trajectories. In parallel, in Figure 4.11d, the pore pressure evolution at the fault (blue curve) and borehole (green) level is plotted. We can clearly observe the inherent delay due to the diffusion phenomena. Initially, the actuator reduces its pressure (fluid extraction) to stabilize the fault system for approximately nine months. The effect of this reduction becomes visible in the fault after a year of the initiation of the controller, i.e. three months of delay. Next,

4.3. Robust control of seismic faults coupled with diffusion processes using distant fluid injections by monitoring only surface deformation

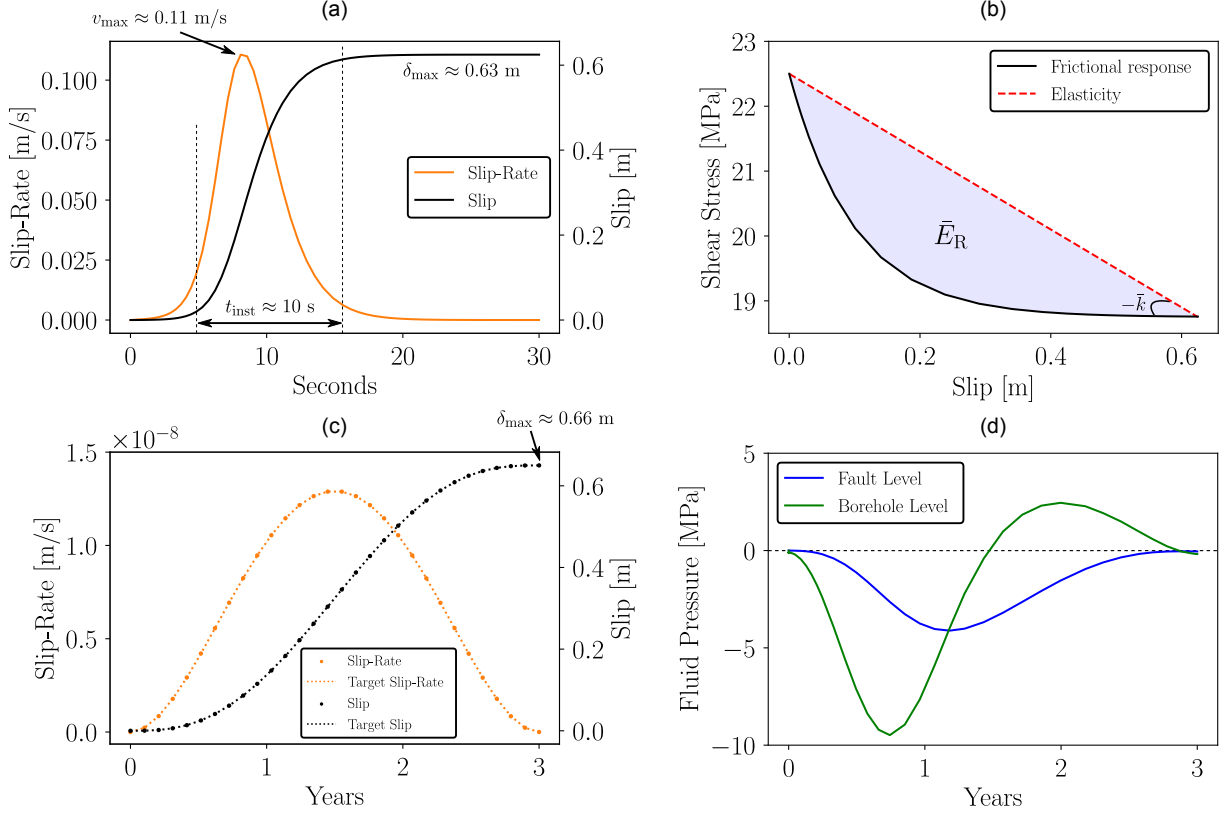


Figure 4.11 – Open-loop response of the strike-slip fault for a single dynamic event with slip-weakening friction ($n_f = 1$ element). (a) Average slip (black) and slip-rate (orange) in terms of time. (b) Corresponding average shear stress evolution in terms of slip. Closed-loop response of the strike-slip fault after the application of the controller adopting slip-weakening friction law ($n_f = 1$ element corresponding to 1 installed well). (c) Average slip (black dotted curve) and slip-rate (orange dotted curve) in terms of time. The controller successfully achieves the target/reference slip (black dashed line) and slip-rate (orange dashed line). (d) Evolution of the average applied fluid pressure change in the fault (blue curve) and the borehole level (green curve).

the actuator increases the pressure (fluid injection) in order to allow the fault to slip as the tracking trajectory demands. When the system reaches its steady-state, the average pressure both in the fault and the borehole becomes zero.

The pressure evolution at the borehole level (green curve in Figure 4.11d) strongly depends on the operation time of the control strategy, t_{op} , and the diffusivity of the surrounding rocks, c_d . These dependencies are not surprising and are depicted in Figure 4.12. In particular, in Figure 4.12a, we observe that as the operation time of the control strategy decreases ($t_{\text{op}} = 3$ years, 1 year, 4 months) the developed pressures (applied flux)

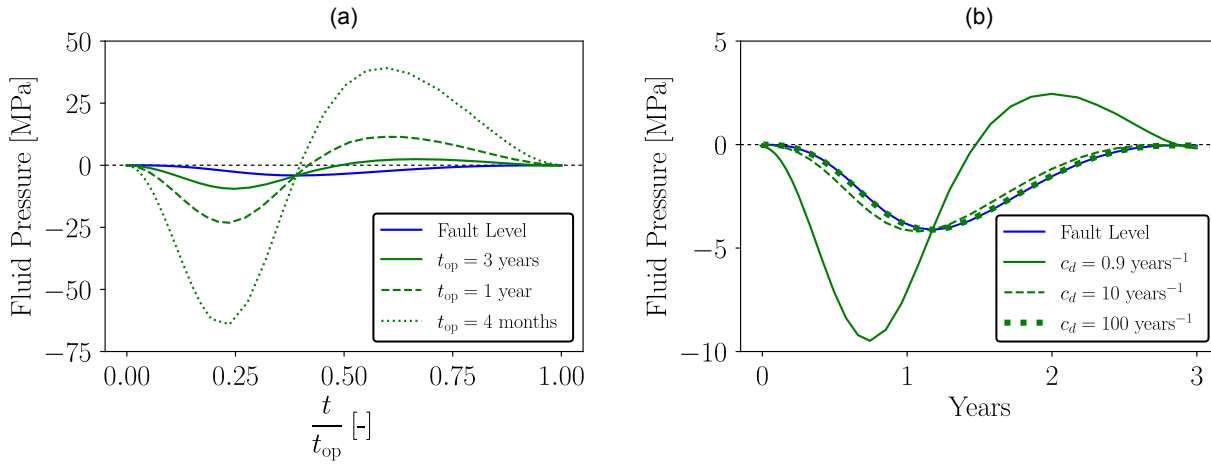


Figure 4.12 – (a) Comparison of average fluid pressure in terms of normalized time for three different operation times ($t_{op} = 3$ years, 1 year, 4 months). (b) Comparison of average fluid pressure with respect to time for three different values for diffusivity ($c_d = 0.9, 10, 100$ years $^{-1}$). For both graphs the pressure at the fault level is illustrated with the blue solid line.

close to the level of the well increase significantly. Of course, as t_{op} decreases, the expected maximum slip-rate in the fault region increases as well.

In general, t_{op} is a free parameter and can be chosen according to practical criteria related to the site and the pumping system. In Figure 4.12b, we show the influence of the diffusivity, c_d , on the average pressure evolution of the fault. Specifically, as the diffusivity increases ($c_d = 0.9, 10, 100$ years $^{-1}$), the pressure at the borehole level tends to coincide with the one in the fault level. Notice that the average pressure at the fault level (blue curve) is independent from the operation time and the diffusivity. Variations in diffusivity could be attributed to changes in the hydraulic diffusivity/permeability of the rocks surrounding the fault area and/or the effective distance of the well from the fault. The influence of the latter factor (L_d) and of the number of the wells is explored in the following subsection.

4.3.2 Application with multiple sources

In the case where multiple wells are considered, the region of influence of each well reduces allowing us to place the wells closer to the fault area (see Figure 4.9). This action practically reduces the diffusivity, c_d , and, eventually, leads to reduced pressures at the borehole level (see Figure 4.12b). Even though the distance between the wells and the

4.3. Robust control of seismic faults coupled with diffusion processes using distant fluid injections by monitoring only surface deformation

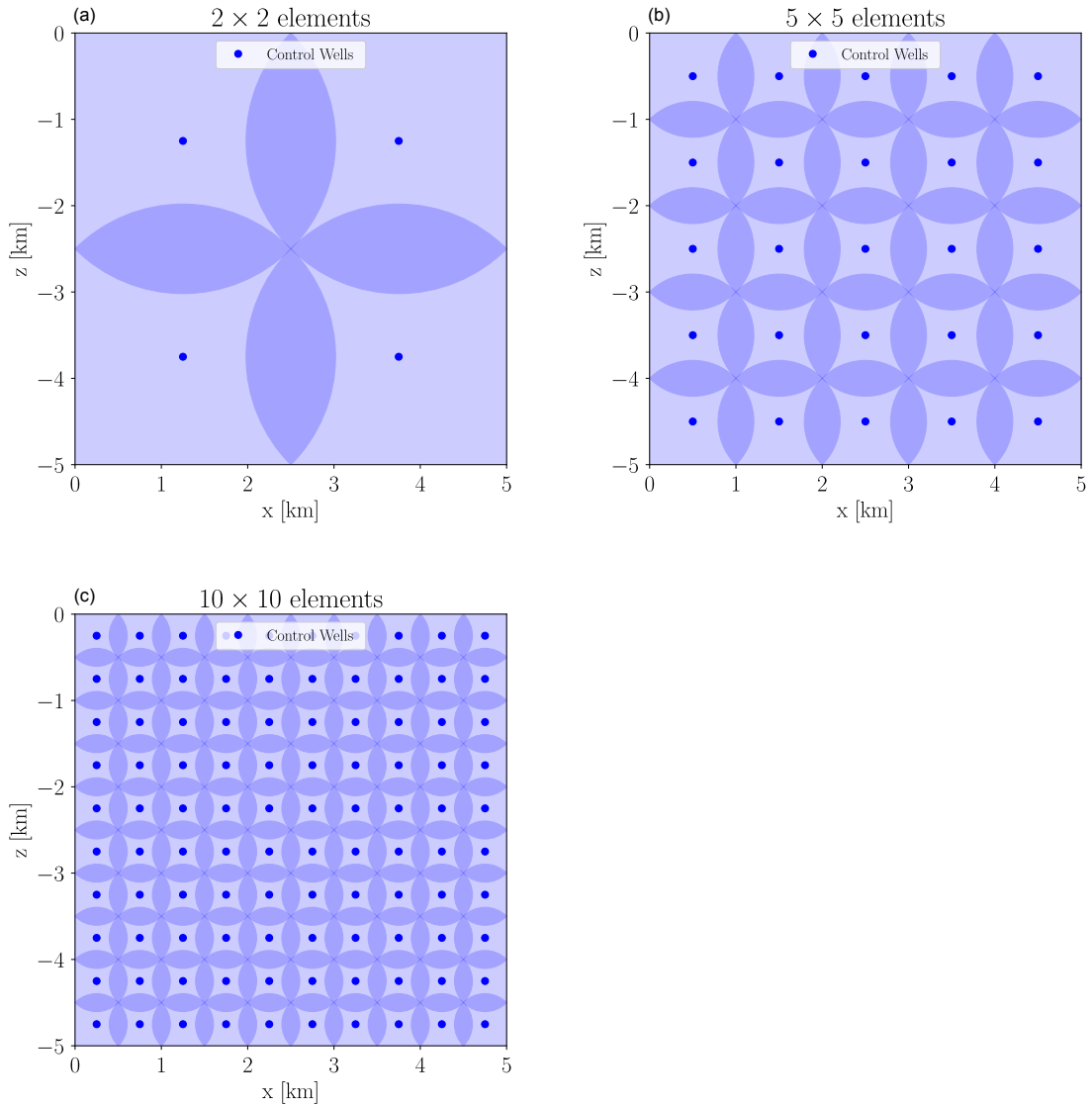


Figure 4.13 – Projection of the wells (blue dots) on the fault interface for three different scenarios: (a) 4 wells, (b) 25 wells, and (c) 100 wells. The blue shaded circles correspond to the region of influence of each well. The darker areas indicate overlapping regions.

fault is decreased, it remains sufficient to assume a quasi-uniform pressure front at each region on the fault interface. Here, three different scenarios are examined including each time 4, 25, or 100 wells. For each application, the projection of the wells on the fault interface is depicted in Figure 4.13.

The design of the controller takes into account parameter uncertainties as provided in Table 4.3 and generally discussed in this Chapter. The fault area is divided into that many elements as the total number of installed wells for each scenario. Moreover, the

only measurement we acquire is the average deformation of the fault at the surface (see also Figure 4.9). We remind that this deformation could be obtained by state-of-the-art technologies (e.g. surveying, GPS, INSAR, etc.). For this purpose, an observer is designed as well, in order to recreate the states of the system and feed them back to the controller. The operation time remains the same ($t_{\text{op}} = 3$ years) as in the previous examples (see Section 4.3.1). For these applications, the target of each well is to drive its region of influence (see Figure 4.13) to a new equilibrium point of lower energy, following a smooth slip trajectory as the one illustrated in Figure 4.10. Therefore, 4, 25, and 100 reference trajectories are being tracked during each simulation, respectively.

In Figure 4.14, the first two applications are presented. More specifically, in Figure 4.14a-b, the scenario where 4 wells are installed at a distance of $L_d = 2.5$ km from the fault is depicted. In Figure 4.14c-d, the scenario where 25 wells are installed in a distance of $L_d = 1$ km from the fault is illustrated. We can observe that the average response of the fault system (Figure 4.14a,c) for both scenarios is identical to the one in Figure 4.11c,d (single well). However, even though the average pressure over the fault area is the same, large deviations from the previous single well example can be observed in the pressure profiles of each borehole point. These deviations reduce as the distance from the fault decreases and the pressure evolution at the borehole level tends to approach the one at the fault level (smaller delay). Notice that the envelopes of the respective pressures completely overlap in the case of 25 wells (see Figure 4.14d). However, the minimum pressure at the borehole level remains unchanged at around 8 MPa between all three applications presented so far (see Figures 4.11d, 4.14b and 4.14d) and can be decreased by increasing, for instance, the operation time. This minimum pressure peaks corresponds to an individual or a group of boreholes. In other words, not all the wells have to reach this pressure level.

Finally, the scenario of 100 installed wells at a distance of $L_d = 0.5$ km from the fault is depicted in Figure 4.15. Again the response of the system is identical to the previous examples. Furthermore, the pressure evolution at the boreholes completely overlaps the one at the fault level.

It is worth emphasizing that the control strategy presented in the above examples was performed by just measuring the average slip of the fault at the surface. In order to reconstruct the state-space of the whole fault region, we built an observer. This observer uses the available measurement in order to derive estimations for the states of the system. Notice that the observer is designed in such a way that the error between the actual state

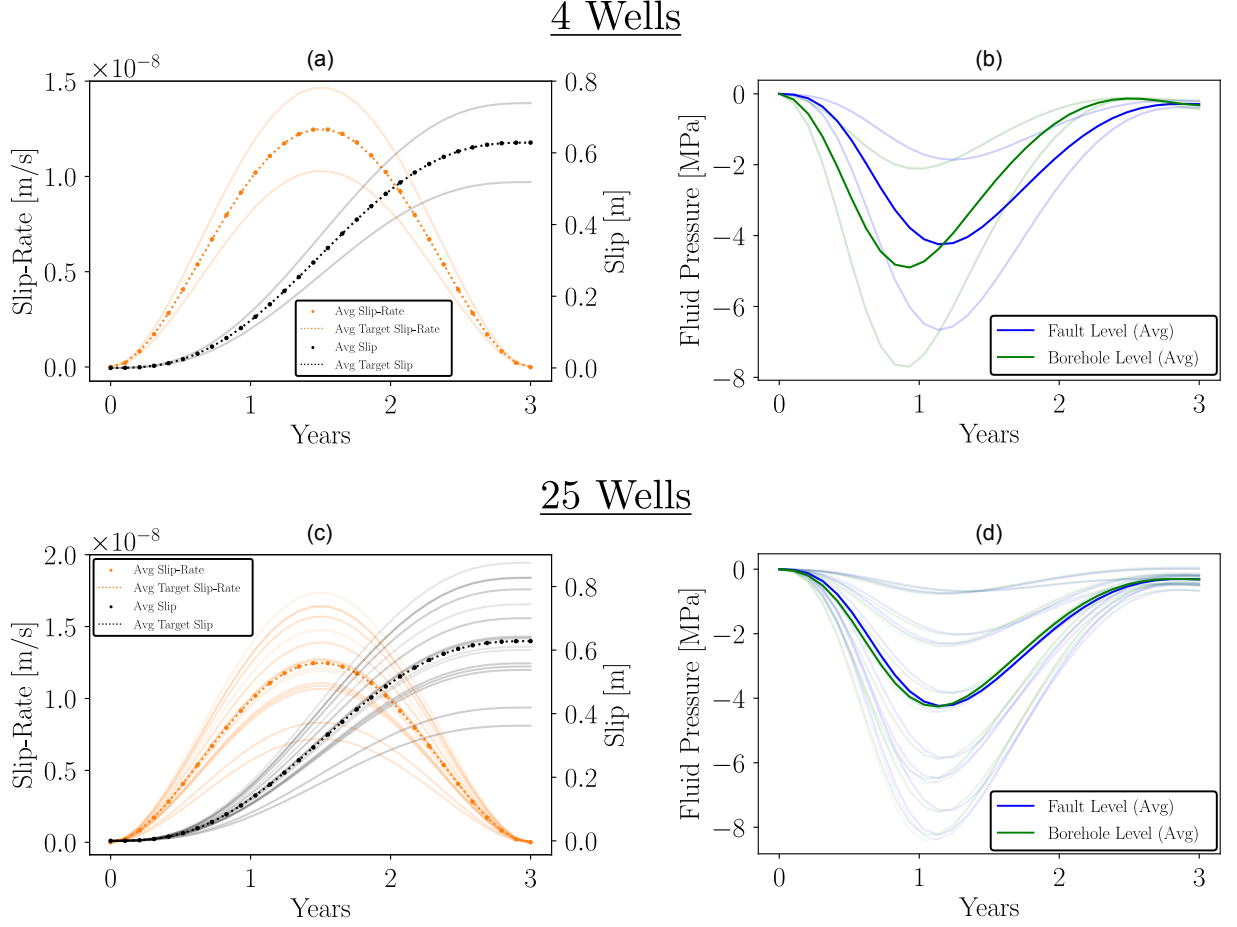


Figure 4.14 – Closed-loop response of the strike-slip fault after the application of the controller adopting slip-weakening friction law: (a), (b) $n_f = 4$ elements corresponding to 4 installed wells, and (c), (d) $n_f = 25$ elements corresponding to 25 installed wells. (a), (c) Average slip (black dotted curve) and slip-rate (orange dotted curve) in terms of time. The controller successfully achieves the target/reference slip (black dashed line) and slip-rate (orange dashed line). (b), (d) Evolution of the average applied fluid pressure change in the fault (blue curve) and the borehole level (green curve). The translucent curves indicate the evolution of the respective variables for individual elements.

and its estimation to tend to zero exponentially as time goes to infinity. A feeling of the range of these errors is given through Figure 4.14c-d. On the left, the error of the slip is plotted for all 100 elements of the discretized fault area, while on the right the respective error concerning the slip-rate appears. We can see that the error of the slip is of the order of microns, while the one of slip-rate is of the order of mm/year. Therefore, we can safely conclude that the observer managed to maintain the error of the states in really low (even negligible) levels.

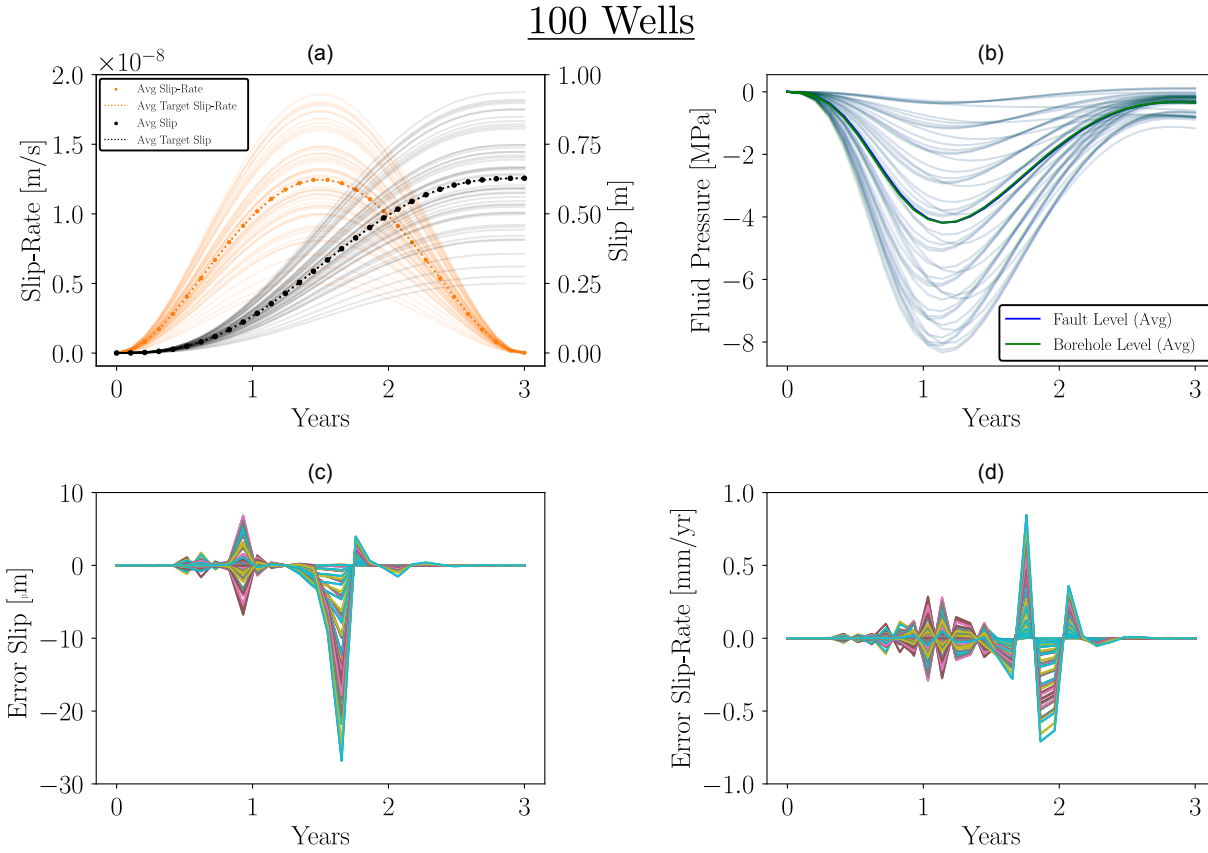


Figure 4.15 – Closed-loop response of the strike-slip fault after the application of the controller adopting slip-weakening friction law ($n_f = 100$ elements corresponding to 100 installed wells). (a) Average slip (black dotted curve) and slip-rate (orange dotted curve) in terms of time. The controller successfully achieves the target/reference slip (black dashed line) and slip-rate (orange dashed line). (b) Evolution of the average applied fluid pressure change in the fault (blue curve) and the borehole level (green curve). The translucent curves indicate the evolution of the respective variables for individual elements. The evolution of the error between the actual state and the estimated one for all the elements involved in the simulation: (c) Slip error, (d) Slip-rate error.

The above academic examples indicate that earthquake prevention of large magnitudes may be possible if we use the control theory presented in this Section and in Chapter 3. Even in the presence of diffusion processes and the acquisition of just a single measurement, the robust controller and observer managed to drive the fault system to a new equilibrium point of lower energy, assuring stability, all the time. However, further analyses should be done in order to account for poroelastic effects, parameter uncertainties in the observer as well as more complex phenomena and unmodeled dynamics at finer scales that could appear.

4.4 Non-local robust control of seismicity rate

In the previous Sections, we showed that the control of the unstable dynamics of an isolated fault using distant fluid injections and/or extractions is possible, despite the presence of uncertainties in friction, elasticity, and diffusivity, among others. In other words, using the control approach developed in Chapter 3, an earthquake of magnitude $M_w \approx 6$ can be prevented. However, in this Section, we proceed a step further with a non-local case, where we investigate the possibility of stabilizing the seismicity in a reservoir by adequately adjusting the flux in the installed wells assuring, in the meantime, the desired fluid production levels (Tzortzopoulos, Jarry-Cammas, et al., 2021).

More specifically, we consider a subsurface reservoir located in a seismogenic region as illustrated in Figure 4.16. This reservoir has a square cross-section with dimensions 3×3 km² (15×15 nodes) in the x- and y-directions, respectively, while it maintains a constant thickness of 100 m in the z-direction. In this area, there are two injection (“static”) wells (red dots), each one of which injects fluid in the reservoir with a constant flux of ~ 1 m³/s. Additionally, there are five “control” wells (blue dots) which can stabilize the seismicity in the region, while maintaining a constant fluid production per unit of time. In a real case scenario, the “static” wells would correspond to waste disposal wells, while the “control” wells to production wells, which could either inject and/or extract fluid to/from the reservoir according to the requirements of the applied control strategy.

In order to model the variation of pressures in the reservoir, we adopt a 2-D diffusion equation considering averaging in the z-direction and assuming equal flux for the top and bottom boundary layers (z-direction). The developed pressure changes in the seismogenic region increase the seismicity only inside the reservoir. The corresponding seismicity rate can be modeled using the differential equation provided in Segall and Lu (2015) (see also J. Dieterich, 1994). For this example, we consider Dirichlet boundary conditions, i.e. constant pressure at the boundaries (drained conditions). For simplicity, also, a single fluid is employed, that of CO₂ in supercritical condition. A two-phase flow will be considered in future works employing two distinct fluids, for instance water or CO₂ for disposal and oil or gas for extraction.

The open-loop response of the reservoir is depicted in Figure 4.17. In this case, only the “static” wells (red dots in Figure 4.16) are active. Each one of these wells injects fluid with a constant flux of ~ 1 m³/s (see red dashed line in Figure 4.17a). We can observe that due to the presence of this perturbation, the average seismicity in the seismogenic region has

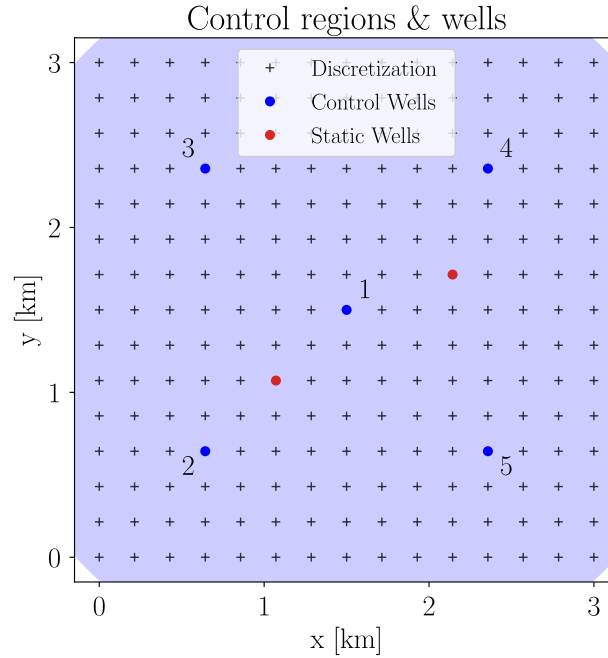


Figure 4.16 – Square cross-section (x- and y-directions) of a 3×3 km² reservoir. In the z-direction, the reservoir has a constant thickness of 100 m. The + marks correspond to the discretization points, the red dots to the “static” injection wells, while the blue ones to the wells installed for controlling the average seismicity in the region (blue shaded area).

been increased more than two orders of magnitude (see point I in Figure 4.17b). The fluid pressure profile, at this point, along the reservoir, is shown in Figure 4.17c. Moreover, in Figure 4.17d, the local seismicity rate for each node is plotted in terms of time, where we can see that locally there is approximately a million-fold increase of the seismicity rate. Finally, after ~ 200 years, we observe that the seismicity rate in the region drops to its initial level (see Figures 4.17b,d) due to the influence of the drained boundary conditions.

In order to prevent this increase of the seismicity in the region, while industrial operations take place, we design a robust controller and observer using the tools provided in Chapter 3. More specifically, we adopt as control inputs the flux of each “control” well (blue dots in Figure 4.16). Additionally, we introduce a constraint such that the total fluid production of the “control” wells to be equal to ~ 1.2 m³/s. Furthermore, we assume that the only acquired measurement is the average seismicity rate all over the region¹. The objective of the control strategy is to maintain the seismicity of the region to the initial level (which is equal to unity) while fluid disposal (“static” wells) and fluid production

1. Local/pointwise seismicity rates, pressure estimates, subsidence or other measurements can be used as well.

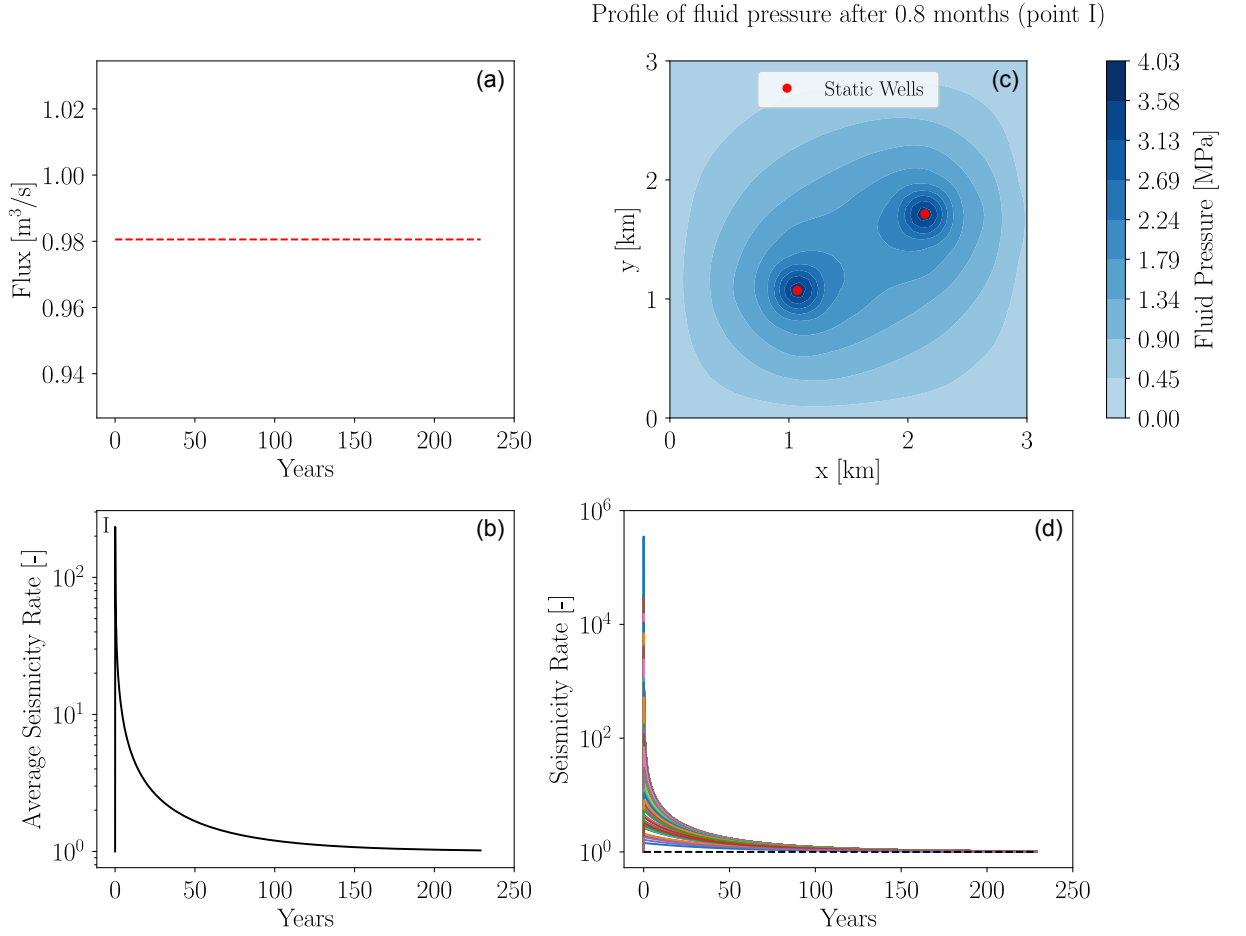


Figure 4.17 – Open-loop response of the reservoir. Only the “static” wells (red dots in Figure 4.16) are active. (a) Flux of each “static” well in function of time. (b) Average seismicity rate (logarithmic scale) in the seismogenic region in terms of time. (c) Snapshot of fluid pressure distribution along the reservoir region at the point when the maximum average seismicity rate is occurred (point I in subfigure (b)). (d) Seismicity rate (logarithmic scale) in terms of time for all the points of the mesh grid. The black dashed line corresponds to the initial seismicity rate which is equal to the unity.

(“control” wells) processes securely operate.

The system of this study is stabilizable and detectable but not controllable and observable (for these definitions see Franklin et al., 2018; Ogata, 2010) as in Section 4.3, for instance. However, due to the inherent stable dynamics of the system (diffusion equation), this will not raise any issues during the control design.

The response of the closed-loop system of the reservoir is illustrated in Figure 4.18. In Figure 4.18a, we show the evolution of fluxes of each well. Positive flux corresponds

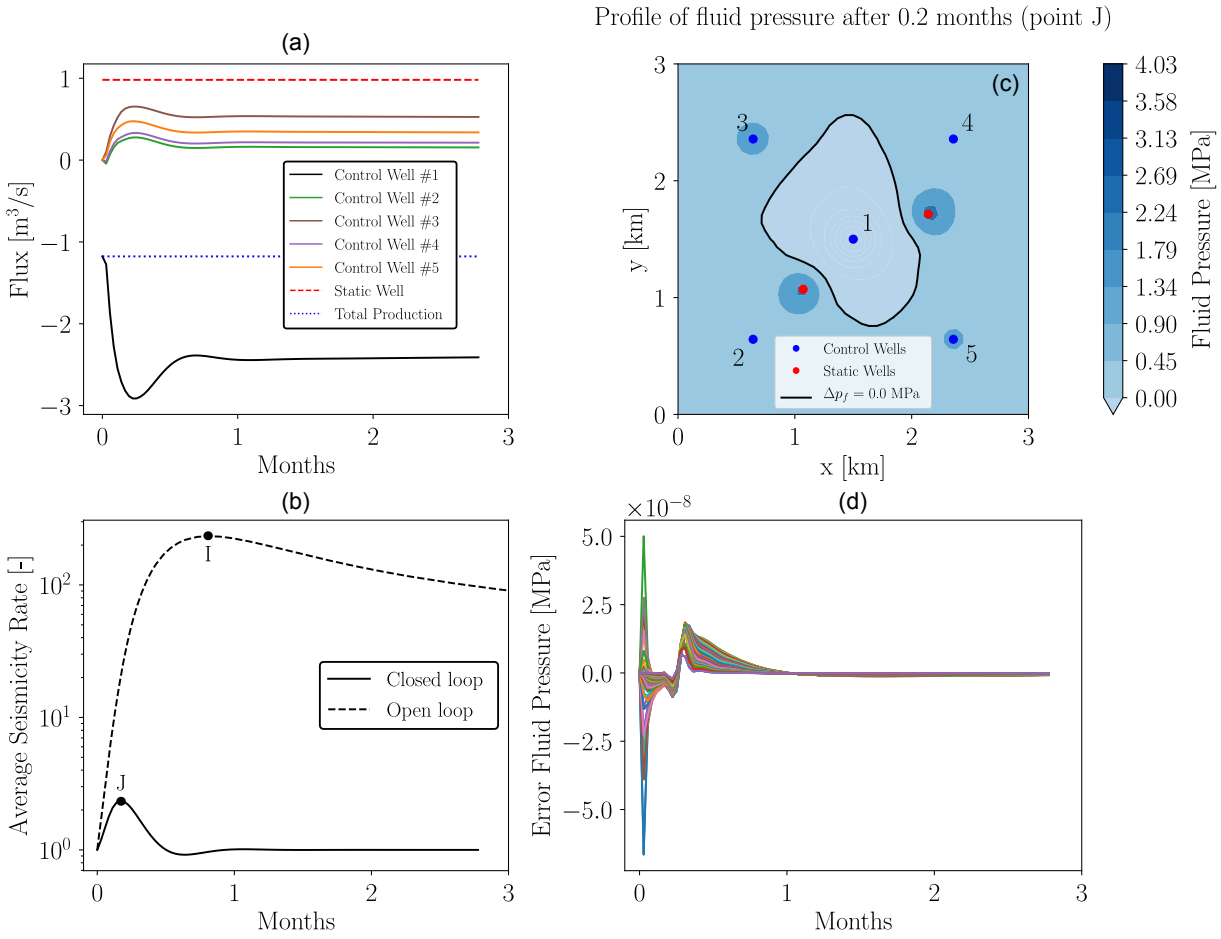


Figure 4.18 – Closed-loop response of the reservoir. Both the “static” (red dots in Figure 4.16) and the “control” (blue dots in Figure 4.16) wells are active. (a) Flux of each “static” (red-dashed line) and “control” well in function of time. The total fluid production of the “control” wells is indicated with the blue dotted line. (b) Average seismicity rate (logarithmic scale) in the seismogenic region in terms of time for both the open-loop (black dashed curve) and the closed-loop (black continuous curve) response. (c) Snapshot of fluid pressure distribution along the reservoir region at the point when the maximum average seismicity rate is occurred (point J in subfigure (b)). The black contour line corresponds to zero fluid pressure. (d) The evolution of the error between the actual fluid pressure and the estimated one (from the observer) for all the elements of the grid.

to fluid injection, while negative flux to fluid extraction. We observe that the targets of constant fluid disposal (red dashed line) and fluid production (blue dotted line) are satisfied throughout the whole operation of the control strategy. Notice also that only the #1 “control” well (black curve) extracts fluid from the reservoir while the remaining four constantly inject fluid. This behavior depends on the weight we set to each “control”

well. In the presented example, #1 “control” well is fully weighted, as at $t = 0$, this well has to extract as much fluid as the control objective indicates ($-1.2 \text{ m}^3/\text{s}$). Different configurations can be considered, for instance, by equally distributing the weights along all five “control” wells. However, this investigation is out of the scope of this Thesis.

The comparison of the open-loop (black dashed curve) and closed-loop (black continuous curve) responses is plotted in Figure 4.18b. We observe that the target to stabilize the average seismicity rate to unity has been reached after approximately one month from the initiation of the control strategy. Until that point, the increase of seismicity was kept low, i.e. two orders of magnitude lower than the maximum seismicity that occurred during the open-loop response. In Figure 4.18c, the fluid pressure distribution in the reservoir is depicted when the average seismicity rate occurs (see point J in Figure 4.18b). The black contour line indicates the zero pressure region. Inside that region, the fluid pressure is negative, while outside it is positive.

As we mentioned in the previous paragraphs, an observer was designed to estimate the state-space of the system acquiring only a single measurement, that of the average seismicity rate in the region. The estimated error of the fluid pressure for all the nodes is illustrated in Figure 4.18d.

This illustrative example reveals the effectiveness of the proposed control strategy in non-local problems where the presence of the fault network is not precisely known. This toy model raised very important questions, though. One of them is related to the optimal location of the “control” wells (see for instance Cihan et al., 2015). Another is related to the applicability of this methodology to real case reservoirs, like the Groningen gas field (Heimisson et al., 2021; Smith et al., 2021; Tzortzopoulos, Jarry-Cammas, et al., 2021). The answers to the above questions will be addressed in future works under the CoQuake framework.

Design of a novel double-direct shear apparatus for controlling earthquakes in the laboratory

In the previous Chapters, we developed and tested numerically continuous-time robust controllers for the active stabilization of isolated fault regions. Here, we go one step further and we design, assemble and calibrate a novel triplet apparatus for performing double-direct shear experiments of decimetric scale that allows (a) to reproduce earthquake-like instabilities in the laboratory and (b) to prevent them by active fluid pressure adjustment. A detailed description of the chosen experimental configuration, the sensors, the material used for the specimen, and basic identification experiments is provided in this Chapter. Due to the relatively slow sampling rate, the controller design is performed in the discrete domain using an emulation technique.

5.1 Review on pre-existing triplet machines for reproducing earthquake-like instabilities

To-date, there are no experimental devices, in the literature, that can control earthquake-like instabilities in the laboratory. This is shown by the significant number of double-shear devices mentioned in the literature, which allow the reproduction of earthquake-like instabilities in the laboratory, but they cannot prevent them. Therefore, no similar technical solution exists for the needs of our study. Without being exhaustive, we list some of the most known triplet apparatuses that exist in the literature:

- J. H. Dieterich (1972): An inner block with planar and parallel faces is pushed between the outer blocks. The contact area is $6 \times 6 \text{ cm}^2$. A horizontal hydraulic jack applies the normal force.

- J. H. Dieterich (1981a): Two layers of gouge are sheared between three blocks made of granite. The contact area is $5 \times 5 \text{ cm}^2$.
- Linker and Dieterich (1992): The same double-direct shear apparatus as above but modified to allow rapid servo-control of the normal stress. A step in normal stress of 2.5 MPa requires less than 150 ms.
- Boettcher and Marone (2004): Double-direct shear apparatus for testing gouge layers. The contact area is $5.25 \times 5 \text{ cm}^2$. According to the results, the authors imposed sinusoidal oscillations in the normal stress, where a change of 1 MPa was reached in $\sim 700 \text{ ms}$.
- Knuth and Marone (2007b): Double-direct shear configuration using a servo-controlled, biaxial testing apparatus. Two identical gouge layers are sheared between three steel forcing blocks. The contact area is $10 \times 10 \text{ cm}^2$.
- M. M. Scuderi et al. (2015): The same as in Knuth and Marone (2007b), but with an additional pressure vessel to allow a true-triaxial stress field. The contact area is $5.4 \times 6.2 \text{ cm}^2$.
- Saber et al. (2016): Double-direct shear configuration. The load frame is equipped with a hydraulic cylinder that can compress the sample assembly statically in the horizontal direction. The contact area is $5 \times 7.5 \text{ cm}^2$.
- M. Scuderi, Collettini, and Marone (2017): Bi-Tri-Axial Press (BRAVA) at RMP - INGV is an apparatus in a double-direct shear configuration within a pressure vessel to allow the application of a triaxial stress field. The specimen is comprised of three stainless steel blocks that confine and shear two layers of fault gouge. The loading can be stress or displacement controlled. The contact area is $5.54 \times 5.55 \text{ cm}^2$.
- Lieou et al. (2017): Two layers of simulated gouge are sheared between three blocks. The contact area is $10 \times 10 \text{ cm}^2$.
- M. Scuderi, Collettini, Viti, et al. (2017): Double-direct shear configuration in a biaxial deformation apparatus, testing gouge layers. They reduced the shear loading stiffness by inserting an elastic element in the loading column.
- Kilgore et al. (2017): Double-direct shear configuration for shearing granite faults of $5 \times 5 \text{ cm}^2$ surface. Changes of normal stress were performed during the experiments. The duration for reaching the new target was $\sim 170 \text{ ms}$ in step increase while $\sim 300 \text{ ms}$ in step decrease.

5.2 Description of the experimental apparatus

In this Chapter, we perform double direct-shear experiments of decimetric scale using a novel triplet (sandwich) apparatus (French Patent No: FR2109102, Stefanou et al., 2021) made of stainless steel (Figure 5.1). Two loading systems are used in order to apply shear (displacement controlled vertical loading system) and normal (pressure controlled horizontal loading system) stress to the sheared interfaces. In our machine, the horizontal loading system consists of an inflatable rubber bag whose pressure can be controlled, in real-time, through a fast response electro-pneumatic pressure regulator. An air compressor with a volume of 100 L and a maximum pressure of 1 MPa is used to supply air to the rubber bag through a network of tubes. This system can simulate fluid injection/extraction in/from the fault interface by properly adjusting the air pressure in the rubber bag to desired levels resulting in variations of the effective normal stress in the sheared interfaces.

In this study, no actual fluid is used. Therefore, various phenomena related to the effect of water on friction (pore-pressure diffusion) and poro-elasto-plasticity are ignored. These effects could be considered by a hybrid experimental setup, where diffusion and poro-elasto-plasticity are modeled numerically in the computer. In this case, the controller would adjust the fluid of a well far from the fault and the numerical model would adapt in real-time the pressure on the fault area, which is present in the physical experiment. Hybrid tests are common in engineering (McCrum & Williams, 2016), but such an implementation goes beyond the scope of this Thesis. Alternatively, fluids could be injected directly on the fault-like surface (on going work). In any case, our controller is robust and able to tackle with these phenomena which play the role of uncertainties and unmodeled dynamics (see also Appendix F).

In this device, the vertical loading frame is not embedded in the machine, but instead it is part of an existing triaxial apparatus. The stiffness of the vertical loading system used (vertical loading frame + aluminum cone + aluminum internal cylinder + aluminum base) is measured to be equal to $k_{\text{machine}} = 257 \text{ kN/mm}$, which is stiff enough for the purpose of our experiments. The dead weight of the vertically moving parts is taken into account in order to correct the measured shear stress on the interfaces in all the tests presented herein.

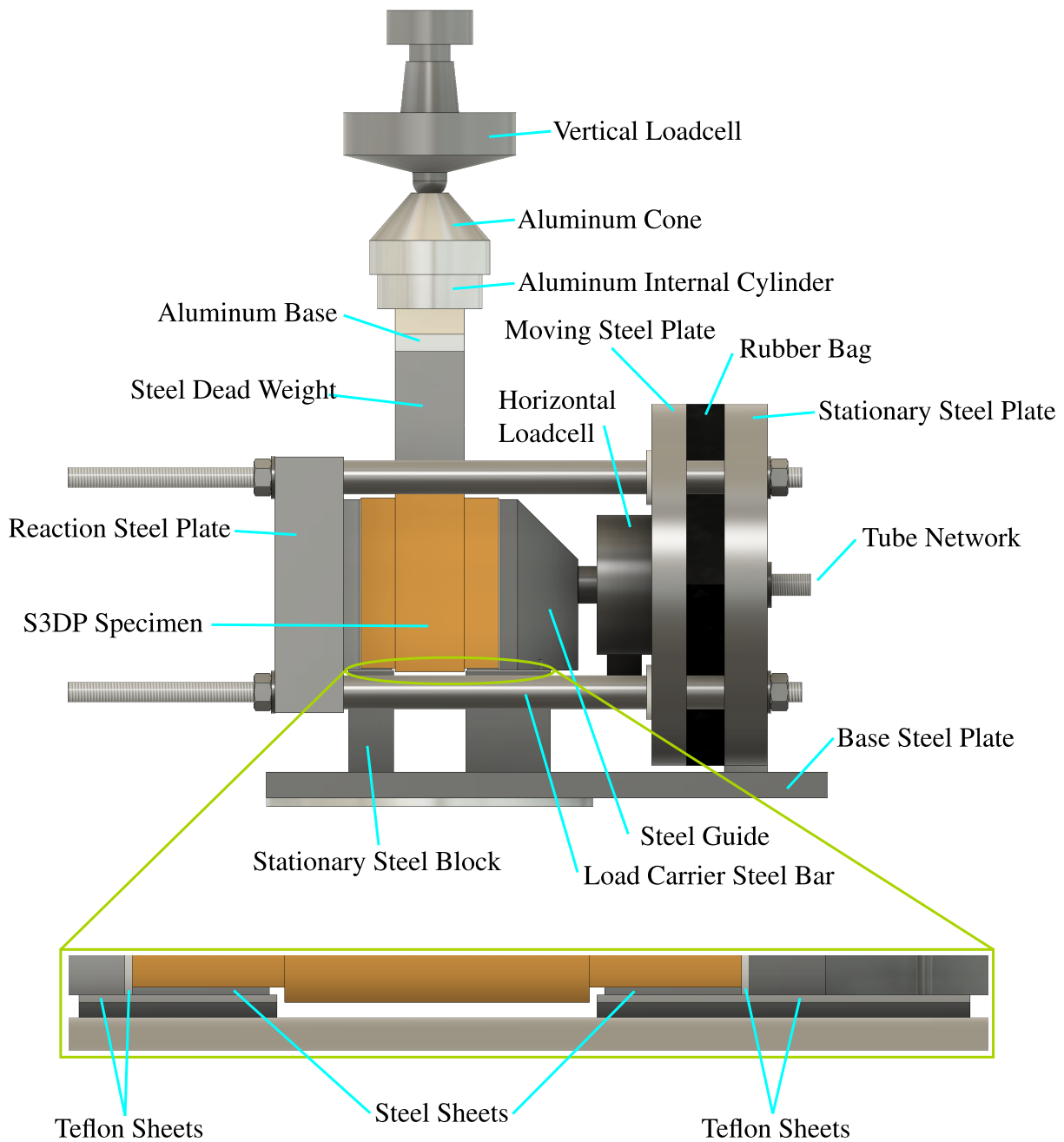


Figure 5.1 – Configuration of the novel double-direct shear apparatus.

5.3 Sensors, data acquisition and real-time data processing

During our experiments, loadcells, Linear Variable Differential Transformers (LVDTs) and the pressure regulator are used for acquiring measurements. In particular, for measuring the applied vertical load, we use a loadcell which is attached to a servo-controlled ram with a maximum force of 2 kN and accuracy of $\pm 0.1\%$ ($\pm 0.1\% \times 2 \text{ kN} = \pm 2 \text{ N}$). The horizontal forces are measured by a loadcell with a maximum force of 10 kN and accuracy of $\pm 0.02\%$ ($\pm 0.02\% \times 10 \text{ kN} = \pm 2 \text{ N}$). Moreover, we use two vertically-placed LVDTs to measure the average vertical displacement of the middle block and an additional horizontally-placed one to measure dilatancy/compaction of the interfaces. All of them cover a range of $\pm 12.5 \text{ mm}$ with an accuracy of $\pm 0.1\%$ ($\pm 0.1\% \times 12.5 \text{ mm} = \pm 12.5 \text{ }\mu\text{m}$). Finally, an internal pressure sensor with an integrated Proportional-Integral-Derivative (PID) controller is contained by the manufacturer inside the electro-pneumatic pressure regulator controlling the pressure in the rubber bag. The rubber bag can sustain pressures up to 1 MPa with an accuracy of $\pm 0.1\%$ ($\pm 0.1\% \times 1 \text{ MPa} = \pm 1 \text{ kPa}$). All sensors have been meticulously calibrated and are shielded.

These sensors are connected to a data acquisition device (cDAQ-9174 with 32 bits digital resolution) made by National Instruments (NI). First, the data are acquired in the NI hardware with a frequency of 25 kHz which in turn, they pass to the NI LabVIEW software in order to be processed in real-time. Apart from only plotting and storing data, LabVIEW can also update, in real time, the pressure in the rubber bag based on our controller.

Due to limitations related to the operating system (OS: Windows 10) and complexity of the developed LabVIEW code, the pressure control can be updated with a frequency of 500 Hz. In other words, in the time interval of 2 ms^1 , 50 raw samples per sensor can be acquired. This time resolution can be further reduced, but this level is enough for our experiments. Moreover, achieving control with slower sampling rate is even more challenging as one could argue, because we approach to real conditions regarding possible applications of the method in the real scale.

The functions that the developed LabVIEW code processes in the time interval of 2 ms are the following:

1. This sampling period corresponds to $\sim 0.5 \text{ s}$ in a real-scale scenario (see derived Scaling Laws in Appendix E).

1. acquisition of the most recent 50 raw samples per sensor
2. average of raw samples to get the current measurement per sensor
3. average the displacement measurements of the two vertically-placed LVDTs
4. estimation of the averaged block velocity applying the backward difference formula
5. filter averaged velocity measurements with a lowpass filter using a cutoff frequency of 0.2 Hz to reduce noise
6. use the designed digital controller to calculate the target force on the horizontal loadcell
7. use a PID controller for reaching the desired force in loadcell by adjusting the pressure in the rubber bag
8. send target pressure command to the electro-pneumatic pressure regulator to update the pressure in the rubber bag
9. store data to a file
10. repeat

The backward difference formula employed to estimate the velocity of the middle mobilized block (function No. 4) uses the two most recent displacement measurements acquired by the average behavior of the two vertically-placed LVDTs. However, this formula inherently introduces disturbances and errors (noise) to the estimated output. In order to overcome this issue, a lowpass filter is used with a cutoff frequency of 0.2 Hz (function No. 5). This frequency has been obtained through trial and error attempts so that the loss of information that the filter could cause is minimized. More sophisticated techniques are available in order to differentiate a discrete signal (Levant & Livne, 2020), but the above approach worked well in our case. More advanced controllers are also explored in Appendix F, where a robust filtering differentiator is employed.

The PID controller mentioned above (function No. 7) is implemented also in LabVIEW in order to adjust the pressure in the rubber bag in such a way that a desired target force is reached as measured by the loadcell. In this way, we are able to directly set the force on the horizontal loadcell (normal force to the sheared interfaces) and, therefore, the effective pressure on the sample interfaces. The above mentioned hybrid approach considering diffusion and poro-elasto-plastic effects would replace this PID controller with a more sophisticated one, but as mentioned this exceeds the objectives of this Thesis.

5.4 Specimen properties

The double-direct shear specimen is comprised of three blocks. The outer blocks are identical with dimensions $100 \times 100 \times 20 \text{ mm}^3$. The inner block has dimensions of $120 \times 100 \times 40 \text{ mm}^3$. The middle block is taller in order to maintain constant area of contact throughout the whole duration of the experiments (see also J. H. Dieterich, 1972). In addition, in order to reduce, even eliminate, phenomena due to parasitic bending and achieve homogeneous stress fields in the sheared interfaces, the width of each of the outer blocks is half the width of the middle block. This is in accordance with J. H. Dieterich (1981b), but it was also explored before the design of the machine through detailed Finite Element Analysis (Tzortzopoulos et al., 2019, see also Appendix D). Actually, the whole apparatus and experiment was modeled in the computer before construction. This phase was important for the successful design of the experimental setup.

In order to reduce parasitic friction between the steel guide/reaction steel plate and the outer blocks, Teflon sheets of thickness 1 mm are used (see Figure 5.1). Furthermore, a steel sheet of thickness 1.5 mm is glued at the bottom of each of the outer blocks to achieve a low-frictional Steel-Teflon contact interface (see Figure 5.1).

The blocks in this study are made of Sand-based 3D-Printed (S3DP) material (see Appendix B for more details). *3D-printing* gives the advantage of controlling several properties of the material such as the roughness, the exact geometry of the asperities, the maximum and minimum apparent friction coefficient, the exact evolution of friction with slip, and the characteristic slip-weakening distance, d_c^{sw} , of the frictional interfaces. Silica sand is employed for the powder component and Furfurylic alcohol for the binder. The mean grain size of the sand is $140 \text{ }\mu\text{m}$. The Young modulus of this material is $E \approx 3 \text{ GPa}$ (Braun et al., 2021). A Poisson's ratio of $\nu \approx 0.3$ is assumed (Perras & Vogler, 2019). Consequently, the shear modulus of the S3DP material is $G = E/2(1 + \nu) \approx 1.2 \text{ GPa}$. The printer settings and material characteristics are presented in Table 5.1 and more thoroughly in Braun et al. (2021) and in Appendix B. The sheared interfaces are flat.

The frictional properties of the S3DP interfaces were extensively studied in this Thesis (see Appendix B) using a direct shear apparatus and inclined tests. The frictional interface showed a combined slip-weakening and rate-and-state friction. For more details see Braun et al. (2021) and Appendix B. In order to assure that the triplet device functions well, identification tests were performed. The developed frictional response was compared with the more detailed tests described in Braun et al. (2021).

Table 5.1 – Printer settings applied for S3DP specimen fabrication.

Silica sand mean grain diameter	140 μm
Binder type	Furfurylic alcohol
Binder content	3.8 wt% of sand
Recoating speed	0.26 m/s
x resolution	20 μm
y resolution	101.6 μm
z resolution (layer thickness)	280 μm
Activator content (sulfonic acid)	0.2 wt% of sand
Infra-red curing lamp temperature	32 $^{\circ}\text{C}$

5.5 Frictional properties and nominal friction

Part of the identification tests mentioned in Section 5.4, are the characterization experiments for acquiring the frictional response of the sheared interfaces. For these experiments, the configuration shown in Figure 5.2 is used (see also Figure 5.1). The normal load is kept constant throughout the whole experiment at $F_n = 1000$ N. Vertical shear load is developed by setting constant displacement-rate at 0.5 mm/min to the servo-controlled ram. When the sheared interfaces reach their maximum shear strength, a slip-weakening frictional behavior is observed.

This behavior is depicted in Figure 5.3a for a test conducted before the control experiments. Notice that here we show only the post-peak displacement of the block. The coefficient of friction presented in this graph is not the apparent one but instead it's the global measured by the vertical and horizontal loadcells. This is calculated by taking the ratio between half the vertical force (two sheared interfaces in parallel) and the horizontal one, i.e. $\frac{F_s}{F_n}$. We can observe that the raw data show an oscillatory behavior. In order to identify the source of these oscillations, a closer look at a smaller window is needed. A zoomed image of the raw data is shown in the purple framed graph. The characteristic length of the oscillations is ~ 20 μm , which is 7 times smaller than the mean grain size. Therefore, we can safely conclude that the observed oscillations are a result of measurement noise and not due to dynamic instabilities related to the grain size.

In order to estimate the frictional characteristics from the raw data (grey curve), an exponential fitting is attempted (red continuous line). According to this, when the friction reaches its maximum value ($\mu_{\text{max}} = 0.609$), it reduces exponentially down to its residual value ($\mu_{\text{res}} = 0.502$) over a characteristic distance of $d_c^{\text{sw}} = 2.496$ mm (~ 18 grains). The

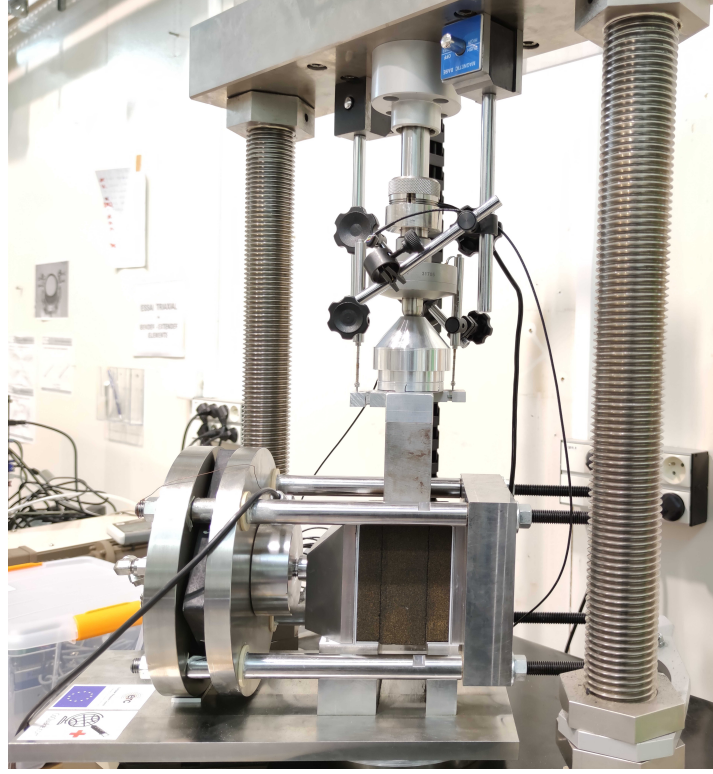


Figure 5.2 – Actual configuration of the characterization experiments.

slip-weakening friction law takes the form (see also Sections 1.1.1 and 1.2.1).

$$\mu(\delta) = \mu_{\text{res}} + \Delta\mu \cdot e^{-\delta/d_c^{\text{sw}}}, \quad (5.1)$$

where $\Delta\mu = \mu_{\text{max}} - \mu_{\text{res}} = 0.107$. The slight offset of the exponential fitting curve (red curve) to the lower part of the raw data is a result of the noise presented in the zoomed window. To validate this, we also present in Figure 5.3a the filtered data (black curve) using a low-pass filter with a cutoff frequency of 0.2 Hz.

Following the studies of Kanamori and Brodsky (2004), Scholz (2002), Stefanou (2019), and Tzortzopoulos, Braun, et al. (2021, among others), we can calculate the critical stiffness of each of the sheared interfaces using the exponential fitting presented in Figure 5.3a (see also Eq. 1.43):

$$k_c^{\text{sw}} = \frac{\Delta\mu \cdot F_n}{d_c^{\text{sw}}} = 42.9 \text{ N/mm}. \quad (5.2)$$

By comparing the critical stiffness of the interfaces, k_c^{sw} , considering slip-weakening effects with the stiffness of the vertical loading system, k_{machine} (see red dashed line in Figure 5.3a

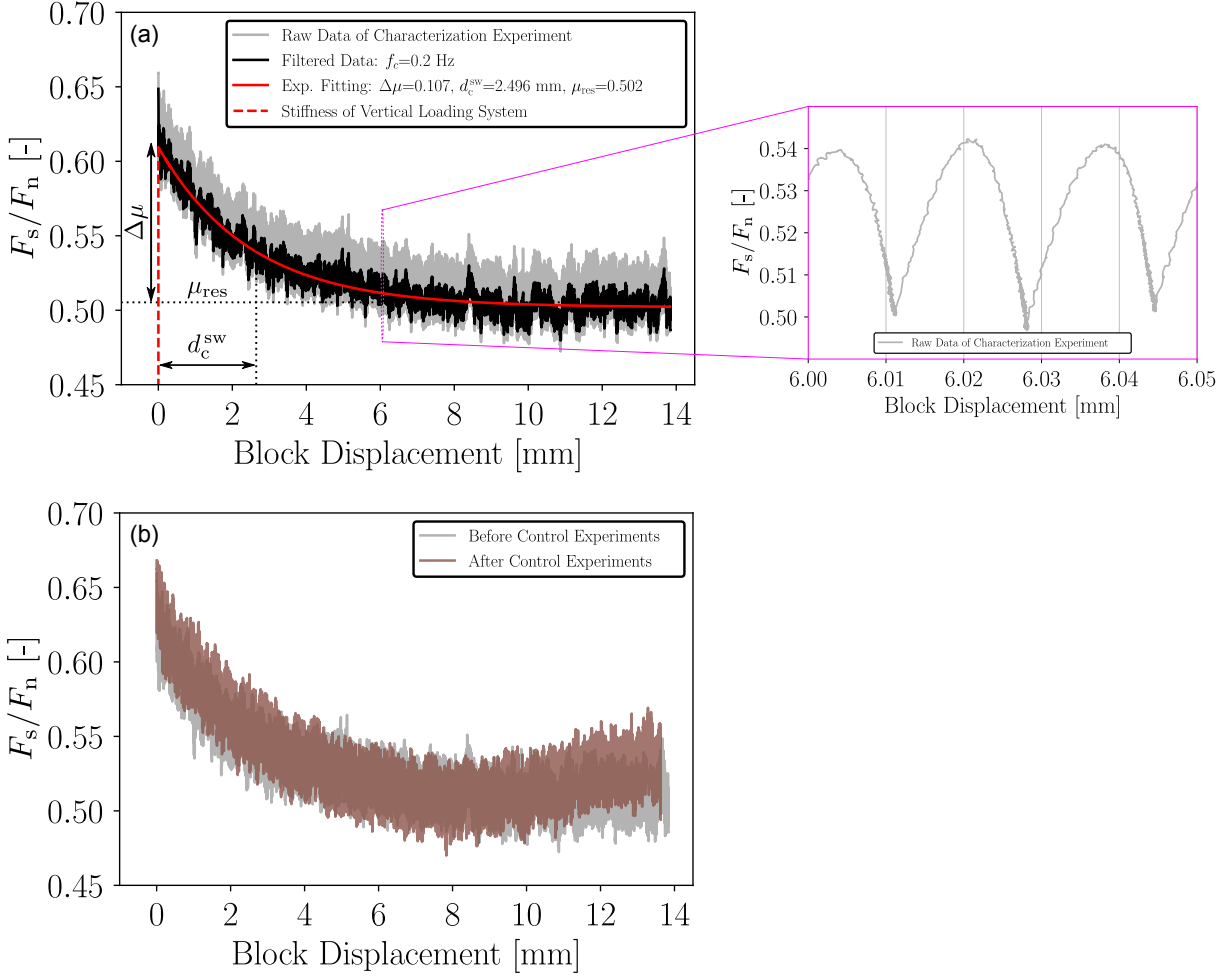


Figure 5.3 – Raw experimental data of the characterization experiments. (a) Slip-weakening frictional response of the characteristic test before the control experiments. Along with the raw data (grey curve), the filtered data (black curve) and the exponential fitting (red curve) are also presented. The red dashed line indicates the stiffness of the vertical loading system. The purple framed zoom window corresponds to a zoom in the noisy raw data. (b) Comparison between the raw slip-weakening frictional response before (grey curve) and after (brown curve) the control experiments.

and also Section 5.2), we validate that the former is at least one order of magnitude smaller than the latter ($k_c^{sw} = 42.9$ N/mm \ll $\frac{k_{machine}}{2} = 129$ kN/mm). Therefore, we are able to study the characteristic frictional response of the sheared interfaces with the existing experimental configuration (dynamic instabilities are excluded in this characterization tests).

We should mention here that the same specimen is used for all the experiments presented in this work. In this way, we can study the robustness of the proposed control

method in potential frictional variations (see Section 5.7). More specifically, from one experiment to another, several grains are detached, in form of wear, from the sheared interfaces (see Braun et al., 2021) which can alter the frictional characteristics of the specimen. After each test, this produced gouge is carefully removed and the specimen is properly placed again in the apparatus. The effect of this technique is depicted in Figure 5.3b, where the characteristic response of the material before and after the control experiments is presented.

More particularly, in Figure 5.3b, we illustrate the frictional response of the used specimen before and after the control experiments. We can observe minor differences between the two tests. These small discrepancies could help us test the efficiency of the designed control method under frictional disturbances/uncertainties. In any case, friction is one of the biggest unknowns in our problem (and in the field) and its exact determination is a very difficult and tedious task (if not impossible in the field). Therefore, intentional variations of friction will let us test the robustness of the controller obtained in Section 5.7.

Notice that more complicated physics (RSF, alignments, non-uniform vertical stress, heterogeneities, multiphysics, etc.) are not considered for the design of the controller, because they will be tackled through robustness, as well.

5.6 Reproducing earthquake-like instabilities

For the dynamic experiments, an elastic spring of stiffness $k_{\text{spring}} = 45.1 \text{ N/mm}$ is installed in series with the middle block (see Figure 5.4 and also M. Scuderi, Collettini, Viti, et al., 2017; Tzortzopoulos, Braun, et al., 2021). Notice that an internal steel rod is placed inside the spring in order to avoid buckling of the elastic spring during the experiments (see Figure 5.4a). The stiffness of the spring is such that the following instability condition is satisfied (see Scholz, 2002; Stefanou, 2019; Tzortzopoulos, Braun, et al., 2021, and also Section 1.2.1):

$$\frac{k_{\text{spring}}}{2} < k_c^{\text{sw}} \Rightarrow 22.55 \text{ N/mm} < 42.9 \text{ N/mm}. \quad (5.3)$$

As a result, earthquake-like instabilities are expected. The loading procedure followed is exactly the same as the one described for the characterization experiments in the previous Section. Only the loading displacement-rate differs, which has been set to 10 mm/min in the servo-controlled vertical ram. This faster rate allows the middle block to

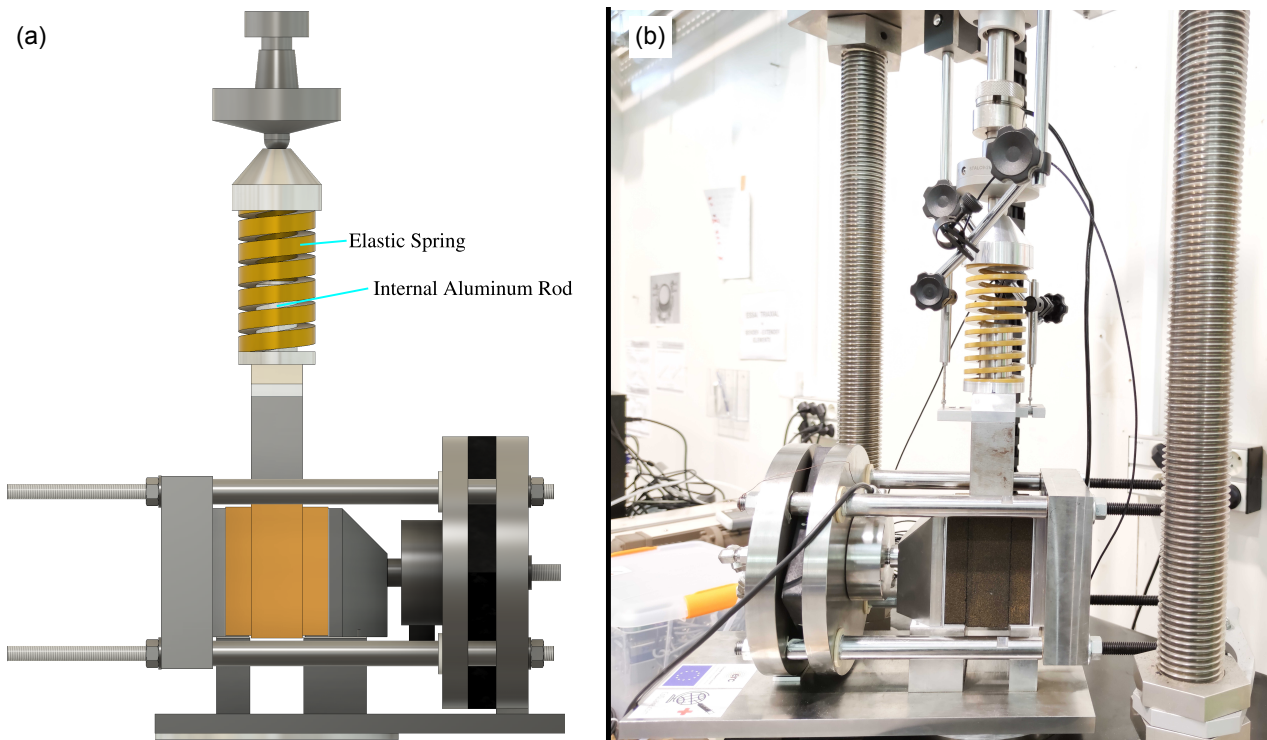


Figure 5.4 – (a) Configuration of the double-direct shear apparatus when an elastic spring is attached in series with the middle block. (b) Actual configuration of the dynamic experiments.

slide approximately with the same rate (in series connection with the spring) used for the characterization experiments, i.e. 0.5 mm/min (see Section 5.4).

In Figure 5.5a, the displacement (black line) and velocity (orange line) of the mobilized (middle) block is plotted with respect to time for three consecutive dynamic events. Focusing only on the first event, which is the most dominant, we can observe that during this “laboratory earthquake”, the block slides ~ 7 mm in ~ 50 ms developing a maximum velocity of ~ 0.35 m/s (see Figure 5.5b).

In Figure 5.5c, we show the frictional response of the system during the three dynamic events presented in Figure 5.5a. Notice that the raw data of both the characteristic (grey curve) and dynamic (black curve) experiments are plotted for comparison. Here, we show only the post-peak behavior of the specimen. The red dashed line corresponds to the spring response after nucleating the first event. It doesn’t match exactly to the slip-weakening response of the dynamic experiment due to inertia effects (large weight of the mobilized block: steel block + S3DP middle sample). The difference between the spring (red-dashed line) and the characteristic (grey curve) responses is the released to the environment

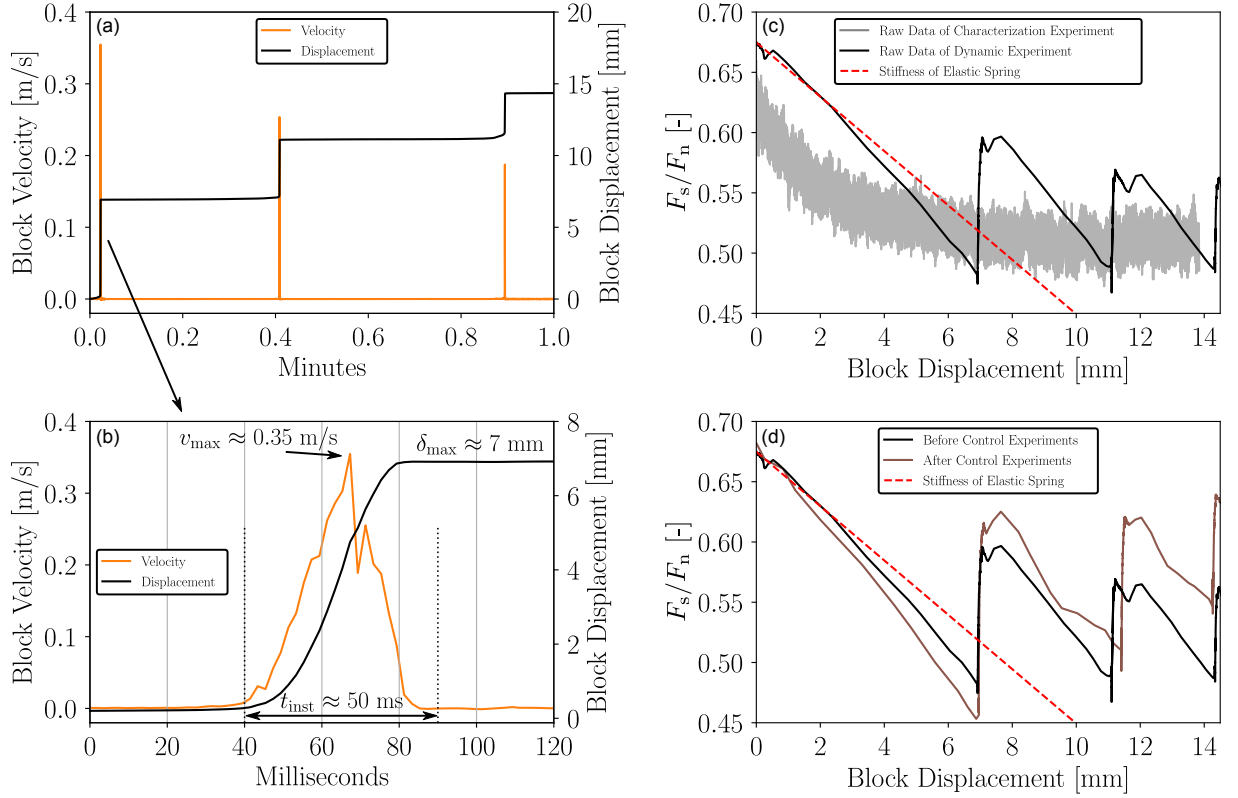


Figure 5.5 – Raw experimental data of the dynamic experiments. (a) Displacement (black line) and velocity (orange line) evolution of three dynamic events before the control tests. (b) Zoom in the first (dominant) dynamic event. (c) Frictional response of the dynamic test before the control experiments (black curve). The raw data of the respective characterization experiment is also plotted for comparison (grey curve). (d) Comparison between the raw dynamic response of the tested configuration before (black curve) and after (brown curve) the control experiments. The red dashed line in subplots (c) and (d) corresponds to the spring response.

elastic energy. The subsequent two events are a result of restrengthening of the frictional interface (healing) which can be expressed through rate-and-state equations (see Section 1.1.3). Their effect is considered as uncertainty in the design of the robust controller in Section 5.7.

Finally, in Figure 5.5d, we illustrate the frictional response of the dynamic experiments of the used specimen before and after the control experiments. Small differences can be observed between the two tests. These discrepancies along with the unmodeled dynamics (i.e. rate-and-state friction, transition from kinetic to static friction) show the robustness of the designed controller (see Section 5.7).

5.7 Design of a digital controller

Let the class of continuous-time nonlinear systems with matched uncertainties as it is introduced in Section 3.2 and particularly in Eq. (3.4) be represented by the following system of differential equations in matrix form:

$$x' = A_0x + \Delta B(t, x)u + B_0(u + h(t, x)), \quad (5.4)$$

where $h(t, x) = B_0^+(\Delta A(t, x)x + g(t, x))$ is a Lipschitz continuous function with $\|h(t, x)\| \leq \|Gx\|$, where $\|\cdot\|$ denotes the Euclidean norm (2-norm).

The structure of Eq. (5.4) resembles the form used in the *Lyapunov Redesign* method and other equivalent techniques dealing with matched uncertainties that exist in the literature (Khalil, 2013, 2015, see also Section 3.2). Alternatively, we can translate the above robust control problem into a linear optimal control problem for the nominal system by properly choosing a cost function which takes into account the aforementioned uncertainties and nonlinearities in $h(t, x)$ function (Lin, 2000; Lin et al., 1992; Lin & Olbrot, 1996). Consequently, the linear nominal system that we could study instead is:

$$x' = A_0x + B_0u. \quad (5.5)$$

For stabilizing the above system, we will find a full-state ($C_o = I_n$, where I_n is the identity matrix of size n) negative feedback control u such that the following cost function is minimized:

$$\int_0^\infty \left(\|R^{1/2}\|^2 x^T G^T G x + x^T Q_0 x + u^T R u \right) dt, \quad (5.6)$$

where $Q_0 \in \mathfrak{R}^{n \times n}$ and $R \in \mathfrak{R}^{p \times p}$ are positive-definite matrices to be determined during the design process according to performance requirements. The first term corresponds to the cost of uncertainties and nonlinearities contained in function $h(t, x)$, the second to the cost of regulations and the third to the cost of control. Let the minimum value of Eq. (5.6) to bring Eq. (5.5) from an initial state x_0 to the origin be:

$$V(x_0) = \min_u \int_0^\infty \left(\beta^2 \|R^{1/2}\|^2 x^T x + x^T Q_0 x + u^T R u \right) dt. \quad (5.7)$$

In this case, the Hamilton-Jacobi-Bellman (HJB) equation (Lewis et al., 2012) is:

$$\min_u \left(\|R^{1/2}\|^2 x^T G^T G x + x^T Q_0 x + u^T R u + V_x^T(x) (A_0x + B_0u) \right) = 0, \quad (5.8)$$

where $V_x(x) = \frac{\partial V(x)}{\partial x}$. If u^* is the solution to the optimal control problem defined above, Eq. (5.8) can be rewritten as:

$$\begin{cases} \left\| \|R^{1/2}\|^2 x^T G^T G x + x^T Q_0 x + u^{*T} R u^* + V_x^T(x) (A_0 x + B_0 u^*) \right. = 0, & (5.9a) \\ \left. 2u^{*T} R + V_x^T(x) B_0 \right. = 0. & (5.9b) \end{cases}$$

In Lin et al. (1992), the authors prove a Theorem stating that the above feedback control u^* of the linear optimal control problem (Eqs. (5.5) and (5.6)) can stabilize also the closed-loop robust control problem (Eq. (5.4)) making its origin globally Lyapunov exponentially stable. The proof follows the one provided in Section 3.2. The Lyapunov candidate of Eq. (5.4) as defined also in Eq. (5.7) is chosen as $V(x) = x^T \Theta x > 0 \forall x \neq 0$ ($V(0) = 0$), where $\Theta = \Theta^T \succ 0$. From Eq. (5.9b), the optimal full-state feedback control u^* is determined:

$$u^* = -Kx = -R^{-1}B_0^T \Theta x, \quad (5.10)$$

where the matrix $K = R^{-1}B_0^T \Theta$ contains the constant control gains and Θ is the unique positive definite solution of the CARE in Eq. (3.10).

5.7.1 Digitization of the cost function of continuous-time linear systems

In the previous paragraph, we showed that the continuous-time nonlinear robust control problem of Eq. (5.4) can be translated into a continuous-time linear optimal control problem by finding a full-state feedback control u^* given by Eq. (5.10) which minimizes the cost function in Eq. (5.6). This controller u^* should be implemented in a digital system. Comparing the block diagram of a continuous-time closed-loop system (Figure 3.2) with a sampled-data system (Figure 5.6), some additional components should be added, such as sampler of analog signals, analog to digital conversion (ADC), digital to analog conversion (DAC) and a hold filter. All these procedures introduce a delay of approximately half the sampling period and therefore should be taken into account in the design process of the controller (Åström & Wittenmark, 1997; Franklin et al., 1998).

More specifically, the digitization of a continuous-time controller is expected to be effective only if the sampling rate of the measurements is at least 30 times faster than the bandwidth of the closed-loop system (Åström & Wittenmark, 1997; Franklin et al.,

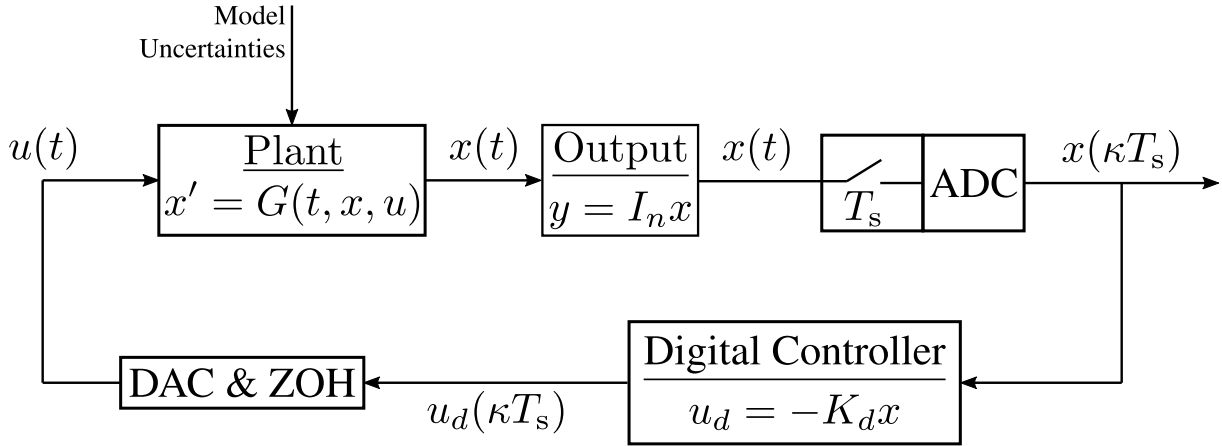


Figure 5.6 – Block diagram of a sampled-data system. The continuous plant and its cost function, which incorporates structured model uncertainties, are discretized using ZOH (Franklin et al., 1998). The design of the full-state negative feedback digital controller is based on the discretized plant.

1998). This case is investigated thoroughly in Appendix F, where three continuous-time controllers are being implemented in LabVIEW using the relatively fast sampling rate of 1000 Hz. We show that all of them managed to control the dynamics of the experimental configuration and drive the system to a new equilibrium point of lower energy.

For the purposes of this Chapter, though, we perform experiments with slower sampling rate (500 Hz), which is only 25 times faster than the characteristic frequency of the open-loop response (see Section 5.7.3). Slow sampling rate better represents the physical problem as the frequency of the measurements we can acquire in-situ might be sparse and delays might be present. Therefore, in this case, we have to discretize the plant and design a controller in the discrete domain.

Assuming Zero-Order-Hold (ZOH), which inherently considers the half sampling period delay explained above, we can discretize the nominal linear plant of Eq. (5.5) as follows:

$$\begin{cases} x(\kappa T_s + T_s) = \Phi_0 x(\kappa T_s) + \Gamma_0 u(\kappa T_s), & (5.11a) \\ y(\kappa T_s) = C_d x(\kappa T_s) + D_d u(\kappa T_s), & (5.11b) \end{cases}$$

where T_s is the sampling period and κ an integer. ZOH means that the input (here the pressure) remains constant in the sampling period. The nominal discretized matrices Φ_0 ,

Γ_0 , C_d and D_d take the form:

$$\begin{aligned} \Phi_0 &= e^{A_0 T_s} \quad , \quad \Gamma_0 = \left(\int_0^{T_s} e^{A_0 \tau} d\tau \right) B_0, \\ C_d &= C \quad , \quad D_d = 0. \end{aligned} \quad (5.12)$$

Following the emulation procedure described in Åström and Wittenmark (1997) and Franklin et al. (1998), we can discretize the corresponding continuous-time cost function in Eq. (5.6) as follows:

$$\sum_{\kappa=0}^{\infty} \left(\left\{ x^T(\kappa T_s) \quad u^T(\kappa T_s) \right\} \begin{bmatrix} Q_d & N_d \\ N_d^T & R_d \end{bmatrix} \begin{Bmatrix} x(\kappa T_s) \\ u(\kappa T_s) \end{Bmatrix} \right), \quad (5.13)$$

where

$$\begin{bmatrix} Q_d & N_d \\ N_d^T & R_d \end{bmatrix} = \int_0^{T_s} \left(\begin{bmatrix} \Phi_0^T(\tau) & 0 \\ \Gamma_0^T(\tau) & I \end{bmatrix} \begin{bmatrix} Q & 0 \\ 0 & R \end{bmatrix} \begin{bmatrix} \Phi_0(\tau) & \Gamma_0^T(\tau) \\ 0 & I \end{bmatrix} \right) d\tau. \quad (5.14)$$

A method to compute the discretized cost gains in Eq. (5.14) is proposed by Van Loan (1978). Therefore, in order to obtain the digitized full-state feedback controller u_d^* , a discrete optimal control problem should be considered defined by the plant in Eq. (5.11) and the discrete cost function in Eq. (5.13).

For solving the above problem, the following generalized Discrete Algebraic Riccati Equation (DARE) is employed:

$$\Phi_0^T \Theta_d \Phi_0 - \Theta_d - (\Phi_0^T \Theta_d \Gamma_0 + N_d) (\Gamma_0^T \Theta_d \Gamma_0 + R_d)^{-1} (\Gamma_0^T \Theta_d \Phi_0 + N_d^T) = -Q_d \quad (5.15)$$

obtaining the unique positive-definite solution Θ_d . Eventually, the digitized controller u_d^* has the form:

$$u_d^*(\kappa T_s) = -(\Gamma_0^T \Theta_d \Gamma_0 + R_d)^{-1} (\Gamma_0^T \Theta_d \Phi_0 + N_d^T) x(\kappa T_s) = -K_d x(\kappa T_s), \quad (5.16)$$

where the matrix $K_d = (\Gamma_0^T \Theta_d \Gamma_0 + R_d)^{-1} (\Gamma_0^T \Theta_d \Phi_0 + N_d^T)$ contains the constant control gains.

Notice that the resulted digitized controller does not guarantee the same levels of robustness as the ones obtained through the continuous design. Therefore, a thorough check of the robustness margins and the inter-sampling behavior of the continuous-time plant along with the discrete-time controller should be explored by numerical simulations

(Ackermann, 1985; Åström & Wittenmark, 1997; Franklin et al., 1998). This is done for the problem at hand in Section 5.7.3.

5.7.2 Integral control for tracking a reference input

The controller u_a^* , derived in Section 5.7.1, stabilizes the discrete system of Eq. (5.11) to the origin. Alternatively, if we want to drive the system in order to follow a predefined trajectory, we should design the controller for tracking a reference input. Notice that for perfect tracking, it is necessary to have as many control inputs as there are reference signals to track (Lewis et al., 2012). For the purposes of this study, we employ the integral control method as it is introduced in Section 3.2.2. Particularly, we augment the model of the discrete plant with a single integrator so as to obtain the integral error between the reference inputs and the corresponding measurements. Consequently, we design the discretized controller in such a way that this error converges to zero asymptotically.

According to Franklin et al. (1998), in order for a system to follow a reference input $r(\kappa T_s)$ in a robust way, the integral $\xi(\kappa T_s)$ of the error $e(\kappa T_s) = x_t(\kappa T_s) - r(\kappa T_s)$ should be captured by an integrator which has the following form:

$$\xi(\kappa T_s + T_s) = \xi(\kappa T_s) + C_t x(\kappa T_s) - r(\kappa T_s), \quad (5.17)$$

where C_t is given by the output equation of the reference system, namely $x_t(\kappa T_s) = C_t x(\kappa T_s)$ (Franklin et al., 1998). By augmenting the plant model (Eq. (5.11)) with Eq. (5.17), we get:

$$\underbrace{\begin{Bmatrix} x(\kappa T_s + T_s) \\ \xi(\kappa T_s + T_s) \end{Bmatrix}}_{x_a(\kappa T_s + T_s)} = \underbrace{\begin{bmatrix} \Phi_0 & 0 \\ C_t & 1 \end{bmatrix}}_{\Phi_a} \underbrace{\begin{Bmatrix} x(\kappa T_s) \\ \xi(\kappa T_s) \end{Bmatrix}}_{x_a(\kappa T_s)} + \underbrace{\begin{bmatrix} \Gamma_0 \\ 0 \end{bmatrix}}_{\Gamma_a} u(\kappa T_s) - \begin{bmatrix} 0 \\ 1 \end{bmatrix} r(\kappa T_s), \quad (5.18)$$

where the subscript a denotes the matrices and the vectors of the augmented system. Solving the corresponding DARE (Eq. (5.15)), we obtain the full-state feedback control gains K_a as described in Section 5.7.1. Therefore, the control law u_a^* will be the following:

$$u_a^*(\kappa T_s) = - \underbrace{\begin{bmatrix} K_d & K_\xi \end{bmatrix}}_{K_a} \underbrace{\begin{Bmatrix} x(\kappa T_s) \\ \xi(\kappa T_s) \end{Bmatrix}}_{x_a(\kappa T_s)} + K_d N_x r(\kappa T_s), \quad (5.19)$$

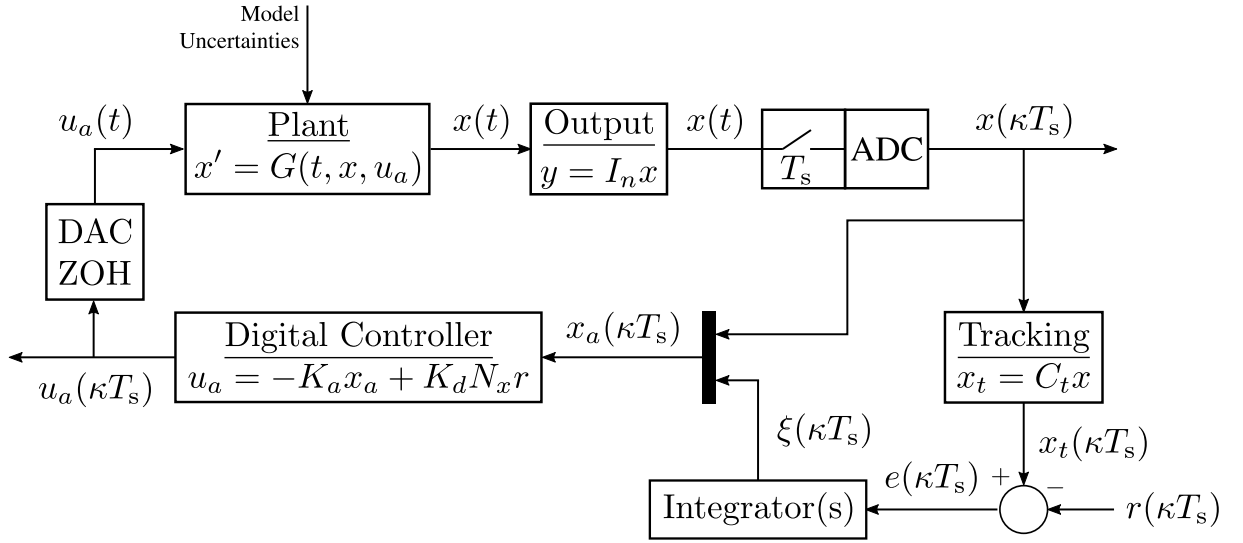


Figure 5.7 – Block diagram of a sampled-data system for tracking a reference input. The continuous plant and its cost function, which incorporates structured model uncertainties, are discretized using ZOH (Franklin et al., 1998). For the reference tracking, integral action is employed. The design of the full-state negative feedback digital controller is based on the augmented discretized plant.

where N_x can be retrieved using:

$$\begin{bmatrix} N_x \\ N_u \end{bmatrix} = \begin{bmatrix} \Phi_0 - I & \Gamma_0 \\ C_r & 0 \end{bmatrix}^{-1} \begin{bmatrix} 0 \\ I \end{bmatrix}. \quad (5.20)$$

N_u is a feedforward control term that we ignore in the current design procedure (see also Franklin et al., 1998). The block diagram which is associated with the tracking procedure described in this Section is illustrated in Figure 5.7.

5.7.3 Nominal system and uncertainties

The dynamics of the experimental configuration described in Section 5.2 can be simulated using the analogue spring-slider model (Kanamori & Brodsky, 2004; Scholz, 2002; Stefanou & Tzortzopoulos, 2021; Stefanou, 2019; Tzortzopoulos, Braun, et al., 2021; Tzortzopoulos et al., 2019, among others). This model is illustrated in Figure 1.1 and it was discussed

in detail in Chapter 1. The matrix form of Eqs. (1.38) is:

$$\underbrace{\begin{Bmatrix} \tilde{q}' \\ \tilde{d}' \end{Bmatrix}}_{x'} = \underbrace{\begin{bmatrix} -\hat{\eta} & -\hat{k} \\ 1 & 0 \end{bmatrix}}_{A(t)} \underbrace{\begin{Bmatrix} \tilde{q} \\ \tilde{d} \end{Bmatrix}}_x + \underbrace{\begin{bmatrix} \mu(\tilde{d} + d^*)\hat{N} \\ 0 \end{bmatrix}}_{B(t,x)} \underbrace{\{\tilde{p}\}}_u + \underbrace{\begin{bmatrix} -[\mu(\tilde{d} + d^*) - \mu(d^*)]\sigma'_n\hat{N} \\ 0 \end{bmatrix}}_{g(t,x)}. \quad (5.21)$$

The above form resembles Eq. (3.1). This nonlinear system has a single input ($p = 1$) which is the perturbed fluid pressure in the sheared interfaces and outputs the whole, deviated from the equilibrium point, state ($n = m = 2$) formed by the displacement and velocity of the middle block. Therefore, the procedure described in Section 5.7 can be followed in order to design a digital controller for tracking a reference input.

More specifically, for the design of the robust continuous-time controller (Section 3.2), the uncertainties of the $A(t)$ and $B(t, x)$ matrices should be taken into consideration. According to Eq. (3.2):

$$A(t) = \underbrace{\begin{bmatrix} -\hat{\eta}_0 & -\hat{k}_0 \\ 1 & 0 \end{bmatrix}}_{A_0} + \underbrace{\begin{bmatrix} -\Delta\hat{\eta} & -\Delta\hat{k} \\ 0 & 0 \end{bmatrix}}_{\Delta A(t)}, \quad (5.22)$$

$$B(t, x) = \underbrace{\begin{bmatrix} \mu_{\min}\hat{N} \\ 0 \end{bmatrix}}_{B_0} + \underbrace{\begin{bmatrix} \Delta\mu\hat{N} \\ 0 \end{bmatrix}}_{\Delta B(t,x)}, \quad (5.23)$$

where $\hat{\eta}_0$ and \hat{k}_0 are the nominal values of system's viscosity and elasticity, respectively. The nominal matrix B_0 should be designed with the minimum coefficient of friction which could appear during the experiment (including a safety factor if necessary). The contact area, A , and the mobilized mass, m , are supposed to be constant during the experiment and therefore \hat{N} isn't expected to vary significantly. The quantities with the prefix ' Δ ' correspond to the uncertainties of the respective variables. The pseudoinverse matrix of B_0 is:

$$B_0^+ = \begin{bmatrix} \frac{1}{\mu_{\min}\hat{N}} & 0 \end{bmatrix}. \quad (5.24)$$

Notice that, by definition, $B_0^+ B_0 = 1$. The nonlinear vector $h(t, x)$, defined in Eq. (5.4),

becomes:

$$h(t, x) = B_0^+ (\Delta A(t)x + g(t, x)) = -\frac{1}{\mu_{\min} \hat{N}} \left(\Delta \hat{\eta} \tilde{q} + \Delta \hat{k} \tilde{d} + [\mu(\tilde{d} + d^*) - \mu(d^*)] \sigma'_n \hat{N} \right). \quad (5.25)$$

We want $h(t, x)$ to be a Lipschitz continuous function with respect to the states. Indeed:

$$\begin{aligned} \|h(t, x)\| &= \left| -\frac{1}{\mu_{\min} \hat{N}} \left(\Delta \hat{\eta} \cdot \tilde{q} + \Delta \hat{k} \cdot \tilde{d} + [\mu(\tilde{d} + d^*) - \mu(d^*)] \sigma'_n \hat{N} \right) \right| \\ &= \left| \frac{1}{\mu_{\min} \hat{N}} \left[\Delta \hat{\eta} \quad \Delta \hat{k} + \frac{\mu(\tilde{d} + d^*) - \mu(d^*)}{\tilde{d}} \sigma'_n \hat{N} \right] \begin{bmatrix} \tilde{q} \\ \tilde{d} \end{bmatrix} \right| \\ &\leq \underbrace{\left| \frac{1}{\mu_{\min} \hat{N}} \left[\Delta \hat{\eta}_{\max} \quad \Delta \hat{k}_{\max} + \underbrace{\left| \frac{\partial \mu(\partial \tilde{d})}{\partial \tilde{d}} \right|_{\max}}_{\mu_d^{\max}} \sigma'_n \hat{N} \right] \begin{bmatrix} \tilde{q} \\ \tilde{d} \end{bmatrix} \right|}_G = |Gx|. \end{aligned} \quad (5.26)$$

The subscript ‘max’ denotes the maximum variation from the respective nominal values that could appear in the system in absolute terms. The bound μ_d^{\max} corresponds to the maximum absolute softening slope of the obeyed friction law. Notice that a safety factor can be added in all the bounds related to uncertainties in order to increase the robustness of the system with the trade-off of reducing its performance.

Table 5.2 summarizes the nominal values of the variables of interest along with their maximum tolerances for the experimental configuration chosen for this study (see Section 5.2) and the tested material characterized in Section 5.4. Column “Simulation” corresponds to the estimated experimental values for each respective variable. Columns “Nominal Value” and “Max. allowed Uncertainty” depict the values used for the design of the robust controller. Interestingly, for this controller, only the minimum friction and the maximum softening slope should be known from the frictional behavior of the sheared interfaces in order to design the robust continuous-time controller (see also Stefanou & Tzortzopoulos, 2021). Other controllers (see Appendix F) need even less information about friction, i.e. they need only its minimum value.

Notice that the friction law adopted for the simulations and the design of the controller is not the one depicted in Figure 5.3a fitting the experimental raw data (red line). Instead, due to observed noise, we choose the frictional parameters to represent the worst case scenario, i.e. $\mu_{\text{res}} = 0.48$, $\Delta\mu = 0.17$ and $d_c^{\text{sw}} = 2.5$ mm.

Table 5.2 – Experimental, nominal and maximum uncertainty values which are taken into account during the design of the robust continuous-time controller.

Variable	Symbol	Unit	Simulation	Nominal Value	Max. allowed Uncertainty
mobilized mass	m	g	2770	2770	0
total contact area	$2A$	m ²	0.02	0.02	0
initial effective normal stress	σ'_n	kPa	100	100	0
damping ratio	ζ	-	1	0.6	0.5
spring stiffness	k	N/mm	45.1	40.6	9.0
residual coefficient of friction	μ_{res}	-	0.48	0.38	≥ 0.38
absolute softening slope	$ \mu_d^{\text{max}} $	mm ⁻¹	0.07	0.70	≤ 0.70

The design matrices Q_0 and R , which need to be defined for solving the CARE in Eq. (3.10), are chosen as:

$$Q_0 = I_2, \quad (5.27)$$

$$R = 20. \quad (5.28)$$

Combining the values provided in Table 5.2, the nonlinear bound in Eq. (5.26) and the design matrices Q_0 and R , a robust continuous-time controller of the form $u = -Kx$ can be designed. However, as discussed in Section 5.7.1, the input of the system (equivalent to fluid pressure in the sheared interfaces) is updated through the LabVIEW software (digitization). Therefore, there is need of designing a discrete-time controller, $u_d = -K_d x$, for stabilizing the sampled-data system consisting of a continuous plant (experiment) and a digital controller. This is accomplished by discretizing the continuous plant and cost function using the ZOH filter as shown in Section 5.7.1. In this Chapter, the sampling period is $T_s = 2$ ms. We assume that this sampling rate remains constant throughout the control experiments.

In the case of tracking a reference input, an integrator should be taken into account monitoring the error $e(\kappa T_s) = x_t(\kappa T_s) - r(\kappa T_s)$. For the system of interest adopted in this study, $x_t(\kappa T_s) = \tilde{d}(\kappa T_s)$. Therefore, the output matrix of the reference system C_t and the design matrix N_x are equal to (see Section 5.7.2):

$$C_r = N_x^T = \begin{bmatrix} 0 & 1 \end{bmatrix}. \quad (5.29)$$

We choose the reference (tracking) trajectory to be a sigmoid function, r , as defined below

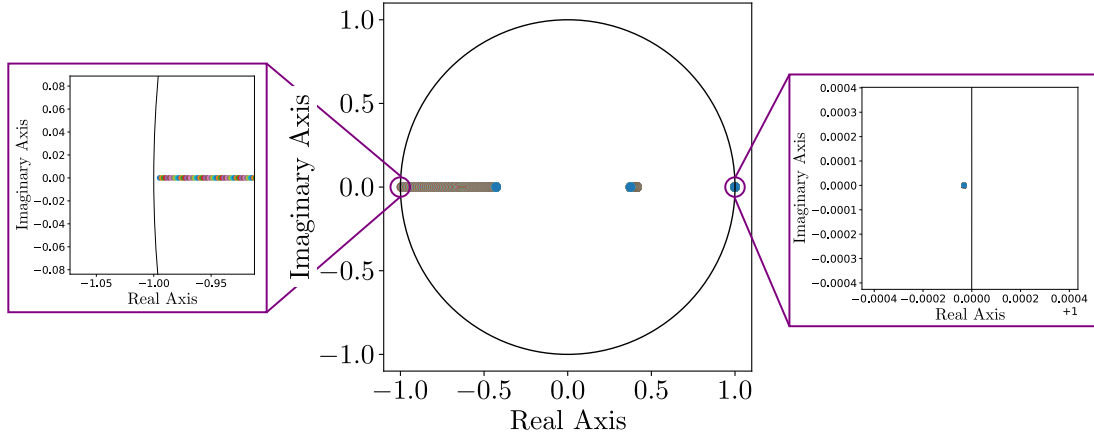


Figure 5.8 – Robustness of discrete-time closed-loop system. The zoom windows validate the presence of all the eigenvalues of the closed-loop system inside the unit circle.

(see also Chapter 4):

$$r(\kappa T_s) = d_{\max} s^3 (10 - 15s + 6s^2), \text{ with } s(\kappa T_s) = \frac{\kappa T_s}{t_{\text{oper}}}, \quad (5.30)$$

where t_{oper} is the operation time of the controller and d_{\max} the maximum displacement that we want to be reached after the completion of the control strategy. The maximum tracking velocity is then equal to $\dot{r}_{\max} = \dot{r}(0.5t_{\text{oper}}) \approx 2d_{\max}/t_{\text{oper}}$.

The robustness range of parameters uncertainties of the derived sampled-data system (continuous plant and discrete controller) are not necessarily the same as its respective robust continuous-time counterparts. When the sampling rate is at least 30 times faster than the characteristic time of the closed-loop system, the behavior of the sampled-data system converges to the continuous solution. However, in our case, due to the relatively slow sampling period ($T_s = 2$ ms) in comparison with the characteristic time of the instability ($t_{\text{inst}} \approx 50$ ms, i.e. $t_{\text{inst}}/T_s = 25$, see Section 5.6), the validation of robustness and the intersampling behavior of the sampled-data system through numerical simulations is necessary.

For this purpose, in Figure 5.8, the eigenvalues of the closed-loop discrete system are illustrated in form of colored dots. The viscosity and elasticity values used for the simulation are taken from Table 5.2. The friction evolves as shown by the fitting curve in Figure 5.3a. The unit circle represents the stability barrier of discrete-time systems. If at least one eigenvalue is placed outside the unit circle, the system is unstable, otherwise it is asymptotically stable. As we can observe, all the eigenvalues are situated inside the

unit circle resulting in an asymptotically stable closed-loop discrete system. Therefore, our discrete control design is ready to be implemented and tested under laboratory conditions.

Controlling earthquake-like instabilities in the laboratory

In this Chapter, two scenarios are investigated experimentally using discrete control design (slow sampling rate). In the first scenario, the system is loaded close to its instability point and then fluid is injected aiming at provoking a seismic event. In this case, we observe how the controller automatically adjusts the fluid pressure in order to prevent instabilities and immobilize the system. In the second scenario, the controller adjusts the fluid pressure automatically in order to drive the system in a new stable equilibrium of lower energy in an aseismic manner. Despite the inherent unstable behavior of the system and various uncertainties related to friction, elasticity, and multi-physical couplings, earthquake-like events are avoided and controlled. Under adequate scaling laws, these experimental results allows us to generate and then control an earthquake of magnitude $M_w \approx 6$.

6.1 Stabilization

The control experiments, in this Chapter, can be divided into two types: stabilization and tracking (see Chapter 3 and Section 5.7). For both, we follow the same experimental procedure as the one described in Section 5.6. When $\sim 90\%$ of the maximum shear strength has been reached, we stop loading and the controller is activated. As we have mentioned in Section 5.2, in our current experimental configuration, no actual fluid is used for the control experiments. Any pressure variations occur directly on the sheared interfaces by varying the pressure in the rubber bag.

In the stabilization experiments, when $\sim 90\%$ of the shear strength is reached a “virtual” perturbation is applied to the input pressure. This perturbation can be translated into a pressure decrease on the sheared interfaces with a constant rate of $r_p = 50$ Pa/s, namely:

$$p = u_a + r_p t. \tag{6.1}$$

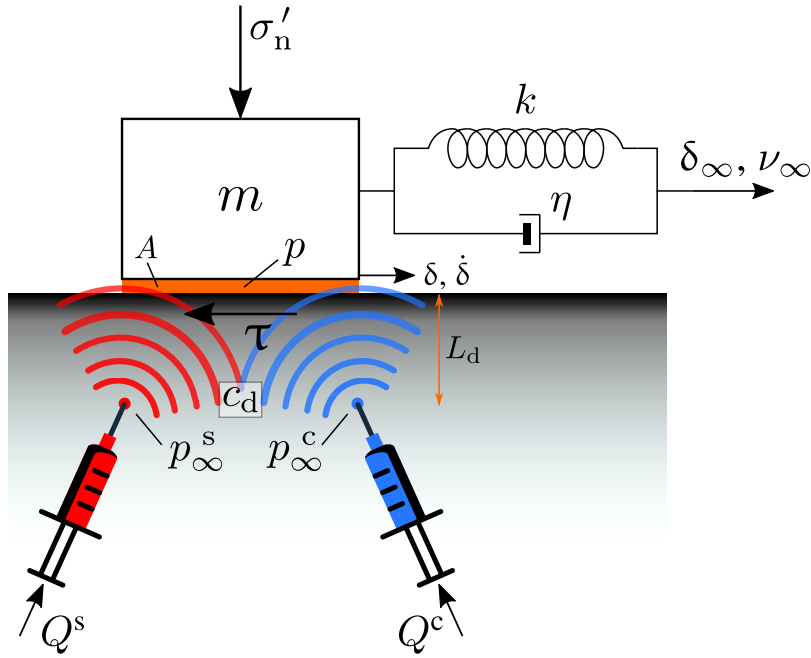


Figure 6.1 – Sketch of the spring-slider analogue system considering two distinct networks of sources far from the sheared interface. The static wells are denoted with the red color and the superscript s , while the control wells with the blue color and the superscript c .

In an idealized fault as the one discussed in Section 6.3 and Appendix E, this external perturbation represents a network of injection (static) wells which inject fluids, increase the pore-fluid pressure and this can reactivate the present fault and nucleate a large seismic event. In parallel with the static wells, though, we activate a network of “control wells” in order to secure the ongoing operation of the static wells and assure that the fault will remain immobile even if it’s reactivated by the static wells. This configuration is illustrated schematically in Figure 6.1 using a spring-slider representation. The static wells are denoted with the red color and the superscript s , while the control wells with the blue color and the superscript c . The sources are placed at a distance L_d from the fault. p_∞ corresponds to the fluid pressure at the point of the sources, while Q corresponds to the respective flux. Diffusion processes will be considered only at post-processing of the experimental data in Section 6.3 giving qualitative results for the real fault scale (see also Section 5.2 for hybrid tests).

The response of the stabilization experiment is illustrated in Figure 6.2. The pressure perturbation of constant rate is illustrated with the red linear curve in Figure 6.2a. In parallel, the controller has been activated setting zero displacement as the reference track-

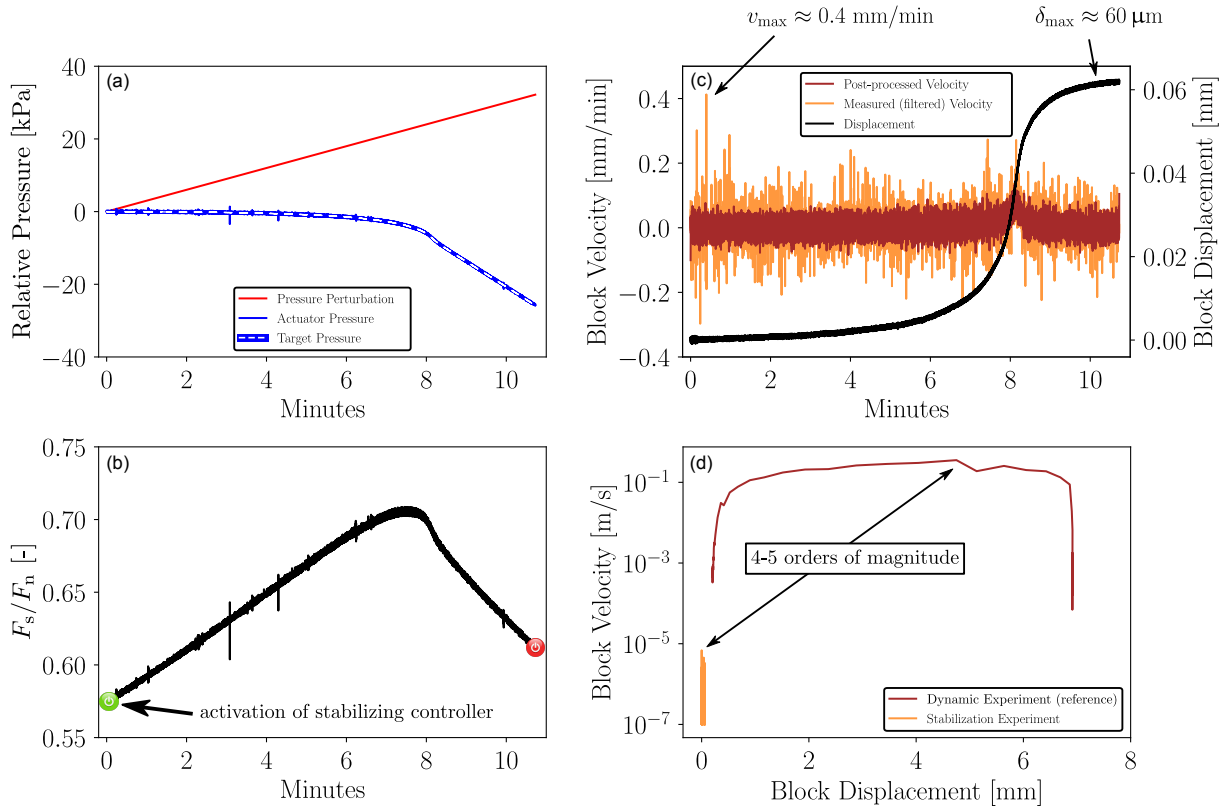


Figure 6.2 – Raw experimental data of the stabilization experiment by applying a “virtual” perturbation to the input pressure. (a) The pressure perturbation is depicted with the red linear curve. In parallel, the controller’s target and actuator pressure are illustrated with white-dashed and blue curves, respectively. (b) The frictional response of the system in terms of time is plotted. The activation and termination of the controller are indicated using the switch on and off icons. (c) Velocity (orange and brown curves) and displacement (black curve) evolution of the system. The orange velocity response corresponds to the measured velocity used as a state measurement for the controller, while the brown one corresponds to post-processed filtering of the measured displacement. (d) Block velocity in terms of block displacement for the instability (brown curve) and the stabilizing (orange curve) experiments. The vertical axis is in logarithmic space and velocities slower than 10^{-7} m/s have been truncated. The velocities developed during the stabilizing experiment are 4-5 orders of magnitude slower than the laboratory earthquake provoked in Figure 5.5b.

ing trajectory (see Section 5.7.2). The target and the measured pressure on the sheared interfaces are plotted with the white-dashed and blue curves, respectively. Both lines are indistinguishable from one another, as it should. In addition, the frictional response of the sample in terms of time (black curve) is shown in Figure 6.2b. We can observe that

by “virtually” increasing the pressure, the mobilized coefficient of friction increases until reaching a peak (equilibrium point). After that peak, the sheared interfaces are considered to be reactivated and the controller tends to stabilize the system to this equilibrium point by decreasing the pore pressure (equivalent to fluid extraction from the control well in Figure 6.1). It is worth emphasizing that the controller is agnostic to all these data. The only available measurements are the vertical displacement and velocity of the block with a frequency of 500 Hz. This frequency is also quite high given that the characteristic frequency of the instability is approximately 20 Hz.

The response of the system is depicted in Figure 6.2c, where the velocity (orange and brown curves) and displacement (black curve) evolution of the sheared interfaces is plotted. We can observe that the system slips approximately only half a grain before it is stabilized by the designed controller. The developed velocity due to this step was measured in real-time using the filter described in Section 5.3. This velocity is 4-5 orders of magnitude smaller than the maximum dynamic event observed in Figure 5.5b and therefore the resulted slip can be considered as a “stable-slow event” (see also Figure 6.2d).

For better visualization of the velocity at post-processing, we apply a third order Savitzky-Golay filter (brown curve in Figure 6.2c) estimating the derivative of the measured displacement response (black curve in Figure 6.2c). We can observe that the velocity measurements used as feedback for the controller (orange curve in Figure 6.2c) are very noisy/disturbed and can be misleading to the overall response of the system that the controller monitors. This is a proof of robustness and effectiveness of the designed controller, which even under high disturbances due to noisy measurements and input perturbations, it succeeds in stabilizing the system to the desired equilibrium point.

Finally, in Figure 6.3, the same plots as in Figure 6.2a,c are presented showing the repeatability of the stabilization experiments. It is clear that the response of the system is approximately the same. Any deviations are due to the use of the same specimen for both experiments and also due to numerous unmodeled uncertainties.

In Chapter 2 and specifically in Figure 2.6c, we showed that when a conventional earthquake mitigation strategy commences after 80% of the shear strength of the fault, this leads instantly to an abrupt earthquake event. However, the experiments presented in this Section depicted that the immobilization of the sheared block subjected to a “virtual” perturbation is possible even when the stabilizing controller is activated at around 90% of the shear strength of the interfaces.

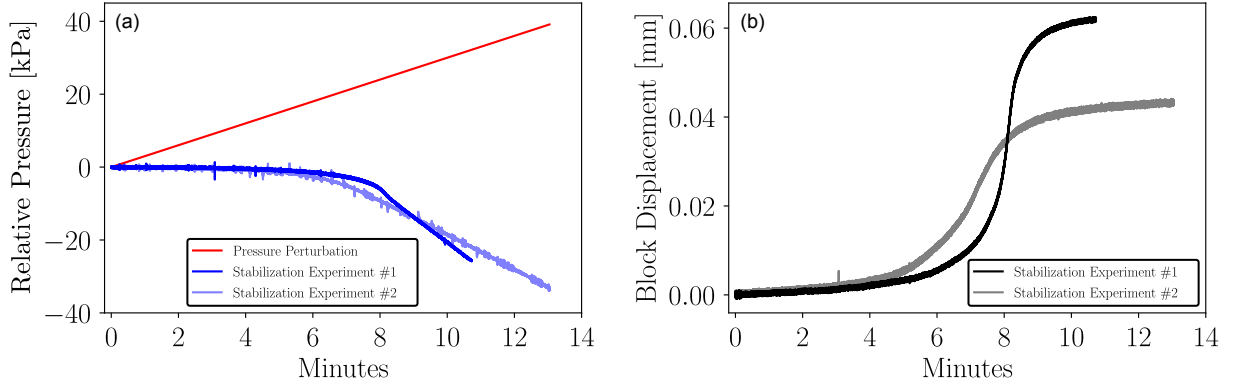


Figure 6.3 – Same plots as in Figure 6.2a,c. The repeatability of the stabilization experiments is presented.

6.2 Inducing controlled, slow slip - Tracking

In the tracking experiments, only the control well is used (see Figure 6.1). The reference tracking trajectory corresponds to an S-curve as defined in Eq. (5.30). Consequently, by applying the designed controller, the middle block will have to slide 7.5 mm in a time window of 1 hour. The slip of 7.5 mm is the maximum displacement of the block in the dynamic experiments considering a safety factor of ~ 1.1 (see Figures 5.5a-c).

In an idealized real fault scenario (see Section 6.3 and Appendix E), the objective of the tracking controller would be to drive the system to a desired new equilibrium point of lower energy aseismically as discussed in Chapter 4.

The response of the tracking experiment is illustrated in Figure 6.4. The displacement (black curve) and velocity (orange curve) evolution during this experiment are plotted in Figure 6.4a. As a reference, the target displacement (grey dashed line) and target velocity (brown dashed line) are also included. The response of the system follows almost exactly the reference trajectory resulting in a stable behavior with a slow developed velocity (4 orders of magnitude smaller than the instability event, see also Figure 6.4b). All the observed spikes in the velocity curve are due to the step-like response of the specimen. This behavior can be attributed to interlocking phenomena that take place between the grains in the sheared-interfaces.

In Figure 6.4c, the target (white curve) and measured (blue curve) pressure variations are presented. We can observe that any deviation from the calculated pressure is a result of measurement noise. Notice that because the activation of the tracking controller occurs at the elastic regime of the interface ($\sim 90\%$ of the shear strength), the pressure has to

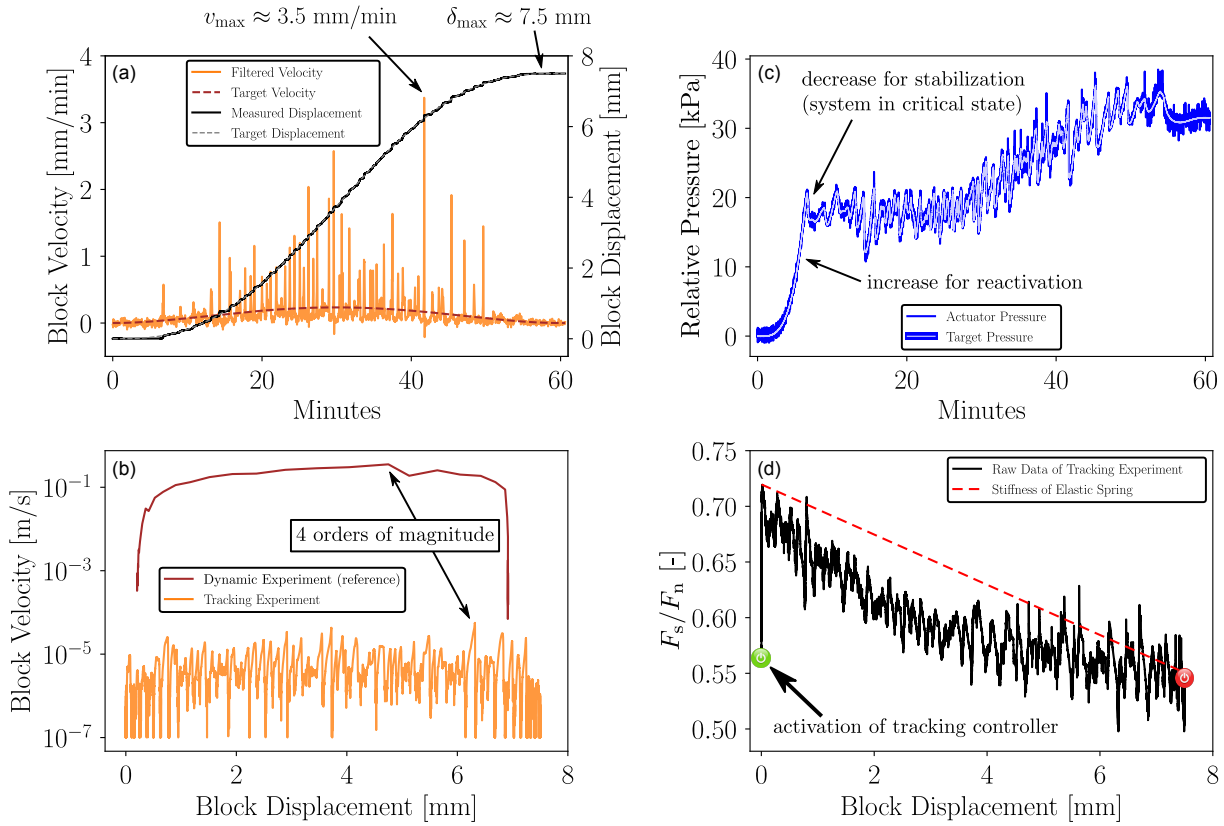


Figure 6.4 – Raw experimental data of the tracking experiment using as a reference trajectory an S-curve. (a) The reference (grey dashed line) and the measured displacement of the block (black curve) are plotted along with the filtered velocity evolution (orange curve) and the target velocity (brown dashed line). (b) Block velocity in terms of block displacement for the instability (brown curve) and the tracking (orange curve) experiments. The vertical axis is in logarithmic space and velocities slower than 10^{-7} m/s have been truncated. The tracking experiment is 4 orders of magnitude slower than the laboratory earthquake provoked in Figure 5.5b. (c) The resulting measured (blue curve) and target (white curve) pressure evolution is illustrated. (d) Coefficient of friction as a function of block’s displacement (black curve). The controller is activated when the system is loaded up to the green dot. For reference, the stiffness of the elastic spring (red dashed line) is also presented.

increase in the beginning in order to reactivate the interfaces (equivalent to fluid injection) and let the block slide. This response can be also observed in Figure 6.4d, where the mobilized coefficient of friction in terms of block’s displacement (black curve) is plotted. As a reference, the spring response (red-dashed line) is included, as well.

In Figure 6.5, the same plots as in Figure 6.4a,c are presented showing the repeatability of the tracking experiments. It is clear, that the response of the system is approximately

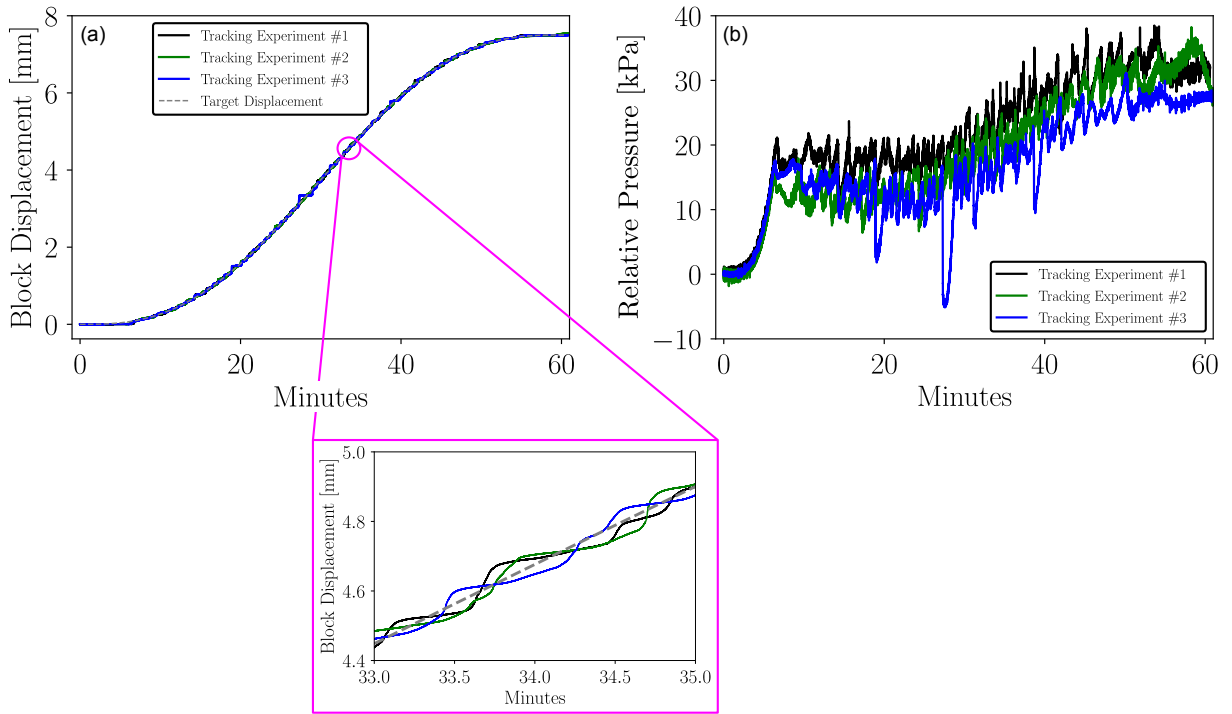


Figure 6.5 – Same plots as in Figure 6.4a,c. The repeatability of the tracking experiments is presented.

the same. Any deviations are due to the use of the same specimen for all three experiments and also due to numerous unmodeled uncertainties.

Finally, the tracking experiments showed that it's possible to steadily drive the experimental configuration to a new equilibrium point of lower energy. By developing velocities which are 4 orders of magnitude smaller than the respective dynamic event (see Section 5.6), we managed to prevent a laboratory earthquake by slowly relaxing its stored elastic energy.

6.3 Upscaling to a real fault scenario

Consider an idealized fault with a length of $L_{ac} = 5$ km as the one depicted in Figure 6.6. The density of the surrounding rocks is $\rho = 2500$ kg/m³, while the shear modulus is $G = 30$ GPa. The applied effective normal stress to the fault interface is $\sigma'_n = 50$ MPa. Finally, the friction coefficient has the same characteristic evolution as described in Section 5.2 and illustrated in Figures 5.3a and 5.5c satisfying constitutive similarity (see Appendix E). For these parameters, the corresponding characteristic slip-weakening

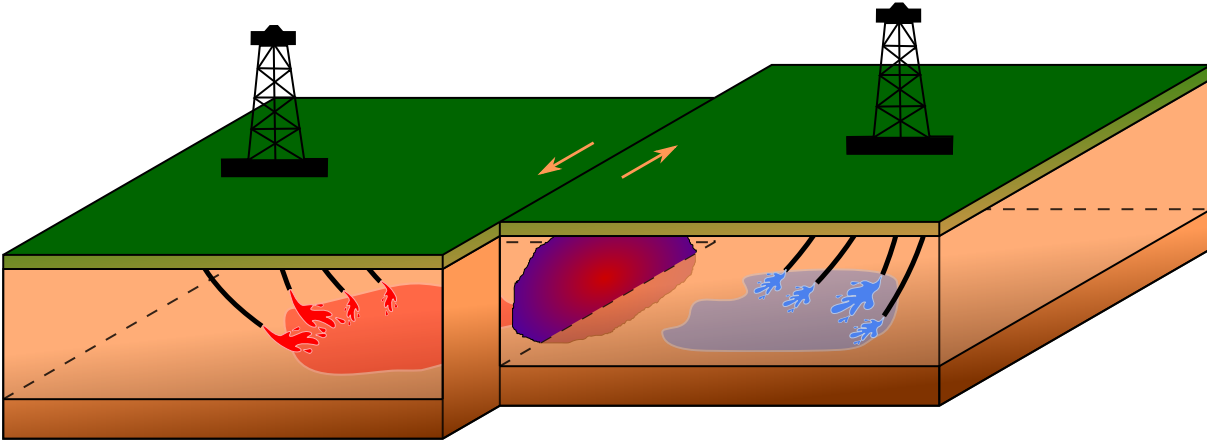


Figure 6.6 – Sketch of a 3D representation of a strike-slip fault.

distance is $d_c^{\text{sw}} = 50$ mm and the shear stress drop is $\Delta\tau = 5$ MPa. This isolated fault is an upscaling example of the experimental configuration presented in this Chapter obeying the scaling laws presented in Appendix E.

The dynamic behavior of the aforementioned fault is depicted in Figure 6.7. We can observe that the maximum developed slip-rate is ~ 0.35 m/s and the duration of the dominant first dynamic event is approximately 9 s, when upscaled. The resulting earthquake magnitude of the event presented in Figure 6.7b is $M_w = 5.8$ (see Chapter 1 and Appendix E).

Therefore, the objective of the control design developed in Section 5.7 is to prevent this relatively large earthquake and assure the stability of the fault system. For that, in a distance L_d from the fault level (see Figure 6.1), two networks of wells have been installed. The first one is comprised of static injection wells (represented by red fluid) which can be considered as external perturbations and the second one of control wells (represented by blue fluid) which can inject and/or extract fluid in/from the fault interface (see Figure 6.6). Therefore, diffusion processes must be taken into account in order to post-process the effect of fluid injection through the wells on pressure variations in the fault interface.

Neglecting any poroelastic effects, the single degree of freedom diffusion equation, we study herein, has the following form (Segall & Rice, 1995):

$$\dot{p} = c_d \cdot (p_\infty - p), \quad (6.2)$$

where $c_d = c_{\text{hy}}/L_d^2$ is the diffusivity, c_{hy} the hydraulic diffusivity and L_d a characteristic diffusion length which here corresponds to the distance of the well from the fault. p_∞

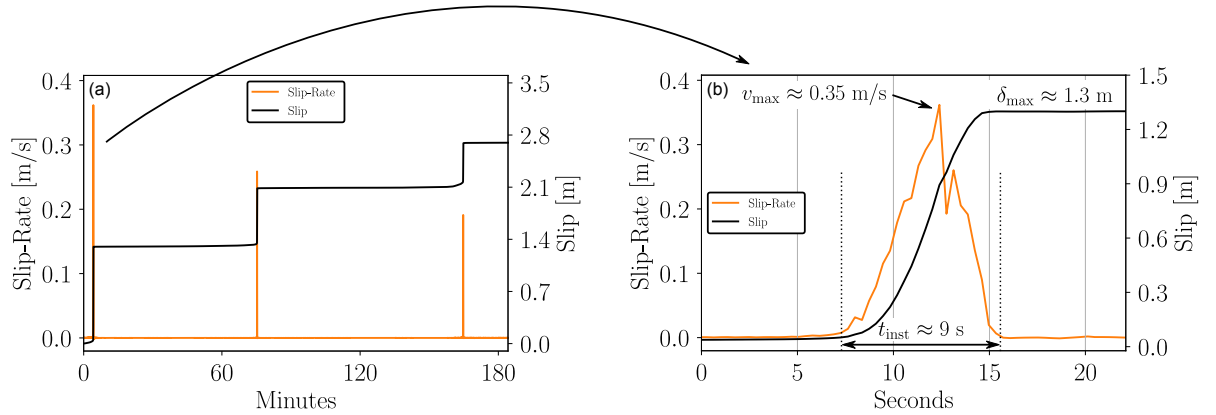


Figure 6.7 – Dynamic response of the upscaled isolated strike-slip fault. (a) Slip and slip-rate evolution for three consequent dynamic events. (b) Zoom in the first (dominant) event in order to quantify the dynamic response of the system. The slip and slip-rate correspond to the respective average values over the whole fault area.

represents the pore pressure at the point source. This pressure is connected with the corresponding flux, Q , as follows:

$$Q = c_d \beta^* V_w p_\infty \quad (6.3)$$

where V_w is the representative volume of influence of the well and β^* the compressibility of the mixture (see also Figure 6.1). For the purposes of this case study, we assume that all the wells inject and extract water in the earth's crust leading to a hydraulic diffusivity of $c_{\text{hy}} = 5 \text{ m}^2/\text{s}$ (permeability, $k_{\text{per}} = 10^{-13} \text{ m}^2$) and a compressibility of $\beta^* = 10^{-4} \text{ MPa}^{-1}$ (Rattez et al., 2018b).

In this example, a third order Savitzky-Golay filter is employed in order to differentiate *a posteriori* the upscaled pressure and displacement signals acquired from the experiments. The applied filter window is adequately large in order to remove as much measurement noise as possible.

6.3.1 Earthquake prevention by stabilization

Let the static network of wells (see red-colored well in Figures 6.1 and 6.6) start a geothermal operation by injecting water with a constant rate of $r_p = 25 \text{ kPa/s}$ (see also Eq. (6.1)). This network consists of 49 boreholes. Undoubtedly, as we have discussed throughout this Thesis, such intervention in the earth's crust could result in the earthquake presented in Figure 6.7b of magnitude $M_w = 5.8$. In order to secure the ongoing operation, the

control network (see blue-colored wells in Figures 6.1 and 6.6) which is also comprised of 49 boreholes is installed and the controller described in Section 5.7 is implemented.

Each borehole is responsible to actuate on $1/49$ of the fault area, i.e. an area of 700×700 m² each one. In addition, each network is placed at a distance of $L_d \approx 700$ m away from the fault interface. Therefore, the volume of influence of each borehole can be considered as $V_w = 700^3$ m³. The distance L_d is sufficient in order to assure a quasi-uniform pore pressure front at the fault level. The objective of the stabilization control strategy is to stabilize the system at its nucleation point preventing the earthquake event.

The response of the stabilization strategy can be observed in Figure 6.8. In the top left plot, we can see the linearly increasing perturbation added to the fault system through each static injection wells. This external perturbation is compensated by the network of control wells. The pore pressure evolution of each control well at the borehole level during the total operation of ~ 32 hours is illustrated in Figure 6.8b. Up to ~ 15 hours, where the fault is still stable, the performance of the control network is minimal. However, when the fault slip starts accelerating, the controller reacts instantly and in a time period of approximately 10 hours, it manages to stabilize the fault system at its nucleation point. Only a slip of ~ 13 mm is observed (Figure 6.8c), which can be considered as negligible. During this slip a maximum slip-rate of ~ 0.08 mm/min is developed which is 5 orders of magnitude slower (Figure 6.8d) than the earthquake event of Figure 6.7b.

Even if in this scenario an exaggerated perturbation is used, the stabilizing controller was able to compensate it along with other unmodeled dynamics. Therefore, the earthquake of magnitude $M_w = 5.8$ is prevented, while the static injection wells securely operate. However, if the controller is turned-off, the expected earthquake event will occur, as without the controller, the system is on the verge of unstable dynamic slip.

6.3.2 Earthquake prevention by energy relaxation

In Section 6.3.1, a controller is used in order to prevent an earthquake while an in-situ industrial operation was taking place. The previously followed stabilization strategy stabilizes the system at its initially unstable equilibrium point. Even in the presence of high perturbations, the mitigation strategy was successful. This wasn't the case, though, in the example provided in Chapter 2. There, any mitigation attempt started above $\sim 80\%$ of the frictional strength of the fault provoked a large seismic event comparable to the natural earthquake (see Section 2.4).

The next challenge of our control design is to dissipate the stored elastic energy

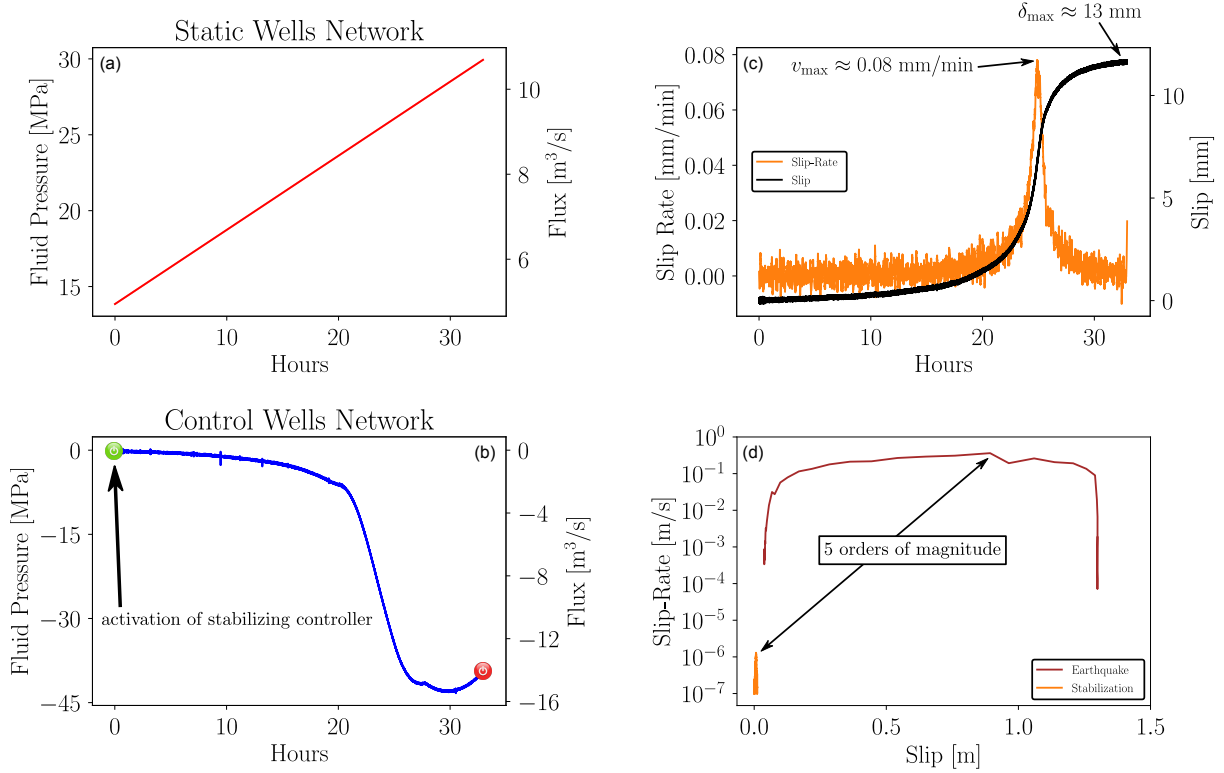


Figure 6.8 – Response of the upscaled isolated strike-slip fault during the stabilization control strategy. Pore pressure and flux in terms of time for each (a) static and (b) control wells network. (c) Slip (black curve) and slip-rate (orange curve) evolution. (d) Slip-rate in terms of slip for the earthquake (brown curve) and the stabilization (orange curve) scenario.

smoothly into the environment by unloading the system upto its new equilibrium point. For that, a reference slip trajectory is provided to the controller. This trajectory has an S-shape allowing a maximum slip of 1.3 m in approximately 8 days. No static injection wells (external perturbation) are used in this case study.

In Figure 6.9, the response of the tracking strategy is presented. The slip and slip-rate follow perfectly the reference trajectories (see Figure 6.9a) resulting in a process where the maximum developed slip-rate is 5 orders of magnitude slower than the potential earthquake (see Figure 6.9b). In addition, the pressure and flux evolution of each control well can be observed in Figure 6.9c. Initially, the pore pressure in the control wells network’s level is increased in order to reactivate the fault and enable it to slide. After this point, the pressure is adjusted in such a way to assure stability of the fault system. At this point, the controller can be safely deactivated without the risk of seismic event.

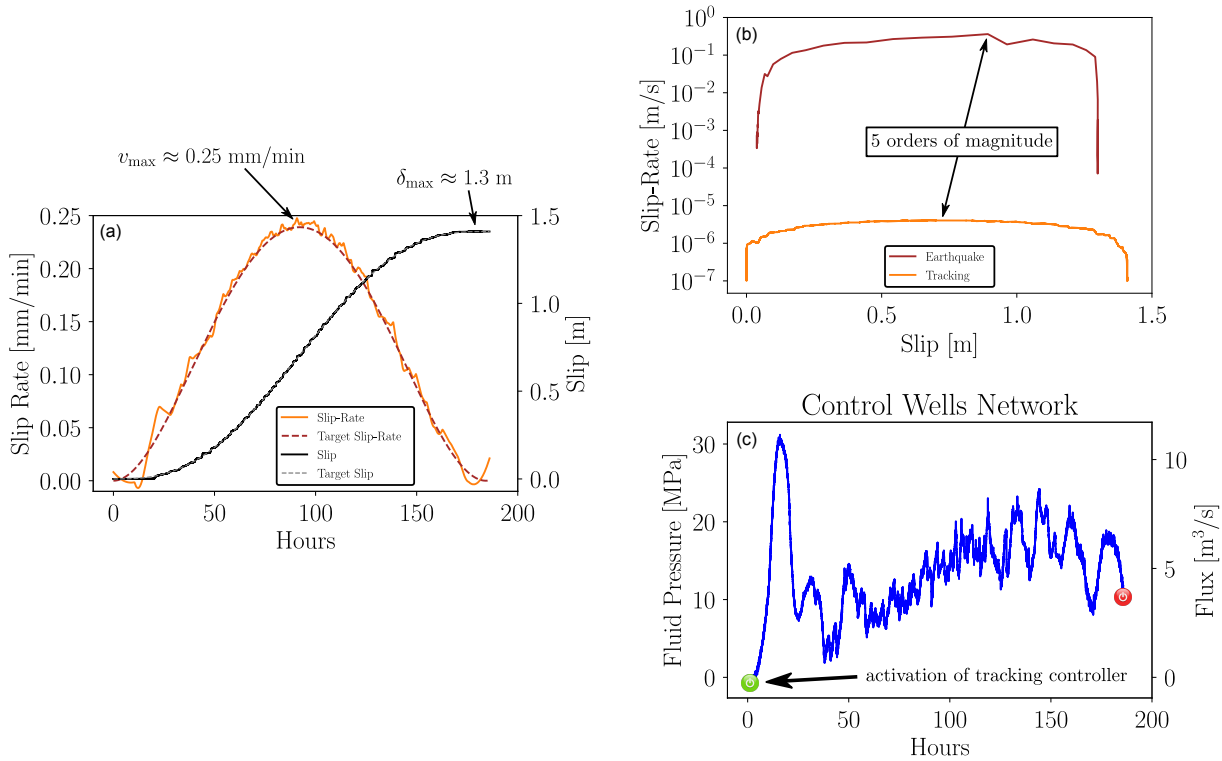


Figure 6.9 – Response of the upscaled isolated strike-slip fault during the tracking control strategy. (a) Slip (black curve) and slip-rate (orange curve) evolution. The target slip (grey dashed curve) and slip-rate (brown dashed curve) curves are also plotted for comparison. (b) Slip-rate in terms of slip for the earthquake (brown curve) and the tracking (orange curve) scenario. (c) Pore pressure and flux in terms of time for each control well.

6.4 Limitations and perspectives

A direct implication of this Chapter is inevitably related to earthquakes and induced/triggered seismicity. An interesting point of this mathematical framework is the possibility of deriving rigorous proofs about the controllability of the salient unstable dynamics of earthquake faults.

Moreover, control is possible without knowing the exact properties of the system and its physics. For instance, the detailed knowledge of faults' frictional parameters, which is practically impossible to acquire in practice, is not a *sine qua non* condition. Notice that friction is a major unknown (Erickson et al., 2011) in earthquake science. However, our control approach needed minimal and not precise information about the frictional characteristics of the fault system, which can be acquired in practice. Based on this limited information, we showed how the system can be driven to a new state of lower energy in

a totally controlled and aseismic way. Moreover, our approach guaranteed aseismic, slow-slip and smooth energy relaxation and did not require the knowledge of the exact current stress state and tectonic setting. Finally, the system was controlled independently of being far or close to its critical points, i.e. to an earthquake event.

Without any doubt, claiming that controlling anthropogenic or natural seismicity is possible, based on the experiments presented herein, is a speculation and further research is needed. Several theoretical and techno-economical investigations have to be pursued further in order to show into what extent man-made or natural earthquakes can be prevented (or the opposite). For example, some direct limitations of the proposed theory have to do with the actual technological means for fluid injections in the earth's crust (e.g. number of wells, pressure limits of pumps, response time). In this case special analyses have to be performed to adjust the operation time and incorporate the limitations of the pumping system in the design of the controller.

The sampling-rate of the observations is also an important factor. Here, we presented examples of discrete-time control. But there might be even slower data acquisition systems and therefore more elaborated techniques will be needed. A possibility for tackling the discrete-time is *Artificial Intelligence* (AI) techniques. A first attempt towards this direction is presented in Papachristos and Stefanou (2021). Moreover, measurements of the states of the system are never free of errors. These errors can be considered as disturbances (Khalil, 2015) and tackled with other controllers that are more resilient and robust. Indeed, in Appendix F, a comparison of several non-linear, robust to disturbances controllers is made on the base of numerical simulations and of our experimental setup simulating fault instabilities.

Finally, this control design has to be tested in a larger scale. For that, a meter-scale direct shear apparatus is about to be constructed. This new machine will allow to study in more details rupture propagation phenomena and their arrest/control along the sheared interface using the theories presented in this work.

Conclusions and future work

Concluding remarks

The main objectives of this Thesis were to:

1. Design and perform experiments in the laboratory, capturing the main dynamics of the earthquake instability and the effect of fluid injections using analogue materials such as Paper Towel and Sand-based 3D-Printed (S3DP) materials;
2. Design, assemble and calibrate a novel double-direct shear apparatus of decimetric scale;
3. Develop a mathematical framework based on *Control Theory* for earthquake prevention using fluid injections and/or extractions incorporating diffusion phenomena and sparse measurements in space;
4. Perform laboratory experiments to explore the possibility of earthquake control.

This Thesis is comprised of 6 Chapters. The main developments and findings are summarized below:

Chapter 1

The first Chapter of this Thesis focuses on presenting the qualitative behavior of isolated earthquake dynamic events. To this end, a reduced-order model was employed coupled with either slip-weakening or rate-and-state friction law. Linear Stability Analysis (LSA) was performed in both cases re-deriving the instability condition for the slip-weakening case (see Section 1.2.1), but also extending the current bound of the rate-and-state friction accounting also for viscous forces (see Section 1.2.2). A qualitative comparison between slip-weakening and rate-and-state friction law coupled with the spring-slider model showed that if we focus on an isolated dynamic event, the response of the reduced-order model, for either friction law, is similar in terms of the overall dynamic response and energy (see Section 1.2.3 and Figures 1.2 and 1.3). Moreover, the effect of fluid pressure on friction was illustrated setting the basis for the next Chapters.

Chapter 2

In this Chapter, paper towel was used as a surrogate rock-like material for building understanding regarding possible mitigation strategies of the earthquake phenomenon. These strategies were inspired by current techniques used in industry such as the Traffic Light Systems. A detailed characterization of the paper towel material can be found in Appendix A. Besides the in-situ stress level, our experiments uncovered two additional factors which govern the magnitude of induced events. These factors are the segment-activation rate (injection rate and diffusivity) and the number of segments that our samples are divided into (number of wells). By adequately adjusting these parameters (see Section 2.5 and Figure 2.7), we managed to mitigate an earthquake of magnitude $M_w = 5.9$ to five smaller ones whose maximum magnitude was $M_w = 4.7$ (one unit less in the logarithmic/magnitude scale). However, in practice these parameters are hard to infer and adjust showing the limitations of such techniques for earthquake mitigation. A complete and rigorous mathematical framework and strategies like the one proposed in the next Chapters could provide efficient alternatives.

Chapter 3

After a brief introduction in control theory, robust controllers were developed, in this Chapter, for a class of nonlinear dynamical systems. considering either matched or unmatched parameter uncertainties (see Sections 3.2 and 3.3, respectively). These controllers can be applied in both stabilization and tracking problems requiring only minimum (but not necessarily exact) information concerning the properties of the system of interest. More specifically, our control design with unmatched uncertainties (see Section 3.3) can tackle uncertainties in the input matrix without adding constraints to the evolution of the state and/or the input trajectories.

Chapter 4

This mathematical framework was implemented in Chapter 4 to achieve earthquake control in a strike-slip fault configuration and drive the system to a stable equilibrium point of lower energy (tracking), assuring stability all the time. Simulations showed that, even in presence of diffusion phenomena and sparse spatial measurements, the proposed control approach managed to prevent an earthquake event of magnitude $M_w \approx 6$.

In particular, two different control strategies were explored. In the first one, we were

able to control the pressure at each distinct element on the fault area by monitoring the whole state-space and neglecting diffusion processes (see Section 4.2). For this scenario, both rate-and-state and slip-weakening friction laws were adopted and compared. For the slip-weakening case, we observed a smooth pore pressure evolution (see Section 4.2.2). Due to the absence of rate-dependencies, the system reached its predefined equilibrium point calculated based on the rupture event. On the contrary, with rate-and-state friction, we showed that the system was able to reach a stable regime earlier than expected depending on the operation time of the control strategy (see Section 4.2.1). Finally, for the operation time used for these simulations, we succeeded in mitigating the large natural event and driving the system to a stable equilibrium point assuring aseismic slip with a maximum developed velocity, which was two orders of magnitude slower than the dynamic event. By increasing the operation time, we could reduce even more the maximum developed slip-rate in the fault area.

In the second control strategy, we took into account diffusion phenomena (see Section 4.3). For the control, we were able to actuate on finite number of distant wells by measuring only the average slip of the fault at the surface. For the sake of robustness in parameter uncertainties, we were restricted to discretize the fault to as many elements as the available “control” wells. In this sense, we ignored (here) the effect of unmodeled dynamics of finer scales emerging from the mechanical system. However, even in presence of the inherent and important delay that the diffusion equation introduces to the system, our controller managed to stabilize the system and drive it to a new steady-state of lower energy assuring aseismic slip. Furthermore, we performed parametric analyses in order to highlight the influence of the operation time of the control strategy, the hydraulic diffusivity/permeability, and the number of available injection/extraction sources on the pressure evolution at the level of the boreholes (see Sections 4.3.1 and 4.3.2).

Going a step further, we applied the theoretical developments of Chapter 3, in a “non-local” scenario, where a fault network is not explicitly defined (see Section 4.4). An academic example considering a CO₂ reservoir was presented. It was shown that by adequately adjusting the flux in the adjacent wells, it is possible to stabilize and control regional seismicity and limit it to acceptable levels with desired production rates.

Chapter 5

In order to test in the laboratory the mathematical developments presented in the previous Chapters, a novel double-direct shear apparatus of decimetric scale was designed,

constructed and calibrated as shown in this Chapter and in Appendix D. For the specimen material, we exploited the 3D-printing technology with sand particles as an alternative to produce fault-like surrogate materials (see Section 5.4 for more details). The mechanical and frictional (both static friction and rate and state characteristics) properties of this novel material were obtained by performing uniaxial and direct-shear experiments (see Appendix B). Based on our experimental campaign, this material showed a high potential for surrogate laboratory experiments involving frictional rock-like interfaces as its frictional properties can be adjusted as desired by customizing the roughness of the interfaces (see Appendix C). This new apparatus was mainly designed to accommodate the control experiments. For that, a discrete-time controller was designed using the emulation technique (see Section 5.7). Its robustness to parameter variations and its intersampling behavior was validated numerically and, eventually, it was applied in Chapter 6.

Chapter 6

In this Chapter, the digital controller designed in the previous Chapter was implemented in the LabVIEW software and its effectiveness was tested experimentally performing a series of laboratory tests. In particular, the controller managed to stabilize the system when an external perturbation was acting on the interfaces (see Section 6.1) preventing a harsh dynamic instability. This scenario corresponds to fault stabilization during the operation of large industrial projects. In addition, selecting a reference slip trajectory, the controller managed to safely drive the system to a new equilibrium point of lower energy assuring stability and aseismic slow slip, all the time (see Section 6.2). Therefore, we were able, for the first-time, to control “laboratory earthquakes” despite the presence of measurement noise, unmodeled dynamics and external disturbances (robustness). Applying adequate scaling laws (see Appendix E), we upscaled these experimental results to a real fault configuration (see Section 6.3). According to these scalings, an earthquake of magnitude $M_w \approx 6$ was completely prevented using the proposed control strategy. Going a step further and increasing the sampling rate, we designed, implemented, tested and compared experimentally three different robust continuous-time controllers (see Appendix F) showing even better performance for earthquake control.

Key points

For clarity, the contributions of this Thesis (both primary and secondary, technical and theoretical) are presented below in the form of a list:

- We showed in Section 1.1 that the most widely used friction laws in fault mechanics are *Lipschitz* (bounded) functions. This property is of great interest in order to apply the theoretical developments presented in Chapter 3.
- Adopting a single-degree-of-freedom spring slider (reduced order) model and performing LSA, we derived an extension of the instability condition proposed by Rice and Ruina (1983), which incorporates not only elastic and inertial forces, but also viscous ones (see Section 1.2.2).
- The qualitative comparison between Slip-Weakening (SW) and Rate-and-State Friction (RSF) using a spring-slider model (see Section 1.2) or a multi-degrees-of-freedom fault (see Section 4.1) showed that for studying isolated events, the adoption of SW friction law suffices to capture the dynamic characteristics of the earthquake event.
- Absorbent porous paper can be an ideal low-cost surrogate material for reproducing earthquake-like instabilities in the laboratory (see Appendix A). Wetting the absorbent paper allowed us not only to weaken the material but also to induce small instabilities. By deriving adequate scaling laws, we show how we can simulate fluid injections in faults and study the transition from seismic (unstable, sudden) to aseismic (stable, creep-like) slip of an idealized fault based on energy considerations.
- According to our surrogate experiments with paper towel, preceding small seismic events do not guarantee the avoidance of large ones. Subsequent injections can drive the system faster towards its instability point, provoking large events (see Section 2.4 and Figure 2.6). Assuring fast saturation during injections and relatively low initial stress levels, the earthquake mitigation strategy was successful (reduction of the magnitude of the main event by one unit).
- Some of the key parameters that govern a successful earthquake mitigation strategy were identified by performing experiments with absorbent porous paper sheets (see Section 2.5). These parameters have to be known in order to expect a successful earthquake mitigation attempt. Otherwise, we risk to drive the fault system faster to its nucleation resulting to a large seismic event. Therefore, the application of such practices seems very limited.

-
- A robust controller for a class of nonlinear systems is developed accounting for both matched and unmatched parameter uncertainties (see Sections 3.2 and 3.3, respectively). Only minimum and not even exact information is required to be known for the system in order to design this controller.
 - In order the control design to be feasible, the nonlinearities and the uncertainties of the system have to be Lipschitz functions. In Section 3.2, we relaxed this condition allowing these functions to satisfy a less conservative constraint (see inequality given in Eq. (3.5)).
 - Unlike the studies of Khalil (2013) and Mattei (2015, among others), our controller design with unmatched uncertainties for the class of nonlinear systems presented in Section 3.3 can tackle also parameter uncertainties in the input matrix. For that, no constraints have to be applied on the state and/or input trajectories (see Section 3.3).
 - The control designs can be used for both stabilization and tracking problems. In case of tracking, the integral action method was applied assuming a constant reference trajectory. However, for time-varying targets, we expect a steady-state error, which can be attenuated by simply adding either more integrators or increasing the relevant integral action gains (see Section 3.2.2).
 - The control approach developed in Chapter 3 was tested numerically adopting a strike-slip fault configuration (see Chapter 4). For a robust control design only minimum (and not exact) information regarding friction, elasticity, viscosity, and permeability is needed.
 - In Section 4.2, we showed that as the operation time of the control strategy increases, the system with RSF friction was able to reach a stable regime earlier than the SW case. This was due to the intrinsic rate-dependency of the RSF and led to a more time/money-friendly approach as the target of reaching a new stable equilibrium point was achieved faster, even if the relaxation of the stored-elastic energy in the fault system was less in this case. Therefore, the slip-weakening friction law seemed to represent the worst case scenario as far as it concerns the unstable dynamics of the system.
 - A scenario accounting for diffusion phenomena and sparse spatial measurements was simulated numerically in Section 4.3. By measuring only the average deformation of the fault at the surface, we managed to adequately adjust the fluxes at the distant (from the fault) wells in order to prevent completely an earthquake of magnitude $M_w \approx 6$.
 - Hydraulic diffusivity, permeability, operation time and the distance of the wells from the

fault influenced the developed pressure profile at the injection level (see Sections 4.3.1 and 4.3.2). In a more realistic scenario, these parameters could be adjusted in order to respect technological limitations related to the pumping system and the geo-system, in general.

- Major faults can be accompanied by other neighboring and unidentified minor or major faults. For this purpose, we proposed a non-local control approach which can be combined for reducing the seismic risk over larger areas (see Section 4.4). This approach can also be used for minimizing regional seismicity and limit it to acceptable levels with desired production rates in reservoir engineering.
- A novel double-direct shear apparatus of decimetric scale was designed, assembled and calibrated in the frame of this Thesis (see Chapter 5). The setup was first modeled with Finite Elements before its construction. This allowed to reveal, beforehand, problems that might emerge in practice (see Appendix D) and to optimize this new device for the needs of this work.
- Due to the needs of the control experiments, this device differs from other existing ones (see Section 5.1).
- The pressure variations that the controller demands were applied through a fast response electro-pneumatic pressure regulator, which adjusts the effective stress at the interfaces. The LabVIEW code developed for this experimental campaign (see Sections 5.2 and 5.3) is well optimized and can acquire measurements every 1 ms (see Appendix F), 2 ms (see Chapter 6) or higher. However, successful experiments were run with even slower sampling rates (5 ms) in order to push our control approach to the limits.
- The material used for the experiments in Chapters 5 and 6 was a Sand-based 3D-Printed (S3DP) surrogate material (see Appendix B), which was extensively characterized during this Thesis. This material shows a high potential for surrogate laboratory experiments involving frictional rock-like interfaces as its frictional properties can be customized by adjusting the roughness of the interfaces (see Appendix C).
- In Appendix C, we showed how to adequately design the printed geometry of the sliding interfaces of the S3DP specimen in order to obtain custom a) maximum, minimum and residual apparent frictional properties, b) characteristic slip-weakening distance, c) evolution of friction coefficient with slip and d) dilatancy.
- Experiments validated our design approach for achieving custom evolution of the apparent friction coefficient, which could be used to reproduce earthquake-like instabilities

in the laboratory. Using adequate printing patterns, these earthquake-like instabilities could be designed to be periodic, as well, mimicking the earthquake cycle. Moreover, it is possible to control, to a certain extent, the creation of a gouge-like layer by modifying the geometry of the asperities and the binder content. This could provide tools for future studies on the influence of gouge on frictional properties and roughness.

- The controller was designed in discrete-time. The design required the knowledge of only the possible minimum friction, the maximum softening slope, and the maximum discrepancies in elasticity and viscosity from some predefined nominal values (see Section 5.7.3). Due to the discrete nature of the controller, numerical analyses were needed to show that the closed-loop system is indeed stable under the adopted set of parameters.
- The first-ever control experiments conducted in the laboratory for earthquake control were presented in Chapter 6. Both stabilization and tracking experiments were attempted. All these tests were successfully reached the desired target and induced aseismic slow slip despite uncertainties and unmodeled dynamics (e.g. geometry, imperfections, noise in measurements, unknown frictional rheology, disturbances, misalignments, etc.).
- Applying scaling laws (see Appendix E), we upscaled the experimental raw data to an equivalent real-fault configuration. Without the activation of the controller, an earthquake of magnitude $M_w \approx 6$ was measured. However, our developed control strategy managed to prevent this large seismic event and stabilize the fault system to a (stable) new equilibrium point aseismically.
- In Appendix F, an extension of the discrete-time control experiments presented in Chapter 6 was discussed. The sampling period was halved (1 ms) and robust continuous-time controllers were designed to perform tracking of a slow reference. Two kinds of controllers were compared: one based on sliding-mode control and the other based on Linear Quadratic Regulator (LQR) control. The first controller results in local finite-time convergence of the tracking error, while the other one presents global exponential stability. Both controllers generate a continuous control signal and both use the integral action to compensate different kinds of perturbations. We observed that all the controllers responded more or less the same with no spectacular differences.

Main Limitations

The main limitations of this work are listed below:

-
- The robust control design proposed in Chapter 3 and more specifically in Section 3.3 can be applied only for the specific class of nonlinear systems, which accounts for matched uncertainties in the mechanical system. However, when distant wells are installed and diffusion processes are considered, a discretization of the fault area containing as many elements as the available “control” wells is needed in order the uncertainties of the mechanical system to be matched with the available inputs (see Section 4.3). Therefore, in the numerical simulations in Section 4.3, we don’t explore the effect of unmodeled dynamics of finer scales emerging from the mechanical system. These unmodeled dynamics are tackled by a new generation of controllers, developed in the CoQuake group.
 - The observer used for the numerical simulations presented in Chapter 4 and more specifically in Section 4.3 does not consider parameter uncertainties. More advanced design is needed in order to create a robust observer. However, we know that such an observer exists as the system of study is observable.
 - Claiming that controlling anthropogenic or natural seismicity is possible, based on the experiments and the numerical simulations presented in this work, is a speculation and further research is needed. Several theoretical and techno-economical investigations have to be pursued further in order to show into what extent man-made or natural earthquakes can be prevented (or the opposite).
 - Some direct limitations of the proposed theory have to do with the actual technological means for fluid injections in the earth’s crust (e.g. number of wells, pressure limits of pumps, response time). In this case special analyses have to be performed to adjust the operation time and incorporate the limitations of the pumping system in the design of the controller.
 - The sampling-rate of the observations is also an important factor. In Chapter 6, we presented experiments of discrete-time control, while in Appendix F of continuous-time control. But there might be even slower data acquisition systems and actuators. Therefore, more elaborated techniques may be needed for discrete-time control. One of the possibilities for tackling the discrete-time is *Artificial Intelligence* (AI) techniques. A first attempt towards this direction is presented in Papachristos and Stefanou (2021).
 - Measurements of the states of the system are never free of errors. These errors can be considered as disturbances (Khalil, 2015) and tackled with other controllers that are more resilient and robust. A first approach was considered in Appendix F, where nonlinear controllers were employed.

-
- Poroelastic couplings were ignored in this work. Their addition does not seem to pose any particular difficulties, but their implementation was beyond the scope of this Thesis. A simplified 1D equation was used for accounting for diffusion phenomena per injection point. A full 3D continuum formulation should be incorporated in the future.
 - For the experiments in Chapter 6, diffusion phenomena were considered only in post-processing. Direct fluid injections at the sheared interfaces are needed to be implemented in the current experimental configuration because diffusion processes introduce time-delays, which can make the design of robust controllers more challenging especially when they are tested in a real-time experiment. Another alternative is to perform hybrid tests (see Perspectives).

Contributions

The work presented in this Thesis is a result of a close collaboration among myself, Dr. Philipp Braun, Dr. Diego Gutiérrez-Oribio and Prof. Ioannis Stefanou. The following paragraphs are devoted to list who participated in each part of this work and to what extent. More specifically, the proof of Lipschitz continuity of the most-widely used friction laws in Fault Mechanics was developed by me and Prof. Ioannis Stefanou (Section 1.1). The extension of the (in)stability condition of the rate-and-state friction law considering elastic, inertial and also viscous forces was derived by me (Section 1.2.2).

The Paper-Quake experiments as well as their testing procedure (Chapter 2 and Appendix A) were conceptualized by me, Dr. Philipp Braun and Prof. Ioannis Stefanou. All the experiments presented in Chapter 2 and Appendix A were mainly conducted by me and Dr. Philipp Braun, while the post-processing of the experimental data was performed solely by me.

The robust stabilizing and tracking continuous-time controllers for a class of nonlinear systems with matched uncertainties (Section 3.2) were derived by me and Prof. Ioannis Stefanou, while the ones considering unmatched uncertainties (Section 3.3) were derived exclusively by me.

The dynamics of the strike-slip fault coupled with slip-weakening (Section 4.1.2) or rate-and-state (Section 4.1.1) friction were simulated by me and Prof. Ioannis Stefanou. This code then was upgraded to incorporate the control algorithm (Sections 4.2 and 4.3) as well as to account for diffusion phenomena and distant fluid injections (Section 4.3). The non-local scenario for robust control of the seismicity rate (Section 4.4) was also

developed by me and Prof. Ioannis Stefanou. All the simulations presented in Section 1.2.3 and Chapter 4 were run and post-processed by me.

The conceptualization, design and assemble of the novel double-direct shear apparatus of decimetric scale, introduced in Chapter 5, were performed by me, Dr. Philipp Braun and Prof. Ioannis Stefanou. More specifically, the preliminary design of the experimental configuration based on Finite Elements (Appendix D) was performed by me. The mechanical designs of the machine were drawn by Dr. Philipp Braun. The assemble of the machine was conducted by me, Dr. Philipp Braun and Prof. Ioannis Stefanou. The calibration of all the installed sensors, the development of the *LabVIEW* code (Section 5.3) along with the implementation and derivation of the discrete-time control algorithm (Section 5.7) were conducted by me.

The Sand-Based 3D-Printed surrogate material, used in the sandwich experiments, was conceptualized by Dr. Philipp Braun and Prof. Ioannis Stefanou. The characterization of the bulk properties of the material (Appendix B.2) was performed by Dr. Philipp Braun, while the direct shear experiments on flat and wavy interfaces as well as the inclined tests (Appendices B.3 and C.3) were performed by me and Dr. Philipp Braun. The characterization of the rate-and-state properties of the frictional interfaces made of this material were explored by me (direct shear experiments + post-processing). The modeling of the frictional response of this material (Appendices C.1 and C.2) and experimental data post-processing (Appendices B and C) were conducted by Dr. Philipp Braun.

All the experiments, presented in Chapters 5 and 6, and the experimental data post-processing were performed by me. The scaling laws (Appendix E) applied in Section 6.3 were mainly derived by me. Finally, the experimental campaign presented in Appendix F was performed by me and Dr. Diego Gutiérrez-Oribio. In particular, the sliding-mode based robust continuous-time controller (Appendix F.2.1) was derived by Dr. Diego Gutiérrez-Oribio, while the LQR based robust continuous-time controller (Appendix F.2.2) was derived by me. The post-processing of the experimental data was performed by me.

Perspectives

Future work is needed around the following axes:

1. Perform hybrid tests by simulating numerically in real-time diffusion and/or poro-elasto-plasticity and combining them with the laboratory experiments of Chapter 6.

In this case, the controller would adjust the flux of a well far from the fault and the numerical model would adapt the effective normal stress in the fault area, which is modeled in the physical experiment.

2. Upgrade the double-direct shear apparatus in order to accommodate direct fluid injections in the sheared interfaces. The design will allow the full monitoring of the specimen without the usage of any membrane.
3. Design and construct a meter-scale apparatus. The design will be such that to allow rupture initiation, propagation, and termination inside the frictional interface. Moreover, our advanced control strategies will be implemented in order to control the dynamics of this new complex experimental configuration. The dimensions of this apparatus are justified on the basis of the scaling laws.
4. Test the developed control algorithms in more elaborated codes which are specifically developed to deal with complex fault systems containing the most important Thermo-Hydro-Chemo-Mechanical-Couplings.
5. Improve the existing controllers, study further their performance and propose new ones to tackle the limitations of the ones developed in this Thesis.
6. Apply the non-local approach presented in Section 4.4 to real reservoirs, like the Groningen gas field.

The aforementioned perspectives are explored under the CoQuake (Controlling earth-Quakes, <http://coquake.eu/>) - ERC project.

References

- Ackermann, J. (1985). *Sampled-data control systems: analysis and synthesis, robust system design*. Springer Berlin Heidelberg. (See pp. 2, 116).
- Andrews, D. J. (1976). Rupture velocity of plane strain shear cracks. *Journal of Geophysical Research (1896-1977)*, 81(32), 5679–5687. <https://doi.org/10.1029/JB081i032p05679> (see p. 3)
- Anthony, J. L., & Marone, C. (2005). Influence of particle characteristics on granular friction. *Journal of Geophysical Research: Solid Earth*, 110(B8). <https://doi.org/https://doi.org/10.1029/2004JB003399> (see p. 1)
- Aoude, A. (2021). *Study the Constitutive Behavior of Frictional Interfaces beyond the Rate-and-State Regime* (Master's thesis). École Centrale de Nantes. (See pp. 195, 196).
- Åström, K. J., & Wittenmark, B. (1997). *Computer-controlled systems (3rd ed.)* Prentice-Hall, Inc. (See pp. 113, 115, 116, 239).
- Bacciotti, A., & Rosier, L. (2005). *Lyapunov functions and stability in control theory*. <https://doi.org/10.1007/b139028>. (See p. 232)
- Baker, W., Westine, P., & Dodge, F. (1991). *Similarity methods in engineering dynamics: theory and practice of scale modeling*. Elsevier. <https://books.google.fr/books?id=loNRAAAAMAAJ>. (See p. 221)
- Barbot, S., Lapusta, N., & Avouac, J.-P. (2012). Under the Hood of the Earthquake Machine : Toward Predictive Modeling. *Science*, 336(6082), 707–710. <https://doi.org/10.1126/science.1218796> (see p. 2)
- Barbot, S. D. (2019a). Modulation of fault strength during the seismic cycle by grain-size evolution around contact junctions. *Tectonophysics*, 765(April), 129–145. <https://doi.org/10.1016/j.tecto.2019.05.004> (see p. 5)
- Barbot, S. D. (2019b). Slow-slip, slow earthquakes, period-two cycles, full and partial ruptures, and deterministic chaos in a single asperity fault. *Tectonophysics*, 768(August), 228171. <https://doi.org/10.1016/j.tecto.2019.228171> (see pp. 22, 59)

-
- Barras, F., Aldam, M., Roch, T., Brener, E. A., Bouchbinder, E., & Molinari, J. F. (2019). Emergence of Cracklike Behavior of Frictional Rupture: The Origin of Stress Drops. *Physical Review X*, 9(4), 41043. <https://doi.org/10.1103/PhysRevX.9.041043> (see p. 5)
- Barton, N. (1973). Review of a new shear-strength criterion for rock joints. *Engineering Geology*, 7(4), 287–332. [https://doi.org/https://doi.org/10.1016/0013-7952\(73\)90013-6](https://doi.org/10.1016/0013-7952(73)90013-6) (see p. 195)
- Bernuau, E., Efimov, D., Perruquetti, W., & Polyakov, A. (2014). On homogeneity and its application in sliding mode control [Special Issue on 2010-2012 Advances in Variable Structure Systems and Sliding Mode Algorithms]. *Journal of the Franklin Institute*, 351(4), 1866–1901. [https://doi.org/https://doi.org/10.1016/j.jfranklin.2014.01.007](https://doi.org/10.1016/j.jfranklin.2014.01.007) (see p. 232)
- Bhattacharya, P., Rubin, A. M., Bayart, E., Savage, H. M., & Marone, C. (2015). Critical evaluation of state evolution laws in rate and state friction: fitting large velocity steps in simulated fault gouge with time-, slip-, and stress-dependent constitutive laws. *Journal of Geophysical Research: Solid Earth*, 120(9), 6365–6385. <https://doi.org/10.1002/2015JB012437> (see p. 193)
- Bhattacharya, P., & Viesca, R. C. (2019). Fluid-induced aseismic fault slip outpaces pore-fluid migration. *Science*, 364(6439), 464–468. <https://doi.org/10.1126/science.aaw7354> (see pp. 2, 5, 34)
- Birkeland, K. W., & Landry, C. C. (2002). Power-laws and snow avalanches. *Geophysical Research Letters*, 29(11), 49–1–49–3. <https://doi.org/10.1029/2001GL014623> (see p. 24)
- Boettcher, M. S., & Marone, C. (2004). Effects of normal stress variation on the strength and stability of creeping faults. *Journal of Geophysical Research: Solid Earth*, 109(B3). [https://doi.org/https://doi.org/10.1029/2003JB002824](https://doi.org/10.1029/2003JB002824) (see p. 100)
- Bommer, J. J., Crowley, H., & Pinho, R. (2015). A risk-mitigation approach to the management of induced seismicity. *Journal of Seismology*, 19(2), 623–646. <https://doi.org/10.1007/s10950-015-9478-z> (see p. 2)
- Bommer, J. J., Oates, S., Cepeda, J. M., Lindholm, C., Bird, J., Torres, R., Marroquín, G., & Rivas, J. (2006). Control of hazard due to seismicity induced by a hot fractured rock geothermal project. *Engineering Geology*, 83(4), 287–306. [https://doi.org/https://doi.org/10.1016/j.enggeo.2005.11.002](https://doi.org/10.1016/j.enggeo.2005.11.002) (see p. 33)

-
- Boyd, J. P. (2000). *Chebyshev and Fourier Spectral Methods: second edition* (2nd). Dover Publications. (See pp. 22, 59).
- Brauer, F., & Nohel, J. (2012). *The qualitative theory of ordinary differential equations: an introduction*. Dover Publications. <https://books.google.fr/books?id=9qPsbRl7hBkC>. (See pp. 13–16, 41, 42)
- Braun, P., Tzortzopoulos, G., & Stefanou, I. (2021). Design of sand-based, 3d-printed analogue faults with controlled frictional properties [e2020JB020520 2020JB020520]. *Journal of Geophysical Research: Solid Earth*, n/a(n/a), e2020JB020520. Zenodo. <https://doi.org/https://doi.org/10.1029/2020JB020520> (see pp. 105, 109, 185)
- Brune, J. N., & Anooshehpour, A. (1998). A physical model of the effect of a shallow weak layer on strong ground motion for strike-slip ruptures. *Bulletin of the Seismological Society of America*, 88(4), 1070–1078. <https://doi.org/10.1785/BSSA0880041070> (see p. 1)
- Brunton, S. L., & Kutz, J. N. (2019). *Data-driven science and engineering: machine learning, dynamical systems, and control*. Cambridge University Press. <https://doi.org/10.1017/9781108380690>. (See p. 83)
- Burridge, R., & Knopoff, L. (1967). Model and theoretical seismicity. *Bulletin of the Seismological Society of America*, 57(3), 341–371. <https://doi.org/10.1785/BSSA0570030341> (see p. 1)
- Byerlee, J. D. (1978). Friction of rocks. *Pure and Applied Geophysics PAGEOPH*, 116(4–5), 615–626. <https://doi.org/10.1007/BF00876528> (see p. 5)
- Candela, T., Renard, F., Klinger, Y., Mair, K., Schmittbuhl, J., & Brodsky, E. E. (2012). Roughness of fault surfaces over nine decades of length scales. *Journal of Geophysical Research: Solid Earth*, 117(8), 1–30. <https://doi.org/10.1029/2011JB009041> (see p. 199)
- Caniven, Y., Dominguez, S., Soliva, R., Cattin, R., Peyret, M., Marchandon, M., Romano, C., & Strak, V. (2015). A new multilayered visco-elasto-plastic experimental model to study strike-slip fault seismic cycle. *Tectonics*, 34(2), 232–264. <https://doi.org/https://doi.org/10.1002/2014TC003701> (see p. 1)
- Cao, T., & Aki, K. (1987). Effect of slip rate on stress drop. In T. E. Tullis (Ed.), *Friction and faulting* (pp. 515–529). Birkhäuser Basel. https://doi.org/10.1007/978-3-0348-6601-9_7. (See p. 21)

-
- Cappa, F., Scuderi, M. M., Collettini, C., Guglielmi, Y., & Avouac, J.-P. (2019). Stabilization of fault slip by fluid injection in the laboratory and in situ. *Science Advances*, 5(3), eaau4065. <https://doi.org/10.1126/sciadv.aau4065> (see pp. 1, 2, 24, 28, 30)
- Chester, F. M. (1994). Effects of temperature on friction: Constitutive equations and experiments with quartz gouge. *Journal of Geophysical Research*, 99(B4), 7247. <https://doi.org/10.1029/93JB03110> (see p. 5)
- Chinnery, M. (1963). The stress changes that accompany strike-slip faulting. *Bulletin of the Seismological Society of America*, 53(5), 921–932 (see pp. 59, 68).
- Cihan, A., Birkholzer, J. T., & Bianchi, M. (2015). Optimal well placement and brine extraction for pressure management during CO₂ sequestration. *International Journal of Greenhouse Gas Control*, 42, 175–187. <https://doi.org/10.1016/j.ijggc.2015.07.025> (see p. 97)
- Collins-Craft, N. A., Stefanou, I., Sulem, J., & Einav, I. (2020). A Cosserat Breakage Mechanics model for brittle granular media. *Journal of the Mechanics and Physics of Solids*, 141(0), 103975. <https://doi.org/10.1016/j.jmps.2020.103975> (see pp. 5, 214)
- Corbi, F., Funicello, F., Moroni, M., van Dinther, Y., Mai, P. M., Dalguer, L. A., & Faccenna, C. (2013). The seismic cycle at subduction thrusts: 1. insights from laboratory models. *Journal of Geophysical Research: Solid Earth*, 118(4), 1483–1501. <https://doi.org/10.1029/2012JB009481> (see p. 1)
- Cornet, F. H. (2019). The engineering of safe hydraulic stimulations for EGS development in hot crystalline rock masses. *Geomechanics for Energy and the Environment*, 1(1), 100151. <https://doi.org/10.1016/j.gete.2019.100151> (see p. 35)
- Daniels, K. E., & Hayman, N. W. (2008). Force chains in seismogenic faults visualized with photoelastic granular shear experiments. *Journal of Geophysical Research: Solid Earth*, 113(B11). <https://doi.org/10.1029/2008JB005781> (see p. 1)
- Dascher-Cousineau, K., Kirkpatrick, J. D., & Cooke, M. L. (2018). Smoothing of Fault Slip Surfaces by Scale-Invariant Wear. *Journal of Geophysical Research: Solid Earth*, 123(9), 7913–7930. <https://doi.org/10.1029/2018JB015638> (see p. 199)
- Dieterich, J. (1994). A constitutive law for rate of earthquake production and its application to earthquake clustering. *Journal of Geophysical Research: Solid Earth*,

-
- 99(B2), 2601–2618. <https://doi.org/https://doi.org/10.1029/93JB02581> (see p. 93)
- Dieterich, J. H. (1972). Time-dependent friction in rocks. *Journal of Geophysical Research (1896-1977)*, 77(20), 3690–3697. <https://doi.org/https://doi.org/10.1029/JB077i020p03690> (see pp. 99, 105)
- Dieterich, J. H. (1979). Modeling of rock friction: 1. experimental results and constitutive equations. *Journal of Geophysical Research: Solid Earth*, 84(B5), 2161–2168. <https://doi.org/10.1029/JB084iB05p02161> (see pp. 1, 7, 10, 14, 28, 215)
- Dieterich, J. H. (1981a). Constitutive properties of faults with simulated gouge. In *Mechanical behavior of crustal rocks* (pp. 103–120). American Geophysical Union (AGU). <https://doi.org/10.1029/GM024p0103>. (See pp. 1, 5, 100, 193, 213)
- Dieterich, J. H. (1981b). Potential for geophysical experiments in large scale tests. *Geophysical Research Letters*, 8(7), 653–656. <https://doi.org/https://doi.org/10.1029/GL008i007p00653> (see pp. 105, 214)
- Dieterich, J. H., & Kilgore, B. D. (1994). Direct observation of frictional contacts: new insights for state-dependent properties. *pure and applied geophysics*, 143(1), 283–302. <https://doi.org/10.1007/BF00874332> (see pp. 1, 193)
- Dobereiner, L., & Freitas, M. H. D. (1986). Geotechnical properties of weak sandstones. *Géotechnique*, 36(1), 79–94. <https://doi.org/10.1680/geot.1986.36.1.79> (see p. 190)
- Douglas, B. (2020). The map of control theory. (See pp. 37, 38).
- Edwards, B., Kraft, T., Cauzzi, C., Kästli, P., & Wiemer, S. (2015). Seismic monitoring and analysis of deep geothermal projects in St Gallen and Basel, Switzerland. *Geophysical Journal International*, 201(2), 1022–1039. <https://doi.org/10.1093/gji/ggv059> (see p. 33)
- Einav, I., & Guillard, F. (2018). Tracking time with ricequakes in partially soaked brittle porous media. *Science Advances*, 4(10). <https://doi.org/10.1126/sciadv.aat6961> (see p. 24)
- Ellsworth, W. L. (2013). Injection-induced earthquakes. *Science*, 341(6142). <https://doi.org/10.1126/science.1225942> (see p. 23)
- Ellsworth, D., Spiers, C. J., & Niemeijer, A. R. (2016). Understanding induced seismicity. *Science*, 354(6318), 1380–1381. <https://doi.org/10.1126/science.aal2584> (see p. 1)
- Erickson, B. A., Birnir, B., & Lavallée, D. (2011). Periodicity, chaos and localization in a Burridge-Knopoff model of an earthquake with rate-and-state friction. *Geophysical*

-
- Journal International*, 187(1), 178–198. <https://doi.org/10.1111/j.1365-246X.2011.05123.x> (see p. 134)
- Erickson, B. A., Jiang, J., Barall, M., Lapusta, N., Dunham, E. M., Harris, R., Abrahams, L. S., Allison, K. L., Ampuero, J.-p., Barbot, S. D., Cattania, C., Elbanna, A., Fialko, Y., Idini, B., Kozdon, J. E., Lambert, V., Liu, Y., Luo, Y., Ma, X., . . . Wei, M. (2020). The community code verification exercise for Simulating Sequences of Earthquakes and Aseismic Slip (SEAS). *Seismological Research Letters*, 91(2A), 874–890. <https://doi.org/10.1785/0220190248> (see pp. 22, 58, 59)
- Filippov, A. (1988). *Differential equations with discontinuous righthand sides*. Kluwer Academic Publ. (See p. 232).
- Foulger, G. R., Wilson, M. P., Gluyas, J. G., Julian, B. R., & Davies, R. J. (2018). Global review of human-induced earthquakes. *Earth-Science Reviews*, 178, 438–514. <https://doi.org/https://doi.org/10.1016/j.earscirev.2017.07.008> (see pp. 1, 23)
- Francis, B., & Wonham, W. (1976). The internal model principle of control theory. *Automatica*, 12(5), 457–465. [https://doi.org/https://doi.org/10.1016/0005-1098\(76\)90006-6](https://doi.org/https://doi.org/10.1016/0005-1098(76)90006-6) (see p. 237)
- Franklin, G. F., Powell, J. D., & Emami-Naeini, A. (2018). *Feedback control of dynamic systems (8th edition)* (8th). Pearson. (See pp. 2, 38, 53, 68, 83, 95).
- Franklin, G. F., Workman, M. L., & Powell, D. (1998). *Digital control of dynamic systems* (3rd). Addison-Wesley Longman Publishing Co., Inc. (See pp. 2, 113–117, 239).
- Frash, L. P., Fu, P., Morris, J., Gutierrez, M., Neupane, G., Hampton, J., Welch, N. J., Carey, J. W., & Kneafsey, T. (2021). Fracture caging to limit induced seismicity [e2020GL090648 2020GL090648]. *Geophysical Research Letters*, 48(1), e2020GL090648. <https://doi.org/https://doi.org/10.1029/2020GL090648> (see p. 2)
- Garagash, D. I., & Germanovich, L. N. (2012). Nucleation and arrest of dynamic slip on a pressurized fault. *Journal of Geophysical Research: Solid Earth*, 117(B10). <https://doi.org/10.1029/2012JB009209> (see p. 23)
- Gelet, R., Loret, B., & Khalili, N. (2012). A thermo-hydro-mechanical coupled model in local thermal non-equilibrium for fractured hydrate reservoir with double porosity. *Journal of Geophysical Research: Solid Earth*, 117(B7). <https://doi.org/https://doi.org/10.1029/2012JB009161> (see p. 5)

-
- Gomez, J. S. (2017). *Mechanical Properties Characterization of Printed Reservoir Sandstone Analogues* (Master's thesis). University of Alberta. <https://era.library.ualberta.ca/items/49660e82-3446-4a9a-9a74-e5ff2ab38470/download/7e82347e-42db-4031-bc32-12134e5441d7>. (See pp. 186, 190)
- Gomez, J. S., Chalaturnyk, R. J., & Zambrano-Narvaez, G. (2019). Experimental Investigation of the Mechanical Behavior and Permeability of 3D Printed Sandstone Analogues Under Triaxial Conditions. *Transport in Porous Media*, 129(2), 541–557. <https://doi.org/10.1007/s11242-018-1177-0> (see pp. 186, 190)
- Grigoli, F., Cesca, S., Rinaldi, A. P., Manconi, A., López-Comino, J. A., Clinton, J. F., Westaway, R., Cauzzi, C., Dahm, T., & Wiemer, S. (2018). The november 2017 mw 5.5 pohang earthquake: a possible case of induced seismicity in south korea. *Science*, 360(6392), 1003–1006. <https://doi.org/10.1126/science.aat2010> (see p. 34)
- Gu, J.-C., Rice, J. R., Ruina, A. L., & Tse, S. T. (1984). Slip motion and stability of a single degree of freedom elastic system with rate and state dependent friction. *Journal of the Mechanics and Physics of Solids*, 32(3), 167–196. [https://doi.org/https://doi.org/10.1016/0022-5096\(84\)90007-3](https://doi.org/https://doi.org/10.1016/0022-5096(84)90007-3) (see p. 193)
- Gualandi, A., Avouac, J.-P., Michel, S., & Faranda, D. (2020). The Predictable Chaos of Slow Earthquakes. *Science Advances*, *Accepted* (see p. 2).
- Guenoune, I., Glumineau, A., Plestan, F., & Chermitti, A. (2015). Control of wind turbine driven a permanent magnet synchronous generator using backstepping-mtpa strategy control. *2015 4th International Conference on Electrical Engineering (ICEE)*, 1–6. <https://doi.org/10.1109/INTEE.2015.7416760> (see p. 39)
- Guenoune, I., Plestan, F., & Chermitti, A. (2017). Robust integral backstepping control for twin wind turbines structure. *IFAC World Congress*. <https://hal.archives-ouvertes.fr/hal-01726040> (see p. 39)
- Guglielmi, Y., Cappa, F., Avouac, J.-P., Henry, P., & Elsworth, D. (2015). Seismicity triggered by fluid injection–induced aseismic slip. *Science*, 348(6240), 1224–1226. <https://doi.org/10.1126/science.aab0476> (see pp. 1, 2, 23, 34)
- Gupta, H. K. (2002). A review of recent studies of triggered earthquakes by artificial water reservoirs with special emphasis on earthquakes in koyna, india. *Earth-Science Reviews*, 58(3), 279–310. [https://doi.org/https://doi.org/10.1016/S0012-8252\(02\)00063-6](https://doi.org/https://doi.org/10.1016/S0012-8252(02)00063-6) (see p. 23)

-
- Gutenberg, B., & Richter, C. F. (1954). *Seismicity of the earth and associated phenomena* (2nd, Vol. 40). Princeton University Press, Princeton, N. J. <https://nla.gov.au/nla.cat-vn2276307>. (See p. 23)
- Gutiérrez-Oribio, D., Mercado-Uribe, J. Á., Moreno, J. A., & Fridman, L. (2021). Robust global stabilization of a class of underactuated mechanical systems of two degrees of freedom. *International Journal of Robust and Nonlinear Control*, 31(9), 3439–3454. <https://doi.org/10.1002/rnc.5176> (see pp. 232, 233, 236)
- Hamilton, R. M., Smith, B. E., Fischer, F. G., & Papanek, P. J. (1972). Earthquakes caused by underground nuclear explosions on pahute mesa, nevada test site. *Bulletin of the Seismological Society of America*, 62(5), 1319–1341. <https://doi.org/10.1785/BSSA0620051319> (see p. 23)
- Harris, R. A. (1998). Introduction to special section: stress triggers, stress shadows, and implications for seismic hazard. *Journal of Geophysical Research: Solid Earth*, 103(B10), 24347–24358. <https://doi.org/10.1029/98JB01576> (see p. 30)
- Heimisson, E. R., Smith, J. D., Avouac, J.-P., & S., B. (2021). Coulomb threshold rate-and-state model for fault reactivation: application to induced seismicity at groningen. *EarthArXiv*. <https://doi.org/10.31223/X5489T> (see p. 97)
- Heslot, F., Baumberger, T., Perrin, B., Caroli, B., & Caroli, C. (1994). Creep, stick-slip, and dry-friction dynamics: experiments and a heuristic model. *Phys. Rev. E*, 49, 4973–4988. <https://doi.org/10.1103/PhysRevE.49.4973> (see pp. 1, 24)
- Hofmann, H., Zimmermann, G., Farkas, M., Huenges, E., Zang, A., Leonhardt, M., Kwiatek, G., Martinez-Garzon, P., Bohnhoff, M., Min, K. B., Fokker, P., Westaway, R., Bethmann, F., Meier, P., Yoon, K. S., Choi, J. W., Lee, T. J., & Kim, K. Y. (2019). First field application of cyclic soft stimulation at the Pohang Enhanced Geothermal System site in Korea. *Geophysical Journal International*, 217(2), 926–949. <https://doi.org/10.1093/gji/ggz058> (see p. 2)
- Hosseini, S. M., Goebel, T. H. W., Jha, B., & Aminzadeh, F. (2018). A probabilistic approach to injection-induced seismicity assessment in the presence and absence of flow boundaries. *Geophysical Research Letters*, 45(16), 8182–8189. <https://doi.org/10.1029/2018GL077552> (see pp. 23, 34)
- Huang, J., & Turcotte, D. L. (1992). Chaotic seismic faulting with a mass-spring model and velocity-weakening friction. *Pure and Applied Geophysics PAGEOPH*, 138(4), 569–589. <https://doi.org/10.1007/BF00876339> (see p. 6)

-
- Hulbert, C., Rouet-Leduc, B., Johnson, P. A., Ren, C. X., Rivière, J., Bolton, D. C., & Marone, C. (2019). Similarity of fast and slow earthquakes illuminated by machine learning. *Nature Geoscience*, *12*(1), 69–74. <https://doi.org/10.1038/s41561-018-0272-8> (see p. 1)
- Hunfeld, L. B., Chen, J., Niemeijer, A. R., & Spiers, C. J. (2019). Temperature and gas/brine content affect seismogenic potential of simulated fault gouges derived from groningen gas field caprock. *Geochemistry, Geophysics, Geosystems*, *20*(6), 2827–2847. <https://doi.org/10.1029/2019GC008221> (see p. 193)
- Jones, L. (2018). *The big ones: how natural disasters have shaped us (and what we can do about them)* [ISBN 978-178578-436-1]. Doubleday. (See p. 1).
- Kammer, D. S., & McLaskey, G. C. (2019). Fracture energy estimates from large-scale laboratory earthquakes. *Earth and Planetary Science Letters*, *511*, 36–43. <https://doi.org/https://doi.org/10.1016/j.epsl.2019.01.031> (see p. 1)
- Kanamori, H., & Brodsky, E. E. (2004). The physics of earthquakes. *Reports on Progress in Physics*, *67*(8), 1429–1496. <https://doi.org/10.1088/0034-4885/67/8/r03> (see pp. 3, 5, 6, 9, 12, 19, 20, 27, 28, 107, 117, 180, 182, 218)
- Kanamori, H., & Rivera, L. (2006). Energy partitioning during an earthquake. In *Earthquakes: radiated energy and the physics of faulting* (pp. 3–13). American Geophysical Union (AGU). <https://doi.org/https://doi.org/10.1029/170GM03>. (See p. 20)
- Ke, C.-Y., McLaskey, G. C., & Kammer, D. S. (2018). Rupture termination in laboratory-generated earthquakes. *Geophysical Research Letters*, *45*(23), 784–792. <https://doi.org/https://doi.org/10.1029/2018GL080492> (see p. 1)
- Kenigsberg, A. R., Rivière, J., Marone, C., & Saffer, D. M. (2020). Evolution of Elastic and Mechanical Properties During Fault Shear: The Roles of Clay Content, Fabric Development, and Porosity. *Journal of Geophysical Research: Solid Earth*, *125*(3), 1–16. <https://doi.org/10.1029/2019JB018612> (see p. 5)
- Khalil, H. (2013). *Nonlinear systems*. Pearson Education Limited. (See pp. 2, 38, 41, 46, 47, 49, 112, 142, 233, 237).
- Khalil, H. (2015). *Nonlinear control, global edition*. Pearson Education Limited. (See pp. 3, 38–41, 43, 44, 46, 49–51, 53, 55, 56, 82–84, 112, 135, 145).
- Khalil, H. (2017). *High-gain observers in nonlinear feedback control*. Society for Industrial; Applied Mathematics. <https://doi.org/10.1137/1.9781611974867>. (See p. 83)

-
- Kilgore, B., Beeler, N. M., Lozos, J., & Oglesby, D. (2017). Rock friction under variable normal stress. *Journal of Geophysical Research: Solid Earth*, *122*(9), 7042–7075. <https://doi.org/https://doi.org/10.1002/2017JB014049> (see p. 100)
- King, C.-Y. (1975). Model seismicity and faulting parameters. *Bulletin of the Seismological Society of America*, *65*(1), 245–259. <https://doi.org/10.1785/BSSA0650010245> (see p. 24)
- King, C.-Y. (1994). Earthquake mechanism and predictability shown by a laboratory fault. *pure and applied geophysics*, *143*(1), 457–482. <https://doi.org/10.1007/BF00874338> (see p. 1)
- Knuth, M., & Marone, C. (2007a). Friction of sheared granular layers: role of particle dimensionality, surface roughness, and material properties. *Geochemistry, Geophysics, Geosystems*, *8*(3). <https://doi.org/https://doi.org/10.1029/2006GC001327> (see p. 1)
- Knuth, M., & Marone, C. (2007b). Friction of sheared granular layers: role of particle dimensionality, surface roughness, and material properties. *Geochemistry, Geophysics, Geosystems*, *8*(3). <https://doi.org/10.1029/2006GC001327> (see pp. 24, 100)
- Krokavec, D., & Filasová, A. (2000). Unmatched uncertainties in robust lq control [3rd IFAC Symposium on Robust Control Design (ROCOND 2000), Prague, Czech Republic, 21-23 June 2000]. *IFAC Proceedings Volumes*, *33*(14), 329–334. [https://doi.org/https://doi.org/10.1016/S1474-6670\(17\)36250-X](https://doi.org/https://doi.org/10.1016/S1474-6670(17)36250-X) (see p. 46)
- Kwiatek, G., Saarno, T., Ader, T., Bluemle, F., Bohnhoff, M., Chendorain, M., Dresen, G., Heikkinen, P., Kukkonen, I., Leary, P., Leonhardt, M., Malin, P., Martínez-Garzón, P., Passmore, K., Passmore, P., Valenzuela, S., & Wollin, C. (2019). Controlling fluid-induced seismicity during a 6.1-km-deep geothermal stimulation in Finland. *Science Advances*, *5*(5), eaav7224. <https://doi.org/10.1126/sciadv.aav7224> (see p. 2)
- Lachenbruch, A. H. (1980). Frictional heating, fluid pressure, and the resistance to fault motion. *Journal of Geophysical Research*, *85*(B11), 6097. <https://doi.org/10.1029/JB085iB11p06097> (see p. 5)
- Larochelle, S., Lapusta, N., Ampuero, J.-P., & Cappa, F. (2021). Constraining Fault Friction and Stability With Fluid-Injection Field Experiments. *Geophysical Research Letters*, *48*(10), 1–17. <https://doi.org/10.1029/2020GL091188> (see pp. 2, 22, 59)

-
- Latour, S., Voisin, C., Renard, F., Larose, E., Catheline, S., & Campillo, M. (2013). Effect of fault heterogeneity on rupture dynamics: an experimental approach using ultrafast ultrasonic imaging. *Journal of Geophysical Research: Solid Earth*, *118*(11), 5888–5902. <https://doi.org/10.1002/2013JB010231> (see pp. 1, 24)
- Levant, A. (2005). Homogeneity approach to high-order sliding mode design. *Automatica*, *41*(5), 823–830. <https://doi.org/10.1016/j.automatica.2004.11.029> (see pp. 232, 236)
- Levant, A., & Livne, M. (2020). Robust exact filtering differentiators [Finite-time estimation, diagnosis and synchronization of uncertain systems]. *European Journal of Control*, *55*, 33–44. <https://doi.org/10.1016/j.ejcon.2019.08.006> (see pp. 104, 240)
- Lewis, F., Vrabie, D., & Syrmos, V. (2012). *Optimal control*. Wiley. (See pp. 3, 38, 42, 44, 53, 67, 81, 112, 116, 229, 235).
- Li, T., Cai, M., & Cai, M. (2007). A review of mining-induced seismicity in china. *International Journal of Rock Mechanics and Mining Sciences*, *44*(8), 1149–1171. <https://doi.org/10.1016/j.ijrmms.2007.06.002> (see p. 23)
- Li, Y., Oh, J., Mitra, R., & Hebblewhite, B. (2016). A constitutive model for a laboratory rock joint with multi-scale asperity degradation. *Computers and Geotechnics*, *72*, 143–151. <https://doi.org/10.1016/j.compgeo.2015.10.008> (see p. 197)
- Li, Z., Elsworth, D., Wang, C., Boyd, L., Frone, Z., Metcalfe, E., Nieto, A., Porse, S., Vandermeer, W., Podgorney, R., Huang, H., McLing, T., Neupane, G., Chakravarty, A., Cook, P. J., Dobson, P. F., Doughty, C. A., Guglielmi, Y., Hopp, C., . . . McClure, M. W. (2021). Constraining maximum event magnitude during injection-triggered seismicity. *Nature Communications*, *12*(1), 1–9. <https://doi.org/10.1038/s41467-020-20700-4> (see pp. 2, 33)
- Lieou, C. K. C., Daub, E. G., Guyer, R. A., Ecke, R. E., Marone, C., & Johnson, P. A. (2017). Simulating stick-slip failure in a sheared granular layer using a physics-based constitutive model. *Journal of Geophysical Research: Solid Earth*, *122*(1), 295–307. <https://doi.org/10.1002/2016JB013627> (see p. 100)
- Lim, H., Deng, K., Kim, Y., Ree, J.-H., Song, T.-R. A., & Kim, K.-H. (2020). The 2017 mw 5.5 pohang earthquake, south korea, and poroelastic stress changes associated with fluid injection [e2019JB019134 2019JB019134]. *Journal of Geophysical Research: Solid Earth*, *125*(6), e2019JB019134. <https://doi.org/10.1029/2019JB019134> (see p. 34)

-
- Lin, F. (2000). An optimal control approach to robust control design. *International Journal of Control*, 73(3), 177–186. <https://doi.org/10.1080/002071700219722> (see pp. 46, 112)
- Lin, F., Brandt, R. D., & Sun, J. (1990). Robust control of nonlinear systems: compensating for uncertainty. *1990 American Control Conference*, 3048–3049. <https://doi.org/10.23919/ACC.1990.4791280> (see p. 46)
- Lin, F., Brandt, R. D., & Sun, J. (1992). Robust control of nonlinear systems: compensating for uncertainty. *International Journal of Control*, 56(6), 1453–1459. <https://doi.org/10.1080/00207179208934374> (see pp. 112, 113)
- Lin, F., & Olbrot, A. W. (1996). An lqr approach to robust control of linear systems with uncertain parameters. *Proceedings of 35th IEEE Conference on Decision and Control*, 4, 4158–4163 vol.4. <https://doi.org/10.1109/CDC.1996.577433> (see pp. 46, 112)
- Lin, F., & Zhang, W. (1993). Robust control of nonlinear systems without matching condition. *Proceedings of 32nd IEEE Conference on Decision and Control*, 2572–2577 vol.3. <https://doi.org/10.1109/CDC.1993.325660> (see p. 46)
- Linker, M. F., & Dieterich, J. H. (1992). Effects of variable normal stress on rock friction: observations and constitutive equations. *Journal of Geophysical Research: Solid Earth*, 97(B4), 4923–4940. <https://doi.org/https://doi.org/10.1029/92JB00017> (see p. 100)
- Lockner, D. A., Byerlee, J. D., Kuksenko, V., Ponomarev, A., & Sidorin, A. (1991). Quasi-static fault growth and shear fracture energy in granite. *Nature*, 350(6313), 39–42. <https://doi.org/10.1038/350039a0> (see pp. 2, 28)
- Lockner, D. A., Okubo, P. G., & Dieterich, J. H. (1982). Containment of stick-slip failures on a simulated fault by pore fluid injection. *Geophysical Research Letters*, 9(8), 801–804. <https://doi.org/10.1029/GL009i008p00801> (see p. 1)
- Logan, J. (2013). *Applied mathematics*. Wiley. <https://books.google.fr/books?id=uEVYKvk8EnIC>. (See pp. 221, 222)
- Lyapunov, A. M. (1966). *Stability of Motion*. Academic Press. (See p. 41).
- Marone, C., Raleigh, C. B., & Scholz, C. H. (1990). Frictional behavior and constitutive modeling of simulated fault gouge. *Journal of Geophysical Research: Solid Earth*, 95(B5), 7007–7025. <https://doi.org/10.1029/JB095iB05p07007> (see p. 197)
- Marone, C., & Scholz, C. (1989). Particle-size distribution and microstructures within simulated fault gouge [Friction phenomena in rock]. *Journal of Structural Geology*,

-
- 11(7), 799–814. [https://doi.org/https://doi.org/10.1016/0191-8141\(89\)90099-0](https://doi.org/https://doi.org/10.1016/0191-8141(89)90099-0)
(see p. 197)
- Mattei, G. (2015). *Robust nonlinear control: from continuous time to sampled-data with aerospace applications* (Doctoral dissertation). Université Paris Sud. Paris, France.
(See pp. 39, 46, 47, 142).
- McCrum, D., & Williams, M. (2016). An overview of seismic hybrid testing of engineering structures. *Engineering Structures*, 118, 240–261. <https://doi.org/https://doi.org/10.1016/j.engstruct.2016.03.039> (see p. 101)
- McGarr, A. (2014). Maximum magnitude earthquakes induced by fluid injection. *Journal of Geophysical Research: Solid Earth*, 119(2), 1008–1019. <https://doi.org/10.1002/2013JB010597> (see p. 34)
- McGarr, A., Simpson, D., & Seeber, L. (2002). 40 - case histories of induced and triggered seismicity. In W. H. Lee, H. Kanamori, P. C. Jennings, & C. Kisslinger (Eds.), *International handbook of earthquake and engineering seismology, part a* (pp. 647–661). Academic Press. [https://doi.org/https://doi.org/10.1016/S0074-6142\(02\)80243-1](https://doi.org/https://doi.org/10.1016/S0074-6142(02)80243-1). (See pp. 1, 2, 23)
- Mclaskey, G. C., & Yamashita, F. (2017). Slow and fast ruptures on a laboratory fault controlled by loading characteristics. *Journal of Geophysical Research: Solid Earth*, 122(5), 3719–3738. <https://doi.org/https://doi.org/10.1002/2016JB013681> (see p. 1)
- Mercado-Uribe, J. Á., & Moreno, J. A. (2020). Discontinuous integral action for arbitrary relative degree in sliding-mode control. *Automatica*, 118, 109018. <https://doi.org/https://doi.org/10.1016/j.automatica.2020.109018> (see pp. 232, 236)
- Mitra, S., Rodríguez de Castro, A., & El Mansori, M. (2018). The effect of ageing process on three-point bending strength and permeability of 3D printed sand molds. *International Journal of Advanced Manufacturing Technology*, 97(1-4), 1241–1251. <https://doi.org/10.1007/s00170-018-2024-8> (see p. 185)
- Mollon, G., Quacquarelli, A., Andò, E., & Viggiani, G. (2020). Can friction replace roughness in the numerical simulation of granular materials? *Granular Matter*, 22(2), 42. <https://doi.org/10.1007/s10035-020-1004-5> (see p. 2)
- Moreno, J. A. (2016). Discontinuous integral control for mechanical systems. *2016 14th International Workshop on Variable Structure Systems (VSS)*, 142–147. <https://doi.org/10.1109/VSS.2016.7506906> (see pp. 229, 231)

-
- Nasuno, S., Kudrolli, A., Bak, A., & Gollub, J. P. (1998). Time-resolved studies of stick-slip friction in sheared granular layers. *Phys. Rev. E*, 58, 2161–2171. <https://doi.org/10.1103/PhysRevE.58.2161> (see p. 1)
- Newland, P. L., & Allely, B. H. (1957). Volume changes in drained triaxial tests on granular materials. *Géotechnique*, 7(1), 17–34. <https://doi.org/10.1680/geot.1957.7.1.17> (see p. 195)
- Niemeijer, A. R., & Spiers, C. J. (2007). A microphysical model for strong velocity weakening in phyllosilicate-bearing fault gouges. *Journal of Geophysical Research: Solid Earth*, 112(B10). <https://doi.org/10.1029/2007JB005008> (see p. 1)
- Nussbaum, J., & Ruina, A. (1987). A two degree-of-freedom earthquake model with static/dynamic friction. *Pure and Applied Geophysics*, 125(4), 629–656. <https://doi.org/10.1007/BF00879576> (see pp. 26, 183)
- Ogata, K. (2010). *Modern control engineering*. Prentice-Hall. (See pp. 3, 37, 38, 40, 53, 68, 83, 95).
- Papachristos, E., & Stefanou, I. (2021). Artificial Intelligence in the service of earthquake prevention. *to be submitted* (see pp. 135, 145).
- Papamichos, E., Tronvoll, J., Vardoulakis, I., Labuz, J. F., Skjærstein, A., Unander, T. E., & Sulem, J. (2000). Constitutive testing of Red Wildmoor sandstone. *Mechanics of Cohesive-Frictional Materials*, 5, 1–40. [https://doi.org/10.1002/\(SICI\)1099-1484\(200001\)5](https://doi.org/10.1002/(SICI)1099-1484(200001)5) (see p. 190)
- Patton, F. D. (1966). Multiple modes of shear failure in rock. *Proc. 1st Congr. Int. Soc. Rock Mech.*, 509–513. <https://www.onepetro.org/conference-paper/ISRM-1CONGRESS-1966-087> (see p. 195)
- Perras, M. A., & Vogler, D. (2019). Compressive and tensile behavior of 3d-printed and natural sandstones. *Transport in Porous Media*, 129(2), 559–581. <https://doi.org/10.1007/s11242-018-1153-8> (see p. 105)
- Petersen, I. (1987). Disturbance attenuation and H_∞ optimization: a design method based on the algebraic riccati equation. *IEEE Transactions on Automatic Control*, 32(5), 427–429. <https://doi.org/10.1109/TAC.1987.1104609> (see p. 46)
- Phanomchoeng, G., & Rajamani, R. (2010). Observer design for lipschitz nonlinear systems using riccati equations. *Proceedings of the 2010 American Control Conference*, 6060–6065. <https://doi.org/10.1109/ACC.2010.5531294> (see pp. 39, 53)

-
- Pimienta, L., Fortin, J., & Guéguen, Y. (2015). Experimental study of Young's modulus dispersion and attenuation in fully saturated sandstones. *Geophysics*, *80*(5), L57–L72. <https://doi.org/10.1190/geo2014-0532.1> (see p. 190)
- Pipping, E. (2019). Existence of long-time solutions to dynamic problems of viscoelasticity with rate-and-state friction. *ZAMM Zeitschrift für Angewandte Mathematik und Mechanik*, *99*(11), 1–10. <https://doi.org/10.1002/zamm.201800263> (see pp. 7, 8)
- Pluijm, van der, R. (1999). *Out-of-plane bending of masonry : behaviour and strength* (Doctoral dissertation) [Proefschrift.]. Department of the Built Environment. Technische Universiteit Eindhoven. <https://doi.org/10.6100/IR528212>. (See pp. 174, 213)
- Popov, V., Grzemba, B., Starcevic, J., & Popov, M. (2012). Rate and state dependent friction laws and the prediction of earthquakes: what can we learn from laboratory models? *Tectonophysics*, *532-535*, 291–300. <https://doi.org/https://doi.org/10.1016/j.tecto.2012.02.020> (see pp. 1, 24)
- Power, W. L., Tullis, T. E., & Weeks, J. D. (1988). Roughness and wear during brittle faulting. *Journal of Geophysical Research: Solid Earth*, *93*(B12), 15268–15278. <https://doi.org/10.1029/JB093iB12p15268> (see pp. 197–199)
- Qu, Z. (1992). Global stabilization of nonlinear systems with a class of unmatched uncertainties. *[Proceedings 1992] The First IEEE Conference on Control Applications*, 498–503 vol.1. <https://doi.org/10.1109/CCA.1992.269823> (see p. 46)
- Qu, Z. (1995). Robust control of nonlinear uncertain systems without generalized matching conditions. *IEEE Transactions on Automatic Control*, *40*(8), 1453–1460. <https://doi.org/10.1109/9.402240> (see p. 46)
- Qu, Z., & Dorsey, J. (1991). Robust Control of Generalized Dynamic Systems Without the Matching Conditions. *Journal of Dynamic Systems, Measurement, and Control*, *113*(4), 582–589. <https://doi.org/10.1115/1.2896461> (see p. 46)
- Qu, Z. (1993). Robust control of nonlinear uncertain systems under generalized matching conditions. *1993 American Control Conference*, 117–121. <https://doi.org/10.23919/ACC.1993.4792818> (see p. 46)
- Queener, C., Smith, T., & Mitchell, W. (1965). Transient wear of machine parts. *Wear*, *8*(5), 391–400. [https://doi.org/https://doi.org/10.1016/0043-1648\(65\)90170-5](https://doi.org/https://doi.org/10.1016/0043-1648(65)90170-5) (see p. 197)

-
- Raghavan, S., & Hedrick, J. K. (1994). Observer design for a class of nonlinear systems. *International Journal of Control*, *59*(2), 515–528. <https://doi.org/10.1080/00207179408923090> (see pp. 39, 53)
- Rajamani, R. (1998). Observers for lipschitz nonlinear systems. *IEEE Transactions on Automatic Control*, *43*(3), 397–401. <https://doi.org/10.1109/9.661604> (see pp. 39, 53)
- Rajamani, R., Jeon, W., Movahedi, H., & Zemouche, A. (2020). On the need for switched-gain observers for non-monotonic nonlinear systems. *Automatica*, *114*, 108814. <https://doi.org/https://doi.org/10.1016/j.automatica.2020.108814> (see p. 83)
- Raleigh, C. B., Healy, J. H., & Bredehoeft, J. D. (1976). An experiment in earthquake control at rangely, colorado. *Science*, *191*(4233), 1230–1237. <https://doi.org/10.1126/science.191.4233.1230> (see pp. 1, 2, 23, 24)
- Rattez, H., Stefanou, I., & Sulem, J. (2018a). The importance of Thermo-Hydro-Mechanical couplings and microstructure to strain localization in 3D continua with application to seismic faults. Part I: Theory and linear stability analysis. *Journal of the Mechanics and Physics of Solids*, *115*(March), 54–76. <https://doi.org/10.1016/j.jmps.2018.03.004> (see pp. 5, 197)
- Rattez, H., Stefanou, I., Sulem, J., Veveakis, M., & Poulet, T. (2018a). The importance of Thermo-Hydro-Mechanical couplings and microstructure to strain localization in 3D continua with application to seismic faults. Part II: Numerical implementation and post-bifurcation analysis. *Journal of the Mechanics and Physics of Solids*, *115*, 1–29. <https://doi.org/10.1016/j.jmps.2018.03.003> (see pp. 5, 214)
- Rattez, H., Stefanou, I., Sulem, J., Veveakis, M., & Poulet, T. (2018b). Numerical analysis of strain localization in rocks with thermo-hydro-mechanical couplings using cosserat continuum. *Rock Mechanics and Rock Engineering*, *51*(10), 3295–3311. <https://doi.org/10.1007/s00603-018-1529-7> (see pp. 131, 197, 214)
- Rattez, H., & Veveakis, M. (2020). Weak phases production and heat generation control fault friction during seismic slip. *Nature Communications*, *11*(1), 1–8. <https://doi.org/10.1038/s41467-019-14252-5> (see p. 5)
- Reber, J. E., Hayman, N. W., & Lavier, L. L. (2014). Stick-slip and creep behavior in lubricated granular material: insights into the brittle-ductile transition. *Geophysical Research Letters*, *41*(10), 3471–3477. <https://doi.org/https://doi.org/10.1002/2014GL059832> (see p. 1)

-
- Reid, H. F. (1910). The Mechanics of the Earthquake, The California Earthquake of April 18, 1906. In *Report of the state earthquake investigation commission, vol. 2*. Carnegie Institution of Washington. (See p. 26).
- Rice, J. R., & Ruina, A. L. (1983). Stability of Steady Frictional Slipping. *Journal of Applied Mechanics*, 50(2), 343–349. <https://doi.org/10.1115/1.3167042> (see pp. 3, 16–18, 141, 193)
- Rice, J. R. (1993). Spatio-temporal complexity of slip on a fault. *Journal of Geophysical Research*, 98(B6), 9885. <https://doi.org/10.1029/93JB00191> (see pp. 59, 61, 62, 64, 68)
- Rice, J. R. (2006). Heating and weakening of faults during earthquake slip. *Journal of Geophysical Research*, 111(B5), B05311. <https://doi.org/10.1029/2005JB004006> (see p. 5)
- Ritter, M. C., Leever, K., Rosenau, M., & Oncken, O. (2016). Scaling the sand-box—mechanical (dis) similarities of granular materials and brittle rock. *Journal of Geophysical Research: Solid Earth*, 121(9), 6863–6879. <https://doi.org/https://doi.org/10.1002/2016JB012915> (see p. 1)
- Rosakis, A. J., Samudrala, O., & Coker, D. (1999). Cracks faster than the shear wave speed. *Science*, 284(5418), 1337–1340. <https://doi.org/10.1126/science.284.5418.1337> (see p. 1)
- Roscoe, K. H., Schofield, A. N., & Wroth, C. P. (1958). On the yielding of soils. *Géotechnique*, 8(1), 22–53. <https://doi.org/10.1680/geot.1958.8.1.22> (see p. 191)
- Rosenau, M., Corbi, F., & Dominguez, S. (2017). Analogue earthquakes and seismic cycles: experimental modelling across timescales. *Solid Earth*, 8(3), 597–635. <https://doi.org/10.5194/se-8-597-2017> (see p. 24)
- Rosenau, M., Lohrmann, J., & Oncken, O. (2009). Shocks in a box: an analogue model of subduction earthquake cycles with application to seismotectonic forearc evolution. *Journal of Geophysical Research: Solid Earth*, 114(B1). <https://doi.org/https://doi.org/10.1029/2008JB005665> (see p. 1)
- Rosenau, M., Nerlich, R., Brune, S., & Oncken, O. (2010). Experimental insights into the scaling and variability of local tsunamis triggered by giant subduction megathrust earthquakes. *Journal of Geophysical Research: Solid Earth*, 115(B9). <https://doi.org/https://doi.org/10.1029/2009JB007100> (see p. 1)
- Roshankhah, S., Marshall, J. P., Tengattini, A., Ando, E., Rubino, V., Rosakis, A. J., Viggiani, G., & Andrade, J. E. (2018). Neutron imaging: a new possibility for

-
- laboratory observation of hydraulic fractures in shale? *Géotechnique Letters*, 8(4), 316–323. <https://doi.org/10.1680/jgele.18.00129> (see p. 1)
- Rousseau, Q., Sciarra, G., Gelet, R., & Marot, D. (2020). Modelling the poroelastoplastic behaviour of soils subjected to internal erosion by suffusion. *International Journal for Numerical and Analytical Methods in Geomechanics*, 44(1), 117–136. <https://doi.org/https://doi.org/10.1002/nag.3014> (see p. 79)
- Rubino, V., Rosakis, A. J., & Lapusta, N. (2017). Understanding dynamic friction through spontaneously evolving laboratory earthquakes. *Nature Communications*, 8(1), 15991. <https://doi.org/10.1038/ncomms15991> (see p. 1)
- Rubinstein, J. L., Ellsworth, W. L., Chen, K. H., & Uchida, N. (2012). Fixed recurrence and slip models better predict earthquake behavior than the time- and slip-predictable models: 1. repeating earthquakes. *Journal of Geophysical Research: Solid Earth*, 117(B2). <https://doi.org/https://doi.org/10.1029/2011JB008724> (see p. 1)
- Rubinstein, J. L., & Mahani, A. B. (2015). Myths and Facts on Wastewater Injection, Hydraulic Fracturing, Enhanced Oil Recovery, and Induced Seismicity. *Seismological Research Letters*, 86(4), 1060–1067. <https://doi.org/10.1785/0220150067> (see pp. 1, 23)
- Rudnicki, J. W., & Chen, C. H. (1988). Stabilization of rapid frictional slip on a weakening fault by dilatant hardening. *Journal of Geophysical Research*, 93(B5), 4745–4757. <https://doi.org/10.1029/JB093iB05p04745> (see p. 5)
- Ruina, A. (1983). Slip instability and state variable friction laws. *Journal of Geophysical Research: Solid Earth*, 88(B12), 10359–10370. <https://doi.org/10.1029/JB088iB12p10359> (see pp. 3, 7, 18)
- Saber, O., Chester, F. M., & Alvarado, J. L. (2016). Development of a material-testing machine for study of friction: experimental analysis of machine dynamics and friction of rock. *Experimental Mechanics*, 56(5), 813–831. <https://doi.org/10.1007/s11340-015-0125-y> (see p. 100)
- Schmittbuhl, J., Gentier, S., & Roux, S. (1993). Field measurements of the roughness of fault surfaces. *Geophysical Research Letters*, 20(8), 639–641. <https://doi.org/10.1029/93GL00170> (see p. 199)
- Schneider-Muntau, B., Medicus, G., Desrues, J., Andò, E., & Viggiani, G. (2021). Investigation of uncertainty in strength parameter identification. In M. Barla, A. Di

-
- Donna, & D. Sterpi (Eds.), *Challenges and innovations in geomechanics* (pp. 277–284). Springer International Publishing. (See p. 40).
- Scholz, C. H. (2002). *The mechanics of earthquakes and faulting* (2nd ed.). Cambridge University Press. <https://doi.org/10.1017/CBO9780511818516>. (See pp. 1, 3, 5, 6, 9, 12, 14, 25, 26, 28, 107, 109, 117, 183)
- Schultz, R., Skoumal, R. J., Brudzinski, M. R., Eaton, D., Baptie, B., & Ellsworth, W. (2020). Hydraulic fracturing-induced seismicity [e2019RG000695 2019RG000695]. *Reviews of Geophysics*, 58(3), e2019RG000695. <https://doi.org/10.1029/2019RG000695> (see pp. 1, 23)
- Schulze, D. (2003). Time- and velocity-dependent properties of powders effecting slip-stick oscillations. *Chemical Engineering & Technology*, 26(10), 1047–1051. <https://doi.org/https://doi.org/10.1002/ceat.200303112> (see p. 1)
- Scuderi, M. M., Carpenter, B. M., Johnson, P. A., & Marone, C. (2015). Poromechanics of stick-slip frictional sliding and strength recovery on tectonic faults. *Journal of Geophysical Research: Solid Earth*, 120(10), 6895–6912. <https://doi.org/https://doi.org/10.1002/2015JB011983> (see pp. 1, 100)
- Scuderi, M., Collettini, C., & Marone, C. (2017). Frictional stability and earthquake triggering during fluid pressure stimulation of an experimental fault. *Earth and Planetary Science Letters*, 477, 84–96. <https://doi.org/https://doi.org/10.1016/j.epsl.2017.08.009> (see p. 100)
- Scuderi, M., Collettini, C., Viti, C., Tinti, E., & Marone, C. (2017). Evolution of shear fabric in granular fault gouge from stable sliding to stick slip and implications for fault slip mode. *Geology*, 45(8), 731–734. <https://doi.org/10.1130/G39033.1> (see pp. 28, 100, 109)
- Segall, P., & Lu, S. (2015). Injection-induced seismicity: Poroelastic and earthquake nucleation effects. *Journal of Geophysical Research: Solid Earth*, 120(7), 5082–5103. <https://doi.org/10.1002/2015JB012060> (see pp. 79, 93)
- Segall, P., & Rice, J. R. (1995). Dilatancy, compaction, and slip instability of a fluid-infiltrated fault. *Journal of Geophysical Research: Solid Earth*, 100(B11), 22155–22171. <https://doi.org/https://doi.org/10.1029/95JB02403> (see pp. 46, 79, 130)
- Semblat, J. F., Chaillat, S., Lenti, L., Meza-Fajardo, K., & Santisi d’Avila, M. P. (2021). Modeling seismic wave propagation and interaction: recent advances and future challenges. In M. Barla, A. Di Donna, & D. Sterpi (Eds.), *Challenges and in-*

-
- novations in geomechanics* (pp. 661–668). Springer International Publishing. (See p. 2).
- Semblat, J. F., & Pecker, A. (2009). Waves and vibrations in soils: Earthquakes, Traffic, Shocks, Construction works. In *Waves and vibrations in soils: Earthquakes, Traffic, Shocks, Construction works* (500 p). IUSS Press. <https://hal.archives-ouvertes.fr/hal-00851291>. (See p. 1)
- Shapiro, S. A., Krüger, O. S., & Dinske, C. (2013). Probability of inducing given-magnitude earthquakes by perturbing finite volumes of rocks. *Journal of Geophysical Research: Solid Earth*, *118*(7), 3557–3575. <https://doi.org/10.1002/jgrb.50264> (see p. 33)
- Shtessel, Y., Edwards, C., Fridman, L., & Levant, A. (2015). *Sliding mode control and observation* (1st). Birkhäuser Basel. (See p. 83).
- Skarbek, R. M., & Savage, H. M. (2019). RSFit3000: A MATLAB GUI-based program for determining rate and state frictional parameters from experimental data. *Geosphere*, *15*(5), 1665–1676. <https://doi.org/10.1130/GES02122.1> (see p. 193)
- Smith, J. D., Heimisson, E. R., S., B., & Avouac, J.-P. (2021). Stress-based forecasting of induced seismicity with instantaneous earthquake failure functions: applications to the groningen gas reservoir. *EarthArXiv*. <https://doi.org/10.31223/X5MC96> (see p. 97)
- Stathas, A. (2021). *Numerical modeling of earthquake faults* (Doctoral dissertation). École Centrale de Nantes. Nantes, France. (See p. 5).
- Stefanou, I., & Tzortzopoulos, G. (2021). Control instabilities and incite slow-slip in generalized burridge-knopoff models. *arXiv:2008.03755*. <https://arxiv.org/abs/2008.03755> (see pp. 9, 35, 68, 69, 72, 74, 117, 119)
- Stefanou, I., Tzortzopoulos, G., & Braun, P. (2021). Double-shear apparatus for frictional instabilities [French patent (PENDING): FR2109102]. (See p. 101).
- Stefanou, I. (2019). Controlling anthropogenic and natural seismicity: insights from active stabilization of the spring-slider model. *Journal of Geophysical Research: Solid Earth*, *124*(8), 8786–8802. <https://doi.org/10.1029/2019JB017847> (see pp. 3, 9, 10, 13, 14, 24, 28, 35, 60, 107, 109, 117, 183)
- Svetlizky, I. (2019). Laboratory earthquakes in large-scale rock experiments reveal singular crack-like rupture dynamics. *Journal of Geophysical Research: Solid Earth*, *124*(5), 4639–4641. <https://doi.org/https://doi.org/10.1029/2019JB017779> (see p. 1)

-
- Tal, Y., Rubino, V., Rosakis, A. J., & Lapusta, N. (2020). Illuminating the physics of dynamic friction through laboratory earthquakes on thrust faults. *Proceedings of the National Academy of Sciences*, *117*(35), 21095–21100. <https://doi.org/10.1073/pnas.2004590117> (see p. 2)
- Tinti, E., Scuderi, M. M., Scognamiglio, L., Di Stefano, G., Marone, C., & Collettini, C. (2016). On the evolution of elastic properties during laboratory stick-slip experiments spanning the transition from slow slip to dynamic rupture. *Journal of Geophysical Research: Solid Earth*, *121*(12), 8569–8594. <https://doi.org/https://doi.org/10.1002/2016JB013545> (see p. 2)
- Torres-González, V., Sanchez, T., Fridman, L. M., & Moreno, J. A. (2017). Design of continuous twisting algorithm. *Automatica*, *80*, 119–126. <https://doi.org/https://doi.org/10.1016/j.automatica.2017.02.035> (see pp. 229, 231, 233, 236)
- Tzortzopoulos, G., Braun, P., & Stefanou, I. (2021). Absorbent porous paper reveals how earthquakes could be mitigated [e2020GL090792 2020GL090792]. *Geophysical Research Letters*, *48*(3), e2020GL090792. <https://doi.org/https://doi.org/10.1029/2020GL090792> (see pp. 2, 3, 9, 10, 12, 27, 29, 30, 32, 107, 109, 117)
- Tzortzopoulos, G., Jarry-Cammas, V., Smith, J., Avouac, J.-P., & Stefanou, I. (2021). Controlling seismicity in large projects of geothermal energy and/or co2 sequestration [GMG IAB Meeting 2021: Oral Presentation]. (See pp. 93, 97).
- Tzortzopoulos, G., Stefanou, I., & Braun, P. (2019). Designing Experiments for Controlling earthQuakes (CoQuake) by Fluid Injection. *12th HSTAM 2019 International Congress on Mechanics*. https://www.researchgate.net/publication/340869319_Designing_Experiments_for_Controlling_earthQuakes_CoQuake_by_Fluid_Injection (see pp. 9, 105, 117, 190)
- Upadhyay, M., Sivarupan, T., & El Mansori, M. (2017). 3D printing for rapid sand casting—A review. *Journal of Manufacturing Processes*, *29*, 211–220. <https://doi.org/10.1016/j.jmapro.2017.07.017> (see p. 187)
- van der Elst, N. J., Page, M. T., Weiser, D. A., Goebel, T. H., & Hosseini, S. M. (2016). Induced earthquake magnitudes are as large as (statistically) expected. *Journal of Geophysical Research: Solid Earth*, *121*(6), 4575–4590. <https://doi.org/10.1002/2016JB012818> (see p. 32)
- Van Loan, C. (1978). Computing integrals involving the matrix exponential. *IEEE Transactions on Automatic Control*, *23*(3), 395–404. <https://doi.org/10.1109/TAC.1978.1101743> (see p. 115)

-
- Varamashvili, N., Chelidze, T., & Lursmanashvili, O. (2008). Phase synchronization of slips by periodical (tangential and normal) mechanical forcing in the spring-slider model. *Acta Geophysica*, *56*(2), 357–371. <https://doi.org/10.2478/s11600-008-0006-1> (see p. 1)
- Vardoulakis, I. (2000). Catastrophic landslides due to frictional heating of the failure plane. *Mechanics of Cohesive-Frictional Materials*, *5*(6), 443–467. [https://doi.org/10.1002/1099-1484\(200008\)5:6<443::AID-CFM104>3.0.CO;2-W](https://doi.org/10.1002/1099-1484(200008)5:6<443::AID-CFM104>3.0.CO;2-W) (see p. 5)
- Vardoulakis, A. I. (2012). *Introduction to the mathematical theory of the theory of signals, systems and control*. Tziola. (See pp. 3, 37).
- Vardoulakis, A., Yannakoudakis, A., Wei, C., & Chai, T. (2021). Denominator assignment, invariants, and canonical forms under dynamic feedback compensation in linear multivariable nonsquare systems. *IEEE Transactions on Automatic Control*, *66*(10), 4903–4909. <https://doi.org/10.1109/TAC.2020.3044009> (see p. 37)
- Wood, D. M. (1991). Plasticity and yielding. In *Soil behaviour and critical state soil mechanics* (pp. 55–83). Cambridge University Press. <https://doi.org/10.1017/CBO9781139878272.004>. (See pp. 191, 204)
- Xia, K., & Rosakis, A. J. (2021). Laboratory earthquakes along faults with a low velocity zone: directionality and pulse-like ruptures. *Extreme Mechanics Letters*, *46*, 101321. <https://doi.org/https://doi.org/10.1016/j.eml.2021.101321> (see p. 1)
- Yamashita, F., Fukuyama, E., Xu, S., Mizoguchi, K., Kawakata, H., & Takizawa, S. (2018). Rupture preparation process controlled by surface roughness on meter-scale laboratory fault [Physics of Earthquake Rupture Propagation]. *Tectonophysics*, *733*, 193–208. <https://doi.org/https://doi.org/10.1016/j.tecto.2018.01.034> (see p. 1)
- Zang, A., Zimmermann, G., Hofmann, H., Stephansson, O., Min, K. B., & Kim, K. Y. (2019). How to Reduce Fluid-Injection-Induced Seismicity. *Rock Mechanics and Rock Engineering*, *52*(2), 475–493. <https://doi.org/10.1007/s00603-018-1467-4> (see p. 2)
- Zhou, K., Doyle, J., & Glover, K. (1996). *Robust and optimal control*. Prentice Hall. (See p. 42).
- Zhu, F., & Han, Z. (2002). A note on observers for lipschitz nonlinear systems. *IEEE Transactions on Automatic Control*, *47*(10), 1751–1754. <https://doi.org/10.1109/TAC.2002.803552> (see pp. 39, 53)

List of publications

Journal papers

- (1) Tzortzopoulos, G., Braun, P., & Stefanou, I. (2021). Absorbent porous paper reveals how earthquakes could be mitigated. *Geophysical Research Letters*, 48(3), e2020GL090792. DOI: [10.1029/2020GL090792](https://doi.org/10.1029/2020GL090792).
- (2) Braun, P., Tzortzopoulos, G., & Stefanou, I. (2021). Design of sand-based, 3-D-printed analog faults with controlled frictional properties. *Journal of Geophysical Research: Solid Earth*, 126(5), e2020JB020520. DOI: [10.1029/2020JB020520](https://doi.org/10.1029/2020JB020520).
- (3) Stefanou, I., & Tzortzopoulos, G. (2021). Preventing instabilities and inducing controlled, slow-slip in frictionally unstable systems. Preprint: [10.48550/ARXIV.2008.03755](https://arxiv.org/abs/10.48550/ARXIV.2008.03755). *Submitted*.
- (4) Gutiérrez-Oribio, D., Tzortzopoulos, G., Plestan, F., & Stefanou, I. (2021). Earthquake Control: An Emerging Application for Robust Control. Theory and Experimental Tests. Preprint: [10.48550/ARXIV.2203.00296](https://arxiv.org/abs/10.48550/ARXIV.2203.00296). *Submitted*.
- (5) Tzortzopoulos, G., Braun, P., & Stefanou, I. (2021). Controlling earthquake-like instabilities in the laboratory. *To be submitted*.
- (6) Tzortzopoulos, G., & Stefanou, I. (2021). Robust control of seismic faults coupled with diffusion processes using distant fluid injections. *In preparation*.

Patent

- Stefanou, I., Tzortzopoulos, G., & Braun, P. (2021). Double-Direct Shear for Controlling Lab-Quakes (D-DS/CoLabQuake) apparatus. No: FR2109102. *Pending*.

Conference proceedings

- (a) Tzortzopoulos, G., Stefanou, I., & Braun, P. (2019). Designing Experiments for Controlling earthQuakes (CoQuake) by Fluid Injection. *12th HSTAM 2019 International Congress on Mechanics: Oral Presentation*. Thessaloniki, Greece.
- (b) Braun, P., Tzortzopoulos, G., & Stefanou, I. (2019). Paper Towel as a Surrogate Geomaterial for Simulating Natural and Anthropogenic Earthquakes and their Mitigation. *AGU Fall Meeting 2019: Poster Session*. San Francisco, USA.
- (c) Tzortzopoulos, G., Jarry-Cammas, V., Smith, J., Avouac, J. P., & Stefanou, I. (2021). Controlling seismicity in large projects of geothermal energy and/or CO₂ sequestration. *GMG IAB Meeting 2021: Oral Presentation*. Remote Participation.
- (d) Tzortzopoulos, G., Braun, P., & Stefanou, I. (2021). Design of analogue fault gouges with custom frictional properties using 3D-printing with sand particles. *32th ALERT Workshop 2021: Poster Session*. Aussois, France.
- (e) Tzortzopoulos, G., Braun, P., Gutiérrez-Oribio, D., Plestan, F., & Stefanou, I. (2021). Preventing lab-quakes using advanced control theory. *32th ALERT Workshop 2021: Poster Session*. Aussois, France.
- (f) Aoude, A., Tzortzopoulos, G., & Stefanou, I. (2021). Design of analogue fault-like interfaces with custom rate-and-state frictional properties. *32th ALERT Workshop 2021: Poster Session*. Aussois, France.
- (g) Tzortzopoulos, G., Braun, P., & Stefanou, I. (2021). Controlling Earthquake-like Instabilities in the Laboratory. *AGU Fall Meeting 2021: Oral Presentation*. New Orleans, USA.
- (h) Braun, P., Tzortzopoulos, G., & Stefanou, I. (2021). Using 3D-printing with sand for designing analogue fault gouges in the laboratory. *AGU Fall Meeting 2021: Poster Session*. New Orleans, USA.
- (i) Stefanou, I., Tzortzopoulos, G. (2021). Preventing instabilities and inducing controlled, slow-slip in frictionally unstable systems by active fluid pressure control. *AGU Fall Meeting 2021: Poster Session*. New Orleans, USA.

Paper Towel: experimental characterization, modeling and scaling laws

A.1 Experimental configuration

Absorbent porous paper is used as an analogue material to explore earthquake mitigation. The dimensions of the paper sheet specimen are $15.0 \times 12.0 \text{ cm}^2$ (Figure A.1).

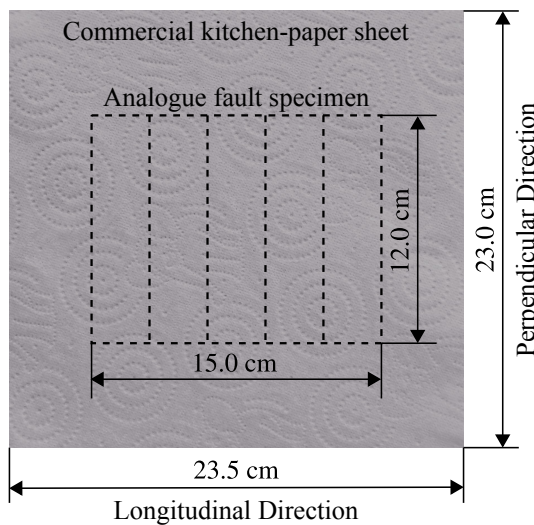


Figure A.1 – Dimensions of the tested sheet of absorbent porous kitchen-paper.

A direct tension apparatus (Adamel DY31) with a 100 N capacity load cell is used for the experiments (Figure A.2). Paper samples are fixed by dual-roller grips into the machine. Different additional assemblies are used depending on the testing configuration (with or without springs, and for single-stripe or five-stripe tests). This includes a metallic plate, a carbon-fiber plate, a metallic hanger and metallic rings. In addition, the paper specimen is attached to the different plates via duct tape. When no springs are used, the rings are directly connected to the metallic hanger.

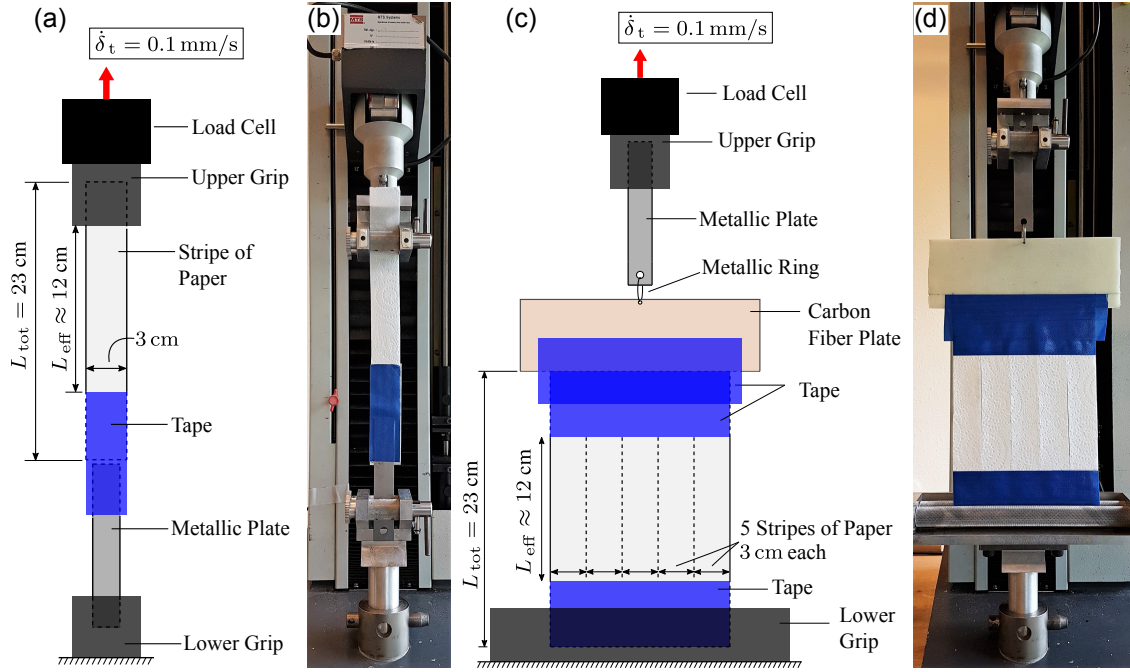


Figure A.2 – (a) Experimental assembly of a single paper stripe with (b) photo of the configuration. The stripe has a width of $W = 3$ cm and an effective length of $L_{\text{eff}} \approx 12$ cm. (c) Assembly of five paper stripes and (d) photo of the configuration. Each paper stripe has a width of $W = 3$ cm and an effective length of $L_{\text{eff}} = 12$ cm.

Commercial kitchen-paper (Brand: *Okay*, Type: *Original*) is bought on rolls, where the rolling direction corresponds to the longitudinal direction (Figure A.1). During the experiments, the principal loading is always applied in the perpendicular direction. Two different types of specimens are cut from these rolls and are installed in the experimental device. The single-stripe specimens (Figures A.2a-b) have a width of $W = 3$ cm (longitudinal direction) and an approximate effective length of $L_{\text{eff}} \approx 12$ cm (perpendicular direction). A five-stripe specimen is composed of five parallel stripes (Figures A.2c-d), each one corresponding to a single-stripe specimen (width: $W = 3$ cm, length: $L_{\text{eff}} = 12$ cm). This helps to increase the equivalent fault length and to avoid parasitic phenomena (heterogeneities and non-uniformities of stress-displacement fields (Pluijm, van der, 1999)) that might occur in large plate element paper sheets.

We use duct tape in order to reinforce the upper and lower regions of the paper. The paper sheet is connected to the upper grip via a carbon fiber plate and a metallic plate. The lower part of the paper is fixed to the lower grip. During the experiments, the loading ram is moving upwards with a constant velocity of $\dot{\delta}_t = 0.1$ or 0.05 mm/s. The vertical

displacement δ_t is recorded by the ram, while the load cell allows to keep track of the vertical tensile force F_t .

A.2 Mechanical properties of absorbent porous paper

Absorbent porous paper properties are investigated in eight different test types. We measure the material response under dry and wet conditions, in which the middle part of the paper stripe has been wetted until saturation before the loading procedure starts. Under both wet and dry conditions, we apply four different testing conditions: single-stripe specimen with and without spring, and five-stripe specimens with and without spring.

The specimens are loaded beyond failure in order to capture both loading and post-peak behavior. The same testing conditions are applied on dry and wet paper specimens. For each experiment, the sample's width W , its effective length L_{eff} , its deformation $\delta_f^{(i)}$ and force $F_f^{(i)}$ at failure are recorded. With the superscript (i), we denote the conditions (dry or wet) in which the experiment is conducted. Their elastic stiffness $k_{\text{el}}^{(i)}$ and post-peak stiffness $k_{\text{pp}}^{(i)}$ are measured through the pre- and post-peak slope of the force-deformation behavior (Figure A.3). These slopes are calculated using linear regression.

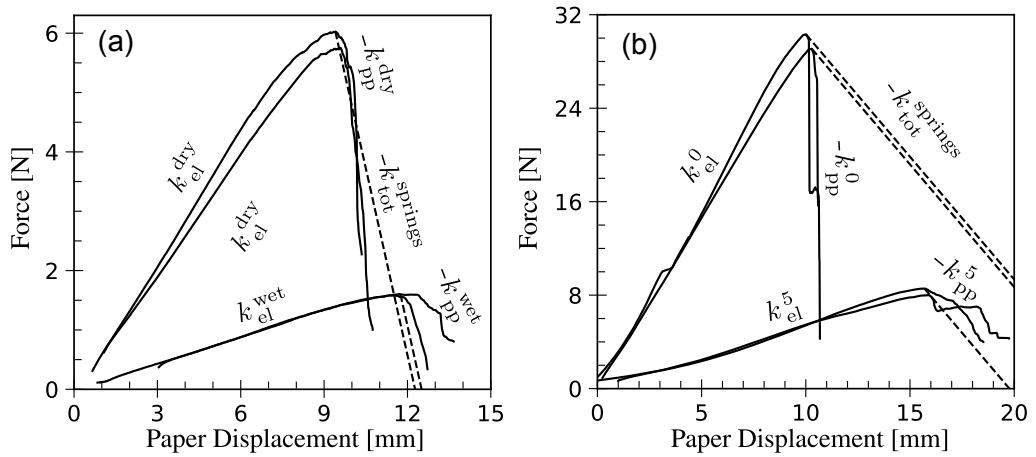


Figure A.3 – Force-paper displacement curves of dry and wet samples without springs. The sample consists of either (a) a single stripe or (b) five parallel stripes. Each stripe has a width of $W = 3$ cm and an effective length of $L_{\text{eff}} = 12$ cm. In each plot, the slopes of each branch are obtained by linear regression and are presented in Table A.1. The dashed lines correspond to the stiffness of the respective elastic springs.

A summary of the different testing types together with the average material properties is presented in Figure A.3 and in Table A.1. Comparing dry and wet properties, we can clearly distinguish a reduced elastic stiffness and peak force, as well as a lower post-peak slope in wet conditions (Figure A.3).

While $F_f^{(i)}$ and $k_{el}^{(i)}$ show comparable values between different samples, one can observe rather large standard deviations for $k_{pp}^{(i)}$. This illustrates the difficulty to characterize the post-peak behavior of a material in a repeatable manner, even under controlled laboratory conditions and for industrially produced specimens.

When we install the paper sample and the spring system in series (Figure 2.4), the force in both components is the same, but their displacement differs. The total displacement δ_t can be written as the sum of paper (δ_t^{paper}) and spring (δ_t^{spring}) displacement. Spring displacement can be derived by Hooke's law ($\delta_t^{\text{spring}} = F_t/k_{\text{tot}}^{\text{springs}}$) and thus the paper displacement is:

$$\delta_t^{\text{paper}} = \delta_t - \frac{F_t}{k_{\text{tot}}^{\text{springs}}} \quad (\text{A.1})$$

It becomes evident that a dynamic instability is generated only in dry conditions, where the material post-peak slope of $k_c^{\text{sw}} = |k_{pp}^{\text{dry}}|$ is higher than that of $k = k_{\text{tot}}^{\text{springs}}$ (dashed lines in Figure A.3, see also Section 1.2.1):

$$k = k_{\text{tot}}^{\text{springs}} < k_c^{\text{sw}} = |k_{pp}^{\text{dry}}| \quad (\text{A.2})$$

Accordingly, the measured post-peak slope in an F_t - δ_t^{paper} curve corresponds to the spring stiffness (Figures 2.3a and c). The magnitude of a paper-quake can be evaluated by the amount of released energy, which can be approximated by the area of the hatched triangle between the material post-peak path and the spring slope (Figures 2.3a and c, see also Section 1.2).

A.3 Spring-paper model

Having determined the material properties of paper specimens, we establish a simple spring-slider-like model for the five-stripe experiments, illustrated in Figure A.4a. This simple model embodies the basic physics of the paper experiments, successfully explains the existing experimental results and allows us to further explore the influence of segmentation and segment activation rate on the proposed injection strategy.

During progressive wetting, the number (i) of wet stripes of the specimen changes.

Table A.1 – Mechanical properties of the paper specimens (single- or five-stripes) in dry and wet conditions, without springs. Samples in wet conditions were completely wetted before loading started.

(a) Single-stripe experiments in dry conditions.						
	W	L_{eff}	δ_f^{dry}	F_f^{dry}	$k_{\text{el}}^{\text{dry}}$	$k_{\text{pp}}^{\text{dry}}$
	[mm]	[mm]	[mm]	[N]	[N/mm]	[N/mm]
Average:	30	119.3	9.08	5.86	0.70	4.18
Std Deviation:	0	5.2	1.10	0.33	0.05	2.35

(b) Single-stripe experiments in completely wet conditions.						
	W	L_{eff}	δ_f^{wet}	F_f^{wet}	$k_{\text{el}}^{\text{wet}}$	$k_{\text{pp}}^{\text{wet}}$
	[mm]	[mm]	[mm]	[N]	[N/mm]	[N/mm]
Average:	30	121.6	12.23	1.67	0.15	0.61
Std Deviation:	0	4.2	1.23	0.08	0.02	0.24

(c) 5-stripe experiments in dry conditions.						
	W	L_{eff}	δ_f^{dry}	F_f^{dry}	$k_{\text{el}}^{\text{dry}}$	$k_{\text{pp}}^{\text{dry}}$
	[mm]	[mm]	[mm]	[N]	[N/mm]	[N/mm]
Average:	150	120	10.15	29.71	3.02	29.28
Std Deviation:	0	0	0.14	0.62	0.10	4.02

(d) 5-stripe experiments in completely wet conditions.						
	W	L_{eff}	δ_f^{wet}	F_f^{wet}	$k_{\text{el}}^{\text{wet}}$	$k_{\text{pp}}^{\text{wet}}$
	[mm]	[mm]	[mm]	[N]	[N/mm]	[N/mm]
Average:	150	120	15.79	8.29	0.54	1.21
Std Deviation:	0	0	0.10	0.29	0.01	0.38

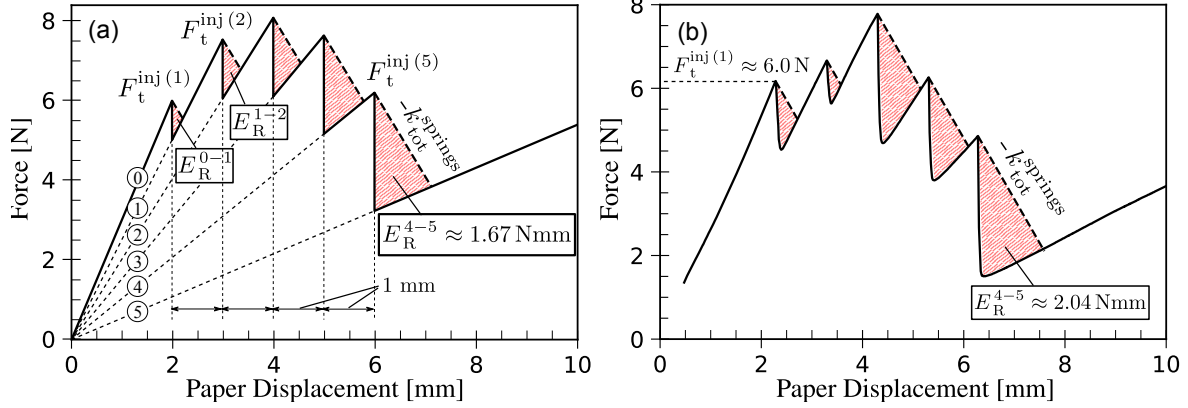


Figure A.4 – (a) Schematic testing procedure of a five-stripe paper model without springs. (b) Experimental force-paper displacement curves of a sample with five stripes and without springs assembled. The injection process for both cases starts at $F_t^{\text{inj}(1)} = 6.0$ N. Stripes are sprayed one after another every 1 mm of total displacement, until all the stripes are wet. Dynamic phenomena (red striped areas) would occur with an elastic spring, releasing $E_R^{(m-n)}$. The superscripts m and n represent the number of wet stripes before and after each injection. $F_t^{\text{inj}(j)}$ denotes the force at the j -th injection. The black dashed lines illustrate the potential stiffness and energy release if springs are used. For each case the maximum released energy is estimated.

Accordingly, the elastic stiffness $k_{\text{el}}^{(i)}$ changes with:

$$k_{\text{el}}^{(i)} = \frac{1}{5} \left(i k_{\text{el}}^{(5)} + (5 - i) k_{\text{el}}^{(0)} \right) \quad (\text{A.3})$$

For the model, we use the measured average elastic stiffness of the five-stripe sheets of $k_{\text{el}}^0 = k_{\text{el}}^{\text{dry}} = 3.02$ N/mm and $k_{\text{el}}^5 = k_{\text{el}}^{\text{wet}} = 0.54$ N/mm (Tables A.1c-d). Similarly, the maximum tensile force $F_f^{(i)}$ becomes after wetting:

$$F_f^{(i)} = \frac{1}{5} \left(i F_f^{(5)} + (5 - i) F_f^{(0)} \right) \quad (\text{A.4})$$

The values of $F_f^0 = F_f^{\text{dry}} = 29.71$ N and $F_f^5 = F_f^{\text{wet}} = 8.29$ N are evaluated on five-stripe samples (Tables A.1c-d). Wetting is carried out under different stress levels, where $F_t^{\text{inj}(j)}$ denotes the force under which the (j) -th wetting occurs.

After wetting the (i) -th stripe, the force-displacement curve follows either the spring slope $k_{\text{tot}}^{\text{springs}}$ or the material post-peak slope $k_{\text{pp}}^{\text{inj}(j)}$ (depending on Eq. (A.2)), before the force re-increases with the new slope of $k_{\text{el}}^{(i+1)}$ (Figure A.4a). The value of $k_{\text{tot}}^{\text{springs}} = 2.10$ N/mm was measured through calibration tests. The post-peak slope is investigated

Table A.2 – (a), (b) Single-stripe experiments in initially dry conditions without springs. At a tensile force of 3 N, water is sprayed on the stripe and the loading continues until failure. Superscripts indicate properties at wetting (inj) and at the final wet failure (wet).

(a)						
	W	L_{eff}	δ_t^{inj}	F_t^{inj}	$k_{\text{el}}^{\text{dry}}$	$k_{\text{pp}}^{\text{inj}}$
	[mm]	[mm]	[mm]	[N]	[N/mm]	[N/mm]
Average:	30	118.5	4.47	3.18	0.71	10.31
Std Deviation:	0	6.6	0.19	0.03	0.04	2.37

(b)						
	d_c^{inj}	ΔF_t^{inj}	δ_f^{wet}	F_f^{wet}	$k_{\text{el}}^{\text{wet}}$	$k_{\text{pp}}^{\text{wet}}$
	[mm]	[N]	[mm]	[N]	[N/mm]	[N/mm]
Average:	0.18	-3.02	13.08	1.65	0.19	0.76
Std Deviation:	0.04	0.05	0.85	0.13	0.01	0.19

in more detail in the following section.

In the case of a dynamic instability upon wetting from $m = i - 1$ to $n = i$ wet stripes, the energy $E_{\text{R}}^{(m-n)}$ is released. The energy is calculated as the triangular area between the material post-peak path and the spring slope (Figure A.4a, see also Section 1.2).

A.4 Induced stress drop upon wetting

While in the previous experiments, samples are wetted before loading, we now spray single-stripe samples during the experiment, at ~ 3 N of loading force (50% of F_f^{dry}). In these experiments no spring system is used, in order to capture only the material behavior, and avoid dynamic instabilities. In Table A.2, displacement δ_t^{inj} , force F_t^{inj} and post-peak stiffness $k_{\text{pp}}^{\text{inj}}$ at the time of injection are displayed. In addition, the (slip-weakening) characteristic distance d_c^{inj} and the force drop ΔF_t^{inj} at the time of injection are given.

We can note that the characteristic distance d_c^{inj} during this stress drop is close to zero and the post-peak segment is approximately vertical, resulting in a relatively large value of the post-peak slope $k_{\text{pp}}^{\text{inj}}$. After wetting, the loading continued until failure with a similar path as the initial wet stripes.

We also carry out progressive wetting in five-stripe experiments without springs. We

start the wetting at a certain percentage of the maximum force by wetting only one stripe. We spray the stripe three times in order to assure fast saturation. After each 1 mm of total displacement we spray the following stripe. This pattern is followed five times until all stripes are wet. To prevent water from wetting adjacent stripes by diffusion, barriers in form of thin plastic sheets are added between the stripes. The loading ram in this series of experiments is moving upwards with a constant velocity of $\dot{\delta}_t = 0.05$ mm/s, in order to assure saturation of the stripe after each injection.

The wetting process starts from outside and then it moves inwards. In that way we minimize the effect of some parasitic phenomena related to the experimental setup and apparatus used that can take place during wetting (mainly tilting). According to our post-process analyses, though, tilting can be considered as negligible. From an energetic point of view, the wetting sequence should not influence the size and the number of the stimulated seismic events (see also spring-slider energetic interpretation in Figure 2.1).

The experimental result with springs (Figure 2.6a) can be compared to the one obtained without springs (Figure A.4b). One can observe that the post-injection slopes are almost vertical. This leads us to the simplification in the model of $d_c^{\text{inj}} = 0$, which has negligible impact on the calculated released energy.

A.5 Real scale fault characteristics

The idealized planar dip-slip fault, depicted in Figure 2.1a, has a length of $L_{\text{ac}}^{\text{real}} = 6.5$ km. The rocks surrounding the fault zone have an apparent shear modulus of $G^{\text{real}} = 30$ GPa, while the average stress normal to the fault plane is $\sigma_n^{\text{real}} = 30$ MPa. Regarding its frictional properties, the fault zone shows an apparent shear stress drop equal to $\Delta\tau^{\text{real}} = \Delta\mu^{\text{real}}\sigma_n^{\text{real}} \approx 0.1 \times 30$ MPa = 3 MPa in a critical slip-weakening distance of $d_c^{\text{real}} = 50$ mm (Kanamori & Brodsky, 2004). $\Delta\mu^{\text{real}}$ denotes the apparent friction coefficient drop due to slip over the fault rupture area A^{real} . All fault's properties are summarized in Table A.3a.

A.6 Scaling laws

Using scaling laws, we can conceptualize the response of a real fault system through absorbent porous paper. The tensile force drop $\Delta F_t^{\text{model}}$ of the paper experiments is scaled by a factor a (units of inverse squared length):

Table A.3 – (a) In-situ properties of the ideal dip-slip fault. (b) Experimental values for the five-stripe model (Table A.1c) adopted for the scaling laws.

(a)					
G^{real}	depth	σ_n^{real}	$\Delta\mu^{\text{real}}$	$\Delta\tau^{\text{real}}$	d_c^{real}
[MPa]	[km]	[MPa]	[-]	[MPa]	[mm]
30000	4-6	30	0.10	3.0	50.0

(b)				
$k_{\text{tot}}^{\text{springs}}$	$\Delta F_t^{\text{model}} = F_f^{\text{dry}}$	d_c^{model}	$k_{\text{pp}}^{\text{model}} = k_{\text{pp}}^{\text{dry}}$	E_R^0
[N/mm]	[N]	[mm]	[N/mm]	[Nmm]
2.10	29.71	1.05	29.28	201

$$\Delta\tau^{\text{real}} = a \cdot \Delta F_t^{\text{model}} \quad (\text{A.5})$$

The characteristic real slip distance d_c^{real} and the model slip distance d_c^{model} are scaled by a factor b :

$$d_c^{\text{real}} = b \cdot d_c^{\text{model}} \quad (\text{A.6})$$

Using Eq. (A.2) for both experimental and in-situ cases, the critical stiffness per fault area \bar{k}_c^{real} for a dynamic instability is:

$$\bar{k}_c^{\text{real}} = \frac{a}{b} k_{\text{pp}}^{\text{model}}, \quad (\text{A.7})$$

where $k_{\text{pp}}^{\text{model}} = \Delta F_t^{\text{model}}/d_c^{\text{model}}$ is the experimental post-peak slope of porous paper. \bar{k}_c^{real} has units of stress over length.

Analogously, we can scale the spring stiffness of the experiments ($k^{\text{model}} = k_{\text{tot}}^{\text{springs}}$) to obtain the apparent stiffness of the rocks surrounding the fault zone \bar{k}^{real} :

$$\bar{k}^{\text{real}} = k^{\text{model}} \frac{a}{b} \quad (\text{A.8})$$

The activated fault length $L_{\text{ac}}^{\text{real}}$ can be calculated by the following expression:

$$L_{\text{ac}}^{\text{real}} = \frac{G^{\text{real}}}{\bar{k}^{\text{real}}}, \quad (\text{A.9})$$

where G^{real} is the apparent shear modulus of the rock material. Applying the characteristics of our dry five-stripe experiment (Table A.3b) and of the idealized dip-slip fault (Table A.3a), we get:

$$\bar{k}^{\text{real}} = 4.5 \text{ MPa/m} < \bar{k}_c^{\text{real}} = 60 \text{ MPa/m} \quad (\text{A.10})$$

This dynamic instability activates a fault length of $L_{\text{ac}}^{\text{real}} \approx 6.5 \text{ km}$ (Eq. (A.9) with $G^{\text{real}} = 30 \text{ GPa}$). The earthquake magnitude can be correlated with the seismic moment in the following expression (Kanamori & Brodsky, 2004, see also Section 1.2):

$$M_w = \frac{2}{3} \log_{10} M_0 - 6.07, \quad (\text{A.11})$$

where M_0 is the seismic moment of the event in [Nm], with $M_0 \approx \Delta\tau^{\text{real}} (L_{\text{ac}}^{\text{real}})^3$. In our scenario, we obtain $M_0 = 10^{17.916} \text{ Nm}$ leading to an earthquake with magnitude $M_w = 5.9$ (Eq. (A.11)).

Kanamori and Brodsky (2004) relate the seismic moment to the released in-situ elastic energy $E_{\text{R}}^{\text{real}}$ as follows:

$$\tilde{e} = \frac{E_{\text{R}}^{\text{real}}}{M_0}, \quad (\text{A.12})$$

where \tilde{e} characterizes the dynamic properties of an earthquake. They state that for earthquakes with magnitudes between 3 and 6, the ratio \tilde{e} equals approximately to 10^{-5} . Consequently, the released energy in the laboratory ($E_{\text{R}}^0 = 201 \text{ Nmm}$) is scaled up to an earthquake with magnitude $M_w = 5.9$, which releases $E_{\text{R}}^{\text{real}} = 10^{12.916} \text{ Nm}$ of elastic energy.

We can write down the ratio between the in-situ upscaled released energy and the released energy measured in the laboratory, denoting the parameter η :

$$\eta = \frac{E_{\text{R}}^{\text{real}}}{E_{\text{R}}^0} \quad (\text{A.13})$$

Note that this energy relationship depends on the previous scaling procedure, therefore η is not an independent scaling factor.

By knowing $\eta = 10^{13.613}$ for this reference event, we can directly transfer the energy of any other event $E_{\text{R}}^{(i)}$ from the model to the real magnitude M_w (Eqs. (A.11) - (A.13)):

$$M_w = \frac{2}{3} \log_{10} (E_{\text{R}}^{(i)}) - 6.07 + \frac{2}{3} \log_{10} \left(\frac{\eta}{\tilde{e}} \right) \quad (E_{\text{R}}^{(i)} \text{ in Nm}) \quad (\text{A.14})$$

Even though in this work we take into account only injections close to the fault area, we could consider injection wells far from the fault as well as low permeabilities of the damage fault zone by just changing these scaling laws.

A.7 Model assumptions and limitations

Even though this experimental campaign can be very instructive regarding earthquake control and induced seismicity, it is based on several assumptions and limitations:

- We focus on an isolated fault and consequently all the energy budget is contained in the paper analogue.
- Our model inherits the characteristics of the spring-slider model (Scholz, 2002; Stefanou, 2019).
- We can simulate fluid injections by simply wetting the paper sheet. In a fault system, the apparent friction drops when fluids under pressure are injected into the fault zone due to the decrease of normal stress. Similarly, porous paper shows a noticeable stress drop when it is wet due to the reduction of its strength (see Figure 2.1f).
- Healing could be considered by drying the paper stripes, but this notion is out of the scope of the present work.
- The diffusion process can be considered through the progressive wetting of many isolated stripes.
- Typical failure modes II and/or III that take place during seismic slip in faults are represented here by a mode I failure of the porous paper. These systems are equivalent in terms of energy budget (Nussbaum & Ruina, 1987), provided that appropriate scaling laws could be applied.
- The initial linear elastic behavior of the porous paper is equivalent to the healing phase of a fault assuming for instance rate-and-state friction law.
- A certain amount of fluid is injected each time assuring fast saturation all over the respective fault segment. Until the completion of the injection strategy, no more fluid is injected on an already saturated segment. Therefore, each injection leads to only one seismic event in a specific fault segment.
- Each fluid injection is accompanied by an instantaneous stress drop and stress redistribution over the intact, dry porous paper stripes (Figure 2.6a). In this setup, the

redistribution is quasi-uniform and may not capture elastodynamic effects related to real fault geometries. At a certain extent, the latter effects could be simulated by strengthening and impregnating the paper following specific geometries. However, this is out of the scope of this work.

- In our experimental work, fluid boundary conditions are expressed through segmentation by adjusting plastic (impermeable) barriers between the stripes.
- One of the investigated key parameters, the stress level of the fault, is most of the times difficult or even impossible to measure in practice. However, injection in critically stressed faults could cause earthquakes comparable in size to the natural event.
- We don't take into account any initial defects or heterogeneities because otherwise the qualitative results of this work would be hidden.
- This work does not focus on technological feasibility. We rather focus on the identification of some key parameters that may lead, either to successful earthquake mitigation, or to failure and earthquake risk increase.

Sand-Based 3D-Printed (S3DP) material: experimental characterization

B.1 Sand-based 3D-printed material composition

Given the important effects of various printing parameters discussed in Braun et al. (2021), we chose for the characterization of the material to vary only two printing parameters, the recoating speed and the binder saturation. The layer orientation and layer thickness remained the same for all specimens (see Braun et al., 2021).

Our Sand-Based 3D-printed (S3DP) specimens were fabricated using combinations of two recoating speeds, $v_r = 0.13$ and 0.26 m/s, and two binder contents, $b = 3.8$ and 7.2 wt% of sand (Table B.1b). Further material and 3D-printer specifications are given in Table B.1a. All four compositions show porosities close to 45%, calculated using the measured sample weight and volume. This porosity is close to the maximum porosity of 48 %, which corresponds to the loosest possible packing of spherical grains with uniform diameter and no binder. Note that we assumed a silica sand density $\rho_s = 2.65$ g/cm³ and a binder density $\rho_b = 1.15$ g/cm³ (Mitra et al., 2018) for the porosity calculation.

To characterize the basic mechanical and frictional properties of the S3DP material, we carried out: a) unconfined compression tests on cylindrical S3DP specimens and b) shear tests on flat S3DP interfaces. The four different material compositions (Table B.1b) were tested in order to analyze the effect of binder content and recoating speed on the mechanical parameters and to choose the most suitable composition for analogue faults.

B.2 Unconfined compression tests

For the unconfined compression test, we used a uniaxial compression frame, which is equipped with a 20 kN loadcell mounted on a servo-mechanical piston. The loading for the following experiments was carried out under displacement control with a rate of 0.1

Table B.1 – (a) Printer settings applied for specimen fabrication. (b) Compositions for sand printing, representing different combinations of binder content b and recoating speed v_r . The resulting average porosity ϕ and its standard deviation (SD) are given.

(a)	
Silica sand mean grain diameter	140 μm
Binder type	Furfurylic alcohol
Binder content	3.8 or 7.2 wt% of sand
Recoating speed	0.13 or 0.26 m/s
x resolution	20 $\mu\text{m}^{(1)}$ or 40 $\mu\text{m}^{(2)}$
y resolution	101.6 μm
z resolution (layer thickness)	280 μm
Activator content (sulfonic acid)	0.2 wt% of sand
Infra-red curing lamp temperature	32 $^{\circ}\text{C}$

⁽¹⁾ for high and ⁽²⁾ for low binder content

(b)				
Composition	b [wt% of sand]	v_r [m/s]	ϕ [%]	SD [%]
R1	3.8	0.13	43.7	0.6
R2	3.8	0.26	47.6	1.0
R3	7.2	0.13	42.8	4.2
R4	7.2	0.26	45.1	2.2

mm/min, measured by an integrated encoder. The vertical displacement of the top of the specimen was recorded by an LVDT. Cylindrical specimens were printed with 20 mm diameter and 40 mm height. The cylinder axis was aligned with the printing direction z (Figure B.1). For the S3DP material, the weakness planes were aligned with the printing plane (Gomez, 2017; Gomez et al., 2019). The printing deposition leads to a transversely isotropic material which, to some extent, could mimic the natural, geological deposition mechanism.

Typical stress-strain curves of the performed UCS tests are presented in Figure B.2. More specifically, we are interested in the unconfined compressive strength (UCS), the Young modulus and the post-peak behavior (ductility/brittleness). Good repeatability was reported for tests of the same material composition.

In all of our experiments, we can observe a linear loading path above an axial stress of $\sigma_1 \approx 5$ MPa, leading to a relatively brittle failure. Below that stress level, the slope of the stress-strain curve is much smaller, indicating a possible plastic compaction due to crack

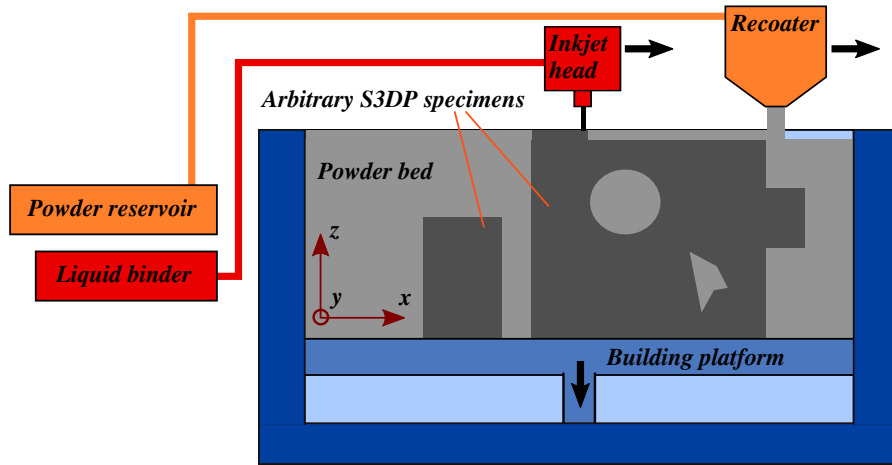


Figure B.1 – Schematic elements of a 3D printer for powder-binder composites, adapted from Upadhyay et al. (2017).

and/or pore closure. After failure, we detect a significant, but gradual softening in the post-peak regime, which can be beneficial in some applications (ductility). Notice that the initial loading section of composition R1 at $\sigma_1 \approx 2$ MPa shows a distinctive plateau, which could also be due to initial misalignment of the specimen or initial local compaction of asperities at the top and bottom end surfaces.

We note that compositions R1 and R3 (low recoating speed) behave similarly, with peak stresses close to 18 MPa. Likewise, compositions R2 and R4 (high recoating speed) show similar responses, but with lower peak strengths, i.e. at around 12 MPa. R2 and R4 specimens showed a more ductile behavior than the others (i.e. shallower and longer strain softening branch). The UCS values are summarized in Figure B.3a, showing the increase of strength with lower recoating speed. Slower recoating induces higher packing density, which seems to favor mechanical strength. The binder content has negligible influence on the compressive strength.

During the loading paths, unloading-reloading cycles were carried out to measure the elastic Young modulus E . This parameter was evaluated through linear regression on the stress-strain curve of each cycle. In Figure B.3b, we plot the Young modulus with respect to the vertical stress at the beginning of the respective cycle. We can observe that E varies from around 0.2 up to 3.7 GPa. While the composition of the specimens does not notably affect the Young modulus E , the vertical stress has a significant impact on the stiffness. Even though we detect a rather large dispersion of values, we can observe an increase of the Young modulus with vertical stress. At $\sigma_1 = 2$ MPa, we measured $E \approx 1.0$

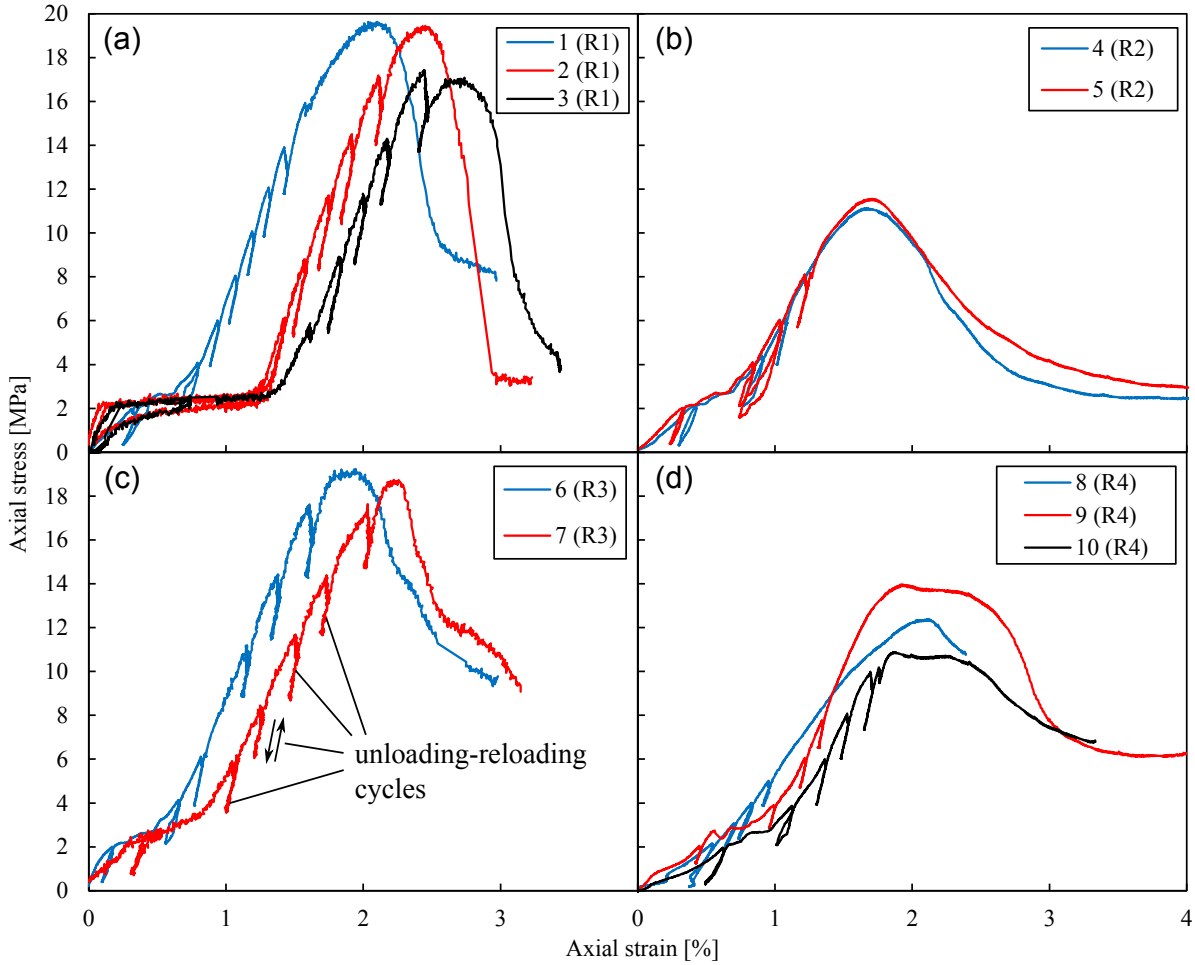


Figure B.2 – Experimental stress-strain behavior obtained from uniaxial compression tests on specimens with different compositions (Table B.1b). The specimens were loaded with a constant displacement rate of 0.1 mm/min. We carried out subsequent unloading-reloading cycles before reaching the peak stress, by unloading each time for about 1.2 to 2.0 MPa, in order to determine the Young modulus from elastic deformations. Strain softening is observed after the peak.

GPa, which increases up to $E \approx 3.3$ GPa at $\sigma_1 = 6$ MPa. For higher stresses, the Young modulus remains practically constant.

Before each unloading-reloading cycle, the displacement was stopped for a certain time, which allowed us to measure the vertical stress relaxation. The decrease of vertical stress, starting from the initial value $\Delta\sigma_1 = \sigma_1 - \sigma_{1,0}$, was analyzed relative to the initial stress $\sigma_{1,0}$, giving the dimensionless relative relaxation. Figure B.3c shows a typical result of the relative relaxation with respect to time, measured on different stages for specimen

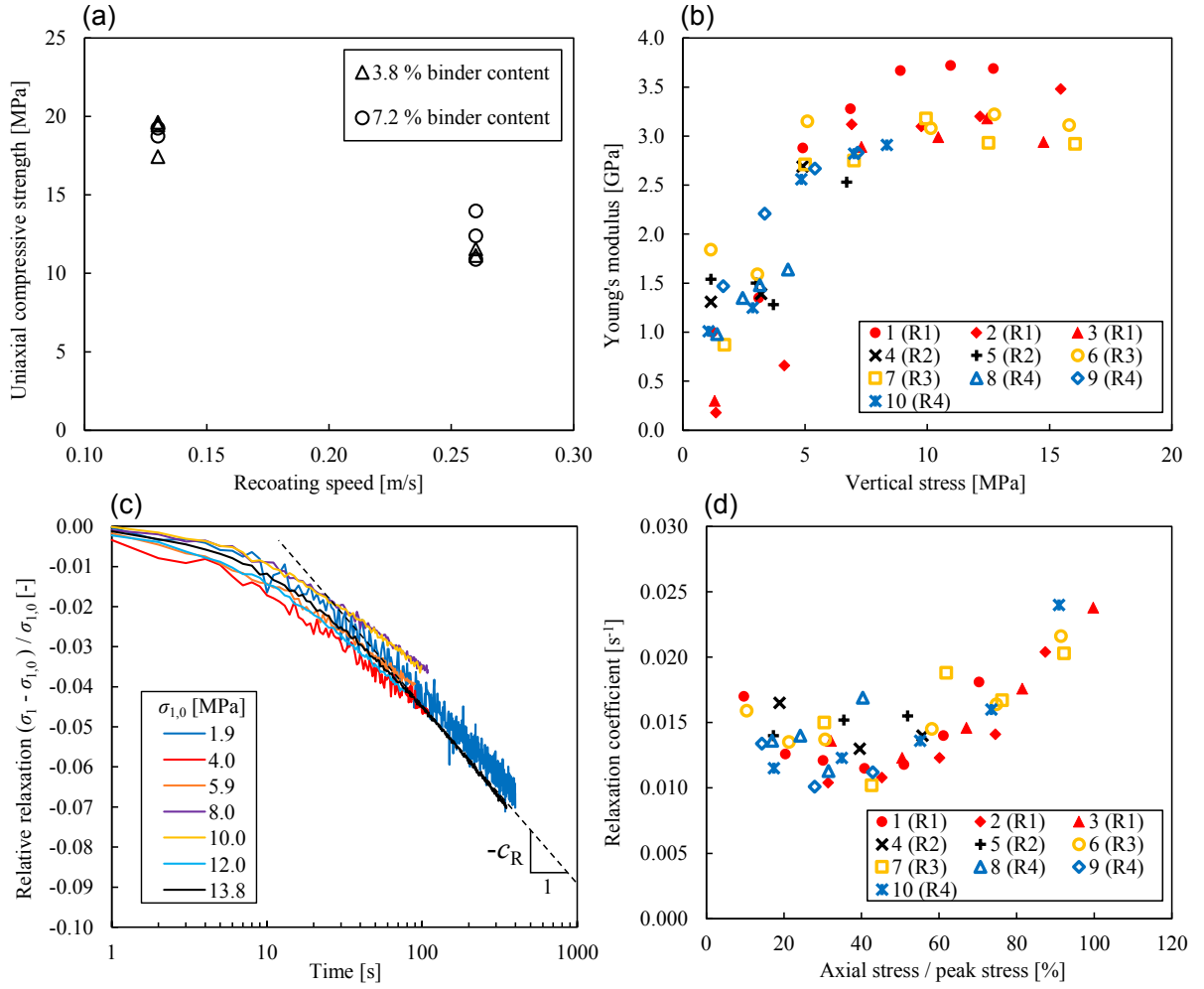


Figure B.3 – Data taken from the unconfined compression tests 1 - 10 in Figure B.2: (a) Influence of the recoating speed on the unconfined compressive strength. Different binder contents (Table B.1b) have no significant effect. (b) Young’s modulus evaluated at unloading-reloading cycles at different axial stress levels. (c) Relaxation coefficient c_R evaluated at constant displacement stages and under different stress levels. The indicated slope provides an estimation of the relaxation coefficient c_R . (d) Relative relaxation with respect to time under various initial axial stress levels $\sigma_{1,0}$.

1 (composition R1). After a time of 30 s, we observe a linear behavior with respect to log-time. The relaxation coefficient c_R can be evaluated from the slope of the curve and its values are presented in Figure B.3d in function of the normalized vertical stress (initial vertical stress over compressive strength). Independently of the sample composition, we find values of c_R varying between 0.010 and 0.017 s⁻¹ at a vertical stress below 80 % of the compressive strength, while above that stress level, c_R increases up to 0.024 s⁻¹ at

100 % compressive strength.

In terms of compressive strength, we found a range of values between 10 and 20 MPa, similar to the values obtained by Gomez et al. (2019) on a similar material. The observed values for compressive strength and Young’s modulus are comparable to those of weak sandstones (porosity of approximately 25 %, Dobereiner & Freitas, 1986; Papamichos et al., 2000). Interestingly, we can observe an evolution of Young’s modulus with vertical stress, such as in natural sandstones (e.g. Pimienta et al., 2015). This behavior is often explained through the closure of micro-cracks, which increases the grain-to-grain contact area and consequently the stiffness.

Note that the Young modulus, the peak strength and the relaxation characteristics were determined in this study always for a loading direction perpendicular to the printing layer. For loading parallel to the layer, one can expect different properties due to the anisotropic micro-structure of the material, but this exceeds the scope of the current work. For instance, Gomez (2017) showed for a similar S3DP material, that under loading parallel to the printing layer with respect to perpendicular loading, the strength decreased from 17.1 to 14.4 MPa, the failure characteristics changed from ductile to brittle and the Poisson ratio increased from 0.19 to 0.25, while the Young modulus remained at 1.7 GPa.

B.3 Direct shear experiments on flat interfaces

For direct shear experiments, we used the direct shear device shown in Figure B.4a, which is designed for specimens composed of two blocks. The bottom one has dimensions equal to 140x100x10 mm³ and the top one equal to 100x100x25 mm³ (length x width x height). These blocks were printed with their height axis perpendicular to the printing layer (see Figure B.1).

The length of the bottom block is higher than the one of the top block, in order to assure constant contact area (100x100 mm²) during shearing. In the vertical direction, the controlled normal force F_n results in a normal stress σ_n , which is quasi-uniform over the interface (Tzortzopoulos et al., 2019). The vertical displacement was measured by an integrated LVDT. In the horizontal direction, a ram permits to move the lower part of the device. We performed displacement controlled (δ) experiments. The horizontal displacement induces a shear stress τ_n , which is considered to be uniformly distributed over the interface. During shearing, loose material might detach from the blocks. However, the sheared interface is 100 mm wide, prohibiting grain removal from the shear interface

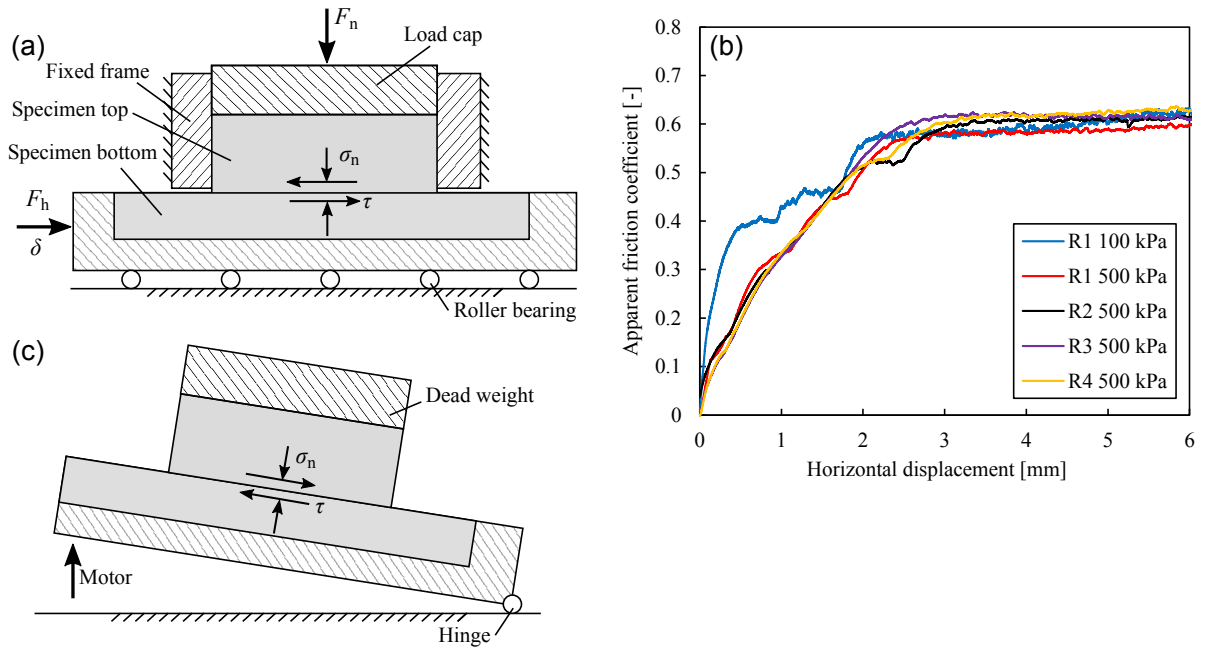


Figure B.4 – (a) Schematic plan of the direct shear apparatus. The normal force F_n and the horizontal displacement δ are controlled. (b) Evolution of the apparent friction coefficient shown on one representative result for each material composition and normal stress level. (c) Configuration of the inclined plane shear test.

(plane-strain conditions). Moreover, the loading frame prevents loss of grains from the lateral sides of the specimen.

For each material composition R1 - R4, we tested two specimens under a normal stress of 500 kPa and a shear displacement rate of 0.5 mm/min. Two additional specimens of composition R1 were sheared under 100 kPa normal stress. The apparent friction coefficient, presented for some typical results in Figure B.4b, reached a constant residual plateau for the investigated shear displacement up to 6 mm. The initial load-displacement branch includes elastic deformation, but also compression and sliding due to alignment of the sample blocks with the loading frame. Moreover, gouge is formed, which then undergoes steady-state shearing. Steady-state or critical-state shearing (Roscoe et al., 1958; Wood, 1991) is accompanied by gouge production due to grain detachment. Between the two phases, a smooth transition is observed. The average values of this residual friction coefficient under 500 kPa normal stress are 0.58 for R1, 0.60 for R2 and 0.63 for R3 and R4. Decreasing the normal stress in tests on composition R1 did not change the apparent friction coefficient, confirming Coulomb's assumption of proportionality. The experiments showed good repeatability.

The measurements from the direct shear tests were verified through additional friction tests on composition R1, using an inclined plane configuration (Figure B.4c). In these verification tests, specimens consisting of lower and upper blocks with flat interfaces (equivalent dimensions as the specimens used for direct shear tests), were placed on a horizontal metal plate. The lower block was prevented from sliding on the plate, while the upper block was unconstrained. An additional weight of 1.0 kg was placed on top of the upper block. The plate was slowly inclined, until the upper block started to slide. By measuring the inclination angle, the friction coefficient of the interface could be determined. We carried out four tests in this way, showing an average friction coefficient $\mu = 0.62$ (corresponding to a friction angle of 31.8°) with a standard deviation of 5.0 %. This friction coefficient is close to the value of 0.58 obtained on the R1 composition using the direct shear apparatus, which confirms the results of the more complex device. Zero cohesion was measured in all the tests.

Proceeding one step further with the characterization of the flat interfaces, we carried out velocity stepping experiments under constant normal load, in order to estimate the rate-and-state parameters a , b and d_c^{rs} (see Section 1.1.3). The same direct-shear apparatus and testing configuration were used as in Figure B.4a. We performed two tests using specimens made of R2 composition under 500 kPa of normal stress. Initially, the specimens were loaded for 5 mm with a constant shear displacement rate of $v_0 = 5 \mu\text{m/s}$ in order to assure steady-state sliding of the mobilized block. An abrupt decrease of the velocity by one order of magnitude to $v_1 = 0.5 \mu\text{m/s}$ followed. This velocity was kept constant for a total displacement of 2 mm, until the velocity increased again instantly to v_0 . After 2 mm of sliding, a last abrupt velocity reduction to v_1 took place. The response of the specimens under these velocity steps can be observed in Figure B.5.

More specifically, in Figure B.5a, the time-history of the horizontal displacement is displayed, where the velocity steps, interchangeably between v_0 and v_1 , are easily distinguishable. In Figure B.5b, the apparent friction coefficient in terms of the horizontal displacement is plotted, along with a closer look to the frictional response due to an abrupt (i) increase (orange framed inset) and (ii) decrease (purple framed inset) of block's velocity. In the case of a velocity increase (inset (i)), an instant frictional strengthening is observed of $\Delta\mu = a \ln(v_0/v_1)$ (from the steady-state). Then an exponential decay of the friction occurs leading to the next frictional steady-state value due to the faster velocity v_0 . The exact opposite happens for a velocity decrease as indicated in the inset (ii). The difference between the averaged steady-state values before and after each velocity step

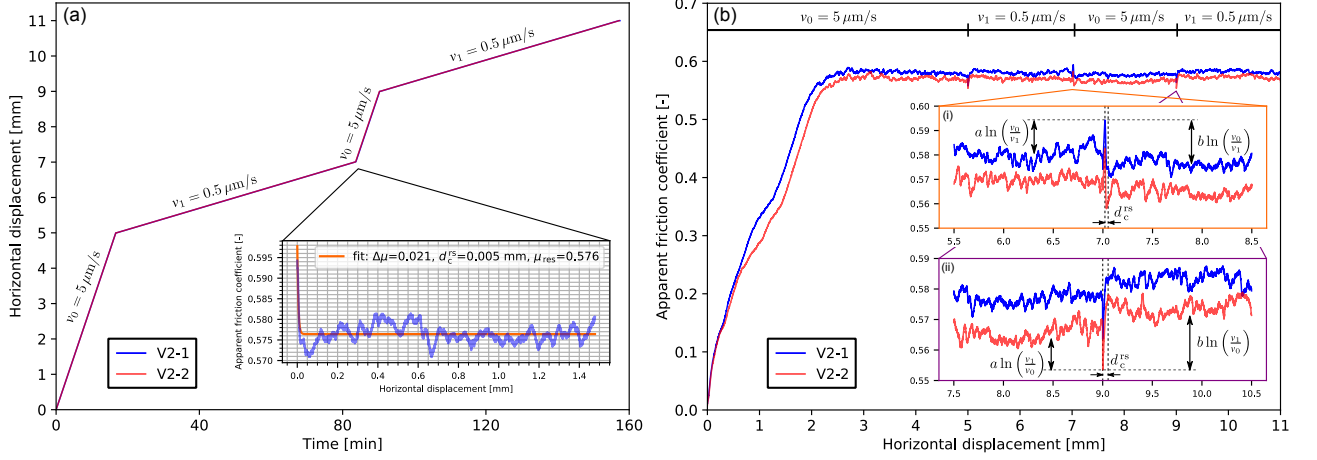


Figure B.5 – (a) Horizontal displacement over time of two different tests with two different samples (blue and red solid lines). The different applied displacement-rates are also illustrated indicating their duration. The inset shows an example of an exponential fitting which is employed for calculating d_c^{rs} for each velocity step. (b) Apparent friction coefficient with respect to the horizontal displacement of the moving block, measured on the two samples. In the insets (i) and (ii), a closer look to an increase and decrease of velocity is presented, respectively.

is denoted as $\Delta\mu_{\text{ss}}$ and is equal to $(a - b) \ln(v_0/v_1)$. The distance that it takes for the friction to reach its new steady-state after a velocity change is noted as d_c^{rs} .

The parameters $a - b$ and d_c^{rs} are involved in the study of the stability of the analogue spring-slider model under the rate-and-state friction (see Sections 1.1.3 and 1.2). By taking into account the average steady-state friction before and after each velocity step and considering an order of magnitude increase of velocity, the average difference $(a - b)_{\text{in}}$ is equal to -0.0019 , while for an equivalent decrease of velocity is $(a - b)_{\text{dcr}} = -0.0037$. For estimating the characteristic rate-and-state distance d_c^{rs} , we performed an exponential fitting to the frictional decay raw data utilizing the least-squares method, as it is illustrated in the inset of Figure B.5a (Bhattacharya et al., 2015; Gu et al., 1984; Rice & Ruina, 1983; Skarbek & Savage, 2019). Consequently, the characteristic distance for the rate-and-state friction law following a factor of 10 rise of the velocity is $d_{c,\text{in}}^{\text{rs}} = 0.005 \text{ mm}$, while for an equivalent drop is $d_{c,\text{dcr}}^{\text{rs}} = 0.014 \text{ mm}$.

These results show that for relatively slow velocities and only if the sliding block has reached its steady-state, the S3DP material displays velocity dependency (using the rate-and-state terminology) (J. H. Dieterich, 1981a; J. H. Dieterich & Kilgore, 1994; Hunfeld et al., 2019). Therefore, considering the micro-behavior of this 3D-printed material, these

experiments give birth to an additional small length-scale of the order of approximately $0.1D_{50}$. However, this rate-and-state behavior plays a secondary role in the design of interfaces with custom (slip-weakening) frictional properties. As shown in Appendix C, this is due to the possibility of adjusting the macro-roughness using 3D-printing.

Design of analogue fault gouges with custom frictional properties using the S3DP material

C.1 Design of interfaces with custom frictional properties

Once the basic mechanical properties of the sand printed material are identified, it is possible to design the geometry of the printed interfaces, in order to give them the desired frictional properties. These properties include the peak friction, the residual friction, and the characteristic slip-weakening distance. Moreover, we can control the exact evolution of friction with slip, giving us important flexibility in experiments (see also Aoude, 2021).

Modeling the frictional behavior allows us to better understand the underlying physical mechanisms and enables us to design interfaces of desired frictional properties. According to Newland and Allely (1957) and Patton (1966), and assuming Coulomb friction, the friction coefficient of rock joints is:

$$\mu = \frac{\tau}{\sigma_n} = \tan(\phi_b + i), \quad (\text{C.1})$$

where ϕ_b is called basic friction angle and i effective roughness, or i -value in the case of rock joints (Barton, 1973). The effective roughness is the inclination of asperities along the interface.

According to Barton (1973), the value of ϕ_b corresponds to the residual friction angle, measured on saturated, planar rough-sawn or sand-blasted surfaces of the rock. This author has summarized literature data for sand-blasted and sawn surfaces, showing that most rocks have basic friction angles of approximately between 25° and 35° . The measured basic friction of the sand-based 3D printed material was found in the same range (around

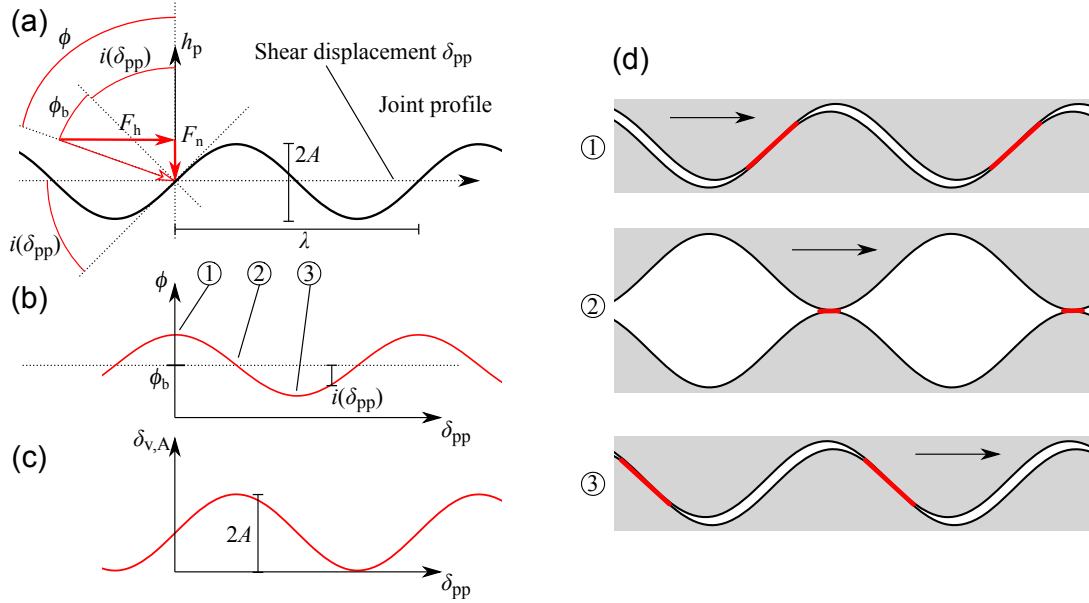


Figure C.1 – Friction model for a joint with periodic asperity geometry, illustrated using a sine-wave profile. (a) Force diagram on the position $\delta_{pp} = 0$, where the asperity inclination i is the highest. The apparent total friction angle, which gives the relationship between F_h and F_n , is the sum of i and ϕ_b . (b) Oscillation of the total friction angle ϕ around the basic friction angle ϕ_b with amplitude i , depending on the shear displacement. (c) Vertical displacement of the top interface. (d) Asperity contact orientation (red in online version), which changes with progressing displacement and affects the total friction. Wear and compaction is neglected in this schema, so that the interface geometry remains unchanged ($A = A_0$).

30° , see Section B.3), which makes it a good candidate for a rock analogue, as far as it concerns frictional properties.

Therefore, by appropriately designing i in terms of slip, one can control the evolution of the apparent friction coefficient μ . In this way it is possible to imitate a great variate of frictional behavior in experiments including RSF (Aoude, 2021). In order to demonstrate this idea, we apply Patton’s friction relation (Eq. (C.1)) for periodic sine-wave asperities. This roughness profile is expressed as a function of the shear displacement δ , defined by an amplitude A_0 and a wavelength λ . In Figure C.1, we present the geometry of the sinusoidal asperities. According to Eq. (C.1), the maximum friction is expected at the maximum profile angle i , where we set $\delta_{pp} = 0$. The profile height, h_p , can be expressed as a function of the shear displacement δ_{pp} , resulting in $h_p(\delta_{pp}) = A_0 \sin(2\delta_{pp}\pi/\lambda)$. The asperity inclination gives us the asperity friction coefficient μ_A , obtained through differ-

entiation of h_p with respect to δ_{pp} :

$$\mu_A(\delta_{pp}) = \tan [i(\delta_{pp})] = \frac{dh_p(\delta_{pp})}{d\delta_{pp}} = 2\pi \frac{A_0}{\lambda} \cos \left(2\pi \frac{\delta_{pp}}{\lambda} \right), \quad (\text{C.2})$$

where the maximum and minimum asperity friction μ_A are given by $\pm 2\pi A_0/\lambda$. Inserting Eq. (C.2) in (C.1), one can calculate the total apparent friction coefficient:

$$\mu(\delta_{pp}) = \frac{\mu_b + \mu_A(\delta_{pp})}{1 - \mu_b \mu_A(\delta_{pp})}, \quad (\text{C.3})$$

where $\mu_b = \tan \phi_b$ is the basic friction coefficient (see Section C.3).

In addition, the oscillating vertical compaction-dilation $\delta_{v,A}$ due to the sliding over asperities (Figure C.1) can be derived from the profile height $h_p(\delta_{pp}) = A_0 \sin(2\pi\delta_{pp}/\lambda)$. Therefore, dilatancy can be designed as well, which, for the sinusoidal asperities, is equal to:

$$\delta_{v,A}(\delta_{pp}) = A_0 \left[1 + \sin \left(2\pi \frac{\delta_{pp}}{\lambda} \right) \right] \quad (\text{C.4})$$

Notice that this relation is purely geometrical and kinematic and neglects any deformations due to high normal stress and/or hertzian contacts. These two factors could be taken into account in a more detailed analysis.

C.2 Wear and gouge formation

In our friction model, we intend to take into account the wear of asperities and the formation of gouge, due to the detachment of grains from the S3DP matrix (Figure C.2). Note that this gouge formation could mimic the creation of gouges in real faults (Marone et al., 1990; Marone & Scholz, 1989; Rattetz et al., 2018a; Rattetz et al., 2018b).

Queener et al. (1965) proposed a general law for wear, composed of an exponential transient and a linear steady-state wear, which is compatible with wear observations in rock joint shear experiments (Power et al., 1988).

Abrasion gradually reduces the asperity amplitude (Y. Li et al., 2016) (Figure C.2) and therefore the asperity friction affected by wear is denoted by $\mu_A^*(\delta_{pp})$. For very large displacements, $\mu_A(\delta_{pp})$ becomes zero and $\mu = \mu_b$ (Eq. (C.3)). We consider here exponential

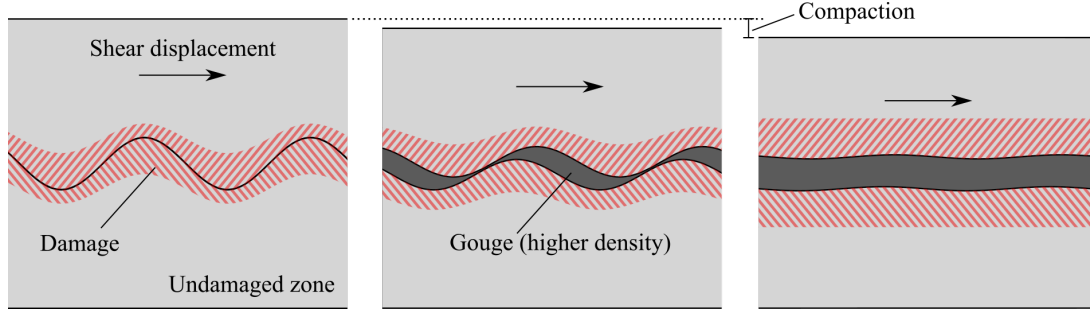


Figure C.2 – Schematic representation of gradual wear of asperities. Abraded grains form a gouge layer between the interfaces. Total compaction can be due to the compaction in the damage zone and in the gouge layer.

abrasion, which reduces the apparent asperity friction coefficient $\mu_A^*(\delta_{pp})$:

$$\mu(\delta_{pp}) = \frac{\mu_b + \mu_A^*(\delta_{pp})}{1 - \mu_b \mu_A^*(\delta_{pp})} \quad (\text{C.5})$$

$$\mu_A^*(\delta_{pp}) = \mu_A(\delta_{pp}) e^{-c_w \delta_{pp}} \quad (\text{C.6})$$

The frictional behavior of this designed interface can therefore be adjusted through two asperity properties and two material parameters. These properties are the wavelength λ , which governs the period in which the friction oscillates, and the amplitude A_0 , which defines the asperity friction. Moreover, the material composition affects the basic friction μ_b and the wear coefficient c_w .

In terms of vertical displacement, the maximum compaction $\delta_{v,\max}(\delta)$ is a function of the total shear displacement δ and can be described by an empirical exponential law (Power et al., 1988):

$$\delta_{v,\max}(\delta) = \delta_{v,\infty} (1 - e^{-c_v \delta}) \quad (\text{C.7})$$

where c_v is the vertical compaction coefficient and $\delta_{v,\infty}$ the final steady state compaction.

Moreover, we can superpose the oscillating vertical compaction-dilation $\delta_{v,A}$ due to the sliding over asperities (Eq. (C.4), see also Figure C.1) to Eq. (C.7). As described above (Eq. (C.6)), the amplitude of the asperities decreases due to wear, governed by the wear coefficient c_w . The asperity dilation accounting for wear is then written as:

$$\delta_{v,A}^*(\delta_{pp}) = A_0 e^{(-c_w \delta_{pp})} \left[1 + \sin \left(\delta_{pp} \frac{2\pi}{\lambda} \right) \right] \quad (\text{C.8})$$

The total vertical displacement is the sum of compaction and asperity dilation:

$$\delta_v(\delta_{pp}) = \delta_{v,\max}(\delta) + \delta_{v,A}^*(\delta_{pp}), \quad \delta = \delta_{pp} + \delta_1 \quad (\text{C.9})$$

where δ_1 is the total shear displacement at the first peak of the apparent friction coefficient. Power et al. (1988) stated that in laboratory shear tests, most of the wear occurs in the “transient wear phase”. Laboratory specimens have a finite roughness scale, and most of that initial roughness is destroyed during the initial, transient wear phase. Moreover, created gouge material often isolates the bare rock interfaces and reduces the apparent friction (Figure C.2). According to these authors, this first transient wear is followed by steady-state wear, which continues in laboratory tests under a relatively slow rate, as most of the asperities are flattened out. In real faults however, fault roughness is self-affine and covers a much larger range of scales (e.g. Candela et al., 2012; Schmittbuhl et al., 1993). As a result, the size of the asperities that must be broken increases approximately linearly with displacement. Hence, real faults never reach a steady state wear as experimental faults do (Power et al., 1988). However, similar to our experimental results, the recent work of Dascher-Cousineau et al. (2018), using numerous samples from fault outcrops, showed that at a small scale (< 10 mm) fault surfaces indeed smoothen with slip. Note that in our experiments, we investigate a finite roughness scale, equal to the size of the sine-waves. Steady state wear is therefore expected to be negligible and not considered in the model.

C.3 Direct shear experiments with designed roughness

Direct shear experiments were performed on S3DP material with controlled roughness properties, to study the effectiveness of our theoretical friction design approach. For this purpose, we printed sine-wave interface asperities with a constant amplitude $A = 3D_{50} = 0.42$ mm and constant wavelength $\lambda = 20D_{50} = 2.80$ mm, as shown in Figure C.3.

A series of direct shear tests under a constant normal stress of 500 kPa was carried out on samples of the four different compositions. The specimens were initially loaded with a normal stress of 500 kPa and sheared under constant normal stress and constant displacement rate of 0.5 mm/min for 10 mm. After the maximum displacement was reached, the specimen was sheared in the reverse direction, until its initial position. In this way,

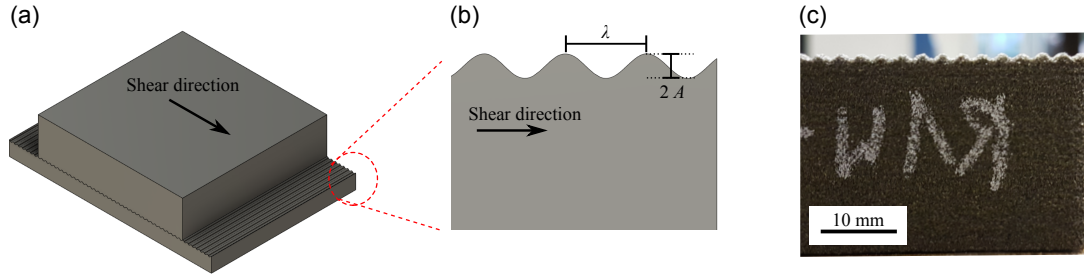


Figure C.3 – (a) 3D model for printing the two direct shear specimen blocks with wave interfaces. (b) Cross-section and zoom on the sine-wave interface with amplitude $A = 0.42$ mm and wavelength $\lambda = 2.80$ mm. (c) Image of a printed specimen, zoomed on the interface.

a full loading cycle was performed, corresponding to a total of 20 mm of accumulated slip. Figures C.4 (compositions R1 and R2) and C.5 (compositions R3 and R4) present the evolution of the measured friction coefficient and the vertical displacement with progressing horizontal displacement. In particular, we show the apparent friction coefficient μ , defined as the ratio of F_h/F_n . Negative values correspond to reverse shearing. One can clearly observe oscillations in the post-peak regime of the friction behavior, due to the wave geometry of the interfaces. The interlocking printed asperities induce a much higher peak friction, close to 1.0, compared to the one measured on the flat surface, close to 0.6. Once we exceed the peak, the friction decreases and drops to a lower level than the one determined on flat specimens (negative asperity friction angle i , see Eq. (C.1)). Then, the friction rises and falls in the form of damped oscillations, due to wear. In terms of vertical displacement, the specimens exhibit an overall compaction during shearing, combined with dilation peaks of decreasing amplitude.

In Table C.1, we present different frictional properties evaluated from the experimental results (Figures C.4 and C.5). The maximum friction coefficient measured at the first peak (μ_1) is shown along with the respective block's displacement (δ_1). At the end of the reverse loading (negative apparent friction), the amplitude of friction oscillations becomes almost zero. Inspecting the specimens after the experiments confirmed that wear has flattened out the sine-wave asperities and left an almost flat interface. One can estimate the residual friction coefficient μ_∞ from the mean friction in this part of the experimental curve, which results in being almost identical to μ_b (asymptotical approximation for infinite sliding). In theory, differences may arise due to a higher amount of gouge material present when evaluating μ_∞ . Comparing the values of μ_∞ with the results from flat interface shear experiments, no significant difference can be observed. The wavelengths λ_1 and λ_2 are the

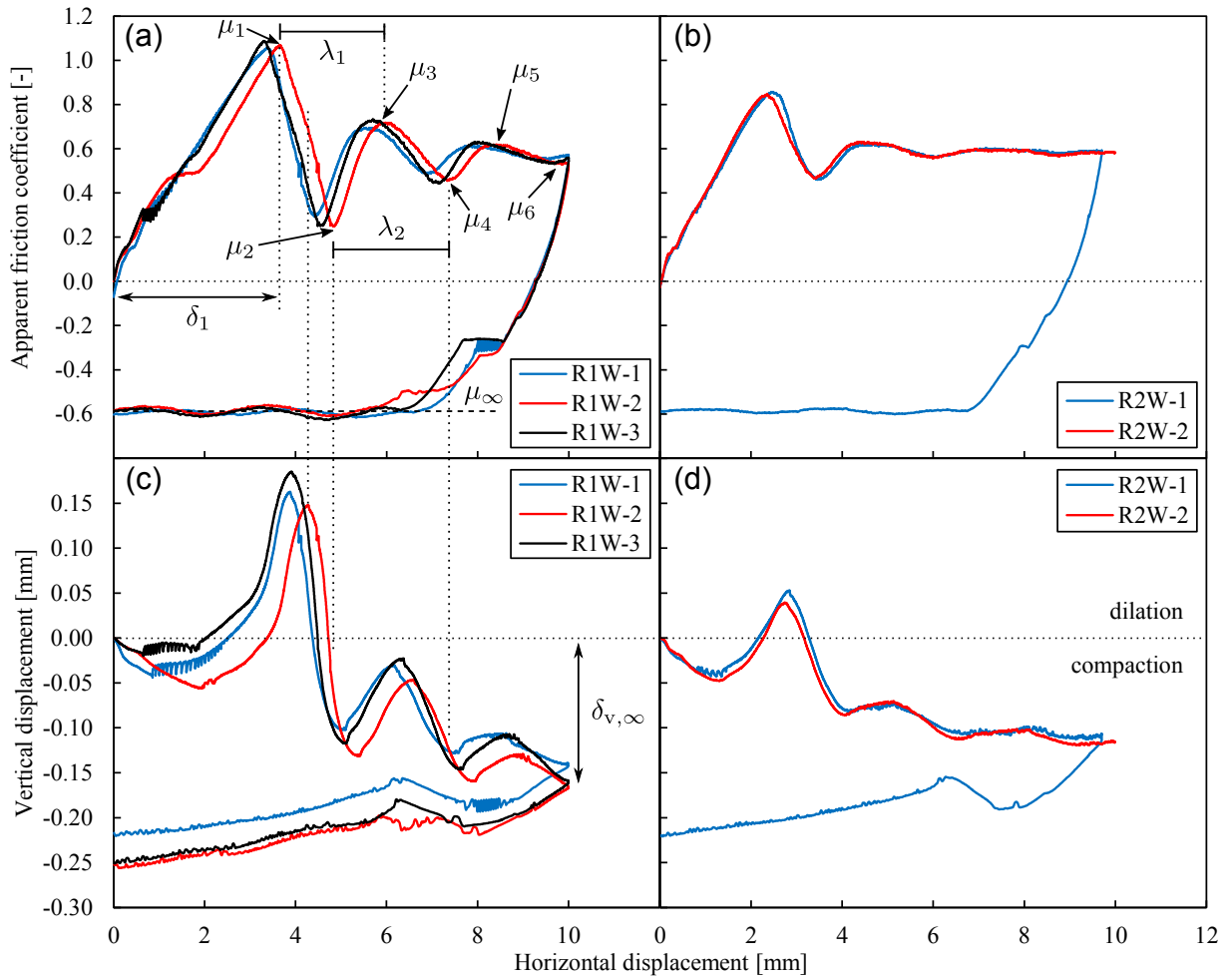


Figure C.4 – Results of direct shear experiments under 500 kPa normal stress on specimens R1 and R2 (Table C.1). (a), (b) Friction coefficient and (c), (d) vertical displacement with respect to horizontal shear displacement. Note that due to technical problems, the reverse shearing of R2W-2 was not carried out.

slip distances between two points of maximum and minimum friction, respectively. Their average value is λ , which corresponds in theory to the wavelength of the printed interface. It is important to note, that the characteristic slip-weakening distance d_c^{sw} , over which the apparent friction decreases from its maximum to its minimum, is here equal to half of the wavelength λ (for sinusoidal interfaces).

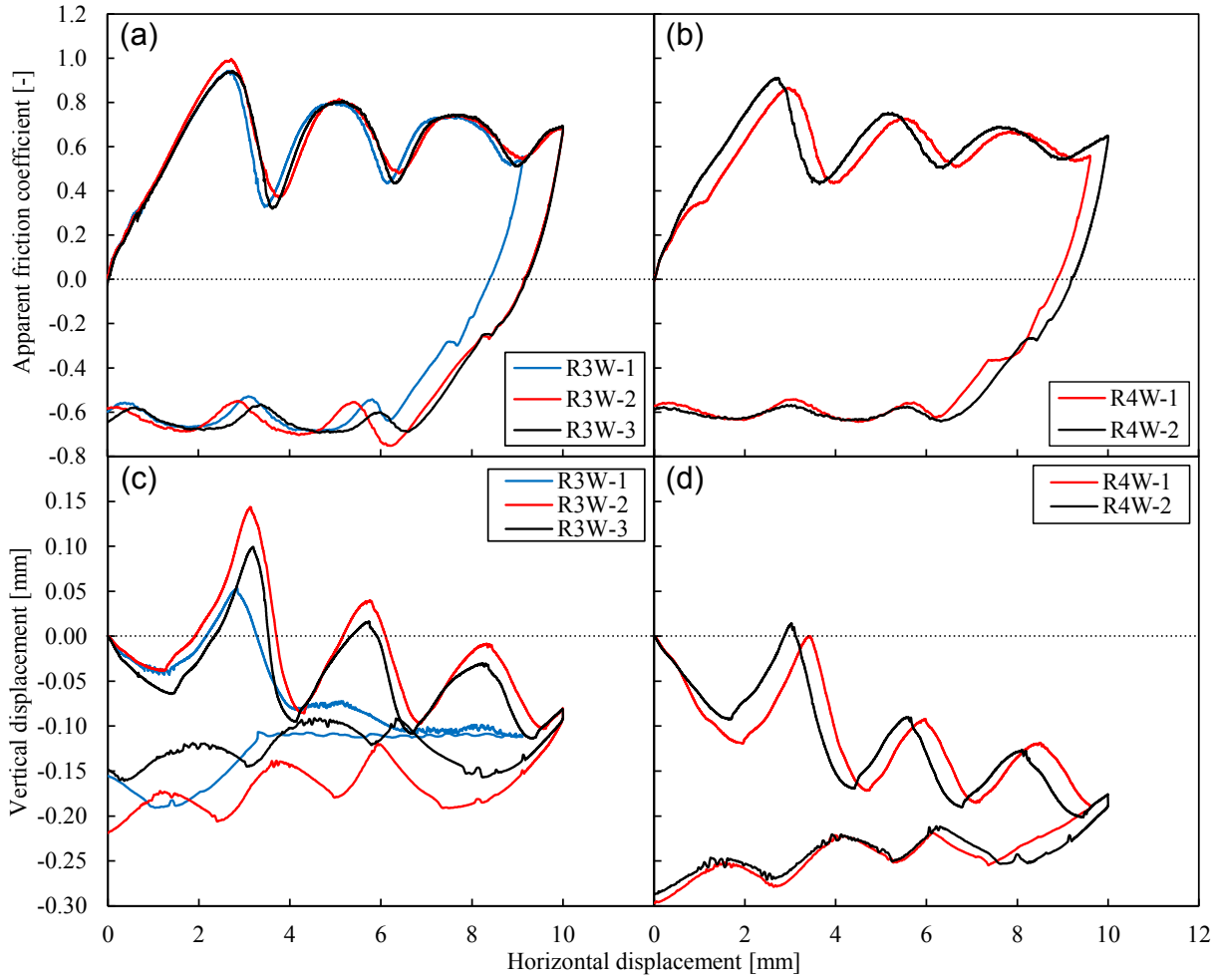


Figure C.5 – Results of direct shear experiments under 500 kPa normal stress on specimens R3 and R4 (Table C.1). (a), (b) Friction coefficient and (c), (d) vertical displacement with respect to horizontal shear displacement.

C.3.1 Effect of material composition

For high binder content, the recoating speed (packing density) appears to have a minor influence on the friction, as we observe similar values $\mu_1 = 0.96$ and 0.93 for R3 and R4, respectively. For low binder content, we measured $\mu_1 = 1.07$ for R1 and 0.88 for R2. According to our results, higher density induces higher friction. Moreover, for high density, the friction is higher under low binder content. This is probably due to a higher possibility for grains to interlock in the absence of binder. The friction for large shear displacement μ_∞ does not appear to be significantly influenced by the material composition, providing values close to 0.6 (Table C.1), which is equal to μ_b measured on flat specimens in Section

Table C.1 – Mean values of the parameters determined from the direct shear tests under $\sigma_n = 100$ and 500 kPa on wave interfaces (see also Figures C.4, C.5 and C.7), and their standard deviation (SD). The amplitude A_0 is back-calculated using Eq. (C.12).

	σ_n [kPa]	μ_1		λ		δ_1		μ_∞		c_w		$\delta_{v,\infty}$		c_v		A_0 [mm]
		mean	SD	mean	SD	mean	SD	mean	SD	mean	SD	mean	SD	mean	SD	
R1	100	1.03	6.0	2.67	1.6	2.13	6.1	0.50	2.8	0.14	17.1	-0.16	24.7	0.40	2.6	0.149
R1	500	1.07	1.8	2.41	4.4	3.45	5.4	0.57	2.0	0.45	26.0	-0.18	5.6	0.21	8.9	0.118
R2	500	0.85	0.8	2.45	2.0	2.41	2.9	0.58	1.2	0.60	4.7	-0.12	10.5	0.36	29.9	0.071
R3	500	0.96	3.2	2.55	0.8	2.71	2.0	0.61	1.9	0.19	12.7	-0.11	4.6	0.42	21.3	0.091
R4	500	0.89	3.6	2.54	1.1	2.86	5.7	0.60	1.2	0.26	0.8	-0.20	7.1	0.43	29.5	0.078

B.3.

Regarding the average wavelength λ , we cannot see any clear influence of the material composition. These values are close to the designed geometric wavelength of the interface $\lambda = 2.40$ mm. Note that the vertical displacement shows the same wavelength, but, as expected, here the oscillations are shifted by $\approx \lambda/4$. This evidences that the behavior of vertical displacement is correlated with the asperity profile. In other words, the friction coefficient reaches its local extrema when the inclination of asperities (the slope of the vertical displacement over horizontal displacement) also has a local extremum (Figures C.4 and C.5).

The decrease of the friction amplitude differs between the compositions due to wear. For the R1 and R2 specimens (low binder content) the reduction of the amplitude is more prominent (Figure C.4), and we observe a nearly constant friction at the end of the first loading phase and during the reverse loading. This residual friction coefficient corresponds to the one of a planar interface, due to complete abrasion of the asperities. This friction reduction can be approximated with an exponential law (Eq. (C.6)). Rewriting Eqs. (C.6) and (C.5), we can determine the relative asperity friction R_w , which is initially equal to 1.0 and decreases to zero for progressing wear:

$$R_w = e^{-c_w \delta_{pp}} = \frac{(|\mu_i - \mu_\infty|)(1 + \mu_1 \mu_\infty)}{(\mu_1 - \mu_\infty)(1 + \mu_i \mu_\infty)} \quad (\text{C.10})$$

The relative asperity friction is plotted for a typical experiment (R1W-1) in Figure C.6a, on which we can obtain the wear coefficient c_w through least square fitting (Table C.1).

We observe a stronger dependency of the wear characteristics on binder content than on recoating speed. Compositions with a binder content $b = 3.8\%$ show c_w between ap-

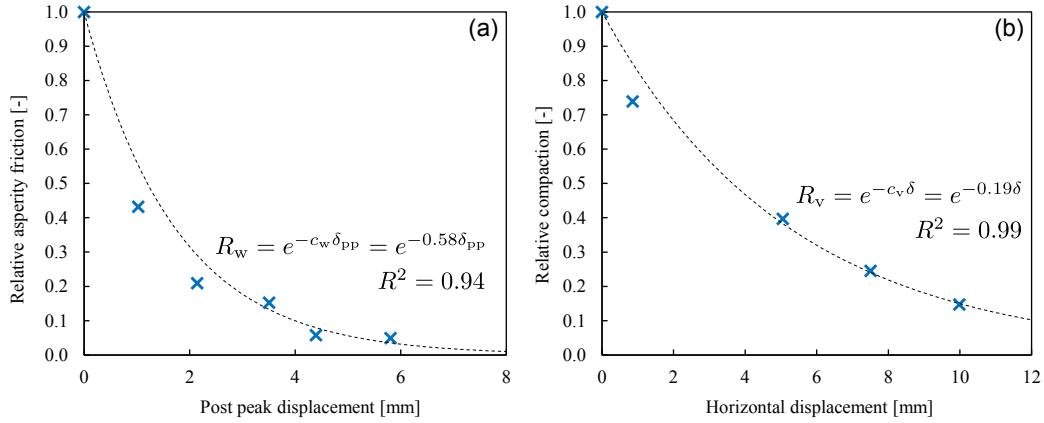


Figure C.6 – (a) Decrease of relative asperity friction with progressing displacement and wear on a typical wave interface shear test (R1W-1). The wear coefficient c_w can be evaluated using an exponential fit. (b) Measured relative vertical compaction on a typical wave shear experiment (R1W-1). The compaction is modeled through an exponential law, where the wear coefficient c_v can be evaluated using an exponential fit.

proximately 0.4 and 0.6, while for $b = 7.2$, we measured c_w between approximately 0.2 and 0.4. Increasing the recoating speed, from 0.13 to 0.26 m/s, the average value of c_w increases for about 0.1.

Evaluating the local minima $\delta_{v,i}$ of the vertical displacement evolution δ_v , one observes a general compaction, which starts immediately at $\delta = 0$, before the first friction peak. For large δ , the curves appear to approach a constant vertical displacement $\delta_{v,\infty}$ (cf. critical state, e.g. Wood, 1991). This global compaction is represented by the exponential law (Eq. (C.7)). Equation (C.7) can be rewritten, to introduce the relative compaction R_v , which can be evaluated at the local peaks of vertical displacement:

$$R_v = e^{-c_v \delta} = 1 - \frac{\delta_{v,i}}{\delta_{v,\infty}} \quad (\text{C.11})$$

The relative compaction values, determined on a typical experiment, are presented in Figure C.6b. One can obtain the values of c_v and $\delta_{v,\infty}$ by a least square error fit. This relationship captures only the overall vertical compaction, while in the experiments, we also observe significant oscillations due to asperities. In the following section, we are able to model these peaks of vertical displacement using Eqs. (C.7) - (C.9) with previously evaluated properties. Consequently, no additional model parameters are required.

C.3.2 Effect of normal stress

In order to explore the influence of the applied normal stress on shear behavior, we carried out the same shear experiments under 100 kPa normal stress on specimens made of composition R1 (Figure C.7, Table C.1). The most important difference between the cases of 100 kPa and 500 kPa is observed on the wear, presented in terms of the wear coefficient c_w in Figure C.7c. Otherwise, Coulomb's assumption of proportionality is valid. By reducing the normal stress, the decay of the friction oscillation is strongly reduced, giving a lower wear coefficient. Due to the lower normal stress, local stresses at the asperities decrease, resulting in less breakage/chipping of the asperities. This becomes also clear on the measured specimen weight loss after the tests, which was almost two times higher for test under 500 kPa normal stress (average loss of ~ 1.7 g under 100 kPa and ~ 3.2 g under 500 kPa).

No effect of the normal stress on the first peak friction coefficient μ_1 was reported (Figure C.7d). Conversely, the residual friction μ_∞ appears to be slightly influenced by the normal stress (Figure C.7e). Higher normal stress (500 kPa) leads to higher friction ($\mu_\infty \approx 0.57$), while under 100 kPa, we recorded $\mu_\infty \approx 0.50$.

C.4 Validation of the designed model for the design of frictional interfaces

We use the parameters evaluated on the five different test configurations (four compositions, one additional normal stress level) and insert them in the model equations for calculating the apparent friction coefficient μ (Eq. (C.5)) and the vertical displacement δ_v (Eq. (C.9)) in function of the shear displacement δ . The effective amplitude A_0 is determined indirectly from the wavelength, the basic friction and the first peak friction coefficient $\mu = \mu_1$ (Eqs. (C.2) and (C.3)):

$$A_0 = \frac{\lambda(\mu_1 - \mu_b)}{2\pi(1 + \mu_1\mu_b)} \quad (\text{C.12})$$

This model parameter A_0 can differ from the design amplitude A due to the printing resolution. Besides possible printing uncertainties, asperity abrasion could also occur during transport and handling of the printed specimens. Moreover, during the mounting of specimens in the experimental devices, loose grains could deposit in the convex areas of

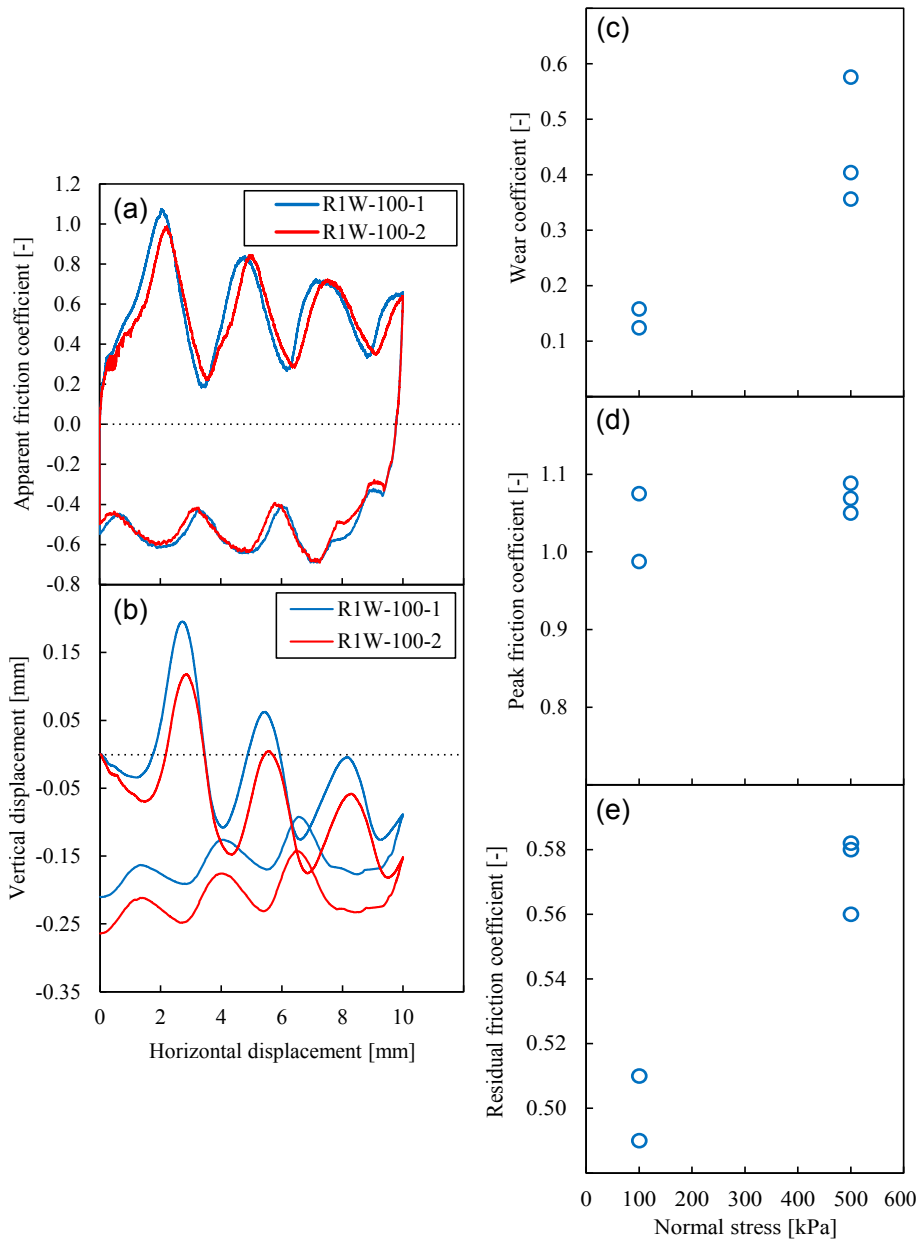


Figure C.7 – (a), (b) Friction experiments carried out on composition R1 under different 100 kPa of normal stress. (c), (d), (e) Effect of normal stress on the friction characteristics: (c) Wear coefficient, (d) first peak friction and (e) final friction of the abraded interface.

the interface, which could prevent a complete interface contact and therefore reduce the effective amplitude from A to A_0 . Given a printing resolution of $280 \mu\text{m}$ (corresponding to two grain diameters), we expect an error of the amplitude A in this range, which is quite high. Therefore, the most reliable way for estimating the amplitude A_0 for the interfaces

designed herein is through Eq. (C.12) (Table C.1).

Using the parameters presented in Table C.1, we are able to calculate the expected friction behavior (Eq. (C.5)) and vertical displacement (Eq. (C.9)) of our laboratory experiments. The results of these calculations are presented in Figures C.8, C.9 and C.10 together with the experimental curves. Notice that our main focus is on modeling the behavior after the first peak of friction. Before this point, in the loading branch, one could use a linear approximation for the shear force over shear displacement response and interpolate the vertical displacement.

Our model mimics very well the measured friction behavior with its oscillations. In addition, the vertical displacement (compaction/dilatancy) can be reproduced well, requiring only the identification of the overall compaction curve (red dashed line) as additional model parameters. The additional oscillations (red solid line) are obtained from the relationships with the friction behavior, which confirm the model presented herein. As a result, this approach could be used for the design of interfaces of custom frictional properties.

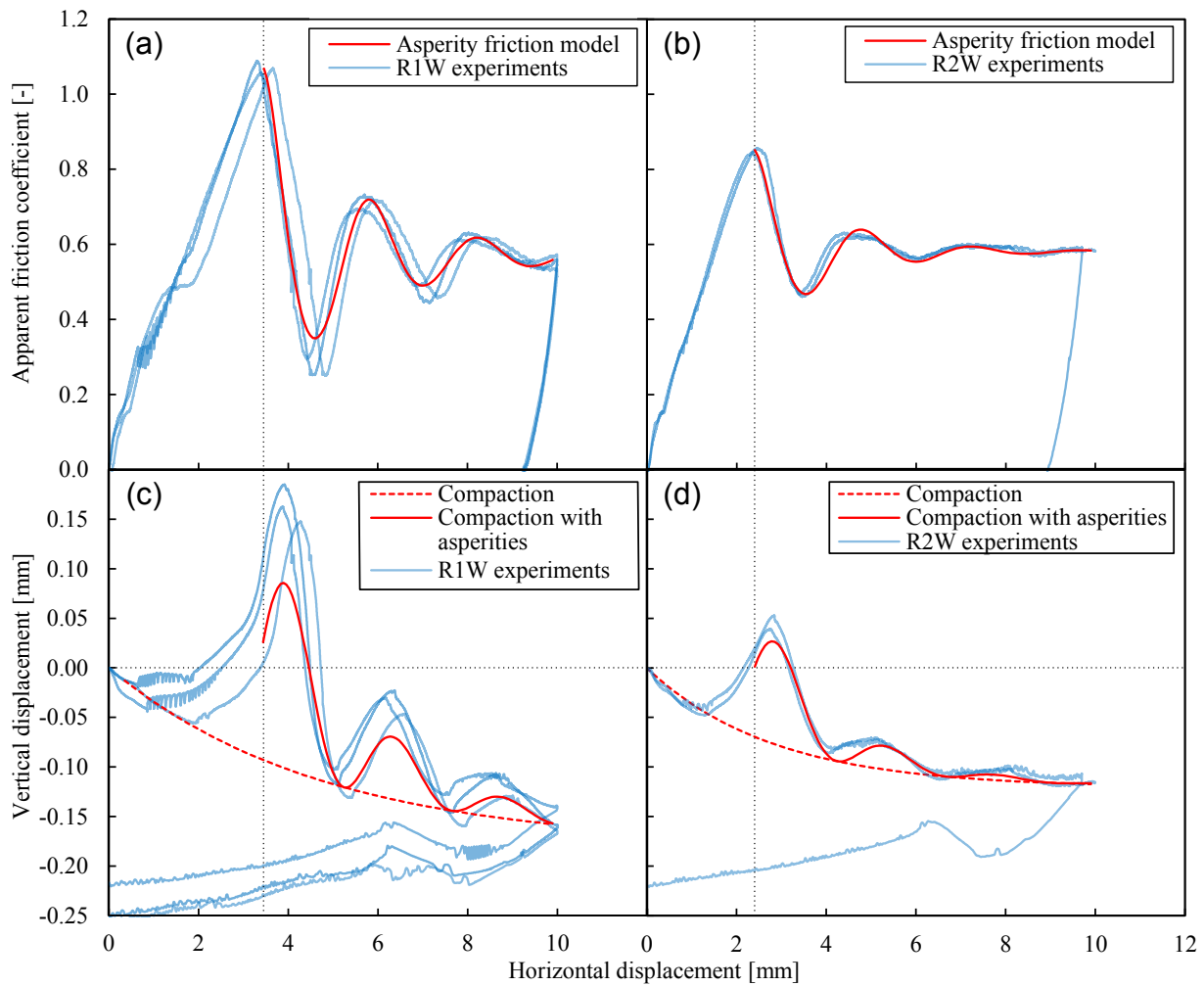


Figure C.8 – (a), (b) Evolution of friction and (c), (d) of vertical displacement with respect to the horizontal displacement, of R1 and R2 specimens under 500 kPa normal stress. The behavior calculated by our friction model (red solid lines) is compared with the experimental data (blue solid lines).

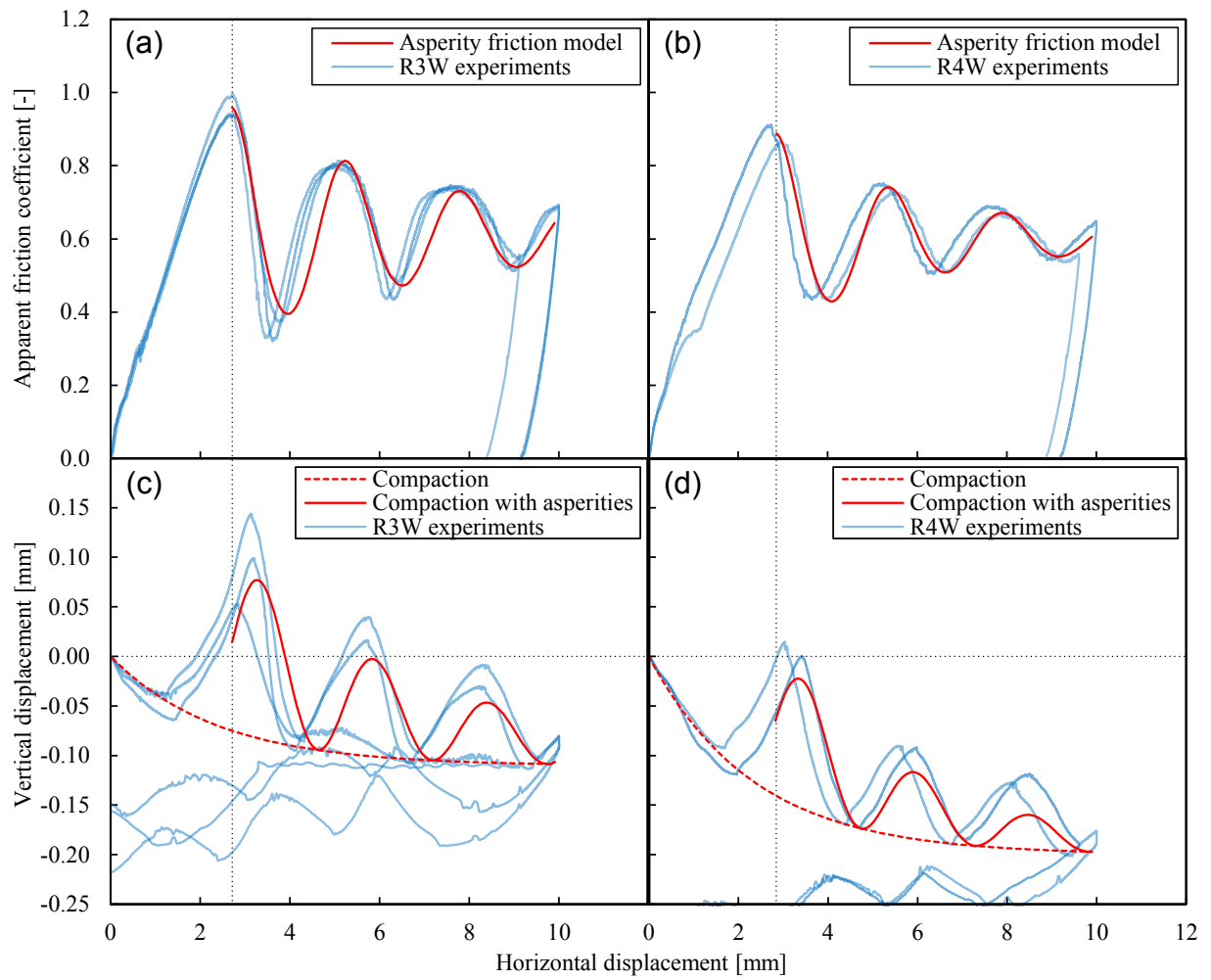


Figure C.9 – (a), (b) Evolution of friction and (c), (d) of vertical displacement with respect to the horizontal displacement, of R3 and R4 specimens under 500 kPa normal stress. The behavior calculated by our friction model (red solid lines) is compared with the experimental data (blue solid lines).

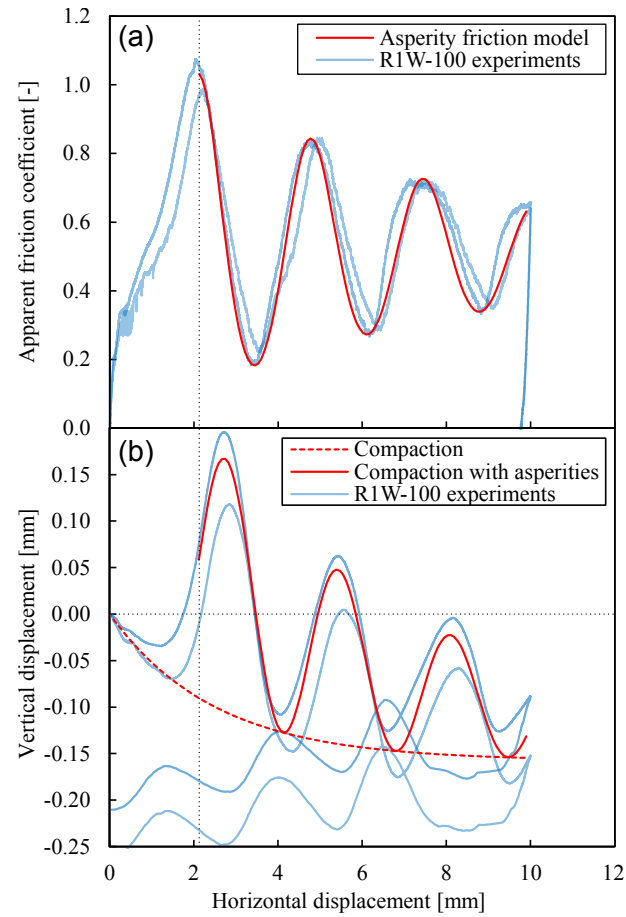


Figure C.10 – (a) Evolution of friction and (b) of vertical displacement with respect to the horizontal displacement, of R1 specimens under 100 kPa normal stress. The behavior calculated by our friction model (red solid lines) is compared with the experimental data (blue solid lines).

Design of the triplet experiment using FEM

D.1 Experimental setup

The configuration of the triplet experiment, which was used for the FEM analyses, is depicted in Figure D.1. Due to the fact that the design is fully symmetric in the $X-Y$ and $Y-Z$ planes, only a quarter of the whole model was studied numerically. The dimensions of the outer blocks were $20 \times 100 \times 100 \text{ mm}^3$ and of the inner block $40 \times 120 \times 100 \text{ mm}^3$. The height of the inner block was bigger than the outer ones in order to keep constant the area of the sliding surface during slip. The material of the blocks was considered linear elastic with shear modulus $G = 30 \text{ GPa}$. We first studied the system in quasi-static conditions without the spring. The inclusion of the spring can lead to unstable, dynamic behavior (see Section D.2).

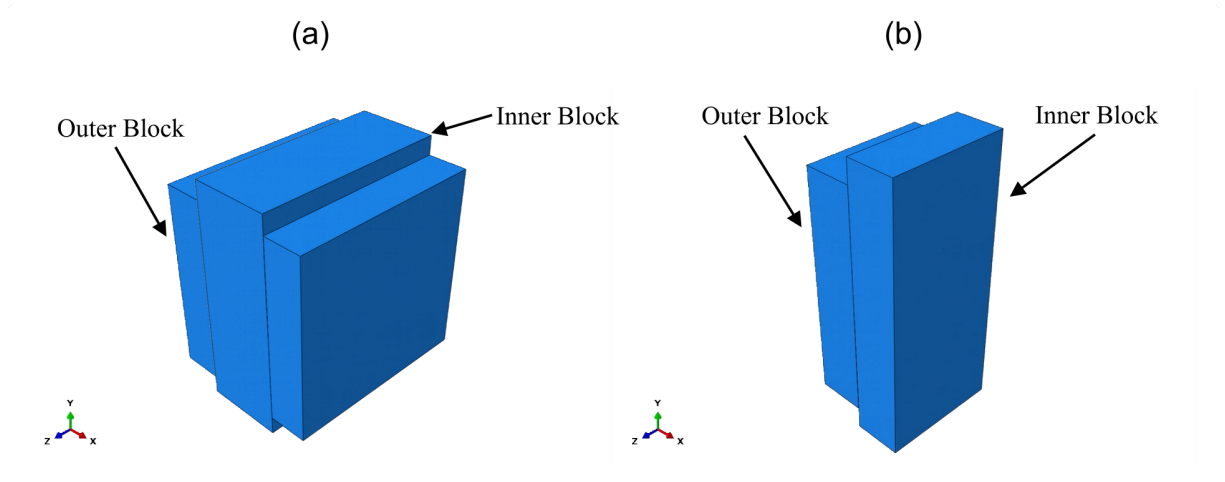


Figure D.1 – (a) Whole model. (b) Symmetric quarter which was finally modeled numerically.

Two loading steps were used. At the first step, we applied a normal stress on the outer blocks, while at the second step we applied a vertical displacement on the upper surface

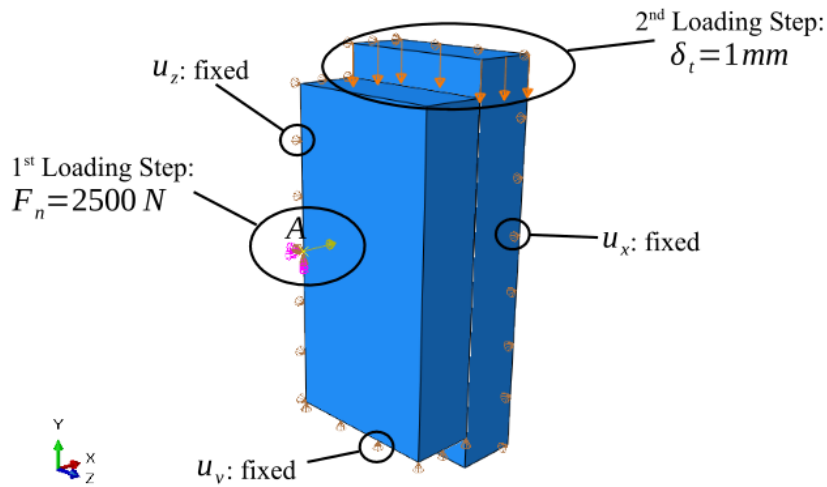


Figure D.2 – The two loading steps and the boundary conditions of the model. The normal load was applied at point A .

of the inner block. Both implicit and explicit analyses were conducted. Mesh convergence analyses were also performed. The normal force in both kind of analyses was applied as a point load at the middle of the outer surface of the fixed block (point A), which was rigidly connected with the whole lateral surface of the block (see Figure D.2). The value of the applied load at point A was $F_n = 2500\text{ N}$, representing a normal stress of 0.5 MPa . In this way, we simulated the loading ram in the laboratory experiment, which has very high stiffness in comparison with the specimen. In explicit analysis, the load was applied using a “smooth step” (the load follows the S-curve in time) in order to be quasi-static. Rayleigh Damping was also used in the explicit analyses to ensure quasi-static conditions.

The second loading step was the vertical displacement of $\delta_t = 1\text{ mm}$. It was applied on the upper surface of the middle block as shown in Figure D.2. Quasi-static conditions allowed to explore various parameters such as FEM mesh convergence, finite elements types, the contact algorithm and the influence of the dimensions of the model. Moreover, it allowed us to verify the precision of the explicit analyses on the base of the more accurate implicit ones. For the remaining boundary conditions, we refer to Figure D.2.

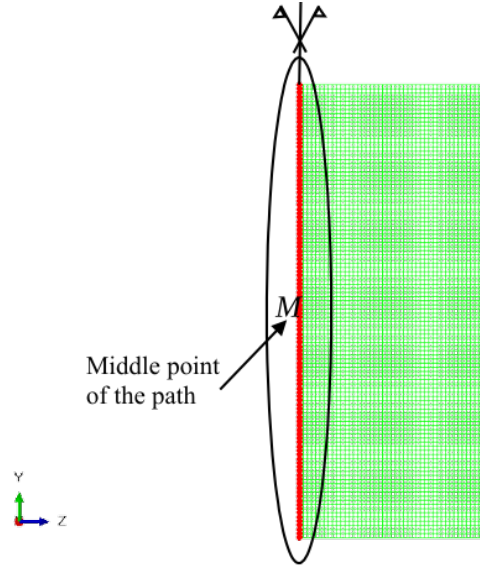


Figure D.3 – Middle path along the contact interface of the inner block. M is the middle point of this path.

D.1.1 Optimization of specimen's geometry

The implicit analysis was conducted in order to find the optimum width of the outer blocks that assures uniformly distributed stresses along the contact interface. Non uniform distribution of normal stresses is a weak point for the triplet setup according to existing experimental evidence (J. H. Dieterich, 1981a; Pluijm, van der, 1999). For this reason, the widths of 10, 20, 40 and 50 mm were examined for the outer blocks. Moreover, we tried to find an efficient FEM discretization for each width.

First, a mesh convergence analysis was performed for each width. Then, for the converged FEM mesh, the normal stress distribution at the path shown in Figure D.3 was compared for each width at the end of the second loading step. The normal stress in that path should be constant and equal to 0.5 MPa. However, this is not the case due to parasitic bending of the blocks around Z -axis (Pluijm, van der, 1999). In Figure D.4, we present the relative error of the developed normal stress compared to the desired uniform value of 0.5 MPa, i.e. $e = \frac{\sigma_n - 0.5}{0.5}$. The normalized cumulative error $\frac{1}{L_y} \int |e| dy$ is equal to 0.368, 0.357, 0.390 and 0.416 for the 10, 20, 40 and 50 mm widths, respectively. Therefore, the minimum cumulative error was found for the width of 20 mm, which was also adopted for further analyses. This is in agreement with J. H. Dieterich (1981a), who based on experiments concluded that the width of the outer block should be half of the one of the inner block.

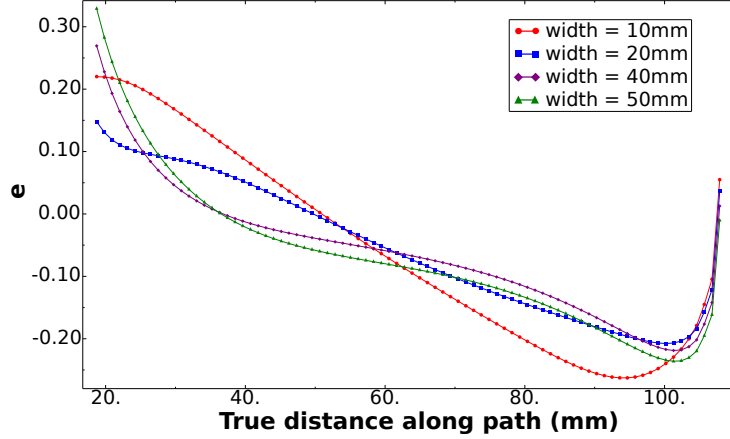


Figure D.4 – Relative error of the developed normal stress compared to the desired value of $\sigma_{\text{ref}} = 0.5$ MPa, i.e. $e = \frac{\sigma_n - \sigma_{\text{ref}}}{\sigma_{\text{ref}}}$.

D.1.2 Coulomb friction laws for the contact interface

We consider a Coulomb-type friction law with frictional softening for the interface between the blocks. The incremental form of this law is given as follows:

$$\dot{F} = k_{\text{pl}} \dot{\delta}, \quad (\text{D.1})$$

where:

$$\dot{F} = \begin{Bmatrix} \dot{F}_t \\ \dot{F}_n \end{Bmatrix}, \quad \dot{\delta} = \begin{Bmatrix} \dot{\delta}_t \\ \dot{\delta}_n \end{Bmatrix}, \quad \text{and} \quad k_{\text{pl}} = \frac{k_t k_n}{H_s F_n + k_t} \begin{bmatrix} \frac{H_s F_n}{k_n} & \mu \\ 0 & \frac{H_s F_n + k_t}{k_t} \end{bmatrix}, \quad (\text{D.2})$$

where F_t and F_n are the forces, δ_t and δ_n are the displacements and k_t and k_n are the stiffnesses in the tangential and the normal direction, respectively. In addition, H_s is a hardening modulus and μ is the coefficient of friction. When $H_s = 0$, the classical Coulomb criterion is obtained (Figure D.5a). $H_s > 0$ denotes hardening, while $H_s < 0$ describes softening (Figure D.5b). Here we consider a piecewise constant hardening modulus such as for the coefficient of friction to evolve from its static value $\mu_s = 0.70$ to the kinetic one $\mu_k = 0.20$ in a characteristic distance $d_c = 0.05$ mm. This characteristic distance depends on the material tested (Collins-Craft et al., 2020; J. H. Dieterich, 1981b; Rattetz et al., 2018a, 2018b) and its internal lengths.

This friction law is implemented in *Abaqus* as a user subroutine *VFRIC*. Other laws are also implemented (e.g. rate-and-state friction law), but their investigation is secondary for the design of the experiment presented in Chapter 5.

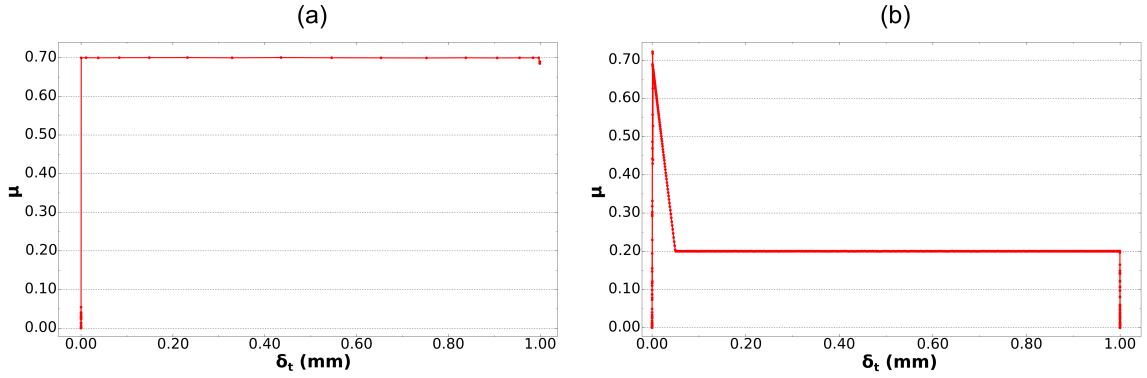


Figure D.5 – Coulomb friction law at point M using (a) perfect plasticity and (b) frictional softening.

D.2 Dynamic instability and earthquake nucleation

A dynamic instability upon shearing represents an earthquake nucleation. According to J. H. Dieterich (1979, among others), the relation that corresponds to this instability is (see also Section 1.2.1):

$$k < k_c = \frac{\Delta\mu F_n}{d_c}, \quad (\text{D.3})$$

where $\Delta\mu$ is the difference between the static (μ_s) and the kinetic (μ_k), coefficient of friction, k_c denotes the critical stiffness and depends on the rheology of the fault and k is the apparent elastic stiffness of the system (see also Chapters 1 and 2). In order to take into account this elastic stiffness in our model and produce the dynamic instability, a spring was assembled on the top of the moving block at point C in Y -direction (Figure D.6).

At point B , we applied constant vertical velocity of 0.01 m/s. This velocity represents the far-field velocity applied to a fault due to the slow movement of the tectonic plates (see also Chapter 5). However, here we take a much higher velocity in order to reduce the calculation time. Nevertheless, the characteristic velocity of the dynamic instability remains much smaller than the applied one at point C , assuring the qualitative equivalency of the system with a real fault system. When the velocity was applied, mass scaling and Rayleigh damping were deactivated for allowing a fully dynamic response.

Using the characteristic values of the Coulomb friction law with softening (Figure

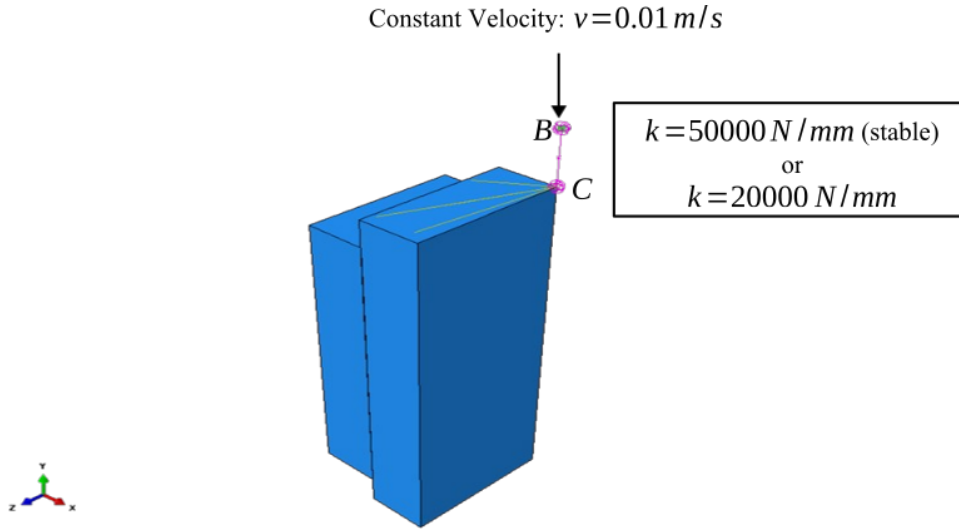


Figure D.6 – A constant velocity was applied at point B of the spring in both unstable and stable cases. The spring was connected with the model at point C .

D.5b) the critical stiffness using Eq. (D.3) is:

$$k_c = \frac{\Delta\mu F_n}{d_c} = \frac{(0.70 - 0.20)2500\text{ N}}{0.05\text{ mm}} = 25000\text{ N/mm} \quad (\text{D.4})$$

In our model, two different cases were examined, case 1 with aseismic slip ($k = 50000\text{ N/mm} > k_c$) and case 2 leading to the expected dynamic instability ($k = 20000\text{ N/mm} < k_c$).

In Figure D.7a, the total reaction at point B is presented for case 1, which reaches the peak of $0.70 \cdot 2500 = 1750\text{ N}$ and then drops to the value of $0.20 \cdot 2500 = 500\text{ N}$ with a slope of $k_c \approx -25000\text{ N/mm}$. This reaction represents the total friction at the interface. The non-linear behavior of the softening branch is due to the non-uniform normal stress distribution over the interface. In Figure D.7b, we show the evolution of the friction coefficient at the middle point M (see Figure D.3), which correctly follows the adopted constitutive law (see Figure D.5b). The small perturbations at some points are due to numerical errors related to the built-in contact algorithms of Abaqus and chosen tolerances. Notice that no dynamic instability occurs in this case, the slip is equal to the applied far-field velocity and therefore slow and “aseismic”. In other words, no dynamic instability happens.

However, when the stiffness of the spring is lower than the critical one, such as in case 2, a dynamic instability occurs (stick-slip motion). The post-peak slope in this case was

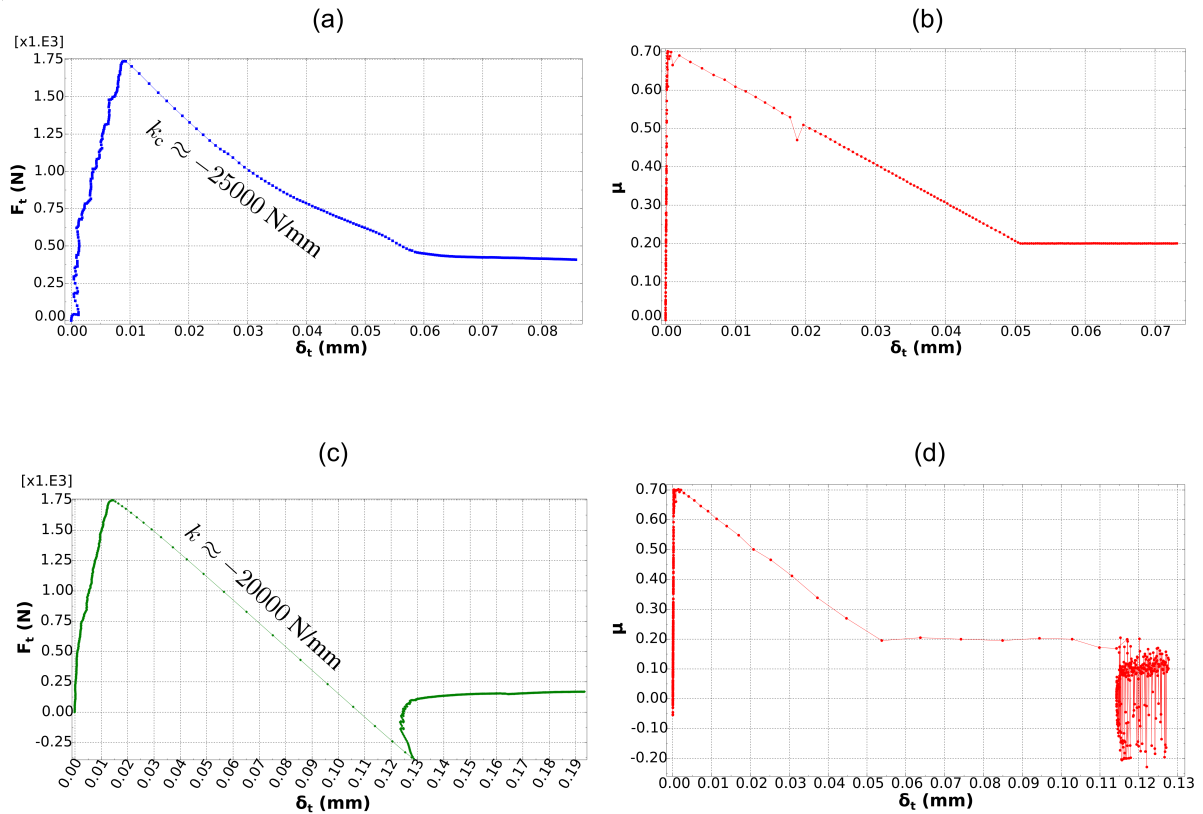


Figure D.7 – Aseismic (stable) slip: (a) Total reaction at point B in function of displacement at point C and (b) Friction coefficient at point M in function of displacement at point M .

Dynamic (unstable) slip: (c) Total reaction at point B in function of displacement at point C and (d) Friction coefficient at point M in function of displacement at point M .

$k \approx -20000$ N/mm (Figure D.7c), which as expected, coincides with the elastic stiffness of the spring. In Figure D.7d, the coefficient of friction in terms of displacement at point M (see Figure D.3) is plotted. The curve follows the Coulomb friction (Figure D.5b).

This dynamic instability is characterized by sudden increase in slip velocity. In Figure D.8, the velocity and the coefficient of friction is plotted in terms of the block’s displacement. The velocity reaches a peak of the order of m/s, which is characteristic of coseismic slip velocities in real faults. Then the slip velocity decreases gradually (deceleration) until the system reaches equilibrium, coinciding with the applied “far-field” velocity of 0.01 m/s. The “spring” line represents the spring’s stiffness divided by the normal force. After the peak in the red curve, the block accelerates because the spring’s force is larger than the friction, but when the spring’s force becomes lower than the friction, the block de-

celerates until equilibrium, phase which is characterized by an oscillatory behavior in the numerical analyses.

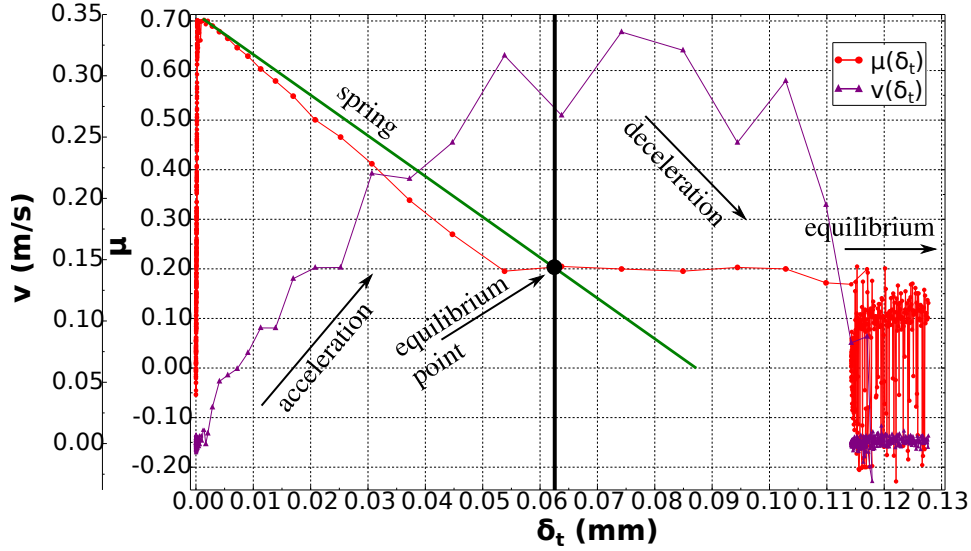


Figure D.8 – Velocity and coefficient of friction in terms of block’s displacement at point M in the case of unstable, seismic slip. The “spring” line represents the spring’s elastic stiffness divided by the normal force.

The same unstable behavior is presented in Figure D.9a, which depicts the evolution of velocity and displacement in terms of time. The key part of this Figure is the backward motion which is observed in block’s displacement. Moreover, in Figure D.9b, we present the kinetic energy, the drop of the elastic energy and frictional dissipation of the system in function of time. One can observe that the frictional dissipation has similar response with the orange curve of Figure D.9a, as expected. This is one more check in order to assure that our model responds properly and it is reliable for designing the experiment of Chapter 5. Finally, in Figure D.10, we can clearly distinguish the seismic from the aseismic slip. The stick-slip motion occurs when the block is dynamically moving driven by the spring’s elastic force. Eventually, using the scaling laws proposed by Kanamori and Brodsky (2004), the released energy E_s (Figure D.10) could be upscaled in real faults of much higher length compared to our specimens.

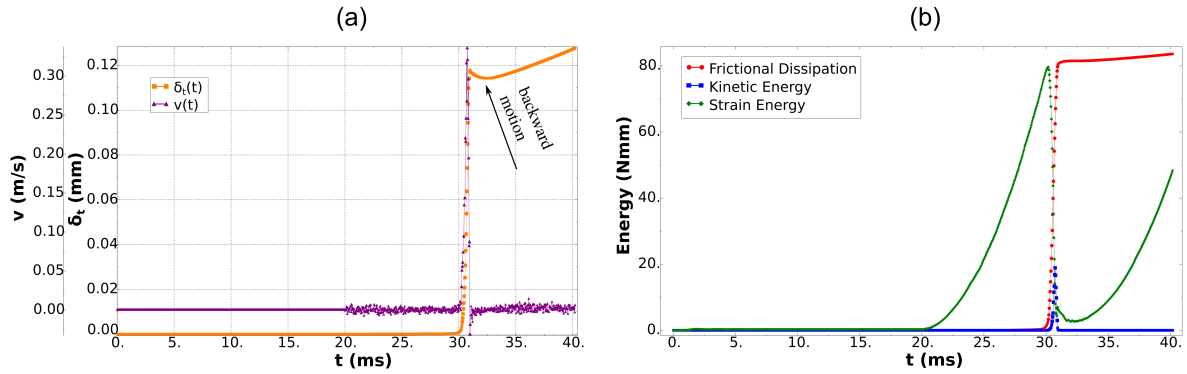


Figure D.9 – (a) Velocity and displacement, (b) kinetic and strain energy and frictional dissipation in terms of time.

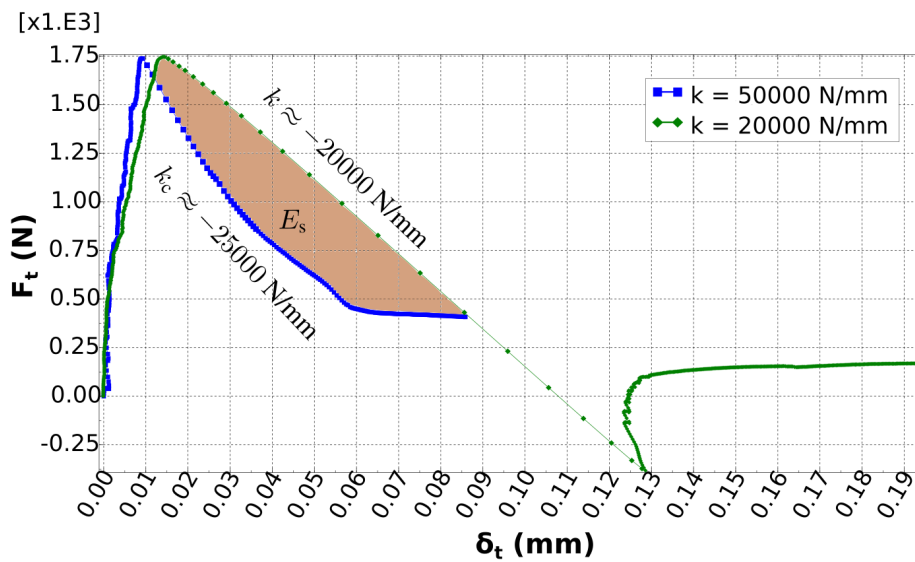


Figure D.10 – Comparison of total friction at point B between seismic and aseismic slip. The shaded area E_s is the released (kinetic) energy.

Scaling laws for the double-direct shear configuration

Using scaling laws, one could upscale experimental results to real earthquake events. To this extent, we employ the Buckingham π theorem (Baker et al., 1991; Logan, 2013), which states that any physical law depending on a sufficient number of dimensioned physical variables can be expressed with an equivalent law depending on a certain number of dimensionless quantities. In this work, we guarantee energetic and constitutive similarity but we allow kinematic and geometric dissimilarity. Energetic similarity can be achieved thanks to the use of a spring, whose stiffness is a free variable and therefore can alter the elasticity of the experimental configuration. Consequently, we achieve imperfect similitude between an idealized fault system (i.e. the prototype) and our experimental setup (i.e. the model) that allows us to reproduce earthquake-like instabilities in the laboratory with greater flexibility. Of course, different scaling laws can be proposed, however, our choice results in energetic equivalence between the prototype and the model during dynamic instabilities.

The dimensioned quantities that play a dominant role during dynamic events are:

$$\begin{aligned}
 [t] &= \text{fast time scale } [T], \\
 [\delta] &= \text{slip } [D], \\
 [\rho] &= \text{density } [R], \\
 [L_{ac}] &= \text{activated length } [L], \\
 [\Delta\tau] &= \text{shear stress drop } [RDLT^{-2}], \\
 [G] &= \text{shear modulus of the material } [RL^2T^{-2}].
 \end{aligned}
 \tag{E.1}$$

Notice that no constitutive assumptions are made at this stage regarding friction. The fundamental dimensions for this problem are T (time), D (slip), L (length) and R (density).

Dimensional analysis Logan, 2013 yields:

$$[\pi] = [t^{\alpha_1} \delta^{\alpha_2} \rho^{\alpha_3} L_{ac}^{\alpha_4} G^{\alpha_5} \Delta\tau^{\alpha_6}] = T^{\alpha_1-2\alpha_5-2\alpha_6} D^{\alpha_2+\alpha_6} R^{\alpha_3+\alpha_5+\alpha_6} L^{\alpha_4+2\alpha_5+\alpha_6} = 1. \quad (\text{E.2})$$

By making the exponents zero, we have:

$$\begin{cases} \alpha_1 - 2\alpha_5 - 2\alpha_6 = 0, \\ \alpha_2 + \alpha_6 = 0, \\ \alpha_3 + \alpha_5 + \alpha_6 = 0, \\ \alpha_4 + 2\alpha_5 + \alpha_6 = 0, \end{cases} \quad (\text{E.3})$$

leading to the following *dimension matrix*:

$$\begin{array}{cccccc} & \alpha_1 & \alpha_2 & \alpha_3 & \alpha_4 & \alpha_5 & \alpha_6 \\ T & \begin{pmatrix} 1 & 0 & 0 & 0 & -2 & -2 \end{pmatrix} \\ D & \begin{pmatrix} 0 & 1 & 0 & 0 & 0 & 1 \end{pmatrix} \\ R & \begin{pmatrix} 0 & 0 & 1 & 0 & 1 & 1 \end{pmatrix} \\ L & \begin{pmatrix} 0 & 0 & 0 & 1 & 2 & 1 \end{pmatrix} \end{array} \quad (\text{E.4})$$

The number of columns is $n = 6$ (number of unknowns) and the rank of the dimension matrix is $r = 4$. Consequently, there are $n - r = 2$ independent dimensionless quantities. Using backward substitution in the system of Eqs. (E.3), we get the vector form of the solution:

$$\begin{pmatrix} \alpha_1 \\ \alpha_2 \\ \alpha_3 \\ \alpha_4 \\ \alpha_5 \\ \alpha_6 \end{pmatrix} = \alpha_5 \begin{pmatrix} 2 \\ 0 \\ -1 \\ -2 \\ 1 \\ 0 \end{pmatrix} + \alpha_6 \begin{pmatrix} 2 \\ -1 \\ -1 \\ -1 \\ 0 \\ 1 \end{pmatrix} \quad (\text{E.5})$$

These two linearly independent vectors define the two independent (dimensionless) variables π_i (see also Buckingham π theorem):

$$\begin{cases} \pi_1 = t^2 \rho^{-1} L_{ac}^{-2} G, & (\text{E.6a}) \end{cases}$$

$$\begin{cases} \pi_2 = t^2 \delta^{-1} \rho^{-1} L_{ac}^{-1} \Delta\tau. & (\text{E.6b}) \end{cases}$$

The scaling parameters between the prototype and the model, $(\text{variable})_p / (\text{variable})_m$, are:

$$\lambda_t \text{ for fast time-scale,} \quad (\text{E.7a})$$

$$\lambda_\delta \text{ for slip length scale,} \quad (\text{E.7b})$$

$$\lambda_L \text{ for fault length scale,} \quad (\text{E.7c})$$

$$\lambda_A \text{ for fault area,} \quad (\text{E.7d})$$

$$\lambda_\rho \text{ for densities,} \quad (\text{E.7e})$$

$$\lambda_m \text{ for mobilized mass,} \quad (\text{E.7f})$$

$$\lambda_{\Delta\tau} \text{ for shear stresses,} \quad (\text{E.7g})$$

$$\lambda_\sigma \text{ for shear stresses,} \quad (\text{E.7h})$$

$$\lambda_G \text{ for shear modulus,} \quad (\text{E.7i})$$

$$\lambda_{\bar{k}} \text{ for normalized stiffnesses,} \quad (\text{E.7j})$$

$$\lambda_{\bar{E}} \text{ for energies per area of slip,} \quad (\text{E.7k})$$

$$\lambda_{M_0} \text{ for seismic moments,} \quad (\text{E.7l})$$

$$\lambda_{M_w} \text{ for earthquake magnitudes,} \quad (\text{E.7m})$$

where the subscript p denotes the prototype and m the model.

The prototype is an idealized fault with a length of $(L_{ac})_p = 5$ km. The density of the surrounding rocks is $\rho_p = 2500$ kg/m³, while the shear modulus is $G_p = 30$ GPa. The applied effective normal stress to the fault interface is $(\sigma'_n)_p = 50$ MPa. The corresponding characteristic slip-weakening distance is $(d_c^{sw})_p = 50$ mm and the shear stress drop is $\Delta\tau_p = 5$ MPa.

The model corresponds to the experimental configuration presented in Chapter 5. The sheared interfaces have a length of $(L_{ac})_m = 100$ mm and the mobilized mass weights $m_m = 1385$ g (per interface). A spring of stiffness $k_m = 22.55$ N/mm (per interface) is used to alter the elasticity of the system. The applied normal stress during the experiments is equal to $(\sigma'_n)_m = 100$ kPa. Concerning the frictional response, during the dynamic instability, a friction drop of $(\Delta\mu)_m = 0.1$ occurs (see also Sections 5.5 and 5.6). After this drop, the specimen rests at the residual friction, i.e. $(\mu_{res})_m = 0.5$. The slip-weakening characteristic distance of this friction law is estimated $(d_c^{sw})_m = 2.5$ mm. Finally, the corresponding shear stress drop is equal to $(\Delta\tau)_m = 10$ kPa.

Comparing the prototype and the experimental model defined above (see also Chapter 5), we can derive the scaling factors of fault length-scale, fault area, mass, density, normal stress, shear stress, normalized elasticity, and shear modulus, respectively, as follows (see Chapter 1 for the relations which connect the properties of the prototype/model used below):

$$\lambda_L = \frac{(L_{ac})_p}{(L_{ac})_m} = 5 \cdot 10^4, \quad (\text{E.8a})$$

$$\lambda_A = \lambda_L^2 = 2.5 \cdot 10^9, \quad (\text{E.8b})$$

$$\lambda_m = \frac{\rho_p (L_{ac})_p^3}{m_m} = 2.26 \cdot 10^{14}, \quad (\text{E.8c})$$

$$\lambda_\rho = \frac{\lambda_m}{\lambda_L^3} = 1.8, \quad (\text{E.8d})$$

$$\lambda_\sigma = \frac{(\sigma'_n)_p}{(\sigma'_n)_m} = 500, \quad (\text{E.8e})$$

$$\lambda_{\Delta\tau} = \frac{\Delta\tau_p}{\Delta\tau_m} = 500, \quad (\text{E.8f})$$

$$\lambda_{\bar{k}} = \frac{G_p / (L_{ac})_p}{k_m / A_m} = 2.7, \quad (\text{E.8g})$$

$$\lambda_G = \lambda_{\bar{k}} \lambda_L = 133038. \quad (\text{E.8h})$$

We can observe that $\lambda_{\Delta\tau}$ and λ_σ are the same allowing us to adopt constitutive similarity between the model and the prototype. Consequently, $(\Delta\mu)_p = 0.1$. Note that the characteristic slip-weakening distance is not necessary to scale with the same scaling factor as the fault slip, i.e. λ_δ . However, it's important, the instability condition to be satisfied in each scale (see Section 1.2.1) and the characteristic distance d_c to be sufficiently smaller than the expected maximum slip (see Chapter 1). The instability condition in the model scale was validated in Section 5.6. In the prototype scale, holds:

$$\bar{k}_p = \frac{G_p}{(L_{ac})_p} = 0.006 \text{ MPa/mm} < (\bar{k}_c)_p = \frac{(\Delta\tau)_p}{(d_c^{sw})_p} = 0.1 \text{ MPa/mm}. \quad (\text{E.9})$$

Therefore, an earthquake rupture is also expected in the prototype scale.

Table E.1 – Scaling parameters.

Quantity	Symbol	Unit	Model (M)	Prototype (P)	Scaling Factor λ (P/M)
characteristic slip-weakening distance	d_c^{sw}	mm	2.5	50	20
effective normal stress	σ'_n	MPa	0.1	50	500
shear stress drop	$\Delta\tau$	MPa	0.01	5	500
normalized elasticity	\bar{k}	MPa/m	2.2	6	2.7
normalized char. stiffness of interface	\bar{k}_c^{sw}	MPa/m	60	100	1.7
instability characteristic time	t_{inst}	s	0.05	9.2	184.2
maximum slip	δ_{max}	mm	7	1315	187.9
earthquake magnitude	M_w	-	-5.4	5.8	11.2 *(P-M)
operation time of control strategy	t_{op}	hours	1	184.2	184.2
sampling period of measurements	T_s	ms	2	368.4	184.2

Taking the ratio between Eqs. (E.6b) and (E.6a) and setting it equal between the prototype and the model, we find:

$$\lambda_\delta = \frac{\lambda_{\Delta\tau}\lambda_L}{\lambda_G} = 187.9. \quad (\text{E.10})$$

Applying $(\pi_1)_p = (\pi_1)_m$ (Eq. (E.6a)), we get:

$$\lambda_t = \sqrt{\frac{\lambda_\rho\lambda_L^2}{\lambda_G}} = 184.2. \quad (\text{E.11})$$

In case of earthquake-like instabilities, the seismic moment M_0 scales with $\lambda_{\Delta\tau}\lambda_L^3$:

$$\lambda_{M_0} = \lambda_{\Delta\tau}\lambda_L^3 = 6.3 \cdot 10^{16}. \quad (\text{E.12})$$

Notice that the earthquake magnitude, M_w , in Eq. (1.36) is a logarithmic function of M_0 . Therefore, the scaling factor of M_w doesn't have the classical form of the ratio between the prototype and model values, but instead:

$$\lambda_{M_w} = (M_w)_p - (M_w)_m = \frac{2}{3}\log_{10}(\lambda_{M_0}) = 11.2. \quad (\text{E.13})$$

Consequently, the corresponding magnitude of the real earthquake is $(M_w)_p = 5.8$.

All the scaling factors and the values both in the model and prototype for each variable are summarized in Table E.1.

Controlling earthquakes in the laboratory using robust continuous-time controllers

F.1 Control objective

In this Appendix, we extend the work presented in Chapters 5 and 6. Here, we reduce the sampling period of the acquired measurements from $T_s = 2$ ms to $T_s = 1$ ms. This change allows us to design different kinds of robust continuous-time controllers and compare their effectiveness in the laboratory using the same triplet apparatus introduced in Chapter 5.

The experimental setup, the loading procedure, the material of the specimen, the elastic spring, the available measurements, and the capabilities of the developed *LabVIEW* code are the same as provided in Chapter 5. The design of the robust controllers is based again on the spring-slider reduced-order model (see Section 1.2 and Figure F.1). Its dynamics are represented by the following differential equation:

$$m\ddot{\delta} = -\mu(t, \delta, \dot{\delta})(\sigma'_n - p)A + k(\delta_\infty(t) - \delta) + \eta(v_\infty - \dot{\delta}) + \varphi_e(t, \delta, \dot{\delta}), \quad (\text{F.1})$$

where $\varphi_e(t, \delta, \dot{\delta})$ is a perturbation affecting the system, e.g. an external perturbation or unmodelled dynamics due to the complex frictional phenomena. The definition of the rest parameters above is provided in Section 1.2 (see also Figure F.1). For the frictional evolution, the slip-weakening friction law is adopted (see Sections 1.1.1 and 5.5):

$$\mu(\delta) = \mu_{\text{res}} + \Delta\mu \cdot e^{-\frac{\delta}{d_c^{\text{sw}}}}, \quad (\text{F.2})$$

with $\Delta\mu > 0$. The coefficient of friction evolves from an initial value $\mu_{\text{max}} = \mu_{\text{res}} + \Delta\mu$ (static friction coefficient), to a residual one μ_{res} (kinetic friction coefficient) in a characteristic slip-weakening distance d_c^{sw} .

Defining the state variables $z_1 = \delta$ and $z_2 = \dot{\delta}$, and using Eq. (F.2) for friction, the

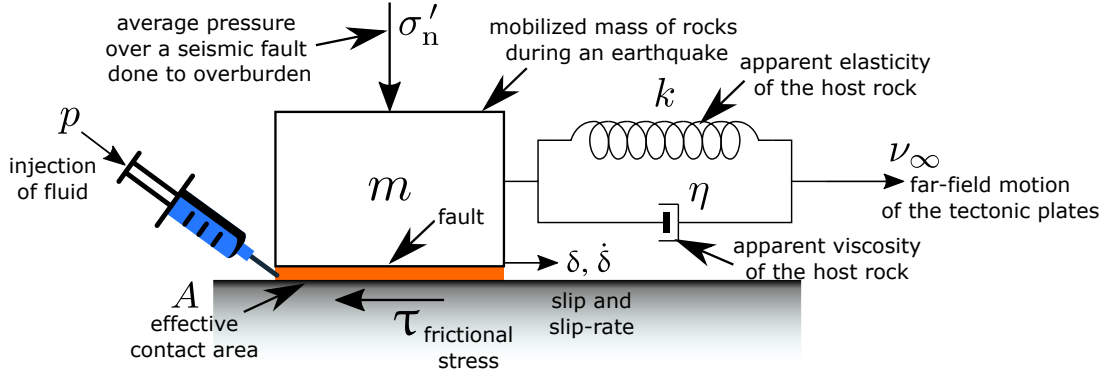


Figure F.1 – Spring-slider reduced order model for reproducing earthquake-like instabilities.

state representation of Eq. (F.1) is:

$$\begin{aligned} \dot{z}_1 &= z_2, \\ \dot{z}_2 &= -\mu(z_1)\hat{N}(\sigma'_n - p) + \hat{k}(\delta_\infty - z_1) + \hat{\eta}(v_\infty - z_2) + \hat{\varphi}_e(t, z_1, z_2), \end{aligned}$$

where $\hat{N} = \frac{A}{m}$, $\hat{k} = \frac{k}{m}$, $\hat{\eta} = \frac{\eta}{m}$, and $\hat{\varphi}_e(t, z_1, z_2) = \frac{\varphi_e(t, z_1, z_2)}{m}$.

The set of equilibrium points (z_1^*, z_2^*) of the above system in open loop ($p = 0$) and without perturbation ($\hat{\varphi}_e(t, z_1, z_2) = 0$), is described by:

$$z_1^* = -\mu(z_1^*)\frac{\hat{N}}{\hat{k}}\sigma'_n + \delta_\infty + \frac{\hat{\eta}}{\hat{k}}v_\infty, \quad z_2^* = 0.$$

Note that the equilibrium (z_1^*, z_2^*) depends on the friction coefficient $\mu(z_1^*)$. Assuming that the friction is maximum at the equilibrium point $z_1^* = 0$, i.e. $\mu(0) = \mu_{\max}$, we define the new state variables $x_1 = z_1 - z_1^*$ and $x_2 = z_2 - z_2^*$ to obtain a new shifted system as:

$$\begin{aligned} \dot{x}_1 &= x_2, \\ \dot{x}_2 &= -[\mu(x_1) - \mu^*]\hat{N}\sigma'_n + \mu(x_1)\hat{N}p - \hat{k}x_1 - \hat{\eta}x_2 + \hat{\varphi}_e(t, x_1, x_2), \end{aligned} \tag{F.3}$$

where $\mu^* = \mu(0) = \mu_{\max}$. Note that if $\hat{\varphi}_e(t, x_1, x_2) = 0$, the system of Eq. (F.3) has an equilibrium point located at the origin ($x_1^* = x_2^* = 0$) in open loop.

The stability of the origin of the system of Eq. (F.3), without the perturbation term $\hat{\varphi}_e(t, x_1, x_2)$, has been extensively studied in Section 1.2.1. There, we show that a dynamic instability takes place when the elastic unloading of the spring cannot be counterbalanced by friction (see Eq. (1.43)).

F.2 Control design

Two control approaches are presented in this section: the first one is based on continuous sliding-mode control theory (Moreno, 2016; Torres-González et al., 2017), whereas the second one is based on LQR control (Lewis et al., 2012, see also Chapter 3). Both of these controllers must be able to force the states of Eq. (F.3) to track a predefined reference, using a continuous control signal, in spite of uncertainties/perturbations of the system.

The desired reference for the output $y = x_1$ is a smooth function reading as:

$$r(t) = d_{\max} s^3 (10 - 15s + 6s^2), \quad (\text{F.4})$$

where $s = \frac{t}{t_{\text{op}}}$, d_{\max} the target displacement and t_{op} the operational time of the tracking strategy. In general, for an earthquake event, d_{\max} can be estimated through the relation provided in Eq. (1.33). This is the distance the fault slides dynamically in order to reach its subsequent stable equilibrium point.

F.2.1 Sliding-Mode based control

To perform the tracking of the desired references $r(t), \dot{r}(t)$, a sliding mode based control is designed. Defining the tracking error variables:

$$e_1 = x_1 - r(t), \quad e_2 = x_2 - \dot{r}(t), \quad (\text{F.5})$$

the error dynamics reads as:

$$\begin{aligned} \dot{e}_1 &= e_2, \\ \dot{e}_2 &= -[\mu(e_1 + r) - \mu^*] \hat{N} \sigma'_n + \mu(e_1 + r) \hat{N} p - \hat{k}(e_1 + r) - \hat{\eta}(e_2 + \dot{r}) + \hat{\varphi}_e(t, e_1 + r, e_2 + \dot{r}) - \ddot{r}. \end{aligned} \quad (\text{F.6})$$

If the exact knowledge of the system parameters and the system dynamics would be available, one could compensate all the known dynamics in \dot{e}_2 , in order to get the nominal error system:

$$\begin{aligned} \dot{e}_1 &= e_2, \\ \dot{e}_2 &= \nu, \end{aligned} \quad (\text{F.7})$$

by designing the control p as:

$$p = \frac{1}{\mu(e_1 + r)\hat{N}} \left\{ \nu + [\mu(e_1 + r) - \mu^*]\hat{N}\sigma'_n + \hat{k}(e_1 + r) + \hat{\eta}(e_2 + \dot{r}) - \hat{\varphi}_e(t, e_1 + r, e_2 + \dot{r}) + \ddot{r} \right\}, \quad (\text{F.8})$$

and with the new control input, ν , designed to force e_1, e_2 towards zero. A solution could be the linear feedback control $\nu = -k_1 e_1 - k_2 e_2$, with any $k_1, k_2 > 0$. However, the system of Eq. (F.7) is valid only in the nominal case. If this is not the case, the application of the state-feedback given by Eq. (F.8) with uncertain parameters will not lead to Eq. (F.7). In this case, consider the following feedback control:

$$p = \frac{1}{\mu_0 \hat{N}_0} \nu, \quad (\text{F.9})$$

where the sub index ‘0’ represents the nominal values of the real system parameters. Notice that some additional nominal parameters could be used in Eq. (F.9), i.e. $\hat{k}_0, \hat{\eta}_0$ or even the known term $\ddot{r}(t)$. However, the objective here is to design a controller requiring a limited amount of information.

Therefore, the closed-loop system obtained from Eq. (F.6) and Eq. (F.9) reads as:

$$\begin{aligned} \dot{e}_1 &= e_2, \\ \dot{e}_2 &= \beta(t, e) [\nu + h(t, e)], \end{aligned} \quad (\text{F.10})$$

where $e = [e_1, e_2]^T$, $\beta(t, e)$ the uncertain control coefficient and $h(t, e)$ a matched perturbation affecting the system. These terms are defined as:

$$\begin{aligned} \beta(t, e) &= \frac{\mu(e_1 + r)\hat{N}}{\mu_0 \hat{N}_0}, \\ h(t, e) &= \frac{1}{\beta(t, e)} \left\{ -[\mu(e_1 + r) - \mu^*]\hat{N}\sigma'_n - \hat{k}(e_1 + r) - \hat{\eta}(e_2 + \dot{r}) + \hat{\varphi}_e(t, e_1 + r, e_2 + \dot{r}) - \ddot{r} \right\}. \end{aligned} \quad (\text{F.11})$$

Both these terms are assumed to fulfill in the operating domain:

$$0 < b_m \leq \beta(t, e) \leq b_M, \quad \left| \frac{dh(t, e)}{dt} \right| \leq \bar{L}, \quad (\text{F.12})$$

with known constants b_m, b_M, \bar{L} .

Remark 1 *The condition for $\beta(t, e)$ in Eq. (F.12) is satisfied because of the definition of $\mu(\delta)$ in Eq. (F.2). The condition for $h(t, e)$ in Eq. (F.12) is satisfied (locally inside a domain) because of the definition of $r(t)$ in Eq. (F.4) and if the external perturbation term $\hat{\varphi}_e(t, e_1 + r, e_2 + \dot{r})$ is Lipschitz with respect to (w.r.t.) time. As a result, the obtained tracking result is valid locally.*

The design of the control input ν able to stabilize Eq. (F.10) at $e_1 = e_2 = 0$, despite the presence of $\beta(t, e), h(t, e)$, results in an aseismic motion of the spring-slider system described by Eq. (F.3). For this purpose, consider the Second-Order Continuous Twisting Algorithm (2-CTA) introduced in Torres-González et al. (2017):

$$\begin{aligned}\nu &= -\lambda^{\frac{2}{3}}k_1 [e_1]^{\frac{1}{3}} - \lambda^{\frac{1}{2}}k_2 [e_2]^{\frac{1}{2}} + \xi_1, \\ \dot{\xi}_1 &= -\lambda k_3 [e_1]^0 - \lambda k_4 [e_2]^0,\end{aligned}\tag{F.13}$$

and the Second-Order Discontinuous Integral Algorithm (2-DIA) introduced in Moreno (2016):

$$\begin{aligned}\nu &= -\lambda^{\frac{1}{2}}k_2 \left[[e_2]^{\frac{3}{2}} + \lambda^{\frac{1}{3}}k_1^{\frac{3}{2}}e_1 \right]^{\frac{1}{3}} + \xi_1, \\ \dot{\xi}_1 &= -\lambda k_3 \left[e_1 + \lambda^{-\frac{1}{2}}k_4 [e_2]^{\frac{3}{2}} \right]^0,\end{aligned}\tag{F.14}$$

where the function $[\cdot]^\alpha := |\cdot|^\alpha \text{sign}(\cdot)$, for any $\alpha \in \mathbb{R}_{\geq 0}$ with $\text{sign}(x) = \begin{cases} 1 & x > 0 \\ [-1, 1] & x = 0 \\ -1 & x < 0 \end{cases}$.

Both of these algorithms consist in a static homogeneous finite-time controller and a discontinuous integral action, aimed at estimating and compensating the uncertainties and perturbations. Notice that the presence of the discontinuous function, $[\cdot]^0$, in the integral action finally results in a continuous control signal.

Theorem 1 *The origin of the system of Eq. (F.10) is locally finite-time stable, despite the presence of the Lipschitz w.r.t. the time uncertainties/perturbations, $h(t, e)$, and bounded uncertain coefficient, $\beta(t, e)$, satisfying Eq. (F.12), if the control ν takes the form of Eq. (F.13) or Eq. (F.14), with gains appropriately chosen.*

As a consequence of Theorem 1, the state variables $\delta, \dot{\delta}$ of the system of Eq. (F.1), are locally driven in finite-time to the desired references $r(t), \dot{r}(t)$ defined in Eq. (F.4).

Proof 1 The closed-loop system of Eq. (F.10), with controller given by Eq. (F.13) reads as:

$$\begin{aligned}\dot{e}_1 &= e_2, \\ \dot{e}_2 &\in [b_m, b_M] \left(-\lambda^{\frac{2}{3}} k_1 [e_1]^{\frac{1}{3}} - \lambda^{\frac{1}{2}} k_2 [e_2]^{\frac{1}{2}} + e_3 \right), \\ \dot{e}_3 &\in -\lambda k_3 [e_1]^0 - \lambda k_4 [e_2]^0 + [-\bar{L}, \bar{L}].\end{aligned}\tag{F.15}$$

If the controller given by Eq. (F.14) is used, one gets:

$$\begin{aligned}\dot{e}_1 &= e_2, \\ \dot{e}_2 &\in [b_m, b_M] \left(-\lambda^{\frac{1}{2}} k_2 \left[[e_2]^{\frac{3}{2}} + \lambda^{\frac{1}{3}} k_1^{\frac{3}{2}} e_1 \right]^{\frac{1}{3}} + e_3 \right), \\ \dot{e}_3 &\in -\lambda k_3 \left[e_1 + \lambda^{-\frac{1}{2}} k_4 [e_2]^{\frac{3}{2}} \right]^0 + [-\bar{L}, \bar{L}].\end{aligned}\tag{F.16}$$

Note that in both cases: $e_3 = \xi_1 + h(t, e)$.

The solutions of both systems are understood in the Filippov's sense (see Filippov, 1988). The definition of weighted homogeneity is introduced below:

Definition 1 (Bacciotti & Rosier, 2005; Bernuau et al., 2014)

Consider the vector $x \in \mathbb{R}^n$. Its dilation operator is defined as $\Delta_\epsilon^r x := (\epsilon^{r_1} x_1, \dots, \epsilon^{r_n} x_n)$, $\forall \epsilon > 0$, where $r_i > 0$ are the weights of the coordinates and $r = (r_1, \dots, r_n)$ is the vector of weights.

A function $V : \mathbb{R}^n \rightarrow \mathbb{R}$ (or a vector field $f : \mathbb{R}^n \rightarrow \mathbb{R}^n$, or vector-set $F(x) \subset \mathbb{R}^n$) is called r -homogeneous of degree $m \in \mathbb{R}$ if the identity $V(\Delta_\epsilon^r x) = \epsilon^m V(x)$ holds (or $f(\Delta_\epsilon^r x) = \epsilon^m \Delta_\epsilon^r f(x)$, or $F(\Delta_\epsilon^r x) = \epsilon^m \Delta_\epsilon^r F(x)$).

Using an homogeneous Lyapunov approach as in Gutiérrez-Oribio et al. (2021) and Mercado-Urbe and Moreno (2020), given a fixed \bar{L} , the origin of systems of Eq. (F.15) and Eq. (F.16) is asymptotically stable, but locally, as a consequence of Remark 1. Moreover, since the systems are homogeneous of negative degree, such origins are finite-time stable (see Levant, 2005).

The scaling factor λ in Eq. (F.15) and Eq. (F.16) is used to obtain a new set of gains for the controllers, with a different Lipschitz constant \hat{L} of the perturbation, i.e. $\hat{L} = \lambda \bar{L}$. For the case of the 2-CTA, the gains are scaled as $(k_1, k_2, k_3, k_4) \rightarrow (k_1 \lambda^{\frac{2}{3}}, k_2 \lambda^{\frac{1}{2}}, k_3 \lambda, k_4 \lambda)$. For the case of the 2-DIA, the gains are scaled

as $(k_1, k_2, k_3, k_4) \rightarrow (k_1\lambda^{\frac{1}{3}}, k_2\lambda^{\frac{1}{2}}, k_3\lambda, k_4\lambda^{-\frac{1}{2}})$ (see Gutiérrez-Oribio et al., 2021; Torres-González et al., 2017, for more details on each scaling).

Then, for arbitrary values of the bounds b_m, b_M, \bar{L} in Eq. (F.12), there exist appropriate values of the gains for the controllers given by Eq. (F.13) or Eq. (F.14). ■

F.2.2 LQR based Control

Following the sliding-mode based control design, this subsection presents an extended Linear Quadratic Regulator (e-LQR). The term *extended* is due to the integral action added to a standard LQR algorithm, in such a way that Lipschitz w.r.t. the states uncertainties are compensated with the resultant control.

Starting from Eq. (F.3), the plant is extended with a double integrator to improve the tracking of the reference trajectory. The stability of this augmented plant controlled by an LQR controller is being proved by a Lyapunov's approach (see Section 3.2). For this purpose, define:

$$\begin{aligned}\dot{\xi}_1 &= x_1 - r(t), \\ \dot{\xi}_2 &= \xi_1.\end{aligned}\tag{F.17}$$

The matrix form of system of Eq. (F.3) is:

$$\underbrace{\begin{bmatrix} \dot{x}_1 \\ \dot{x}_2 \end{bmatrix}}_{\dot{x}} = \underbrace{\begin{bmatrix} 0 & 1 \\ -\hat{k} & -\hat{\eta} \end{bmatrix}}_{A(t)} \underbrace{\begin{bmatrix} x_1 \\ x_2 \end{bmatrix}}_x + \underbrace{\begin{bmatrix} 0 \\ \mu(x_1)\hat{N} \end{bmatrix}}_{B(t,x)} p + \underbrace{\begin{bmatrix} 0 \\ -[\mu(x_1) - \mu^*]\hat{N}\sigma'_n + \hat{\varphi}_e(t, x_1, x_2) \end{bmatrix}}_{g(t,x)},\tag{F.18}$$

whereas the matrix form of (ξ_1, ξ_2) -system is:

$$\underbrace{\begin{bmatrix} \dot{\xi}_1 \\ \dot{\xi}_2 \end{bmatrix}}_{\dot{\xi}} = \underbrace{\begin{bmatrix} 0 & 0 \\ 1 & 0 \end{bmatrix}}_{C_\xi} \underbrace{\begin{bmatrix} \xi_1 \\ \xi_2 \end{bmatrix}}_{\xi} + \underbrace{\begin{bmatrix} 1 & 0 \\ 0 & 0 \end{bmatrix}}_{C_x} \underbrace{\begin{bmatrix} x_1 \\ x_2 \end{bmatrix}}_x + \underbrace{\begin{bmatrix} -r(t) \\ 0 \end{bmatrix}}_{r_\xi(t)}.\tag{F.19}$$

Following a conventional integral control design (see for example Chapter 12 in Khalil, 2013) and supposing a constant reference $r(t) = r_0$, the augmented system composed by

Eq. (F.18)-(F.19) reads as:

$$\underbrace{\begin{bmatrix} \dot{x} \\ \dot{\xi} \end{bmatrix}}_{\dot{x}_a} = \underbrace{\begin{bmatrix} A(t) & O_{2 \times 2} \\ C_x & C_\xi \end{bmatrix}}_{A_a(t)} \underbrace{\begin{bmatrix} x \\ \xi \end{bmatrix}}_{x_a} + \underbrace{\begin{bmatrix} B(t, x) \\ O_{2 \times 1} \end{bmatrix}}_{B_a(t, x_a)} p + \underbrace{\begin{bmatrix} g(t, x) \\ O_{2 \times 1} \end{bmatrix}}_{g_a(t, x_a)}. \quad (\text{F.20})$$

Consider additive (matched) parameter uncertainties for the matrices $A_a(t)$ and $B_a(t, x_a)$ such that:

$$A_a(t) = A_0 + \Delta A(t), \quad (\text{F.21})$$

$$B_a(t, x_a) = B_0 + \Delta B(t, x_a), \quad (\text{F.22})$$

where:

$$A_0 = \begin{bmatrix} 0 & 1 & 0 & 0 \\ -\hat{k}_0 & -\hat{\eta}_0 & 0 & 0 \\ 1 & 0 & 0 & 0 \\ 0 & 0 & 1 & 0 \end{bmatrix}, \quad \Delta A(t) = \begin{bmatrix} 0 & 0 & 0 & 0 \\ -\Delta \hat{k} & -\Delta \hat{\eta} & 0 & 0 \\ 0 & 0 & 0 & 0 \\ 0 & 0 & 0 & 0 \end{bmatrix},$$

$$B_0 = \begin{bmatrix} 0 \\ [\mu(x_1)\hat{N}]_{\min} \\ 0 \\ 0 \end{bmatrix}, \quad \Delta B(t, x_a) = \begin{bmatrix} 0 \\ \Delta[\mu(x_1)\hat{N}] \\ 0 \\ 0 \end{bmatrix}.$$

The sub index ‘0’ represents the nominal value of the respective variable, whereas the quantity with the prefix ‘ Δ ’ corresponds to the uncertainty of the respective variable. In addition, the sub index ‘min’ indicates the minimum value of the control coefficient $\mu\hat{N}$, so that the variation $\Delta B(t, x_a)$ is always positive semi-definite.

From Eqs. (F.20), (F.21) and (F.22), one gets:

$$\dot{x}_a = A_0 x_a + \Delta B(t, x_a) p + B_0 [p + h(t, x_a)], \quad (\text{F.23})$$

where $h(t, x_a) = B_0^+ \Delta A(t) x_a + B_0^+ g_a(t, x_a)$. The matrix B_0^+ denotes the *Moore-Penrose inverse matrix* of B_0 , i.e.:

$$B_0^+ = \begin{bmatrix} 0 & \frac{1}{[\mu(x_1)\hat{N}]_{\min}} & 0 & 0 \end{bmatrix}. \quad (\text{F.24})$$

Then, the nonlinear vector $h(t, x_a)$ can be written as:

$$h(t, x_a) = B_0^+ [\Delta A(t)x_a + g_a(t, x_a)] = -\frac{1}{[\mu(x_1)\hat{N}]_{\min}} \left\{ \Delta\hat{\eta}x_2 + \Delta\hat{k}x_1 + [\mu(x_1) - \mu^*] \sigma_n' \hat{N} - \hat{\varphi}_e(t, x_1, x_2) \right\} \quad (\text{F.25})$$

Assuming the external perturbation $\hat{\varphi}_e(t, x_1, x_2)$ can be written as $\hat{\varphi}_e(t, x_1, x_2) = \hat{\varphi}_{1e}x_1 + \hat{\varphi}_{2e}x_2$ for some known positive constants $\hat{\varphi}_{1e}, \hat{\varphi}_{2e}$, the norm of $h(t, x_a)$ reads as:

$$\begin{aligned} \|h(t, x_a)\| &= \left\| \frac{1}{[\mu(x_1)\hat{N}]_{\min}} \begin{bmatrix} \Delta\hat{k} + \frac{\mu(x_1) - \mu^*}{x_1} \sigma_n' \hat{N} - \varphi_{1e} & \Delta\hat{\eta} - \varphi_{2e} & 0 & 0 \end{bmatrix} x_a \right\| \\ &\leq \left\| \frac{1}{[\mu(x_1)\hat{N}]_{\min}} \begin{bmatrix} \Delta\hat{k}_{\max} + \mu_{x_1}^{\max} \sigma_n' \Delta\hat{N}_{\max} + \varphi_{1e} & \Delta\hat{\eta}_{\max} + \varphi_{2e} & 0 & 0 \end{bmatrix} x_a \right\|, \end{aligned}$$

where the bound $\mu_{x_1}^{\max} = \left| \frac{\partial \mu(x_1)}{\partial x_1} \right|_{\max}$ corresponds to the maximum absolute softening slope of the friction. The subscript ‘max’ denotes the maximum variation in absolute term from the respective nominal values.

Finally, one gets the bounds of the variation coefficient $\Delta B(t, x_a)$ and perturbation $h(t, x_a)$ in Eq. (F.23) as:

$$0 \leq \Delta B(t, x_a), \quad \|h(t, x_a)\| \leq \|Gx_a\|, \quad (\text{F.26})$$

with G defined as:

$$G = \frac{1}{[\mu(x_1)\hat{N}]_{\min}} \begin{bmatrix} \Delta\hat{k}_{\max} + \mu_{x_1}^{\max} \sigma_n' \Delta\hat{N}_{\max} + \hat{\varphi}_{1e} & \Delta\hat{\eta}_{\max} + \hat{\varphi}_{2e} & 0 & 0 \end{bmatrix}. \quad (\text{F.27})$$

Inspired from the original LQR control (see Lewis et al., 2012), the e-LQR control input p designed for the augmented system of Eq. (F.23) is given by:

$$p = -R^{-1} B_0^T \Theta x_a = -[k_1 \quad k_2 \quad k_3 \quad k_4] x_a, \quad (\text{F.28})$$

where R is a *positive definite* matrix to be chosen and Θ the *positive-definite* solution of the following Continuous Algebraic Riccati Equation (CARE):

$$A_0^T \Theta + \Theta A_0 - \Theta B_0 R^{-1} B_0^T \Theta = -Q, \quad (\text{F.29})$$

with

$$Q = Q_0 + \|R^{1/2}\|^2 G^T G, \quad (\text{F.30})$$

and Q_0 a *positive definite* matrix to be chosen.

The following Theorem states the main result of the e-LQR control.

Theorem 2 *The origin of the augmented closed-loop system of Eq. (F.23) is globally exponentially stable, with the presence of the Lipschitz w.r.t. the states perturbation $h(t, x_a)$ and positive semi-definite term $\Delta B(t, x_a)$ satisfying Eq. (F.26) and Eq. (F.27), when the control input p takes the form of Eq. (F.28)-(F.30).*

As a consequence of Theorem 2, the slip, δ , and slip-rate, $\dot{\delta}$, of the original system of Eq. (F.1) are driven globally and exponentially to a desired constant reference $r(t) = r_0$. For the proof of Theorem 2, see Section 3.2.

F.2.3 Control strategies comparison

The presented control strategies have been designed to achieve aseismic response in the spring-slider model (see Eq. (F.1)) by tracking a slow reference, robustly and by using a continuous control signal. Now, some properties of each control strategy are discussed in the following, highlighting the differences between them.

Sliding-mode based control:

- The origin of the system of Eq. (F.10), with bounded control coefficient $\beta(t, e)$ and Lipschitz w.r.t. the time perturbation $h(t, e)$ assumed as in Eq. (F.12), is locally stable in finite-time.
- Calculation of the gains for the 2-CTA (see Eq. (F.13)) and 2-DIA (see Eq. (F.14)) controllers can be obtained using a Sum Of Square algorithm for the 2-CTA (see Torres-González et al., 2017) and by doing a maximization of homogeneous functions for the 2-DIA (see Gutiérrez-Oribio et al., 2021; Mercado-Uribe & Moreno, 2020).
- The reference signal $r(t)$ that can be tracked, has to be chosen as $|r^{(3)}(t)| \leq \gamma$ with a positive constant γ , in order to fulfill the assumptions in Eq. (F.12). Note that the selected reference given by Eq. (F.4) fulfills this condition for all $t \in [0, t_{\text{op}}]$.
- Systems of Eq. (F.15) and Eq. (F.16) are homogeneous vector-set of degree $d = -1$ and weights $(r_1, r_2, r_3) = (3, 2, 1)$. Due to homogeneity properties (Levant, 2005), the theoretical precision of the states after the transient are $|e_1| < \Delta_1 T_s^3$, $|e_2| < \Delta_2 T_s^2$ and $|e_3| < \Delta_3 T_s$, where $\Delta_i > 0$ with $i = \{1, \dots, 3\}$ and T_s the sampling time.

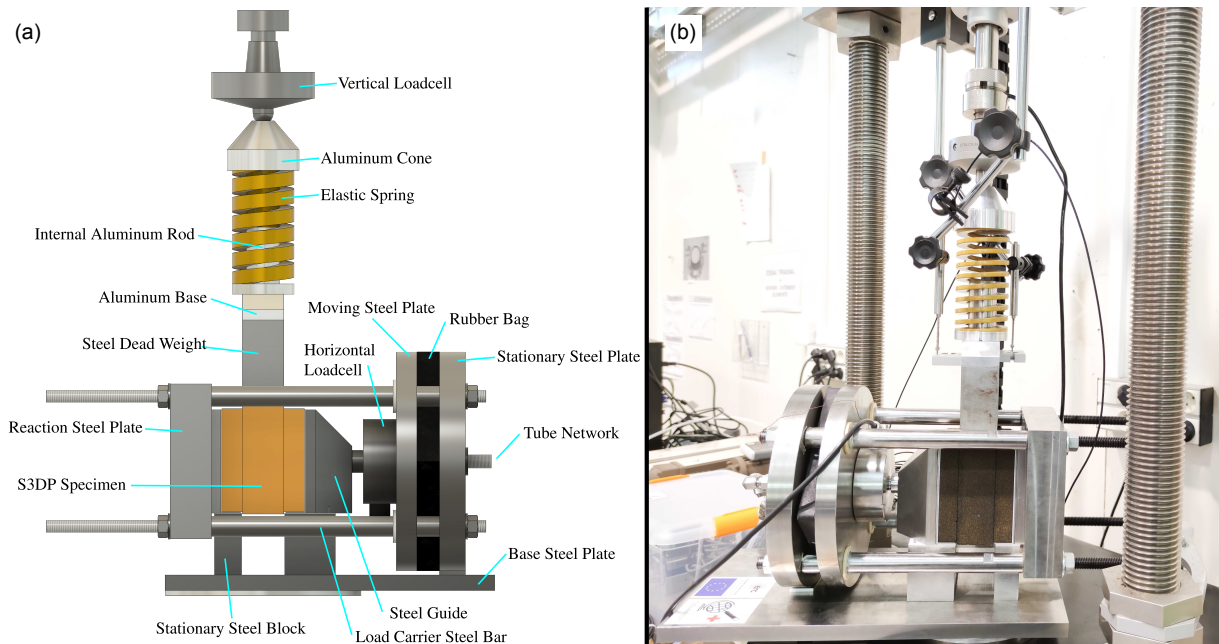


Figure F.2 – Double-direct shear apparatus of decimetric scale: (a) Schematic figure, (b) Real configuration.

LQR-based control:

- The origin of the system of Eq. (F.23), with positive semi-definite variation coefficient $\Delta B(t, x_a)$ and Lipschitz w.r.t. the states $h(t, x_a)$ assumed as in Eq. (F.26), is globally exponentially stable.
- Calculation of the gains for the e-LQR control given by Eq. (F.28) are obtained by solving the CARE in Eq. (F.29)-(F.30).
- The classical version of an integral control will track a constant reference, i.e. $r(t) = r_0$ (see for example Chapter 12 in Khalil, 2013). According to the internal model principle (see Francis & Wonham, 1976), the use of a double integrator (see Eq. (F.17)) will be able to follow linear time references, i.e. $r(t) = \alpha_1 t + \alpha_2$, with some $\alpha_1, \alpha_2 \in \mathfrak{R}$. The steady state error of the target reference given by Eq. (F.4) using the presented control will not be zero, but it will be improved by using this double integrator scheme. In addition, this error can become even smaller by increasing the e-LQR integral gains (see Chapter 3 for more details).

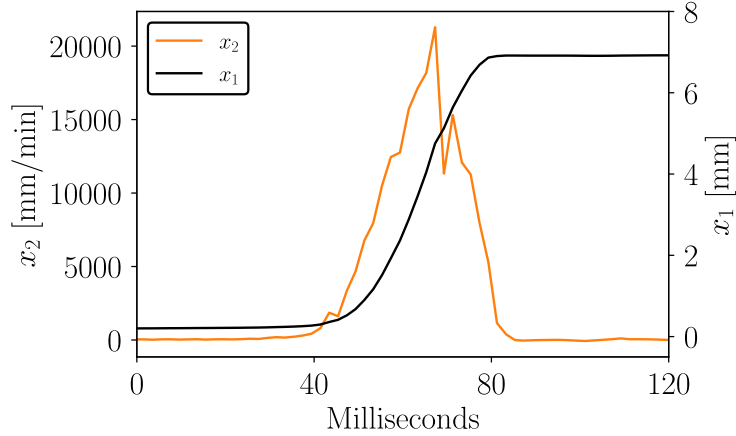


Figure F.3 – Dynamic instability in the laboratory using a triplet apparatus of decimetric scale (see also Section 5.6).

F.3 Experimental comparison of the performance of three continuous-time robust controllers

In order to illustrate the performance of all the previously designed control algorithms, laboratory experiments have been conducted in the experimental configuration introduced in Chapter 5. The experimental setup (see Figure F.2), the loading procedure, the material of the specimen, the elastic spring, the available measurements, and the capabilities of the developed *LabVIEW* code are the same as indicated in Sections 5.2 and 5.3.

Without any controller, an earthquake-like response (equivalent to fast seismic slip) is expected in the laboratory (see also Section 5.6). During this dynamic experiment, the stored elastic energy of the spring ($k_{\text{spring}} = 45.1 \text{ N/mm}$ installed in series with the sheared middle block) is released abruptly. In Figure F.3, the displacement (black line) and velocity (orange line) of the mobilized (middle) block is plotted with respect to time for a single dynamic event (see also Figure 5.5). We can observe that during this “laboratory earthquake”, the block slides $\sim 7 \text{ mm}$ in $\sim 50 \text{ ms}$ developing a maximum velocity of $\sim 20000 \text{ mm/min}$ ($\approx 0.35 \text{ m/s}$, see also Figure 5.5b).

To prevent this “laboratory earthquake” and drive the mobilized (middle) block to a new equilibrium point of lower energy, assuring stability of the experimental setup, all the time, the (a) *2-CTA* (see Eq. (F.9) and Eq. (F.13)), (b) *2-DIA* (see Eq. (F.9) and Eq. (F.14)) and (c) *e-LQR* (see Eq. (F.28) and Eq. (F.17)) control strategies, developed in Section F.2, have been employed. The nominal values of the mechanical and frictional parameters needed for the control design are given in Table F.1. In contrast to the control

Table F.1 – Nominal values of the mechanical and frictional properties needed for the design of the robust continuous-time controllers described in Section F.2.

Parameter	Description	Units	Value
m	mobilized mass per sheared interface	g	1385
k	spring stiffness per sheared interface	N/mm	22.55
L_{ac}	effective length of frictional interface	mm	100
σ'_n	effective normal stress	kPa	100
μ_{res}	residual friction	-	0.4
$\Delta\mu$	friction drop	-	0.17
d_c^{sw}	characteristic SW distance	mm	2.5
d_{max}	maximum target displacement	mm	7.5
t_{op}	operation time of control strategy	hours	1
T_s	sampling time	ms	1

experiments presented in Chapter 6, due to the (relatively) fast sampling time ($T_s = 1$ ms) in comparison with the characteristic time of the dynamic instability ($t_{inst} \approx 50$ ms, i.e. $t_{inst}/T_s = 50$, see Figure F.3), the digitization of the aforementioned continuous-time algorithms is expected to be effective (for more details see Section 5.7 and also Åström & Wittenmark, 1997; Franklin et al., 1998). Therefore, each control algorithm is implemented in the *LabVIEW* code by discretizing their respective differential equations ((a) Eq. (F.13)b, (b) Eq. (F.14)b, (c) Eq. (F.17)) using the Forward Euler Method. More specifically, the controllers' gains are selected as:

- *2-CTA*: $k_1 = 7.5$, $k_2 = 5$, $k_3 = 1.66 \times 10^{-4}$, $k_4 = 7.92 \times 10^{-5}$, $\lambda = 500$, $\mu_0 = \mu_{res}$ and $\hat{N}_0 = \frac{L_{ac}^2}{m}$;
- *2-DIA*: $k_1 = 2$, $k_2 = 5$, $k_3 = 1.44 \times 10^{-4}$, $k_4 = 0$, $\lambda = 500$, $\mu_0 = \mu_{res}$ and $\hat{N}_0 = \frac{L_{ac}^2}{m}$;
- *e-LQR*: $k_1 = 5 \times 10^6$, $k_2 = 3 \times 10^9$, $k_3 = 3 \times 10^8$ and $k_4 = 1 \times 10^6$;

where μ_0 , L_{ac} and m are provided by Table F.1. The reference signal given by Eq. (F.4) is defined with $d_{max} = 7.5$ mm and $t_{op} = 1$ h (see also Table F.1).

The lab-fault system depicted in Figure F.2 only measures the slip, x_1 , of the middle block using two LVDTs (see Sections 5.2 and 5.3 for more details). In order to obtain its slip rate, x_2 , required by the controllers, a robust exact filtering differentiator has been

adopted as follows (Levant & Livne, 2020):

$$\begin{aligned}
\dot{w}_1 &= -5\lambda_d^{\frac{1}{5}} [w_1]^{\frac{4}{5}} + w_2, \\
\dot{w}_2 &= -10.03\lambda_d^{\frac{2}{5}} [w_1]^{\frac{3}{5}} + \hat{x}_1 - x_1, \\
\dot{\hat{x}}_1 &= -9.3\lambda_d^{\frac{3}{5}} [w_1]^{\frac{2}{5}} + \hat{x}_2, \\
\dot{\hat{x}}_2 &= -4.57\lambda_d^{\frac{4}{5}} [w_1]^{\frac{1}{5}} + \hat{x}_3, \\
\dot{\hat{x}}_3 &= -1.1\lambda_d [w_1]^0,
\end{aligned} \tag{F.31}$$

with $\lambda_d = 1 \times 10^{-5}$. In order to implement this differentiator in *LabVIEW*, the above differential equations (see Eq. (F.31)) are discretized using again the Forward Euler Method. Therefore, all the designed control algorithms, p , have been implemented as functions of the estimated slip and slip rate, i.e. $p(\hat{x}_1, \hat{x}_2)$ instead of $p(x_1, x_2)$. This would reduce the possible noise from the estimations due to the LVDTs measurements.

Remark 2 *The differentiator given by Eq. (F.31) provides the second derivative of the input $x_1(t)$ while filtering the signal with a second order filter, if $|x_1^{(3)}(t)| \leq L_d$ and $\lambda_d > L_d$ (see proof in Levant & Livne, 2020). Notice that we are aware of the separation principle problem with nonlinear systems; however, the purpose here consists of experimentally showing the convergence of the full closed loop-system (plant, control and differentiator).*

The response of the laboratory system, during the control experiments, using each of the robust continuous-time control algorithms, developed in Section F.2, is displayed in Figure F.4. We can observe that all the controllers are able to fulfill the task of controlling the earthquake-like instability (see Figure F.3) and drive the system slowly to a new equilibrium point of lower energy (see Figure F.4a-b) by increasing the response time of the system (from ~ 50 ms to ~ 1 h). It takes $t_{ss} \approx 10$ min for each controller to drive the system to a steady state (see inset of Figure F.4a). Focusing on Figure F.4b, during each control strategy, 4 orders of magnitude lower velocities are developed in comparison with the unstable case (see Figure F.3). Finally, Figure F.4c shows the three continuous control signals used for the tracking and Figure F.4d how the measured friction coefficient evolves in terms of slip. Observe that the friction coefficient is always bounded and always higher than the minimum value used for designing the controller ($\mu_{res} = 0.4$).

Assuring a fair comparison between the three presented control strategies is challenging due to the presence of different uncertainties in each experiment. In particular, the tested samples are not the same between each test, the experiments do not initiate at the

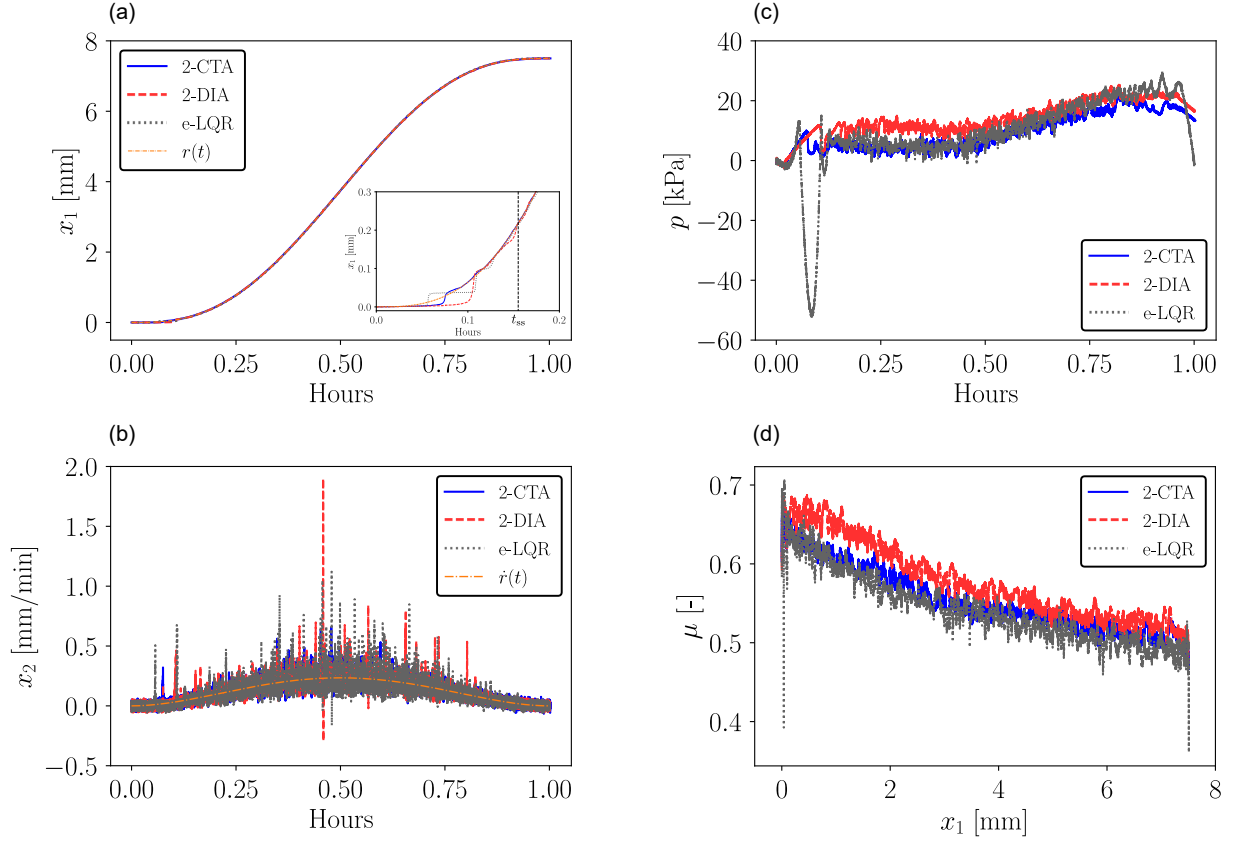


Figure F.4 – (a) Displacement, (b) velocity, and (c) input pressure change in terms of time during the control experiment for the three designed controllers. The reference tracking trajectories (dotted orange curves) are also presented for comparison. (d) Coefficient of friction as a function of displacement during the control experiment for the three designed controllers.

same exact point and better gains may be found to tune the controllers. Furthermore, as discussed in Section F.2, both control strategies present different theoretical properties.

Nevertheless, to attempt a further comparison between the three tested control strategies, the mean integrated error and the maximum absolute error of the slip (Figure F.5a-b) and slip-rate (Figure F.5c-d), as well as the average power of the control input (Figure F.5e) have been calculated and presented in Figure F.5. As initial point for the calculations, we consider the point where the system has reached a steady state, namely at time $t = t_{ss}$ (see inset of Figure F.4a). All these results are normalized w.r.t. the *e-LQR* case. The best behavior (smallest errors and least power) is observed for the *2-CTA* case. However, all the control algorithms show negligible errors proving the robustness of each strategy in uncertainties and unmodelled dynamics. More specifically, the maximum po-

sition error is of the order of ~ 38 microns (see Figure F.5b), which can be considered negligible in a total slip of ~ 7.5 mm. Similarly, the maximum velocity error is of the order of ~ 0.9 mm/min, which is 20000 times smaller than the maximum slip-rate developed during the earthquake-like event (see Figure F.3).

Notice that the lab-fault dynamics can be upscaled to obtain the real-fault dynamics under appropriate scaling laws (see Appendix E). This upscaling will result in a real case scenario almost identical to the one presented in Section 6.3.

To conclude, in this Appendix, the robust control of earthquake-like instabilities in the laboratory was addressed. The controllers were designed to perform tracking of a slow reference trajectory based on a spring-slider reduced-order model. Two kinds of controllers were presented: the first one was based on sliding mode theory, while the second one on LQR control. The first one results in local finite-time convergence of the tracking error, while the other one presents global exponential stability. Both controllers were designed to generate a continuous control signal and use integral action to compensate different kinds of perturbations. The presented algorithms were implemented, tested and compared in a specially designed experimental apparatus, showing that both types of controllers succeed in achieving tracking regardless the presence of unmodelled dynamics and parameter uncertainties in the real system. For the record, the *2-CTA* sliding-mode control algorithm achieved the best behavior.

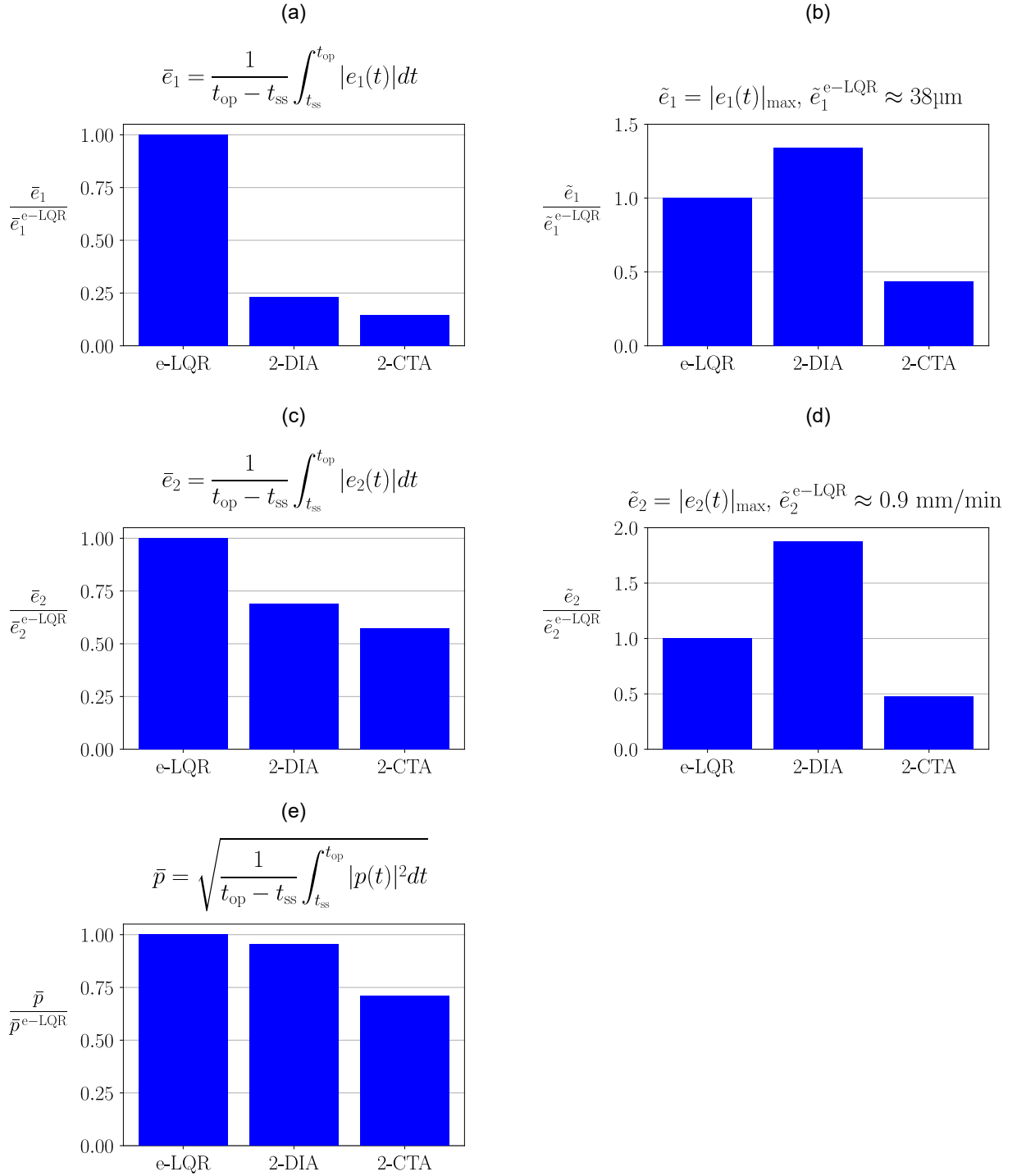


Figure F.5 – The mean integrated error and the maximum absolute error of the slip [(a) and (b), respectively] and slip-rate [(c) and (d), respectively], as well as the average power of the control input (e) are plotted for each control strategy. All the values are normalized w.r.t. the *e-LQR* case.

Titre : Contrôle des séismes en utilisant des techniques pour stimuler les failles sismiques au laboratoire

Mot clés : Controlling earthQuakes (CoQuake) ; Mécanique des Failles ; Contrôle Robuste ; Expériences de Substitution ; Appareil de Cisaillement Double-Direct ; Sismicité Induite.

Résumé : La sismicité anthropique a augmenté depuis les dernières décennies en raison de l'intense activité humaine pour la production d'énergie. Cependant, malgré le fait que la simple injection de fluides peut induire/déclencher des tremblements de terre, dans cette thèse, nous montrons que l'interaction stratégique entre les extractions et les injections de fluides peut contrôler de tels événements sismiques et éventuellement les prévenir. Plus précisément, nous construisons un nouveau cadre mathématique de contrôle robuste des tremblements de terre, qui est ensuite exploité dans des simulations numériques de failles de glissement et de réservoirs de gaz, ainsi que dans de nouvelles expériences de laboratoire à l'échelle décimétrique. Tout d'abord, les paramètres clés qui constituent une stratégie conventionnelle d'atténuation des séismes sont identifiés. Des expériences de substitution sur du papier poreux absorbant montrent que sans la connaissance précise des propriétés de la faille, les injections de fluide risquent de nucléer plus rapidement un grand événement sismique. Afin de faire face à de telles incertitudes, des outils mathématiques rigoureux sont développés en utilisant la théorie moderne du contrôle. Ces outils néces-

sitent un minimum d'informations sur les propriétés de la faille et les caractéristiques de frottement pour assurer la robustesse. Des simulations numériques sur des failles à glissement latéral vérifient que la prévention des séismes est possible, même en présence de processus de diffusion et en l'absence de mesures suffisantes dans le temps et l'espace. En allant plus loin, les techniques de contrôle développées peuvent également être appliquées dans les grands réservoirs de gaz, où la production de gaz souhaitée peut être atteinte en garantissant des niveaux de sismicité acceptables. Enfin, au cours de cette thèse, un nouvel appareil à triplets d'échelle décimétrique a été conçu, construit et calibré en conséquence. Le contrôle de la pression peut être réalisé, dans cet appareil, en temps réel, grâce à un régulateur de pression électro-pneumatique à réponse rapide. Comme preuve de concept, le régulateur développé est branché dans cet appareil et en utilisant des spécimens imprimés en 3D à base de sable (pour promouvoir la répétabilité expérimentale), nous parvenons, pour la première fois, à prévenir les tremblements de terre en laboratoire et à conduire le système de manière aisé vers un point d'équilibre de plus faible énergie.

Title: Controlling earthQuakes (CoQuake) in the laboratory using pertinent fault stimulating techniques

Keywords: Controlling earthQuakes (CoQuake); Fault Mechanics; Robust Control; Surrogate Experiments; Double-Direct Shear Apparatus; Induced Seismicity.

Abstract: Anthropogenic seismicity has been increased since the last decades due to the intense human activity for energy production. However, despite the fact that merely injection of fluids can induce/trigger earthquakes, in this thesis, we show that the strategic interplay between fluid extractions and injections can control such seismic events and eventually prevent them. More specifically, a novel mathematical framework of robust earthquake control is built which in turn is exploited in numerical simulations of strike-slip faults and gas reservoirs, as well as in new laboratory experiments of decimetric scale. First, the key parameters which constitute a conventional earthquake mitigation strategy are identified. Surrogate experiments on absorbent porous paper show that without the precise knowledge of the fault properties, fluid injections risk to nucleate faster a large seismic event. In order to tackle such uncertainties, rigorous mathematical tools are developed using modern control theory. These tools require minimal information of

fault's properties and frictional characteristics to assure robustness. Numerical simulations on strike-slip faults verify that earthquake prevention is possible, even in the presence of diffusion processes and the absence of sufficient measurements both in time and space. Going a step further, the developed control techniques can also be applied in large gas reservoirs, where the desired gas production can be achieved assuring acceptable seismicity levels. Finally, during this thesis, a novel triplet apparatus of decimetric scale has been designed, constructed and calibrated accordingly. Pressure control can be achieved, in this machine, in real-time, through a fast response electro-pneumatic pressure regulator. As a proof of concept, the developed controller is plugged in this apparatus and by using sand-based 3D-printed specimens (to promote experimental repeatability), we manage, for the first time, to prevent laboratory earthquakes and drive the system aseismically to an equilibrium point of lower energy.